Dynamics and Feedback of Massive Binaries in Young Massive Star Clusters

Dynamics and Feedback of Massive Binaries in Young Massive Star Clusters

by
CLAUDE COURNOYER-CLOUTIER, M.Sc., B.Sc.

A Thesis Submitted to the School of Graduate Studies in the Partial Fulfillment of the Requirements for the Degree Doctor of Philosophy

McMaster University

Doctor of Philosophy (2025)
Physics & Astronomy
McMaster University
Hamilton, Ontario, Canada

TITLE:
Dynamics and Feedback of Massive Binaries in Young Massive Star Clusters

AUTHOR:
Claude Cournoyer-Cloutier, M.Sc. (McMaster University), B.Sc. (McGill University)

SUPERVISORS:
Dr. Alison Sills
Professor, Department of Physics & Astronomy,
McMaster University, ON, Canada

Dr. William E. Harris
Professor Emeritus, Department of Physics & Astronomy,
McMaster University, ON, Canada

NUMBER OF PAGES: xviii, 179

ABSTRACT

Star formation is a clustered process, which naturally leads to the formation of binaries and star clusters. This clustering is most important for massive stars, which most often form in dense clusters and in close binaries. Massive stars are the dominant source of energy in young massive star clusters (YMCs) due to the feedback they return to their environments in the form of winds, radiation, and supernovae. The presence of a close companion affects this feedback by triggering mass transfer and changing the subsequent evolution of massive stars. Stellar dynamics within dense star clusters further affect the binaries by modifying their orbits or disrupting them. In this thesis, we use numerical simulations to investigate the interplay between binary stars and their host clusters during star cluster formation. Using initial conditions typical of the disk of the Milky Way, we find that the clusters undergo rapid morphological changes from subcluster mergers driven by the large-scale gas environment during their formation. Expanding our suite of simulations to include initial conditions typical of starburst galaxies, we find that those mergers lead to a decrease in the binary fraction of low and intermediate mass stars, in agreement with the low binary fractions observed in older massive star clusters. Close massive binaries however remain present even in the densest YMCs. We also present the first implementation of feedback from massive interacting binaries coupled to stellar dynamics. We find that mass transfer in binaries enhances feedback in cluster-forming regions, and that this enhancement cannot be accurately predicted by standalone binary evolution simulations due to the effects of nearby stars and gas on the binaries' orbits. We conclude that a treatment of stellar dynamics and mass transfer in binaries are essential to understand the formation of massive star clusters in galaxies.

CO-AUTHORSHIP

Chapters 2, 3, and 4 of this thesis contain original scientific research written by myself, Claude Cournoyer-Cloutier.

Chapter 2 has been published as a peer-reviewed article in the Monthly Notices of the Royal Astronomical Society (MNRAS). The reference for this work is: *Cournoyer-Cloutier, C., Sills, A., Harris, W. E., Appel, S. M., Lewis, S. C., Polak, B., Tran, A., Wilhelm, M. J. C., Mac Low, M.-M., McMillan, S. L. W. and Portegies Zwart, S. 2023. MNRAS Volume 521, pp. 1338–1352.* The second and third authors are my supervisors, Dr. Alison Sills and Dr. William Harris. The fourth through eighth authors, Dr. Sabrina Appel, Dr. Sean Lewis, Dr. Brooke Polak, Dr. Aaron Tran, and Dr. Maite Wilhelm, were at the time of publication graduate students who were along with myself the main users and developers of Torch, the simulation code used in this work. They contributed to the maintenance and development of Torch, and appear in alphabetical order. The remaining authors, Dr. Mordecai-Mark Mac Low, Dr. Stephen McMillan, and Dr. Simon Portegies Zwart, were their respective supervisors, and also appear in alphabetical order. Dr. Mac Low runs the weekly Torch users group meeting and provided feedback on the analysis. All authors provided feedback on the manuscript.

Chapter 3 has been published as a peer-reviewed article in the Astrophysical Journal (ApJ). The reference for this work is: *Cournoyer-Cloutier, C., Sills, A., Harris, W. E., Polak, B., Rieder, S., Andersson, E. P., Appel, S. M., Mac Low, M.-M., McMillan, S. L. W. and Portegies Zwart, S. 2024. ApJ Volume 977, 203.* The second and third authors are Dr. Sills and Dr. Harris. The fourth and fifth authors, Dr. Polak and

Dr. Steven Rieder, made significant contributions to the implementation of the updated stellar dynamics code necessary for this work. The last authors appear in alphabetical order. The sixth and seventh authors, Dr. Eric Andersson and Dr. Appel, contributed to the maintenance and development of Torch. The last three authors are again Dr. Mac Low, Dr. McMillan, and Dr. Portegies Zwart. All authors provided feedback on the manuscript.

Chapter 4 has been accepted for publication in ApJ, with the author list: *Cournoyer-Cloutier, C., Andersson, E. P., Appel, S. M., Lahén, N., Polak, B., Rantala, A., Toonen, S., Sills, A., Rieder, S., Portegies Zwart, S., Mac Low, M.-M., Harris, W. E.* The second through sixth authors are postdoctoral fellows listed in alphabetical order. Dr. Andersson, Dr. Appel, and Dr. Polak contributed to the maintenance and development of Torch. Dr. Natalia Lahén and Dr. Antti Rantala contributed to the conceptual design of the binary interaction code. The remaining authors are faculty members and staff, listed in reverse alphabetical order; the list includes Dr. Sills, Dr. Harris, and Dr. Mac Low. Dr. Silvia Toonen, Dr. Rieder, and Dr. Portegies Zwart provided assistance in adding a new feature to the stellar evolution code SeBa and fixing subsequent bugs. All authors provided feedback on the manuscript.

All previously published or submitted material has been reformatted to conform to the required thesis style. I hereby grant an irrevocable, non-exclusive license to McMaster University and the National Library of Canada to reproduce this material as part of this thesis.

ACKNOWLEDGEMENTS

First and foremost, I would like to extend my heartfelt gratitude to my supervisors, Alison Sills and Bill Harris, for their support over the past six years. Alison, your scientific guidance and your mentorship have been invaluable. Thank you, from the bottom of my heart, for everything you taught me, and for being someone I can trust without reserve. Bill, thank you for broadening my scientific horizons, and for remaining so involved and interested in my project despite how far it grew from your usual research interests. Thank you both for believing in me from the very beginning – none of this would have been possible without you.

My warmest thanks also go to Mordecai-Mark Mac Low. Mordecai, you have been so involved in my research since my very first visit to New York as a not-quite MSc student, and your scientific insights and your support continue to be incredibly helpful – thank you. I am very grateful to Thorsten Naab and Stephen Justham for their hospitality during my visit at the Max Planck Institute for Astrophysics in 2023. You made me feel welcome at MPA from the start, and I cannot wait to be back in a short few months. I would also like to thank Simon Portegies Zwart, who has also been along for the ride since the very beginning – I look forward to many more projects together.

I want to extend a warm thank you to Brooke Polak, Sabrina Appel, and Eric Andersson – working with you is a delight, despite (or maybe because of) our shared frustrations with coding and computing, and I feel privileged to have you as colleagues and friends. I further want to thank James Wadsley, Marta Reina-Campos, Lachlan Lancaster, Ben Keller, and Eric (a second time!) for very engaging scientific discussions. Although our

work together is not part of this thesis, it has been a great source of motivation over the past few months – thank you.

I also want to thank my friends in Hamilton, and back home. My warmest thanks go to Blake, Jeremy, and Veronika, for your precious friendship over the past six years. Although we will be scattered across the globe in a few months, our time together in graduate school will be unforgettable thanks to your friendship. Blake, your positive outlook on life and your drive have been – and continue to be – an inspiration, and I am incredibly grateful for how supportive you have been since the beginning. Jeremy, thank you for being the best academic sibling one might wish for – you made those past six years easy, and I look forward to teasing you about the boat in Lyon when we look at conference pictures in twenty years. Veronika, thank you for being a wonderful friend and office mate, and for always having the best ideas, whether it is starting a water polo team or practicing for our comprehensive exams together.

Marta, you also get a second thank you, this time for your friendship and support – I always feel better after talking with you. Many, many thanks are also owed to Megan and Joey – I am incredibly grateful for your friendship, and working closely with you both for the introductory physics courses has been a pleasure. Kate, thank you for many conversations over the years about baking, cats, and stellar models – sharing an office with you for the past few years has been wonderful. Isabella and Zena, you have been a breath of fresh air this past year, and working closely with you has been incredibly rewarding – thank you. I would also like to thank Jacqueline, Jennifer, and Taavishi for your warm friendship, as well as Dylan, Erik, Hector, Lauren, and Rachel. You have all made my time in Hamilton wonderful.

I would like to extend a very warm thank you to Justine, Jeanne, Cédric, Pier-Alain, Marie-Ève, Antoine, Laurence, and Séverine, for being so curious about my research and so supportive, despite astrophysics being so far from your usual interests. I could not wish for better friends.

Lastly, I want to extend a heartfelt thank you to my parents, Claire and Pierre, for their support over the years. Merci de m'avoir toujours encouragée à suivre mes rêves.

Si beau le monde
À la fin qui s'y attardera
Ici, tout en bas
Qui d'autre se relèvera
Pour regarder les étoiles

La mort des étoiles
Mélanie & Stéphanie Boulay

CONTENTS

LIST OF FIGURES

LIST OF TABLES

ABBREVIATIONS & ACRONYMS

Science terms

AMR	Adaptive mesh refinement
CE	Common envelope
CFE	Cluster formation efficiency
FUV	Far ultraviolet
GC(s)	Globular cluster(s)
GMC(s)	Giant molecular cloud(s)
HG	Hertzsprung gap
HPC	High performance computing
IMF	Initial mass function
IR	Infrared
ISM	Interstellar medium
KS	Kolmogorov-Smirnov
LBV	Luminous blue variable
LMC	Large Magellanic Cloud
MHD	Magnetohydrodynamics
MS	Main sequence

MT	Mass transfer
MW	Milky Way
PDF	Probability distribution function
RLOF	Roche lobe overflow
RMHD	Radiation magnetohydrodynamics
SF	Star formation
SFE	Star formation efficiency
SFR	Star formation rate
SMC	Small Magellanic Cloud
SN(e)	Supernova(e)
UV	Ultraviolet
VMS	Very massive star
Wd	Westerlund
YMC(s)	Young massive cluster(s)
ZAMS	Zero-age main sequence

Software

AMUSE	Astrophysical Multipurpose Software Environment
BPASS	Binary Population and Spectral Synthesis
DBSCAN	Density-Based Spatial Clustering of Applications with Noise
MESA	Module for Experiments in Stellar Astrophysics

Surveys & telescopes

ALMA	Atacama Large Millimeter/submillimeter Array
FLAMES	Fibre Large Array Multi Element Spectrograph
HST	Hubble Space Telescope
JWST	James Webb Space Telescope
LEGUS	Legacy ExtraGalactic UV Survey
MUSE	Multi Unit Spectroscopic Explorer

MYStIX Massive Young Star-Forming Complex Study in Infrared and X-Ray

NGC New General Catalogue of Nebulae and Clusters of Stars

PHANGS Physics at High Angular resolution in Nearby Galaxies

VLT Very Large Telescope

Funding agencies, journals, & organizations

ACCESS Advanced Cyberinfrastructure Coordination Ecosystem: Services & Support

ApJ The Astrophysical Journal

CGS Canada Graduate Scholarship

ESA European Space Agency

ESO European Southern Observatory

MNRAS Monthly Notices of the Royal Astronomical Society

NASA National Aeronautics and Space Administration

NOVA Nederlandse Onderzoekschool Voor Astronomie (Netherlands Research School for Astronomy)

NSERC Natural Sciences and Engineering Research Council of Canada

NSF National Science Foundation

NWO Nederlandse Organisatie voor Wetenschappelijk Onderzoek (Dutch Research Council)

SURF Samenwerkende Universitaire Rekenfaciliteiten (Cooperating University Computing Facilities)

TACC Texas Advanced Computing Center

CHAPTER 1

INTRODUCTION

The formation of massive clusters of stars within galaxies is a complex physics problem, which is challenging to tackle both observationally and numerically due to the large range of physical processes, spatial scales, and timescales involved. Understanding the formation of massive star clusters is key to understanding star formation, stellar evolution, and galaxy evolution. Globular clusters (GCs) – massive, dense clusters of stars that have survived for billions of years – are excellent tracers of galaxy assembly and evolution (Harris 1991; Renaud 2018). In the local Universe, most star formation proceeds in a clustered fashion (Lada & Lada 2003; Portegies Zwart et al. 2010), and regions with abundant star formation tend to form a high fraction of their stars in dense, massive star clusters (Adamo et al. 2020a, and references therein). Massive stars ($M \gtrsim 8$ M$_\odot$), which regulate star formation (e.g., Mac Low & Klessen 2004; McKee & Ostriker 2007) and enrich the interstellar medium (ISM) in galaxies (e.g., Woosley & Weaver 1995; Kobayashi et al. 2006) due to their energetic winds, intense radiation, and supernovae (SNe), often form within young massive star clusters (YMCs, with masses $\gtrsim 10^4$ M$_\odot$). YMCs therefore return significant amounts of energy and matter enriched by stellar nucleosynthesis to their host galaxy through stellar feedback. Whether massive stars inject this energy and matter within the cluster or up to hundreds of parsecs away depends on the effects of stellar dynamics within the cluster, which may result in the production of runaway stars (Naab & Ostriker 2017, and references therein). Such effects are expected to become more important in the presence of rich populations of binary stars, which are observed for massive stars in YMCs (Moe & Di Stefano 2017, and references therein).

Recent observations with the *James Webb Space Telescope* (JWST) have improved our understanding of GC formation, by revealing massive and compact star clusters in the distant Universe (Vanzella et al. 2023; Adamo et al. 2024), which may have formed as early as 13 billions of years ago, shortly after the first galaxies. Those observations join a growing body of evidence proposing that GCs formed at high redshift in a similar manner as YMCs form in the local Universe. Observations of young clusters at high z remain rare, however, and it is challenging to compare them to recent observations of YMCs forming in nearby star-forming galaxies (e.g. He et al. 2022; Sun et al. 2024). Due to the very large distances separating us from those massive clusters, observations cannot resolve individual stars within them, and must estimate the physical properties of the clusters – such as their stellar mass and age – from the total luminosity in ultraviolet (UV), infrared (IR) or radio wavelengths. Although some YMCs within the Milky Way, and the Large (LMC) and Small (SMC) Magellanic Clouds, are near enough to observe individual stars within them (e.g. R136, shown in Figure 1.1), they only inhabit the low-mass end of the YMC mass distribution. Due to those challenges, observations are limited in their ability to shed light on the physical processes driving the formation of massive star clusters.

Numerical simulations are a natural tool to study the physics behind massive cluster formation. YMCs are however challenging to simulate: their formation is dictated by the interactions between turbulent, magnetized gas – ranging from low-density plasma to high-density star-forming gas – and up to millions of stars through gravity, magnetohydrodynamics (MHD), and radiation. The interplay between the stars and their environment is highly complex, as stars influence the nearby gas through feedback – mechanical and radiative processes that heat up and push away the gas from star-forming regions. Simulations must also cover a large range of timescales, from the orbital timescales of binary stars, which can complete an orbit in a day, to the evolutionary timescales of stars, which evolve over millions of years.

This problem is made even more complex by the fact that almost all massive stars form in binaries (Moe & Di Stefano 2017), which can affect the evolution of their host cluster in a surprising range of ways. Massive binaries are important for the gravitational interactions between the stars in the cluster. They are the main source of massive, fast-moving stars escaping from their birth cluster, known as runaway stars: close encounters between pairs of massive binaries can result in the ejection of one or more massive stars from the cluster (Poveda et al. 1967) while the kick from one star in a massive binary exploding as a SN can eject the other star from the cluster (Blaauw 1961). Such massive

FIGURE 1.1: The young massive star cluster R136, in the NGC 2070 cluster-forming region within 30 Doradus, in the LMC, imaged with JWST in the near-IR. Radiative and wind feedback from the central cluster (in light blue) has begun to clear away the surrounding gas, shown in earthy tones. *Image credit: NASA, ESA, CSA, STScI, Webb ERO Production Team.*

runaways are important for the long-term evolution of galaxies (Andersson et al. 2020, 2023; Steinwandel et al. 2023). Most massive binaries accrete material from a companion over their lifetimes (Sana et al. 2012), which increases the amount of UV radiation they emit (Götberg et al. 2018, 2020) as the masses and structures of both stars in the binary change. This mass transfer further changes the time at which both stars explode as SNe (Zapartas et al. 2017) and may even change which stars successfully explode or directly collapse into a neutron star or black hole (Woosley 2019).

The motivation for this work thus arises from two (simplified) statements about star formation: stars form in clusters, and stars form in binaries. Numerical models however usually only account for either clustered star formation – with MHD and feedback, and sometimes stellar dynamics – or binaries with stellar dynamics and binary stellar evolution, in clusters devoid of gas. This dichotomy is due to the computational challenges associated with modeling binaries in young massive clusters, arising from the large range

of physical scales and timescales outlined above. The niche of this thesis is thus *an investigation of the role played by massive binary stars in the formation of star clusters, due to their impact on stellar dynamics and stellar feedback.* Because this research sits at the intersection of different fields, the introduction to this thesis must be broad in nature, by discussing star formation, stellar dynamics, and stellar evolution and feedback. This chapter therefore reviews our current understanding of massive star cluster formation in Section 1.1, provides an overview of the relevant background on binary stars, their dynamics, and their evolution in Section 1.2, and presents the specific research questions tackled by this thesis and the numerical techniques used to address them in Section 1.3.

1.1 Massive star cluster formation

One of the central topics of this thesis is the question of massive star cluster formation. Observations confirm that massive star clusters formed across cosmic time in environments with high star formation rates (see Adamo et al. 2020a, for a recent review). Few massive star clusters are currently forming or have recently formed in the Milky Way, however (see, e.g., Portegies Zwart et al. 2010). Understanding the physical processes driving the formation of YMCs and GC progenitors at high redshift therefore requires us to use tools beyond observations in our Galaxy. To understand how massive star clusters form, we need a combination of resolved observations of the gas and stellar populations in massive star-forming regions in the Local Group, multi-wavelength observations of (very) massive young clusters in other galaxies, and complex, multi-physics simulations.

Stars form in a clustered fashion (Lada & Lada 2003) within giant clouds of molecular hydrogen (GMCs); if sufficiently many stars form within a sufficiently compact region, the stars will remain part of a bound star cluster. Understanding the physics driving the formation of massive star clusters therefore requires an understanding of both star formation and the processes opposing star formation. High-resolution observations of individual stars and star-forming gas in YMCs in the Milky Way and its satellites, summarized in Section 1.1.1, provide us with information about the assembly of YMCs within GMCs. Observations of populations of YMCs in star-forming galaxies, presented in Section 1.1.2, allow us to probe a much larger population of YMCs forming across a wide range of environments. We know from observations that star clusters form in dense gas, and their formation is regulated by the interplay between gravity and feedback; the physical processes promoting and preventing star formation are presented respectively in Sections 1.1.3 and 1.1.4.

1.1.1 Resolved observations of cluster-forming regions

The sample of YMCs for which we can obtain spatial-kinematic information about individual stars is limited to the Milky Way, the LMC and the SMC, which in turn limits it to YMCs with masses below 10^5 $M_\odot$ (Portegies Zwart et al. 2010). The proximity of those clusters however enables observers to glean information about the stars' properties – such as their luminosity, temperature, mass, wind mass loss rate, and age – as well as their motion in two or three dimensions. The kinematic information can then be used to infer the incidence of binary stars as well as probe the clusters' formation processes and early evolution. This information can be combined with observations of the gas in which young clusters are embedded to draw a more complete picture of cluster formation.

Although the lower mass limit for a cluster to be considered a YMC is often taken to be 10^4 $M_\odot$ (see, e.g., Portegies Zwart et al. 2010; Krumholz et al. 2019), there is no fundamental distinction between YMCs and lower mass clusters. Many cluster-forming regions in the Milky Way fail to meet this mass criterion for any given embedded cluster but nonetheless host several clusters more massive than 10^3 $M_\odot$, which themselves contain several massive stars. Such cluster-forming regions will be included in the discussion presented in the section below, in the context of the insights they provide on YMC formation. Few young ($\lesssim 5$ Myr) clusters in the Milky Way have present-day stellar masses above 10^4 $M_\odot$, although the complete list of YMCs in the Milky Way is uncertain due to extinction in regions of abundant star formation – such as the Galactic centre – and the discrepancy between different mass estimates for the same cluster. This is illustrated by the differences between the Galactic YMC lists in the reviews by Portegies Zwart et al. (2010) and Krumholz et al. (2019), for example. We nonetheless present in Table 1.1 a list of well-known Galactic YMCs with their stellar mass and half-mass radius. The table also includes R136, in the LMC, which is the most massive YMC in the Local Group.

The *Hubble Space Telescope* (HST) has been used extensively to study YMCs and lower mass young clusters in the Milky Way, with imaging in visible and near-UV light. An HST false-colour image of the Galactic YMC Westerlund (Wd) 2 is presented in Figure 1.2. The presence of gas and dust in cluster-forming regions has however limited those studies to either exposed stars, or bright, embedded stars affected by reddening. In the last few years, observations conducted with JWST have complemented those previous studies with information about the gas shrouding the clusters (in the mid-IR) and the stars embedded in this gas (in the near-IR). Spectroscopic observations conducted on the *Very Large Telescope* (VLT) with the *Fibre Large Array Multi Element Spectrograph*

Name		Galaxy	M_* ($M_\odot$)	$r_{\rm eff}$ (pc)	Notes
R136	(1, 2)	LMC	6.0 x 10^4	1.7	Central cluster only
Westerlund 1	(3)	MW	4.9 x 10^4	1.5	
Westerlund 2	(4)	MW	2.8 x 10^4	0.9	Main clump only
Arches	(5)	MW	2.0 x 10^4	0.4	
NGC 3603	(6)	MW	1.2 x 10^4	0.8	

TABLE 1.1: Stellar masses and effective radii of young massive star clusters within the Milky Way and LMC. *References: (1) Hunter et al. 1995, (2) McLaughlin & van der Marel 2005, (3) Gennaro et al. 2011, (4) Zeidler et al. 2017, (5) Espinoza et al. 2009, (6) Harayama et al. 2008.*

(FLAMES) and *Multi Unit Spectroscopic Explorer* (MUSE) optical spectrographs provide valuable information about the stars. The spectra can be used to study the stars' composition and wind properties, but also to study kinematics through line-of-sight velocities and to probe the presence of spectroscopic binaries due to variable radial velocities. An interesting insight into YMC formation and early evolution gained via those star-by-star observations is regarding the stellar initial mass function (IMF). Although the IMF appears mostly universal, as it is broadly set by gas physics (see Hennebelle & Grudić 2024, for a recent review), it may be top-heavy in YMCs: there is evidence for an excess of massive stars in the central regions of Wd 1 (Brandner et al. 2008; Lim et al. 2013), in YMCs close to the Galactic centre (such as the Arches cluster, Figer et al. 1999; Hosek et al. 2019) and in the 30 Doradus starburst region, within which R136 is located (Schneider et al. 2018). Several physical processes beyond a genuine variation in the shape of the IMF could explain those observations, however, such as the effects of dynamical mass segregation (see Section 1.2.2) or the presence of binary interaction products (see Section 1.2.3). Another alternative explanation for this excess of massive stars would be a bottom-light IMF, as inferred by Baumgardt et al. (2023) for GCs.

The *Gaia* mission has also provided exquisite five-dimensional spatial-kinematic information about nearby stars in young clusters. Observations of the stars' spatial-kinematic properties reveals evidence of the ongoing hierarchical assembly of massive clusters in the Milky Way. The process of hierarchical cluster assembly, which proceeds from the merging of subclusters of stars partly or fully embedded within their shared parent GMC, is discussed in more detail in Section 1.1.3. The persistence of spatial-kinematic

FIGURE 1.2: The young massive cluster Westerlund 2 imaged with HST. The image is a composite of blue, red, and near-IR filters for the cluster stars, and blue and red filters for the nebular gas. *Image credit: NASA, ESA, the Hubble Heritage Team (STScI/AURA), A. Nota (ESA/STScI), and the Westerlund 2 Science Team.*

substructure after the loss of spatial substructure in a sample of *Gaia* Data Release 3 clusters (Arnold & Wright 2024) provides evidence supporting the idea of hierarchical cluster formation as the normal mode of cluster formation. Observations of embedded clusters with relative velocities suggesting a future merger in the Perseus complex (Dalessandro et al. 2021; Della Croce et al. 2023) also support this picture. There is furthermore evidence that several YMCs are growing via ongoing mergers with smaller clusters located within the same cluster-forming region; this is the case for Wd 1 (Gennaro et al. 2011), Wd 2 (Zeidler et al. 2015, 2021), and R136 (Sabbi et al. 2012; Fahrion & De Marchi 2024). Those mergers may further increase the mass of those YMCs: for example, the stellar mass in the full NGC 2070 cluster-forming region, in which R136 is located, is 8.7 x 10^4 $M_\odot$ (Cignoni et al. 2015), about 45% more than the present-day mass of R136. A JWST false-colour image of R136 and the full NGC 2070 region is provided in Figure 1.1. This image, along with the image of Wd 2 above, illustrates that cluster hierarchical assembly proceeds while the YMCs remain partly embedded in their natal gas clouds. The prevalence of hierarchical cluster formation is confirmed by observations

of the gas in Galactic cluster-forming regions in the mid-IR with *Spitzer* and radio wavelengths with the *Atacama Large Millimeter/submillimeter Array* (ALMA), which have revealed complex, non-symmetric gas structures with shapes and velocity gradients indicative of gas and stars being funneled into a central cluster along filaments (e.g. Hacar et al. 2018; Treviño-Morales et al. 2019; Kumar et al. 2020, 2022; Saha et al. 2022; Liu et al. 2023). Massive stars and dense clusters form preferentially at such intersections of filaments.

Combined with observations of cluster-forming complexes hosting several embedded clusters within the same cluster-forming region (e.g., Kuhn et al. 2014), the observations summarized above paint a picture in which massive clusters form through the hierarchical, substructured collapse of GMCs. In regions with abundant star formation, dense, compact star clusters form within hub-filament systems and merge to form massive clusters. Although it is not possible to confirm observationally whether this formation process scales up to more massive GMCs and YMCs due to the limited sample of YMCs for which we have star-by-star observations – both in terms of the number of observed clusters and in terms of the observed mass range – simulations predict that subcluster mergers do play a central role in the assembly of the most massive YMCs (Howard et al. 2018; Reina-Campos et al. 2025).

1.1.2 Extragalactic observations of young massive clusters

Extending our sample of YMCs and GMCs to other star-forming galaxies increases the number and upper mass limit of observed YMCs by several orders of magnitude. YMCs are an ubiquitous feature of star-forming galaxies, with starburst galaxies hosting very rich populations with very massive YMCs. The most massive YMCs observed in the local Universe have masses around 10^7 $M_\odot$ (Adamo et al. 2020b) and recently-observed likely GC progenitors at high z appear to reach the same masses (e.g., Vanzella et al. 2023; Adamo et al. 2024). We summarize the median properties (per galaxy) of observed extragalactic YMCs in Table 1.2. Over the past ten years, very significant progress has been made in studies of extragalactic YMCs, in large part thanks to HST's *Legacy ExtraGalactic UV Survey* (LEGUS) and the *Physics at High Angular resolution in Nearby Galaxies* (PHANGS) survey with ALMA, HST, JWST and MUSE. Key results and their implications for YMC formation are summarized below.

Star cluster catalogs for a large number of star-forming dwarf, spiral and interacting galaxies were constructed through LEGUS (see Adamo et al. 2017, and the examples below). Studies of the star cluster systems in these galaxies yielded impressively uniform

Name		log M_* ($M_\odot$)	$r_{\rm eff}$ (pc)	Notes
Antennae	(1)	$5.7^{+0.3}_{-0.3}$	$2.3^{+0.8}_{-1.1}$	
M51	(2)	$4.7^{+0.3}_{-0.1}$	$1.1^{+0.2}_{-0.1}$	YMCs with ages below 10 Myr
M82[a]	(3)	$4.4^{+0.5}_{-0.3}$	$1.2^{+0.7}_{-0.4}$	Catalog of 1357 YMCs
M82[b]	(4)	$5.7^{+0.6}_{-0.3}$	$1.6^{+0.8}_{-0.2}$	Catalog of 19 brightest YMCs
M83	(5)	$4.2^{+0.3}_{-0.2}$	$2.5^{+1.2}_{-1.0}$	
NGC 253	(6)	$5.2^{+0.3}_{-0.9}$	$1.3^{+0.2}_{-0.3}$	
NGC 628	(7)	$4.0^{+0.4}_{-0.2}$	$3.1^{+2.2}_{-1.2}$	From LEGUS
NGC 1313	(7)	$4.1^{+0.4}_{-0.3}$	$2.7^{+1.8}_{-1.7}$	From LEGUS
Sunburst Arc	(8)	$6.5^{+0.4}_{-0.5}$	$\leq 7.9^{+14}_{-5.2}$	Upper limits on the radii
Sunrise Arc	(9)	$6.5^{+0.3}_{-0.1}$	$\leq 6.3^{+8.0}_{-0.6}$	Upper limits on the radii
Cosmic Gems	(10)	$6.1^{+0.3}_{-0.1}$	$0.9^{+0.4}_{-0.3}$	

TABLE 1.2: Median stellar masses and radii of YMCs in local (top) and high-z (bottom) star-forming galaxies. When age and mass information were available, the values were calculated only from the young (< 10 Myr) massive (> 10^4 $M_\odot$) clusters; when that was not possible, the median values quoted in the paper were used. The uncertainty corresponds to the 16th and 84th percentile range. *References: (1) He et al. 2022, (2) Chandar et al. 2016, (3) Levy et al. 2024, (4) McCrady & Graham 2007, (5) Ryon et al. 2015, (6) Leroy et al. 2018, (7) Ryon et al. 2017, (8) Vanzella et al. 2022, (9) Vanzella et al. 2023, (10) Adamo et al. 2024.*

cluster properties, although there is variation from galaxy to galaxy in the number of clusters and the mass of the most massive YMCs. The cluster initial mass function, described as the power law

$$\frac{dN}{dM} \propto M^{\alpha} \tag{1.1}$$

yields a power-law index consistent with $\alpha = -2$ for the grand-design spiral NGC 628 (Adamo et al. 2017), the interacting spiral M51 (Messa et al. 2018) and a sample of 19 dwarf and irregular galaxies (Cook et al. 2019). One of those dwarfs, UGCA 281, is shown in a false-colour image in Figure 1.3. The presence of a galaxy-dependent upper mass limit, or truncation mass, is debated (see discussion in Adamo et al. 2020a). The clusters within the LEGUS sample also appear to follow a universal mass-radius relation from cluster masses $\lesssim$ 10^3 $M_\odot$ to $\gtrsim$ 10^5 $M_\odot$, with

$$R \propto M^{0.18} \tag{1.2}$$

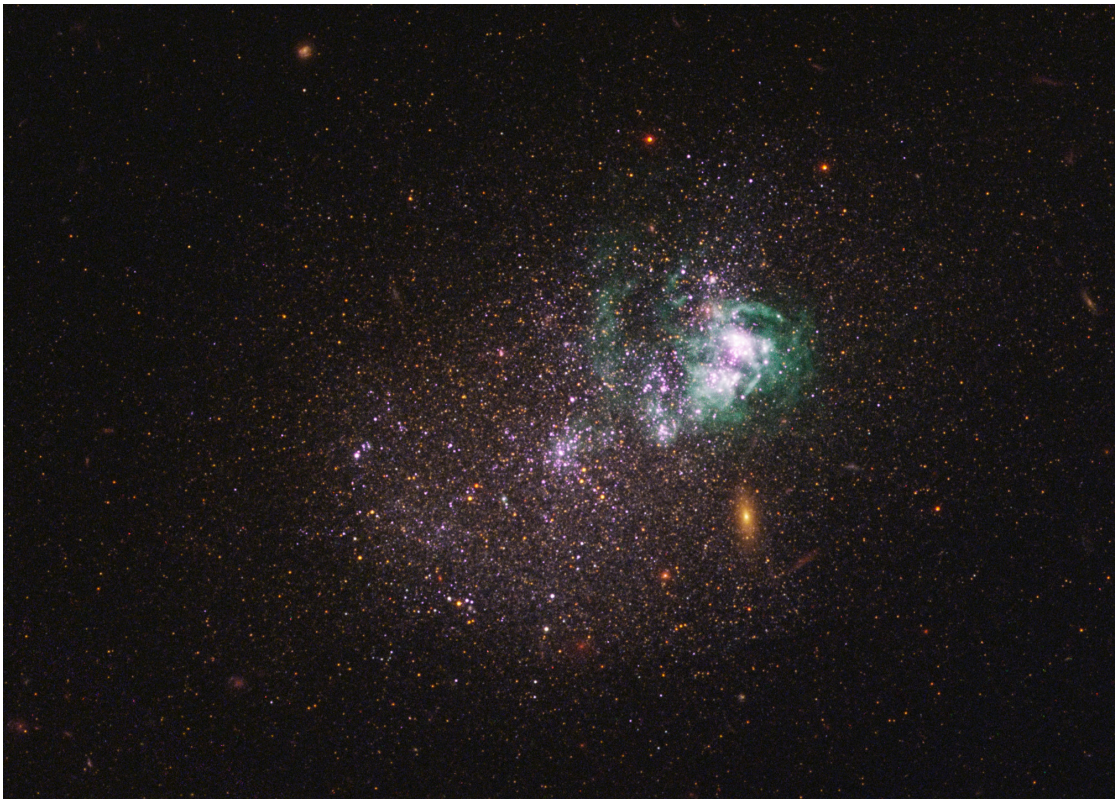

FIGURE 1.3: The blue compact dwarf galaxy UGCA 281 imaged with HST. Two YMCs shrouded in nebular gas (shown in light teal) are visible right of centre. The image is a composite of UV and visible light. *Image credit: NASA, ESA, and the LEGUS team.*

for clusters younger than 10 Myr (Brown & Gnedin 2021). This shallow relation indicates that cluster density increases with cluster mass for YMCs.

The multi-wavelength nature of the PHANGS survey, and in particular the inclusion of JWST near-IR observations, which penetrate the gas, provides an unprecedented view of YMCs still embedded in their natal gas. Mid-IR observations of polycyclic aromatic hydrocarbon emission further contribute to the detection of clusters shrouded in dust. JWST observations of PHANGS (e.g, Whitmore et al. 2023; Rodríguez et al. 2025) and starburst (M82, Levy et al. 2024, NGC 3351, Sun et al. 2024) galaxies greatly increase the sample of extragalactic YMCs, in particular for the youngest sources. An example for M82 is shown in the false-colour image in Figure 1.4. Those observations further confirm the prevalence of massive cluster formation in environments that are actively star-forming. The inclusion of IR data in spectral energy distribution fitting also results in better age estimates for the youngest ($\lesssim$ 4 Myr) clusters (Whitmore et al. 2025).

Combining HST observations with ALMA data further enables observers to probe the earliest stages of cluster formation, as has been done in the Antennae merging galaxies (He et al. 2022). High-resolution ALMA observations of the Firecraker, a massive and compact GMC in the earliest stages of forming a star cluster, provide unique insights into the physical conditions required for massive cluster formation, confirming that the most massive YMCs – with masses consistent with GC progenitors – can only form in environment with high external gas pressure, which is provided in mergers (Finn et al. 2019). Abundant YMC formation, and the formation of YMCs with masses $\lesssim 10^7$ $M_\odot$, has also been found in a larger sample of mergers (Adamo et al. 2020b).

Another major improvement to our understanding of cluster formation across cosmic time has come from recent high redshift ($z \gtrsim 2$) observations of young, compact star clusters with JWST. Notable examples are the sources detected in the Sunburst Arc ($z = 2.37$, Vanzella et al. 2022; Pascale et al. 2023) and the Sunrise Arc ($z \sim 6$, Vanzella et al. 2023), as well as the Cosmic Gems ($z = 10.2$, Adamo et al. 2024), for which mass and radius estimates are provided in Table 1.2. Taken together, those observations suggest that the formation of GC progenitors at high z proceeds in a similar manner to YMC formation in the Local Universe. In the context of this thesis, we use those new results to argue that studying massive cluster formation in conditions typical of the Local Universe – which are now well-constrained by observations – provides valuable insights into the formation of GCs at high z.

1.1.3 Massive star cluster formation within giant molecular clouds

Simulations show clearly that massive star clusters assemble within GMCs from both the inflow of gas towards the cluster – leading to star formation within the cluster – and mergers between subclusters (e.g., Howard et al. 2018; Dobbs et al. 2022; Lahén et al. 2024; Reina-Campos et al. 2025), on timescales of a few megayears. This hierarchical assembly process arises from the density fluctuations within GMCs caused by their supersonic turbulent spectrum (see, e.g., Mac Low & Klessen 2004). The interplay between gravity and turbulence leads to a lognormal density distribution with a high-density power-law tail. The densest gas is available for star formation, although the density threshold at which star formation occurs is environment-dependent (Burkhart 2018; Bemis & Wilson 2023). The timescales relevant to star and cluster formation within a GMC are often expressed in term of its free-fall time (Jeans 1902),

$$t_{\rm ff} = \left(\frac{3\pi}{32G\rho}\right)^{1/2} \tag{1.3}$$

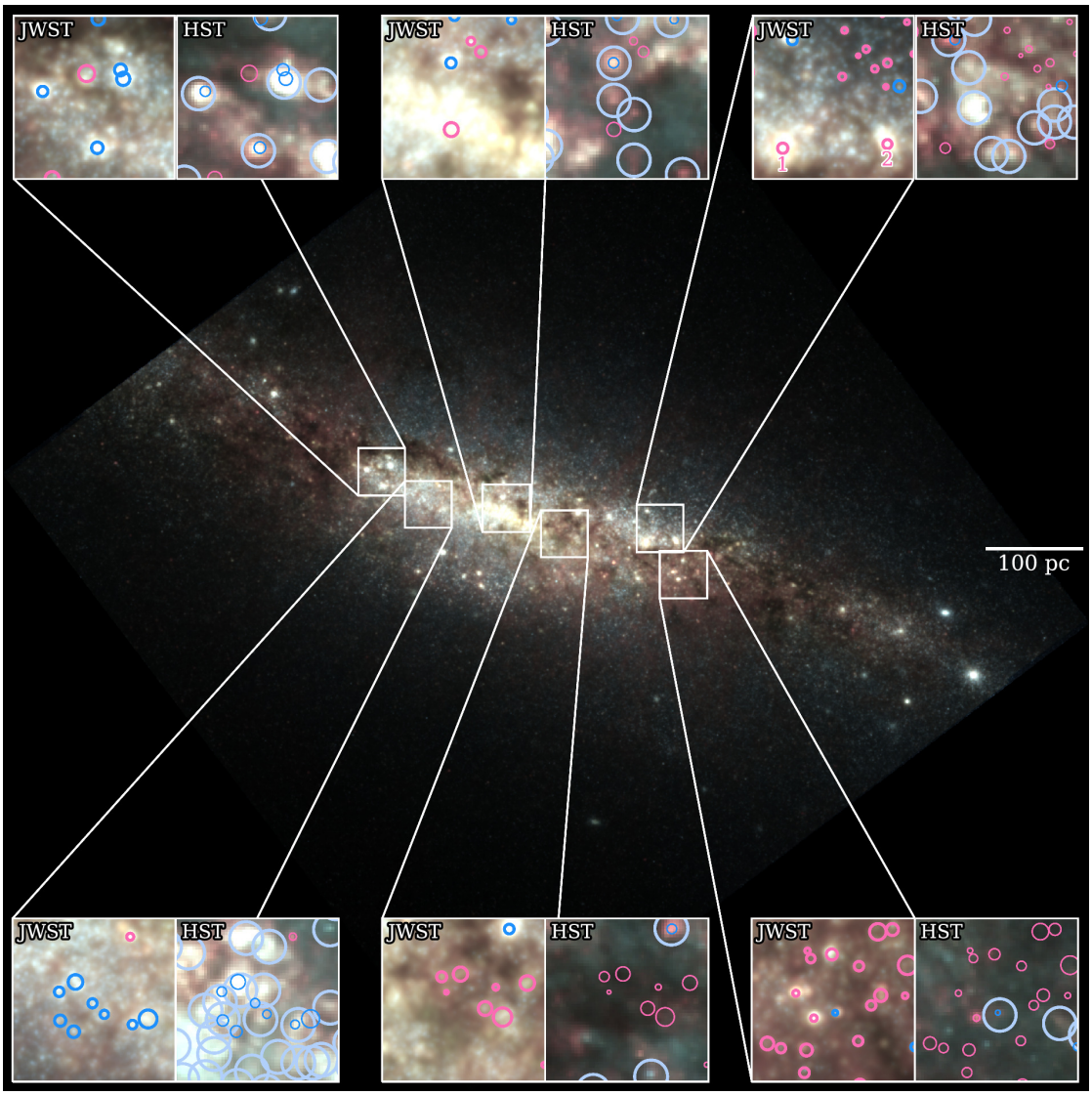

FIGURE 1.4: The central 870 pc of the starburst galaxy M82 imaged with JWST in the near IR. The 50 x 50 pc insets show YMCs identified in the JWST image (in blue and pink), with marker size matching their radii. The blue clusters have optical counterparts observed with HST, while the pink clusters do not. The light blue circles correspond to clusters previously identified in HST images. The image is a composite of three IR filters. *Image adapted from Levy et al. (2024, their Figure 1).*

where ρ is the density of the cloud and G is the gravitational constant. Stars are generally expected to begin forming within one free-fall time. This global measure however assumes a uniform density within the GMC, which is not the case due to the turbulence discussed above. Although turbulence generally provides support against gravity, and therefore opposes star formation, it also promotes star formation locally by giving rise to dense regions within GMCs (Ballesteros-Paredes et al. 2007).

A simplified, yet convenient, approach to studies of the physics of GMCs and their collapse is based on the relationship between gravity and turbulence. A number often used to describe the boundedness of a GMC is the virial parameter $\alpha_{\rm vir}$, which is derived from the virial theorem,

$$2K + U = 0 \tag{1.4}$$

where K is the kinetic energy and U is the gravitational potential energy. For a spherical cloud with uniform density, those can expressed as

$$U = -\frac{3}{5}\frac{GM^2}{R} \tag{1.5a}$$

$$K = \frac{3}{2}M\sigma^2 \tag{1.5b}$$

where M, R, and σ are the mass, radius, and velocity dispersion of the cloud. The virial parameter can then be expressed as

$$\alpha_{\rm vir} = \frac{2K}{|U|} = \frac{5\sigma^2 R}{GM} \tag{1.6}$$

following Bertoldi & McKee (1992). GMCs are gravitationally bound for $\alpha_{\rm vir} \leq 2$; they are sub-virial for $\alpha_{\rm vir} < 1$ and super-virial for $\alpha_{\rm vir} > 1$. The mass, radius, and velocity dispersion of GMCs have long been understood to be interconnected. Observations of GMCs within the Milky Way lead to the so-called Larson (1981) relations, which are often summarized as

1. All GMCs have the same surface density Σ;
2. There exists a size-linewidth relation $R \propto \sigma^2$ between a GMC's size R and its velocity dispersion σ;
3. GMCs are in virial equilibrium, with $\alpha_{\rm vir} = 1$, and therefore gravitationally bound;

(see, e.g., Heyer & Dame 2015). More recent observations however paint a more nuanced picture. Despite correlations between GMC properties, variations of the surface density

and virial parameter are observed both within the Milky Way and between galaxies. Values of $\alpha_{\rm vir}$ observed in galaxies span a very large range of values, from strongly sub-virial ($\lesssim 0.4$) to strongly super-virial ($\gtrsim 100$, see, e.g., Chevance et al. 2023, for a recent review). The surface density of GMCs also varies by more than two orders of magnitude in star-forming galaxies (Sun et al. 2018), with the highest values reached in starbursting mergers and the centres of barred galaxies, where there is abundant massive cluster formation. Contemporary studies therefore often adopt the Heyer-Keto relation (Keto & Myers 1986; Heyer et al. 2009),

$$\frac{\sigma^2}{R} \propto \alpha_{\rm vir}\Sigma \tag{1.7}$$

in lieu of the Larson relations, to account for environmental variations and correlations between GMC properties. This spread in properties is important for the formation of massive star clusters, as more massive YMCs may form in regions with high gas surface density (see the recent reviews by Krumholz et al. 2019; Adamo et al. 2020a, for a discussion).

Another useful, albeit idealized, measure of the properties of dense gas is the Jeans (1902) criterion, which may be expressed as either the Jeans mass M_J – the minimum mass unstable to gravitational collapse – or the Jeans length λ_J – the minimum size unstable to gravitational collapse, assuming a given density ρ. Starting from the virial theorem but assuming kinetic energy to be thermal,

$$K = \frac{3NkT}{2} \tag{1.8a}$$

$$N = \frac{M}{\mu m_{\rm H}} \tag{1.8b}$$

where k is the Boltzmann constant, T is the gas temperature, μ is the mean molecular weight, and $m_{\rm H}$ is the mass of an hydrogen atom, the Jeans criterion can be expressed as

$$M_J = \left(\frac{5kT}{G\mu m_{\rm H}}\right)^{3/2}\left(\frac{3}{4\pi\rho}\right)^{1/2} \tag{1.9a}$$

$$\lambda_J = \left(\frac{15kT}{4\pi G\mu m_{\rm H}\rho}\right)^{1/2}. \tag{1.9b}$$

For an isothermal gas, M_J and λ_J both decrease as density increases, allowing for a cascade of fragmentation down to smaller scales in the densest regions of a star-forming

GMC. This same cascade gives rise to the stellar initial mass function (see Hennebelle & Grudić 2024, for a recent review). Although the exact shape of the IMF remains under debate, it is often expressed as a power law or broken power law of the form

$$\frac{dN}{dM} \propto M^{\alpha} \tag{1.10}$$

where α is constant for a given mass range. The well-known Kroupa (2001) IMF uses $\alpha = -1.3$ for $M < 0.5\,M_{\odot}$ and $\alpha = -2.3$ for $M \geq 0.5\,M_{\odot}$; those values are adopted in this thesis. In addition to the exact shape of the IMF, the slope in the higher-mass regime (beyond 1 $M_{\odot}$) remains a topic of active investigation, as is its possible dependence on environment. Studies of the IMF, and how it relates to the mass function of dense pre-stellar and protostellar cores, is further complicated by the fact that most stars are formed in binaries or higher order systems (Offner et al. 2023), which may form through the fragmentation of a shared protostellar core or protoplanetary disk. Nonetheless, it is well-known that most of the stars, in numbers, are lower-mass stars, with masses below 0.5 $M_{\odot}$, while most of the light and the energy is supplied by high-mass stars.

1.1.4 Feedback and the interruption of star formation

Feedback from massive stars, in the form of energy and momentum deposited into the ISM, is the other factor, along with gravity and turbulence, that sets the SFE and CFE of massive GMCs. Conceptually, stellar feedback is often separated into pre-SN feedback, that acts from the onset of star formation, and SN feedback, that only begins to affect the interstellar medium a few megayears after the formation of the first massive star. Pre-SN feedback can be further split into stellar feedback – radiative and mechanical feedback from massive stars – and protostellar feedback, which includes jets and outflows from stars across the mass spectrum (see, e.g., Bally 2016, for a review). The discussion presented here will focus on pre-SN stellar feedback: those feedback mechanisms act over the same timescales as cluster formation, and dominate over protostellar feedback in regions sufficiently massive to form a YMC (Matzner & Jumper 2015; Plunkett et al. 2015). The YMC masses and radii for which different forms of pre-SN feedback are effective are shown in Figure 1.5, along with the YMCs presented in Tables 1.1 and 1.2. Many of those YMCs lie in the region of parameter space where pre-SN feedback mechanisms are inefficient at opposing star formation.

Radiative feedback appears to dominate in regions forming massive YMCs (see, e.g.,

Krumholz et al. 2019). The radiation emitted by stars is often approximated as blackbody radiation, which provides a good first-order estimate of the frequency (and therefore energy) at which most of the light will be emitted by a star, as a function of its temperature. Radiation from young O- and B-type stars peaks in the UV part of the electromagnetic spectrum, and also provides significant amounts of radiation with energy above 13.6 eV, sufficiently high to ionize hydrogen, while stars stripped of their envelopes further provide large amounts of radiation above the helium ionization threshold of 24.6 eV (Götberg et al. 2017). An example of blackbody radiation at different temperatures, and the stars that would emit a similar spectrum, is provided in Figure 1.6.

Radiation from massive stars heats the nearby gas and ionizes it. The amount of ionizing radiation from a stellar population, as well as the energies of the associated photons, depends on the high-mass end of the IMF and the presence of binaries (see discussion in Eldridge & Stanway 2022). H II regions – bubbles filled with ionized gas around massive stars, carved from the cold ISM by ionizing radiation – have temperatures of 10,000 K or above. Increasing the gas temperature raises M_J as $T^{3/2}$, preventing fragmentation. It also increases the kinetic energy of the gas, allowing it to escape the cluster forming regions if it reaches velocities above the cluster's escape velocity. The escape velocity adopted for Figure 1.5 is $v_{\rm esc} = 15$ km s^{-1}, which corresponds approximately to the speed of sound for ionized hydrogen gas with a temperature of 10,000 K. The escape velocities in dense YMCs are however larger than this velocity threshold, which prevents photoionization from efficiently ejecting the gas. Radiation pressure is also a significant source of feedback in YMCs, and is expected to dominate over ionizing radiation in those regions (Krumholz & Matzner 2009; Howard et al. 2018). This is further supported by observations showing that UV radiation pressure is larger than thermal pressure from photoionization in compact H II regions (Barnes et al. 2021). For the example stars shown in Figure 1.6, most of the ionizing photons will be emitted by the main-sequence (MS) and stripped O-type stars. Although the MS star is more luminous due to its larger radius, the stripped star provides radiation at higher frequencies, and could be more efficient at ionizing other species beyond hydrogen.

The force per unit mass exerted on gas a distance r away from a source of luminosity L by a radiation field can be expressed as

$$F_{\rm rad} = \frac{\kappa L}{c} \frac{e^{-\tau}}{4\pi r^2} \tag{1.11}$$

where κ is the opacity of the gas on which the pressure is exerted, τ is the optical depth of the gas between the source and the gas element, and c is the speed of light (see,

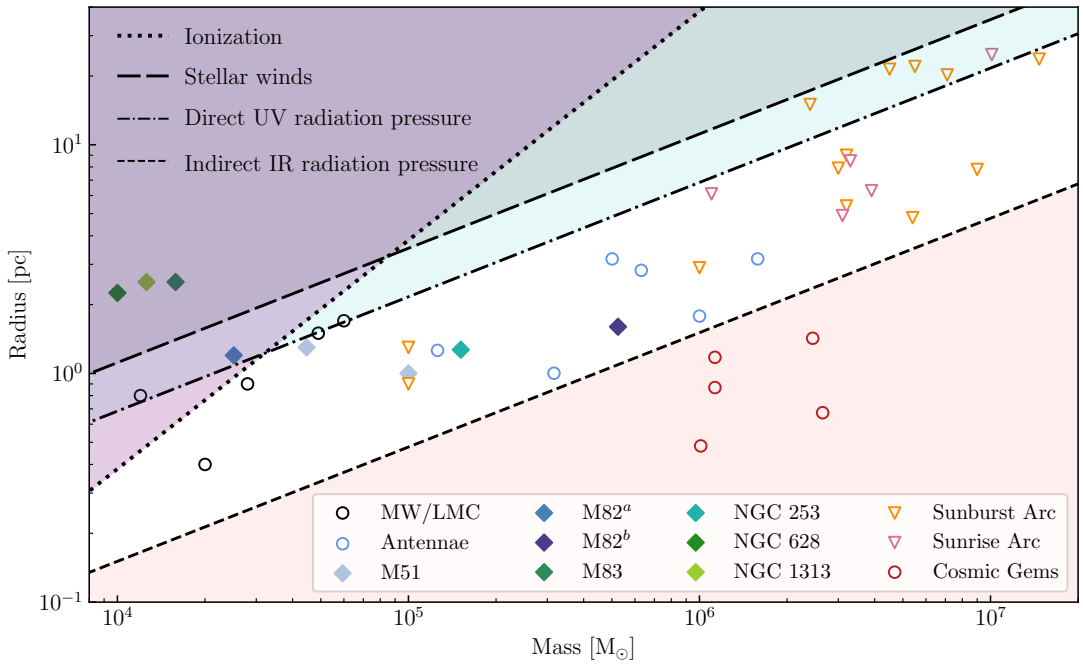

FIGURE 1.5: Radii and masses of YMCs in the local Universe and at high redshift, plotted over the regions of parameter space over which different feedback mechanisms are effective. The shaded regions represent respectively the cluster properties over which indirect IR radiation pressure (below the dashed line, $\Sigma > 7$ x 10^4 $M_\odot$ pc^{-2}), direct UV radiation pressure (above the dashed-dotted line, $\Sigma < 3.4$ x 10^3 $M_\odot$ pc^{-2}), momentum-driven winds (above the long-dashed line, $\Sigma < 1.1$ x 10^3 $M_\odot$ pc^{-2}), and ionization (above the dotted line, $v_{esc} < 15$ km s^{-1}) are effective at removing the gas from a cluster-forming region. The open circles represent individual clusters, the open triangles represent individual clusters for which only upper limits on the radius are available, and the filled diamonds correspond to average values for a galaxy or a mass bin within a galaxy. *The data is taken from the same references as Table 1.1 for the Milky Way and LMC, and from the same references as Table 1.2 for starburst and high redshift galaxies. The radiative feedback lines are taken from Krumholz et al. (2019) and the wind feedback line is calculated following Lancaster et al. (2021b).*

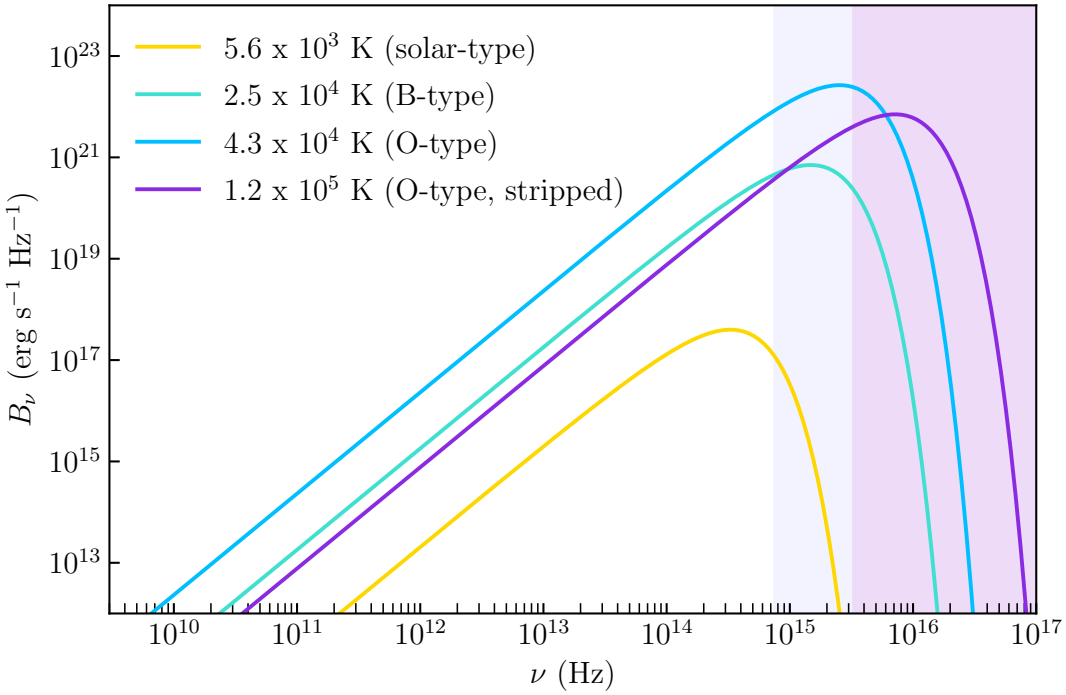

FIGURE 1.6: Luminosity as a function of frequency, for blackbody emitters at the temperature of a zero-age main sequence (ZAMS) solar-type star ($M = 1$ M$_\odot$, yellow), a ZAMS B-type star ($M = 10$ M$_\odot$, cyan), a ZAMS O-type star ($M = 50$ M$_\odot$, blue), and the same O-star stripped by mass transfer in a binary (purple). The blue and purple shaded regions correspond to the frequencies for UV and ionizing radiation. *The temperatures and radii of the stars are calculated with SEBA (Portegies Zwart & Verbunt 1996; Toonen et al. 2012).*

e.g., Krumholz & Matzner 2009; Howard et al. 2018). Radiation pressure is mostly effective in the UV: young stellar populations have large numbers of O and B stars which emit most of their radiation in the UV, and dust is opaque to UV radiation. Such radiation pressure is called direct radiation pressure, as the radiation from the stars exerts directly a force on the gas. IR radiation pressure reprocessed by dust from the stellar UV radiation – often called indirect radiation pressure – may also play a role in very high density environments. As dust is much less opaque to IR radiation than UV radiation, high surface densities are required for this feedback mechanism to be effective; its contributions can however be comparable to UV radiation pressure in some conditions, as the reprocessed photons can be scattered more than once. Reprocessed

IR radiation pressure may dominate the evolution of H II regions at early times, when the H II region is very compact (Olivier et al. 2021), while the combination of direct and indirect radiation pressure can efficiently launch outflows from high-density cluster-forming regions (Menon et al. 2023). The regimes in which UV and IR radiation pressure will be effective in suppressing star formation depend on the gas surface density; we adopt for Figure 1.5 an upper limit of $\Sigma = 3.4 \text{ x } 10^3$ $M_\odot$ pc^{-2} for UV radiation pressure and a lower limit of $\Sigma = 7 \text{ x } 10^4$ for IR radiation pressure, following Krumholz et al. (2019). B-type stars, like the 10 $M_\odot$ star in Figure 1.6, provide most of their feedback as radiation pressure. As they are much more numerous than O stars due to the shape of the IMF, radiation pressure is an important source of feedback, especially in massive YMCs with high escape velocities (see Figure 1.5).

Massive stars also lose mass through line-driven stellar winds, which are triggered by the radiation pressure from the star on its envelope (see Vink 2022, for a recent review). For hot MS stars, those winds have high velocities ($\gtrsim$ 1000 km s^{-1}), and create a shock front at the boundary between the wind bubble and the interstellar medium. Classical models of wind bubble expansion (Castor et al. 1975; Weaver et al. 1977) predict that the radius of a wind bubble should be determined by the density of the surrounding medium and the wind luminosity, which depends on the wind mass loss rate and velocity. Recent work accounting for the turbulent nature of GMCs, which results in a fractal interface between the shocked wind and the ISM (Lancaster et al. 2021b, 2024), finds that wind bubbles cool rapidly, reducing their efficiency as a feedback mechanism, although they may provide stronger contributions when the H II regions are very compact. The wind properties of a star depend on its luminosity, metallicity, and temperature; for MS stars, the mass loss rate is most strongly affected by the luminosity, while the wind velocity exhibits a stronger dependence on temperature (Vink & Sander 2021). In Figure 1.5, we use $\Sigma = 1.1 \text{ x } 10^3$ $M_\odot$ pc^{-2} to denote the surface density below which winds are effective as a feedback mechanism; we however note that due to uncertainties surrounding wind bubble geometry, as well as turbulent mixing and conduction, it should be regarded as a lower bound on the effectiveness of wind feedback (Lancaster et al. 2024). We calculate the surface density threshold following the approach outlined in Lancaster et al. (2021b), assuming that the cluster formed with an SFE of 50% (see Lancaster et al. 2021a) and calculating feedback properties with Starburst99 (Leitherer et al. 1999) for a fully-sampled Kroupa (2001) IMF and non-rotating stars at solar metallicity,.

Core-collapse supernovae inject very large quantities of energy and material into the ISM essentially instantaneously, raising the temperature of the nearby gas and carving a

large-scale cavity around the location of the explosion. Although SNe are very energetic, the first SN in a YMC may only occur at the earliest $\gtrsim 3$ Myr after the formation of the first massive star (for a stellar population with a maximum stellar mass $\lesssim 100$ $M_\odot$, see the recent stellar evolution models by Szécsi et al. 2022; Costa et al. 2025); SNe in clusters therefore occur in regions that have already been affected by radiative and mechanical feedback. Recent observations however suggest that YMCs may become devoid of gas before the first SN explosion within the cluster, indicating that the pre-SN feedback may be sufficient to interrupt star formation and entirely remove the gas from the cluster-forming regions (e.g., Chevance et al. 2022; Hannon et al. 2022; Deshmukh et al. 2024, and the recent review by Schinnerer & Leroy 2024).

Despite this growing body of evidence that SNe are not the most important feedback mechanism at the scale of individual YMCs, they are nonetheless important in driving turbulence at galactic scales (e.g. Mac Low & Klessen 2004). The efficiency with which SN feedback couples to the nearby gas depends on the effects of pre-SN feedback on that gas (Rathjen et al. 2021) and on the timing of previous SN explosions (Walch & Naab 2015): it is therefore critical to model accurately the strength of the pre-SN radiative and mechanical feedback, as well as the timing of SNe. Stellar dynamics within YMCs also play an important role in redistributing SN feedback within a galaxy: few-body interactions (Poveda et al. 1967), hierarchical cluster assembly (Polak et al. 2024b; Stoop et al. 2024), and kicks from a previous SNe in a binary systems (Blaauw 1961) may all result in the ejection of massive stars from the cluster, with high velocities. Such massive runaways, which have been observed around local YMCs (e.g. Kalari et al. 2019; Sana et al. 2022; Stoop et al. 2023, 2024), then subsequently affect galaxy evolution by driving outflows, redistributing metals in the galaxy, and enriching the circumgalactic medium (Andersson et al. 2020, 2023; Steinwandel et al. 2023). One factor that was overlooked in the discussion above is the role played by binary interactions in shaping the feedback from stellar populations; although interacting binaries are very common among massive stars (Sana et al. 2012; Moe & Di Stefano 2017), they are generally not considered in feedback studies.

1.2 Binary stars: stellar evolution and stellar dynamics

Stellar multiplicity is a very common outcome of star formation. Most protostars are found in multiple stellar systems formed through the fragmentation of protostellar cores and protoplanetary disks. Once on the main sequence, stellar multiplicity remains ubiquitous, especially at higher stellar masses, but is also influenced by environment (see

Offner et al. 2023, for a recent review). The interplay between multiple stellar systems, such as binary stars, and stellar dynamics is highly complex, and an important driver of the evolution of dense stellar systems. Stellar multiplicity also affects stellar evolution, by triggering mass transfer in close binaries. Throughout this thesis, the multiplicity fraction MF is defined as

$$MF = \frac{B + T + Q^{+}}{S + B + T + Q^{+}} \tag{1.12}$$

where S is the number of single stars, B the number of binary star systems, T the number of triple star systems, and Q^{+} the number of quadruple or higher order star systems. We refer to the most massive star in a binary as the primary, with mass M_1; the other star is the companion, with mass M_2. The companion frequency CF is the average number of companions per primary, and is calculated from

$$CF = \frac{B + 2T + 3Q^{+}}{S + B + T + Q^{+}} \tag{1.13}$$

where the coefficients in the numerator correspond to the number of companions in a system. While MF is bound between 0 and 1, CF can be greater than 1. Three other orbital parameters are used to describe the orbits of binaries in the following sections: the semi-major axis a, the orbital period P, and the eccentricity e. P and a are related through Kepler's third law,

$$P^2 = \frac{4\pi^2 a^3}{G(M_1 + M_2)} \tag{1.14}$$

and either may be used to describe the orbit, in conjunction with the masses and the eccentricity. The following sections present an overview of observed populations of binary stars (1.2.1), the interplay between binary stars and stellar dynamics (1.2.2), and binary stellar evolution (1.2.3).

1.2.1 Populations of binaries in different environments

Multiple stellar systems are observed in a variety of environments, ranging from the Galactic field to the densest star clusters. The most complete overview of binary statistics to date is the compilation by Moe & Di Stefano (2017), which presents probability distribution functions for the orbital period as a function of mass, the mass ratio as a function of mass and period, and the eccentricity as a function of mass and period. This work compiles observations and corrects them for bias and completeness in a uniform way. The recent review by Offner et al. (2023) confirms the trends identified by the above, and includes a few more recent observations. We use the multiplicity fractions and median semi-major axes compiled by Offner et al. (2023) in Figure 1.7.

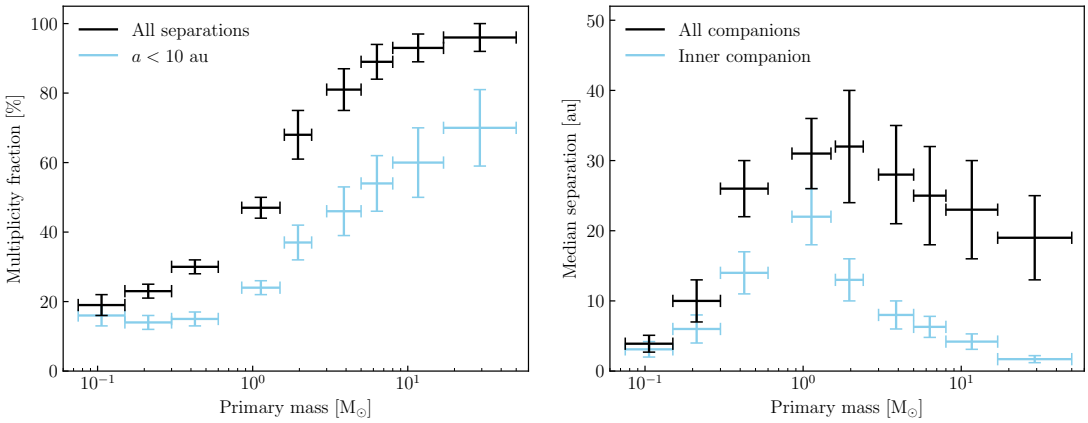

FIGURE 1.7: Multiplicity fraction (left) and median separation (right) as a function of primary mass M_1. The multiplicity fraction across all separations is shown in black, while the multiplicity fraction for companions within 10 au is shown in light blue. For the separation, the black and blue crosses denote respectively all companions and the inner companion in a hierarchical system. *The data is taken from the observations compiled in Offner et al. (2023, their table 1).*

The extensive statistics compiled by Moe & Di Stefano (2017) and reviewed by Offner et al. (2023) are mostly based on observations of the Galactic field, and are explicitly about main sequence stars. Offner et al. (2023) do note that the multiplicity fraction for protostars may be higher than that of MS stars for solar-type and low-mass stars, and that the dynamical processes leading to the build-up of the Galactic field – from the dissolution of associations and clusters – contribute to setting the multiplicity properties. They propose that the field represents a superposition of populations of binaries formed in environments of different densities, and therefore represent an average of those environments, as low- and high-density star-forming regions show respectively an excess and a deficit of wide binaries compared to the Galactic field (e.g. Joncour et al. 2017; Duchêne et al. 2018; Jerabkova et al. 2019). An important nuance to this discussion is however the sample used to derive the multiplicity statistics of O stars. O stars have short lifetimes, and are not expected to be found in the field unless they were ejected from their birth environment as a runaway star. The processes leading to runaway star production are however related to processes that alter or disrupt binaries (Sana et al. 2022, for a recent discussion). Offner et al. (2023) therefore argue that O stars in young clusters represent a more pristine sample.

The multiplicity fraction (shown in Figure 1.7) and the companion frequency both increase monotonically with mass. The multiplicity fraction reaches $\sim 50\%$ at 1 $M_\odot$, where the binary fraction is about 40% and the triple fraction is 10% (Moe & Di Stefano 2017, and references therein). Even M-dwarfs, which are the most abundant stars in the Milky Way, have multiplicity fractions $\gtrsim 20\%$. This result firmly enshrines multiplicity as a natural outcome of the star formation process, rather than an oddity. The observations compiled by Moe & Di Stefano (2017) further show that B-type stars have a multiplicity fraction $\gtrsim 80\%$ and a companion frequency $\gtrsim 1$, with between 30% and 60% (for the highest mass B stars) of B stars in triple or higher order systems. O stars have a multiplicity fraction $\gtrsim 95\%$ and a companion frequency $\gtrsim 2$; about 70% of all O stars are in triple or higher order system, and the same fraction has a companion within 10 au. If the definition of close binary is extended to systems with orbital periods below 5000 days (to account for the large radii of evolved O stars), then $\gtrsim 90\%$ of O stars have a close companion. Although the estimates for the fraction of massive O stars that will interact with a companion vary from $\sim$70% (Sana et al. 2012) to $\gtrsim 90\%$ (Moe & Di Stefano 2017), there is a consensus that binary evolution dominates the evolution of massive stars.

Another key result from the work of Moe & Di Stefano (2017) is the fact that all orbital properties – the period, the mass ratio, and the eccentricity – depend on primary mass, and both the mass ratio and the eccentricity also depend on orbital period. An illustration of this can be found in the right panel of Figure 1.7, showing the median separation as a function of primary mass. The median separation peaks around 1 $M_\odot$ for both the distribution of all companions and that of the inner companion (in a hierarchical system). Both decrease beyond 1 $M_\odot$ but the median separation for the inner companion does so more strongly, reaching $\lesssim 2$ au for O stars (Offner et al. 2023). The results compiled by Offner et al. (2023) further reveal that both the close (< 10 au) and wide (> 100 au) companion frequency increase with mass, which provides hints about the formation process of the systems observed in the Galactic field. Most systems with separations $<$ 100-200 au likely formed through the fragmentation of the protostellar disk around the primary; such fragmentation has been observed both for populations of protostars (e.g. Tobin et al. 2018) and for individual O stars (e.g. Maud et al. 2019; Zapata et al. 2019). Theoretical models (Kratter & Matzner 2006) further argue that such a fragmentation mechanism should be more effective for more massive stars, in agreement with observations, and also favour more equal masses for the closest binaries, also in agreement with the observed excess twin fraction at small separation (Moe & Di Stefano 2017).

At larger separations, binaries likely form from the fragmentation of dense cores or filaments; this idea is supported by the observation of multiple density peaks in cores (e.g. Kirk et al. 2017) or misaligned protostellar outflows from the stars in a binary (e.g. Lee et al. 2016). Wide binaries may also form via dynamical processes in embedded clusters; dynamical interactions naturally reproduce the mass dependence of binary fraction in the absence of primordial binaries (Wall et al. 2019; Fujii et al. 2021; Guszejnov et al. 2023) although they do not reproduce the observed trends for separations and mass ratios (Cournoyer-Cloutier et al. 2021). This paints a picture in which the increased multiplicity with primary mass depends both on the physics of star formation at small separations, and the effects of dynamical interactions at large separations. This would be further consistent with observations of the wide binary fraction varying with stellar density for solar-type stars in star-forming regions while the close binary fraction appears independent of environment for protostars (Tobin et al. 2022).

There exist other factors that may cause disk fragmentation to depend on environment. One of them is metallicity, which affects the opacity of the disk, and therefore its ability to cool and fragment. The close binary fraction for solar-type stars is anti-correlated with metallicity (Moe et al. 2019), and new observations suggest that it may also be the case for B-type stars (Villaseñor et al. 2025). Disks in dense clusters may also be truncated due to close encounters with other stars (e.g. Vincke & Pfalzner 2018; Winter et al. 2024) or evaporate due to the UV radiation from nearby massive stars (e.g. O'Dell et al. 1993; Brandner et al. 2000; Guarcello et al. 2007), although the latter effect is mitigated by shielding from gas within the embedded cluster (Wilhelm et al. 2023). Such processes could cause variations in the properties of primordial binaries formed via disk fragmentation in different environments.

Recent studies of Galactic open clusters with *Gaia* find a large scatter in binary fraction: some find a positive correlation between cluster density and multiplicity fraction (Niu et al. 2020; Cordoni et al. 2023), and there is disagreement on whether the multiplicity fraction increases with primary mass and decreases with cluster age (Donada et al. 2023), or is constant (Cordoni et al. 2023). The binary fractions from those studies range from 6% to 80%; the smallest spread within a single study is for the work of Niu et al. (2020), who find a spread of 26% from 12 open clusters. This large scatter suggests that the binary fraction in open clusters might not be a consequence of the clusters' present-day properties, but rather of their formation process.

The picture is somewhat more uniform for GCs, which generally have low ($\lesssim 15\%$) binary fractions (Milone et al. 2012), aside from the lowest mass GCs in the halo of

the MW (Milone et al. 2016). There appears to be an anti-correlation between cluster mass and binary fraction, but the picture is far from complete. Most studies detect binaries photometrically (from their offset from the MS due to the contributions from the companion, see, e.g., Milone et al. 2012) and are limited to mass ratios $q > 0.5$. As the GCs for which we have star-by-star observations are old (GCs in the MW are $\gtrsim 10$ Gyr old, VandenBerg et al. 2013), their massive stars have long disapeared, and the MS stars used to derive multiplicity fractions have masses $\lesssim 0.8$ $M_\odot$ (see, e.g., Milone et al. 2016). GCs are also relaxed systems, leading to radial variations in the binary fraction from the effects of mass segregation. An additional complication arises from the fact that GCs exhibit peculiar star-to-star abundances variations, with a fraction of their stars enriched in helium, nitrogen, sodium, and aluminum, and depleted in carbon, oxygen, and magnesium (see Bastian & Lardo 2018, for a review). Observations find lower binary fractions for those enriched stars (e.g. Lucatello et al. 2015; Kamann et al. 2020; Milone et al. 2025), which suggests that cluster assembly, at the time of star formation, leaves an imprint on the present-day binary population.

1.2.2 Stellar dynamics

There is a rich interplay between binary stars and stellar dynamics. As discussed in the section below, although it has long been known that the presence of binaries affects long-term cluster evolution, the effects of binaries on cluster assembly are less well-constrained. Dynamical interactions in clusters may result in the formation, modification, or disruption of binaries; such disruption may even eject stars from their host cluster. Such topics have been explored via simulations for decades, but have only recently been linked to the cluster formation process. Consequently, a lot of the classical results we have about binaries in dense star clusters have been derived from models in which star clusters are assumed to be spherical and devoid of gas from the onset of the simulation, in great contrast with the picture of cluster formation we outlined in Section 1.1. We summarize below those classical results, and provide the context necessary to approach the work presented in this thesis.

Repeated encounters in dense stellar systems drive the stars towards equipartition of kinetic energy (Spitzer 1969); this process leads to mass segregation, with heavier stars sinking to the centre of the cluster, with lower velocities. This leads to an increase in the central density (known as core-collapse), which may be halted by the formation of a binary (in the absence of primordial binaries, Heggie 1975; Hills 1975). When accounting for the presence of a primordial population of binaries (and discounting the now-known correlations between binary fraction and mass), mass segregation results in a higher

fraction of binaries in the central regions of the cluster, due to their larger mass (as a system) than single stars; few-body interactions in this dense core then disrupt binaries while slowing the increase in central density (Spitzer & Mathieu 1980). The dynamical cross-sections of binaries depend on their semi-major axes, rather than the stars' physical radii. When accounting for gravitational focusing (see, e.g., Binney & Tremaine 2008), the effects of mass segregation – which lower the center of mass velocity of the binaries – and the higher mass of the binary systems both promote binary-binary interactions over binary-single interactions in clusters with moderate binary fraction (Sigurdsson & Phinney 1993). Few-body interactions with binaries are important for the long-term evolution of star clusters, as they result in the ejection of lower-mass stars.

Another important result about binaries in clusters is the idea of the hard-soft limit (Heggie 1975; Hills 1975): binaries with orbital binding energies larger than the average kinetic energy of a star in the cluster tend to become more bound through repeated encounters, while binaries with binding energies below that value will eventually be disrupted. In this picture, the upper semi-major axis limit for which a binary is expected to survive in a cluster is

$$a \leq \frac{GM_1M_2}{\langle m \rangle \sigma_{3\mathrm{D}}^2} \tag{1.15}$$

where $\langle m \rangle$ is the average mass of a star in the cluster and $\sigma_{3\mathrm{D}}$ is the cluster's three-dimensional velocity dispersion (e.g., Binney & Tremaine 2008; Portegies Zwart et al. 2010). The maximum semi-major axis for a hard binary is inversely proportional to cluster mass (which scales as $\sigma_{3\mathrm{D}}^2$ assuming virial equilibrium), and increases with the masses of its component stars. Three-body interactions may either transfer energy from the binary to the perturber while leaving the binary bound, disrupt the binary, or replace one of the stars in the binary with the third star with which the binary interacts. The expectation in such a case is that the lowest-mass stars will be ejected, and the orbit will widen by a fraction equivalent to the ratio of the masses of the previous and new companion (Sigurdsson & Phinney 1993; Leigh & Sills 2011). The disruption of the binary becomes more likely over an exchange of companions as the semi-major axis, the relative velocity of the incoming stars, and its mass increase (Hut & Bahcall 1983).

More recent work – and in particular work focused on cluster formation – however suggests a more nuanced picture of the interplay between binary stars and star clusters. Subclusters may have sufficient time to mass segregate before merging within GMCs, due to their short dynamical times; this mass segregation is then preserved as the cluster

FIGURE 1.8: Artist's impression of mass transfer in an O-star binary. The more massive, and therefore more evolved primary (on the right) is transferring material to its companion via Roche lobe overflow. Such mass transfer is ubiquitous in massive stars. *Image credit: ESO, M. Kornmesser, and S.E. de Mink.*

assembles from repeated mergers (McMillan et al. 2007). Gas in embedded clusters also appears to play a role in the evolution of populations of binaries: while gas-free clusters can sustain a field-like population of binaries (Parker & Meyer 2014; Torniamenti et al. 2021), embedded clusters of similar mass cannot (Cournoyer-Cloutier et al. 2021). This is likely connected to bursts of binary disruption occurring during cluster mergers, where binaries act as energy sinks, preventing the production of unbound stars from the merger (Cournoyer-Cloutier et al. 2024).

1.2.3 Binary stellar evolution

Mass transfer is a common outcome of the evolution of close binaries at all masses. The discussion presented here will however focus on the consequences of mass transfer in massive binaries, which are the main source of energy – from feedback as well as gravitational binding energy – in YMCs. The pre-SN evolution of massive stars, and therefore the amount of mass and energy released in core-collapse SNe, have been long known to be influenced by binary evolution (Chevalier 1976; Podsiadlowski et al. 1992). There

was however a paradigm shift with the work of Sana et al. (2012), which demonstrated that the pre-SN evolution of most O stars is affected by mass transfer (see Marchant & Bodensteiner 2024, for a recent review). Such mass transfer affects the subsequent feedback from the stars by changing their masses, radii, and surface temperatures, which in turn changes their luminosities, radiation spectra, and mass loss rates. An artist's impression of mass transfer in a massive binary is shown in Figure 1.8.

A binary interacts when one of its components reaches a radius larger than its Roche lobe radius; assuming that the stars in the binary are the same age, and that the binary has not previously interacted, the primary is the one that will fill its Roche lobe first (Kuiper 1941; Morton 1960; Paczyński 1971). For a mass ratio $q = 0.3$ (where the distribution of q peaks for O stars, Moe & Di Stefano 2017), a massive star with a radius $R = 15$ $R_\odot$ will fill its Roche lobe for a semi-major axis below 0.3 au while an evolved massive star with a radius $R = 1000$ $R_\odot$ will fill its Roche lobe for a semi-major axis below 20 au (Eggleton 1983). Recalling from Figure 1.7 that 70% of O stars have a companion within 10 au and that the median separation for the inner companion to an O star is $\lesssim 2$ au (Offner et al. 2023), the ubiquity of Roche lobe overflow (RLOF) in O-star binaries is obvious. Although Sana et al. (2012) found that 71% of O stars will interact, the exact fraction of O stars that will undergo mass transfer may be even larger. Accounting for the dependence of the mass ratio and eccentricity distributions on the period, Moe & Di Stefano (2017) derive a value approaching 100%. They find that 80-90% of O stars have one companion with an orbital period shorter than 5000 days, with which they will undergo RLOF; the remaining 10-20% is predicted to be in a triple or higher-order system, with a second companion within 10 au. Although the exact fate of such systems is even less well-constrained than that of interacting binaries, they are still expected to undergo some form of mass transfer (see Toonen et al. 2020, for a recent discussion).

A very successful approach to modelling binary evolution has been to use one-dimensional simulations of binary evolution with the Module for Experiments in Stellar Astrophysics (MESA, Paxton et al. 2011, 2015). Götberg et al. (2017, 2018, 2019, 2020) have shown that massive stars stripped of their envelope by mass transfer are a significant source of FUV and ionizing radiation, producing photons with large enough energies to ionize helium. Other work with MESA has shown that the composition of the pre-SN (De Mink et al. 2009; Nguyen & Sills 2024) and SN (e.g. Farmer et al. 2021, 2023) ejecta is affected by mass transfer in binaries, as well as the amount of pre-SN ejecta and the timing of SNe (e.g. Zapartas et al. 2017). BPASS (Binary Population

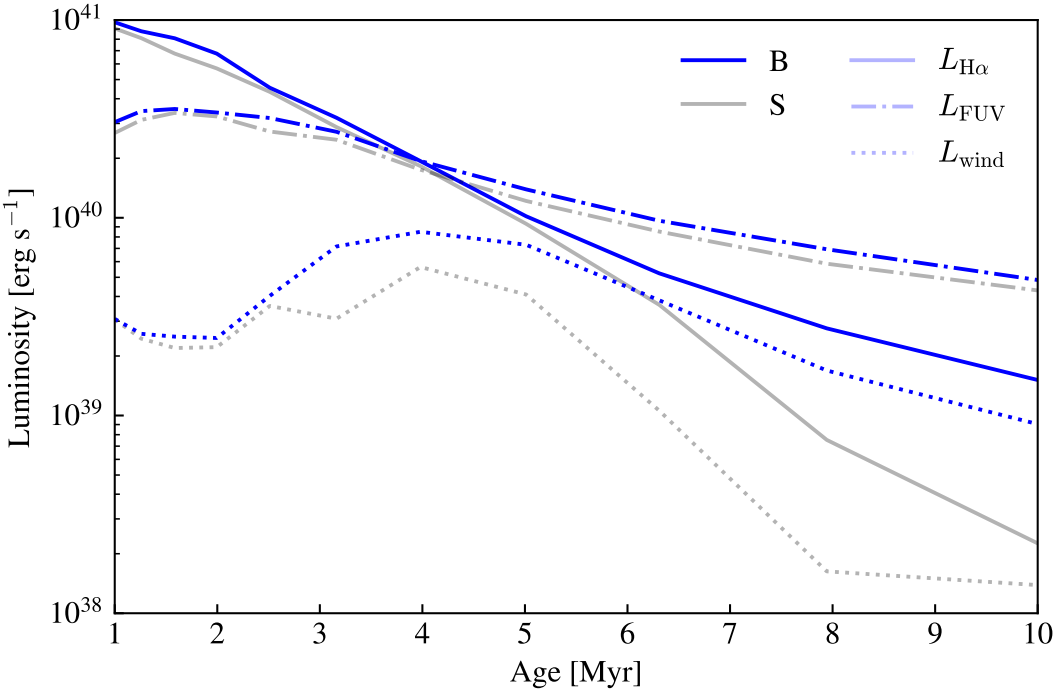

FIGURE 1.9: Ionizing (solid line), FUV (dashed-dotted) and wind (dotted) luminosity for a fully sampled stellar population, as a function of time, for models with (in blue) and without (in black) binary stellar evolution. The energy provided by the stellar population with binaries is larger in every feedback channel. *The figure was generated using the publicly-available BPASS (Stanway & Eldridge 2018) output at Z=0.14, with a Kroupa (2001) IMF with a maximum mass of 300 $M_\odot$.*

and Spectral Synthesis, Eldridge & Stanway 2009; Stanway & Eldridge 2018) has also been used extensively to model the spectra, mass loss rates, and SN rates from stellar populations including binaries; this work has shown better agreement with observations than models based on single stars. An example of the BPASS output for stellar populations with and without binaries is shown in Figure 1.9. Other work on spectral synthesis further suggests that contributions from massive binaries may be needed to explain the observed spectra of high-z galaxies (Steidel et al. 2016) and nearby dwarfs (Senchyna et al. 2017), as well as young, compact star clusters at high z (Pascale et al. 2023).

There are a growing number of observations of binary interaction products. Drout et al. (2023) and Götberg et al. (2023) have recently identified a sample of stars stripped

by mass transfer in the LMC and SMC. At higher stellar masses, Shenar et al. (2016, 2019) found that the populations of Wolf-Rayet stars – evolved massive stars with strong, optically thick winds – observed in the LMC and SMC are formed through a combination of self-stripping from large wind mass loss rates and binary interactions. Companions rejuvenated by mass transfer may also be identified from their rotation velocity: Ramírez-Agudelo et al. (2013, 2015) and Britavskiy et al. (2023) infer from observations of O stars in the LMC and Milky Way that accretors spin up due to mass transfer. This is also consistent with the bimodal distribution of velocities and rotation velocities of runaway O stars around R136 (Sana et al. 2022). Schneider et al. (2014) predict from a combination of stellar evolution simulations and observations that the most massive stars in the Arches and Quintuplet YMCs in the MW are binary interaction products. In fact, De Mink et al. (2014) argue that approximately 30% of the observed O stars are binary interaction products. Observational evidence therefore confirms that binary evolution may be important to the feedback budget of YMCs.

Despite this, however, few studies have explored massive interacting binaries as a source of stellar feedback. Radiative feedback from populations of binaries has been included in cosmological simulations (e.g. Ma et al. 2016; Rosdahl et al. 2018; Secunda et al. 2020; Doughty & Finlator 2021), which have shown that accounting for the bluer spectral energy distribution of stellar populations with binaries is necessary to reproduce reionization. Recently, Fichtner et al. (2024) studied the impact of mass transfer in binaries on the radiative, mechanical, and SN feedback from massive stars in one-dimensional radiation hydrodynamics simulations, while Wagg et al. (2025) investigated how SN kicks in binaries influence the spatial distribution of SNe within a galaxy. A common point between those studies, however, is that they all assume that the binary is isolated, and that its orbit cannot be modified by stellar dynamics as discussed in Section 1.2.2. The interplay between binary evolution and stellar dynamics may however prove itself to be important, as the effects of mass transfer or common envelope evolution – when the envelope from the primary fully engulfs the companion, and is subsequently ejected (Paczynski 1976, see Röpke & De Marco 2023 for a recent review) – both change the binary's orbit. Conservative mass transfer and common envelope evolution both decrease the semi-major axis, while non-conservative mass transfer – during which a significant amount of mass is lost – may result in either an increase or a decrease of the semi-major axis (Portegies Zwart & Verbunt 1996).

1.3 Simulating binaries in young massive star clusters

Our current understanding of YMC formation and massive binaries shows clear areas where the interplay between massive binaries and massive clusters may be important. Most star formation proceeds within star clusters, the most massive of which host rich populations of massive stars. Those stars return energy to the ISM in the form of radiation, winds, and SNe, interrupting star formation. The vast majority of them however have a close companion, which subsequently influences the feedback the massive star can provide. The presence of massive binaries is also important for the dynamics of their host cluster, especially in high density environments such as the most massive YMCs. A crucial ingredient to current and future simulations of massive star cluster formation therefore appears to be binaries. In this thesis, we present work on the interplay between binary stars and star cluster formation, building on the work of Cournoyer-Cloutier et al. (2021). We discuss the specific research questions addressed by the present thesis in Section 1.3.1, present an overview of our simulation methods in Section 1.3.2, and outline the contents of the thesis in Section 1.3.3.

1.3.1 Framing the research questions

This thesis focuses on the role played by binary stars in the formation of star clusters, with the overarching aim of improving our understanding of massive star cluster formation. The past few years have provided new insights into the formation of such massive clusters thanks to advance in numerical methods as well as new telescopes and surveys. Several questions however remain outstanding.

We know from observations of stellar kinematics and gas structure that star clusters assemble hierarchically within GMCs from a combination of mergers between subclusters and star formation from accreted gas. This result is further supported by simulations of massive cluster formation (e.g., Howard et al. 2018; Reina-Campos et al. 2025). Simulations are a useful tool to study the relative contributions of in-situ star formation and the accretion of already-formed stars, as well as to understand how the morphology of embedded clusters evolves during the assembly process. The addition of collisional stellar dynamics (as in Dobbs et al. 2022; Lahén et al. 2025) and binaries may however prove to be critical, due to the short dynamical timescales of the small subclusters (McMillan et al. 2007). In this thesis, we therefore use simulations with coupled star formation, gas – affected by feedback – and collisional stellar dynamics with binaries to ask *how the morphology of embedded clusters evolves during star cluster assembly.*

Another important question is that of the evolution of populations of binaries during star cluster formation. As outlined in Section 1.2.1, GCs have low binary fractions while the YMCs for which we have star-by-star observations display high binary fractions, in particular for their massive stars. Although part of this apparent discrepancy may be due to the different stellar mass ranges probed by observations of GCs and YMCs – as massive stars have long ago evolved into remnants in GCs – the roles of stellar dynamics and the cluster assembly process in setting that binary fraction remain unknown. We now know – from the work presented in Cournoyer-Cloutier et al. (2021) – that populations of binaries are modified early during cluster formation through a combination of binary disruption and dynamical binary formation. This work however only investigated the evolution of binary populations in low-mass embedded clusters, typical of star-forming regions in the Milky Way disk. A natural follow-up is therefore to explore different initial conditions to determine *how populations of binaries evolve during the assembly of clusters of different masses.*

Observations of massive YMCs (summarized in Section 1.1.2) suggest that star clusters emerge from their gaseous environments before the first SN within the cluster, despite their radii and masses indicating that they should not be strongly affected by pre-SN feedback (see Figure 1.5). Massive stars, which power pre-SN feedback in YMCs, have very high close binary fractions, and almost all of them are expected to interact with a companion prior to exploding as SNe. Previous studies of feedback on YMC-scale have however not accounted for the changes to the feedback budget arising from the increased UV luminosity and mass loss from binary interactions. These effects should be considered in concert with stellar dynamics, as close massive binaries are expected to become even closer in dense environments – such as massive YMCs – due to the effects of few-body interactions. The final question we address is this thesis is therefore *what role feedback from massive interacting binaries plays in halting star formation in massive cluster-forming regions.*

1.3.2 Simulation methods

In order to answer the questions outlined above, we need a simulation framework that simultaneously accounts for the cloud-scale collapse of the turbulent gas, leading to star formation in dense regions, as well as the effects of the stars on that gas through stellar feedback, while also resolving gravitational interactions between the stars, down to the scale of short-period binaries. This requires us to model several different physical processes, acting at different scales, concurrently. This is computationally challenging, as it requires expensive simulations; those simulations rely on the coupling of different

codes, optimized for different physical processes. We use the star cluster formation code Torch (Wall et al. 2019, 2020), which uses the Astrophysical Multipurpose Software Environment (Amuse, Portegies Zwart et al. 2009; Pelupessy et al. 2013; Portegies Zwart et al. 2013; Portegies Zwart & McMillan 2019) to couple the radiation magnetohydrodynamics code Flash (Fryxell et al. 2000; Dubey et al. 2014) to collisional stellar dynamics and stellar evolution codes. The effects of gas gravity on the stars and vice-versa are handled by a leapfrog integrator based on Bridge (Fujii et al. 2007). We provide below sufficient information to understand the structure of the Torch code and its main components; further details are provided, as relevant, in Chapters 2, 3, and 4.

Flash evolves the equations of MHD on a cartesian grid, which is adaptively refined in regions with high density, or large pressure and temperature gradients. Regions which have sufficiently high density for λ_J (see Equation 1.9b) to be unresolved at the maximum refinement level are considered eligible for star formation if they are also bound and locally converging (see criteria in Federrath et al. 2010). A sink particle is placed at the centre of a cell meeting the above criteria; the sink may accrete gas from an accretion radius $2.5\Delta x$, where Δx is the cell size. As a sink particle is formed, it samples an IMF and a binary prescription to form single stars (Wall et al. 2019) and binaries (Cournoyer-Cloutier et al. 2021); each single star or binary is formed in order, once the sink has accreted enough mass. This star formation routine allows us to conserve mass locally, and to form primordial binaries with arbitrary separations, which may be smaller than our gas resolution.

Once formed, stars are handled by a collisional stellar dynamics code. Two different sets of stellar dynamics codes are used in this thesis. In Chapter 2, we use the direct N-body code Ph4 (McMillan et al. 2012), which calculates the net gravitational acceleration on each star from the masses and positions of all other stars within the simulation domain. Short-range encounters and stable binaries are handled by the Amuse module Multiples (Portegies Zwart & McMillan 2019), which evolves the encounter as an isolated system. Such an approach is expensive when large numbers of binaries are included in the simulation, as it evolves the binaries and encounters serially. It may also lead to inconsistencies if the time it takes for the encounter to be considered resolved is longer than the simulation timestep; this is likely the case in our models as the simulation timestep is generally dictated by the Flash timestep, on the order of 10's of years. The direct N-body approach in Ph4 may also become prohibitively expensive for systems beyond a few 10^4 stars, which is the case for YMCs. To alleviate those issues, we adopt another collisional stellar dynamics code for Chapters 3 and 4. PeTar (Wang et al.

2020a) has been designed to handle systems with 10^6 stars and a high binary fraction, which leads to a significant speed-up of the N-body calculation. PETAR uses a combination of three different algorithms to handle the gravitational effects of stars at different distances. Stable binaries and close encounters are treated with a slow-down algorithmic regularization approach (SDAR, Wang et al. 2020b), short-range interactions between nearby stars are treated with a direct N-body approach, and long-range interactions are treated with a tree code (Iwasawa et al. 2016). The implementation of PETAR in TORCH is presented in Polak et al. (2024a), with additional details in Chapter 3 regarding the coupling with the binaries.

Stellar evolution is calculated with the rapid stellar evolution code SEBA (Portegies Zwart & Verbunt 1996; Toonen et al. 2012), which provides the luminosity, mass, radius, and surface temperature at every timestep. In the original version of TORCH, as well as in Cournoyer-Cloutier et al. (2021) and Chapters 2 and 3, stellar evolution is recalculated from the zero-age main sequence properties of the stars and their current age at every timestep. SEBA is however designed to calculate the future evolution of a star from both its ZAMS properties and its past history; this is crucial for the coupling of binary stellar evolution to stellar dynamics. Indeed, as we expect dynamical binary formation and exchanges to be ubiquitous in dense stellar clusters, it is likely that a binary interaction product will find itself in a binary with a star that is not its original companion. We have modified both the SEBA and the FLASH interface to AMUSE to enable this capability for Chapter 4. For Chapters 2 and 3, the wind mass loss rates are calculated outside of SEBA, using the fitting formulae from Vink et al. (2000); they are calculated within SEBA for Chapter 4.

The mechanical and radiative feedback is handled directly in FLASH. Winds are injected with a momentum-conserving scheme described in Wall et al. (2020); the velocities are calculated from the fitting formulae of Kudritzki & Puls (2000). Radiative feedback, heating, and cooling are handled with the ray-tracing scheme FERVENT (Baczynski et al. 2015), which follows rays from individual sources (i.e. individual stars). We follow radiation in two bands, 5.6–13.6 eV and > 13.6 eV, which provide respectively direct radiation pressure and ionizing radiation. We calculate the number and average energy of the photons in each band for each massive star; we assume that the star is a blackbody for the FUV band and for ionizing radiation from B stars, while we use the atmospheric model of Lanz & Hubeny (2003) for O stars. Although core-collapse SNe are implemented in TORCH, no star in the simulations presented in this thesis has reached SN.

1.3.3 Thesis outline

This thesis is made up of three separate studies, each addressing one of the questions outlined in Section 1.3.1. Each study also uses its own suite of simulations and its own numerical methods, which are described (as relevant) within each chapter.

In Chapter 2, we present simulations of the formation of embedded clusters within GMCs, with masses typical of Galactic embedded clusters. We use those simulations to investigate the assembly history of the clusters and the evolution of their morphology. We compare our results to observed embedded clusters from the MYStIX survey (Massive Young Star-Forming Complex Study in IR & X-Rays, Kuhn et al. 2014), and connect observable quantities – such as the cluster sizes and shapes – to their assembly history.

In Chapter 3, we explore the evolution of populations of binaries in different environments. We follow the assembly of embedded clusters with stellar masses of 7.8 x 10^3, 3.4 x 10^4 and 1.95 x 10^5 $M_\odot$, which are representative of embedded clusters in the Milky Way, local YMCs (see Table 1.1) and massive YMCs in star-forming galaxies (see Table 1.2). We analyse the time evolution of the binary fraction and binary properties during cluster formation in those clusters, and investigate the survivability of close massive binaries in environments with high stellar densities.

In Chapter 4, we investigate the effects of feedback from massive interacting binaries. We present an innovative framework to couple binary stellar evolution to stellar dynamics and stellar feedback in gas-rich environments. We develop a new feedback model that accounts for the effects of conservative and non-conservative mass transfer, as well as common envelope ejection, on the luminosities, temperatures, and wind mass loss rates of the stars. We demonstrate its use in simulations of isolated massive binaries and clusters of massive binaries, allowing us – for the first time – to consider the effects of binary interactions on the feedback budget of YMCs.

We summarize the results from those studies and connect them to one another in Chapter 5. In this last chapter, we also discuss avenues for future studies and code development, building on the work presented in this thesis.

Bibliography

Adamo A., et al., 2017, ApJ, 841, 131

Adamo A., et al., 2020a, Space Sci. Rev., 216, 69

Adamo A., et al., 2020b, MNRAS, 499, 3267

Adamo A., et al., 2024, Nature, 632, 513

Andersson E. P., Agertz O., Renaud F., 2020, MNRAS, 494, 3328

Andersson E. P., Agertz O., Renaud F., Teyssier R., 2023, MNRAS, 521, 2196

Arnold B., Wright N. J., 2024, MNRAS, 531, 1191

Baczynski C., Glover S. C. O., Klessen R. S., 2015, MNRAS, 454, 380

Ballesteros-Paredes J., Klessen R. S., Mac Low M. M., Vazquez-Semadeni E., 2007, in Reipurth B., Jewitt D., Keil K., eds, Protostars and Planets V. p. 63 (`arXiv:astro-ph/0603357`), doi:10.48550/arXiv.astro-ph/0603357

Bally J., 2016, ARA&A, 54, 491

Barnes A. T., et al., 2021, MNRAS, 508, 5362

Bastian N., Lardo C., 2018, ARA&A, 56, 83

Baumgardt H., Hénault-Brunet V., Dickson N., Sollima A., 2023, MNRAS, 521, 3991

Bemis A. R., Wilson C. D., 2023, ApJ, 945, 42

Bertoldi F., McKee C. F., 1992, ApJ, 395, 140

Binney J., Tremaine S., 2008, Galactic Dynamics: Second Edition. Princeton University Press

Blaauw A., 1961, Bull. Astron. Inst. Netherlands, 15, 265

Brandner W., et al., 2000, AJ, 119, 292

Brandner W., Clark J. S., Stolte A., Waters R., Negueruela I., Goodwin S. P., 2008, A&A, 478, 137

Britavskiy N., et al., 2023, A&A, 672, A22

Brown G., Gnedin O. Y., 2021, MNRAS, 508, 5935

Burkhart B., 2018, ApJ, 863, 118

Castor J., McCray R., Weaver R., 1975, ApJ, 200, L107

Chandar R., Whitmore B. C., Dinino D., Kennicutt R. C., Chien L. H., Schinnerer E., Meidt S., 2016, ApJ, 824, 71

Chevalier R. A., 1976, ApJ, 208, 826

Chevance M., et al., 2022, MNRAS, 509, 272

Chevance M., Krumholz M. R., McLeod A. F., Ostriker E. C., Rosolowsky E. W., Sternberg A., 2023, in Inutsuka S., Aikawa Y., Muto T., Tomida K., Tamura M., eds, Astronomical Society of the Pacific Conference Series Vol. 534, Protostars and Planets VII. p. 1 (arXiv:2203.09570), doi:10.48550/arXiv.2203.09570

Cignoni M., et al., 2015, ApJ, 811, 76

Cook D. O., et al., 2019, MNRAS, 484, 4897

Cordoni G., et al., 2023, A&A, 672, A29

Costa G., et al., 2025, A&A, 694, A193

Cournoyer-Cloutier C., et al., 2021, MNRAS, 501, 4464

Cournoyer-Cloutier C., Karam J., Sills A., Zwart S. P., Wilhelm M. J. C., 2024, ApJ, 975, 207

Dalessandro E., et al., 2021, ApJ, 909, 90

Della Croce A., et al., 2023, A&A, 674, A93

Deshmukh S., et al., 2024, ApJ, 974, L24

Dobbs C. L., Bending T. J. R., Pettitt A. R., Buckner A. S. M., Bate M. R., 2022, MNRAS, 517, 675

Donada J., et al., 2023, A&A, 675, A89

Doughty C., Finlator K., 2021, MNRAS, 505, 2207

Drout M. R., Götberg Y., Ludwig B. A., Groh J. H., de Mink S. E., O'Grady A. J. G., Smith N., 2023, Science, 382, 1287

Dubey A., et al., 2014, The International Journal of High Performance Computing Applications, 28, 225

Duchêne G., Lacour S., Moraux E., Goodwin S., Bouvier J., 2018, MNRAS, 478, 1825

Eggleton P. P., 1983, ApJ, 268, 368

Eldridge J. J., Stanway E. R., 2009, MNRAS, 400, 1019

Eldridge J. J., Stanway E. R., 2022, ARA&A, 60, 455

Espinoza P., Selman F. J., Melnick J., 2009, A&A, 501, 563

Fahrion K., De Marchi G., 2024, A&A, 681, A20

Farmer R., Laplace E., de Mink S. E., Justham S., 2021, ApJ, 923, 214

Farmer R., Laplace E., Ma J.-z., de Mink S. E., Justham S., 2023, ApJ, 948, 111

Federrath C., Banerjee R., Clark P. C., Klessen R. S., 2010, ApJ, 713, 269

Fichtner Y. A., Mackey J., Grassitelli L., Romano-Díaz E., Porciani C., 2024, A&A, 690, A72

Figer D. F., Kim S. S., Morris M., Serabyn E., Rich R. M., McLean I. S., 1999, ApJ, 525, 750

Finn M. K., Johnson K. E., Brogan C. L., Wilson C. D., Indebetouw R., Harris W. E., Kamenetzky J., Bemis A., 2019, ApJ, 874, 120

Fryxell B., et al., 2000, ApJS, 131, 273

Fujii M., Iwasawa M., Funato Y., Makino J., 2007, PASJ, 59, 1095

Fujii M. S., Saitoh T. R., Wang L., Hirai Y., 2021, PASJ, 73, 1057

Gennaro M., Brandner W., Stolte A., Henning T., 2011, MNRAS, 412, 2469

Götberg Y., de Mink S. E., Groh J. H., 2017, A&A, 608, A11

Götberg Y., de Mink S. E., Groh J. H., Kupfer T., Crowther P. A., Zapartas E., Renzo M., 2018, A&A, 615, A78

Götberg Y., de Mink S. E., Groh J. H., Leitherer C., Norman C., 2019, A&A, 629, A134

Götberg Y., de Mink S. E., McQuinn M., Zapartas E., Groh J. H., Norman C., 2020, A&A, 634, A134

Götberg Y., et al., 2023, ApJ, 959, 125

Guarcello M. G., Prisinzano L., Micela G., Damiani F., Peres G., Sciortino S., 2007, A&A, 462, 245

Guszejnov D., Raju A. N., Offner S. S. R., Grudić M. Y., Faucher-Giguère C.-A., Hopkins P. F., Rosen A. L., 2023, MNRAS, 518, 4693

Hacar A., Tafalla M., Forbrich J., Alves J., Meingast S., Grossschedl J., Teixeira P. S., 2018, A&A, 610, A77

Hannon S., et al., 2022, MNRAS, 512, 1294

Harayama Y., Eisenhauer F., Martins F., 2008, ApJ, 675, 1319

Harris W. E., 1991, ARA&A, 29, 543

He H., Wilson C., Brunetti N., Finn M., Bemis A., Johnson K., 2022, ApJ, 928, 57

Heggie D. C., 1975, MNRAS, 173, 729

Hennebelle P., Grudić M. Y., 2024, ARA&A, 62, 63

Heyer M., Dame T. M., 2015, ARA&A, 53, 583

Heyer M., Krawczyk C., Duval J., Jackson J. M., 2009, ApJ, 699, 1092

Hills J. G., 1975, AJ, 80, 809

Hosek Jr. M. W., Lu J. R., Anderson J., Najarro F., Ghez A. M., Morris M. R., Clarkson W. I., Albers S. M., 2019, ApJ, 870, 44

Howard C. S., Pudritz R. E., Harris W. E., 2018, Nature Astronomy, 2, 725

Hunter D. A., Shaya E. J., Holtzman J. A., Light R. M., O'Neil Jr. E. J., Lynds R., 1995, ApJ, 448, 179

Hut P., Bahcall J. N., 1983, ApJ, 268, 319

Iwasawa M., Tanikawa A., Hosono N., Nitadori K., Muranushi T., Makino J., 2016, PASJ, 68, 54

Jeans J. H., 1902, Philosophical Transactions of the Royal Society of London Series A, 199, 1

Jerabkova T., Beccari G., Boffin H. M. J., Petr-Gotzens M. G., Manara C. F., Prada Moroni P. G., Tognelli E., Degl'Innocenti S., 2019, A&A, 627, A57

Joncour I., Duchêne G., Moraux E., 2017, A&A, 599, A14

Kalari V. M., Vink J. S., de Wit W. J., Bastian N. J., Méndez R. A., 2019, A&A, 625, L2

Kamann S., et al., 2020, A&A, 635, A65

Keto E. R., Myers P. C., 1986, ApJ, 304, 466

Kirk H., et al., 2017, ApJ, 838, 114

Kobayashi C., Umeda H., Nomoto K., Tominaga N., Ohkubo T., 2006, ApJ, 653, 1145

Kratter K. M., Matzner C. D., 2006, MNRAS, 373, 1563

Kroupa P., 2001, MNRAS, 322, 231

Krumholz M. R., Matzner C. D., 2009, ApJ, 703, 1352

Krumholz M. R., McKee C. F., Bland-Hawthorn J., 2019, ARA&A, 57, 227

Kudritzki R.-P., Puls J., 2000, ARA&A, 38, 613

Kuhn M. A., et al., 2014, ApJ, 787, 107

Kuiper G. P., 1941, ApJ, 93, 133

Kumar M. S. N., Palmeirim P., Arzoumanian D., Inutsuka S. I., 2020, A&A, 642, A87

Kumar M. S. N., Arzoumanian D., Men'shchikov A., Palmeirim P., Matsumura M., Inutsuka S., 2022, A&A, 658, A114

Lada C. J., Lada E. A., 2003, ARA&A, 41, 57

Lahén N., Naab T., Szécsi D., 2024, MNRAS, 530, 645

Lahén N., Naab T., Rantala A., Partmann C., 2025, submitted to MNRAS, arXiv:2504.18620

Lancaster L., Ostriker E. C., Kim J.-G., Kim C.-G., 2021a, ApJ, 914, 89

Lancaster L., Ostriker E. C., Kim J.-G., Kim C.-G., 2021b, ApJ, 922, L3

Lancaster L., Ostriker E. C., Kim C.-G., Kim J.-G., Bryan G. L., 2024, ApJ, 970, 18

Lanz T., Hubeny I., 2003, ApJS, 146, 417

Larson R. B., 1981, MNRAS, 194, 809

Lee K. I., et al., 2016, ApJ, 820, L2

Leigh N., Sills A., 2011, MNRAS, 410, 2370

Leitherer C., et al., 1999, ApJS, 123, 3

Leroy A. K., et al., 2018, ApJ, 869, 126

Levy R. C., et al., 2024, ApJ, 973, L55

Lim B., Chun M.-Y., Sung H., Park B.-G., Lee J.-J., Sohn S. T., Hur H., Bessell M. S., 2013, AJ, 145, 46

Liu H.-L., et al., 2023, MNRAS, 522, 3719

Lucatello S., Sollima A., Gratton R., Vesperini E., D'Orazi V., Carretta E., Bragaglia A., 2015, A&A, 584, A52

Ma X., Hopkins P. F., Kasen D., Quataert E., Faucher-Giguère C.-A., Kereš D., Murray N., Strom A., 2016, MNRAS, 459, 3614

Mac Low M.-M., Klessen R. S., 2004, Reviews of Modern Physics, 76, 125

Marchant P., Bodensteiner J., 2024, ARA&A, 62, 21

Matzner C. D., Jumper P. H., 2015, ApJ, 815, 68

Maud L. T., et al., 2019, A&A, 627, L6

McCrady N., Graham J. R., 2007, ApJ, 663, 844

McKee C. F., Ostriker E. C., 2007, ARA&A, 45, 565

McLaughlin D. E., van der Marel R. P., 2005, ApJS, 161, 304

McMillan S. L. W., Vesperini E., Portegies Zwart S. F., 2007, ApJ, 655, L45

McMillan S., Portegies Zwart S., van Elteren A., Whitehead A., 2012, in Capuzzo-Dolcetta R., Limongi M., Tornambè A., eds, ASP Conf. Ser. Vol. 453, Advances in Computational Astrophysics: Methods, Tools, and Outcome. San Francisco, p. 129 (arXiv:1111.3987)

Menon S. H., Federrath C., Krumholz M. R., 2023, MNRAS, 521, 5160

Messa M., et al., 2018, MNRAS, 473, 996

Milone A. P., et al., 2012, A&A, 540, A16

Milone A. P., et al., 2016, MNRAS, 455, 3009

Milone A. P., et al., 2025, A&A, 698, A247

De Mink S. E., Pols O. R., Langer N., Izzard R. G., 2009, A&A, 507, L1

De Mink S. E., Sana H., Langer N., Izzard R. G., Schneider F. R. N., 2014, ApJ, 782, 7

Moe M., Di Stefano R., 2017, ApJS, 230, 15

Moe M., Kratter K. M., Badenes C., 2019, ApJ, 875, 61

Morton D. C., 1960, ApJ, 132, 146

Naab T., Ostriker J. P., 2017, ARA&A, 55, 59

Nguyen M., Sills A., 2024, ApJ, 969, 18

Niu H., Wang J., Fu J., 2020, ApJ, 903, 93

O'Dell C. R., Wen Z., Hu X., 1993, ApJ, 410, 696

Offner S. S. R., Moe M., Kratter K. M., Sadavoy S. I., Jensen E. L. N., Tobin J. J., 2023, in Inutsuka S., Aikawa Y., Muto T., Tomida K., Tamura M., eds, Astronomical Society of the Pacific Conference Series Vol. 534, Protostars and Planets VII. p. 275 (arXiv:2203.10066), doi:10.48550/arXiv.2203.10066

Olivier G. M., Lopez L. A., Rosen A. L., Nayak O., Reiter M., Krumholz M. R., Bolatto A. D., 2021, ApJ, 908, 68

Paczyński B., 1971, ARA&A, 9, 183

Paczynski B., 1976, in Eggleton P., Mitton S., Whelan J., eds, IAU Symposium Vol. 73, Structure and Evolution of Close Binary Systems. p. 75

Parker R. J., Meyer M. R., 2014, MNRAS, 442, 3722

Pascale M., Dai L., McKee C. F., Tsang B. T. H., 2023, ApJ, 957, 77

Paxton B., Bildsten L., Dotter A., Herwig F., Lesaffre P., Timmes F., 2011, ApJS, 192, 3

Paxton B., et al., 2015, ApJS, 220, 15

Pelupessy F. I., van Elteren A., de Vries N., McMillan S. L. W., Drost N., Portegies Zwart S. F., 2013, A&A, 557, A84

Plunkett A. L., Arce H. G., Corder S. A., Dunham M. M., Garay G., Mardones D., 2015, ApJ, 803, 22

Podsiadlowski P., Joss P. C., Hsu J. J. L., 1992, ApJ, 391, 246

Polak B., et al., 2024a, A&A, 690, A94

Polak B., et al., 2024b, A&A, 690, A207

Portegies Zwart S., McMillan S. L. W., 2019, Astrophysical Recipes: The Art of Amuse. Institute of Physics Publishing, Bristol

Portegies Zwart S. F., Verbunt F., 1996, A&A, 309, 179

Portegies Zwart S., et al., 2009, New Astron., 14, 369

Portegies Zwart S. F., McMillan S. L. W., Gieles M., 2010, ARA&A, 48, 431

Portegies Zwart S., McMillan S. L. W., van Elteren E., Pelupessy I., de Vries N., 2013, Computer Physics Communications, 184, 456

Poveda A., Ruiz J., Allen C., 1967, Boletin de los Observatorios Tonantzintla y Tacubaya, 4, 86

Ramírez-Agudelo O. H., et al., 2013, A&A, 560, A29

Ramírez-Agudelo O. H., et al., 2015, A&A, 580, A92

Rathjen T.-E., et al., 2021, MNRAS, 504, 1039

Reina-Campos M., Gnedin O. Y., Sills A., Li H., 2025, ApJ, 978, 15

Renaud F., 2018, NewAR, 81, 1

Rodríguez M. J., et al., 2025, ApJ, 983, 137

Röpke F. K., De Marco O., 2023, Living Reviews in Computational Astrophysics, 9, 2

Rosdahl J., et al., 2018, MNRAS, 479, 994

Ryon J. E., et al., 2015, MNRAS, 452, 525

Ryon J. E., et al., 2017, ApJ, 841, 92

Sabbi E., et al., 2012, ApJ, 754, L37

Saha A., et al., 2022, MNRAS, 516, 1983

Sana H., et al., 2012, Science, 337, 444

Sana H., et al., 2022, A&A, 668, L5

Schinnerer E., Leroy A. K., 2024, ARA&A, 62, 369

Schneider F. R. N., et al., 2014, ApJ, 780, 117

Schneider F. R. N., et al., 2018, Science, 359, 69

Secunda A., Cen R., Kimm T., Götberg Y., de Mink S. E., 2020, ApJ, 901, 72

Senchyna P., et al., 2017, MNRAS, 472, 2608

Shenar T., et al., 2016, A&A, 591, A22

Shenar T., et al., 2019, A&A, 627, A151

Sigurdsson S., Phinney E. S., 1993, ApJ, 415, 631

Spitzer Jr. L., 1969, ApJ, 158, L139

Spitzer Jr. L., Mathieu R. D., 1980, ApJ, 241, 618

Stanway E. R., Eldridge J. J., 2018, MNRAS, 479, 75

Steidel C. C., Strom A. L., Pettini M., Rudie G. C., Reddy N. A., Trainor R. F., 2016, ApJ, 826, 159

Steinwandel U. P., Bryan G. L., Somerville R. S., Hayward C. C., Burkhart B., 2023, MNRAS, 526, 1408

Stoop M., Kaper L., de Koter A., Guo D., Lamers H. J. G. L. M., Rieder S., 2023, A&A, 670, A108

Stoop M., et al., 2024, Nature, 634, 809

Sun J., et al., 2018, ApJ, 860, 172

Sun J., et al., 2024, ApJ, 967, 133

Szécsi D., Agrawal P., Wünsch R., Langer N., 2022, A&A, 658, A125

Tobin J. J., et al., 2018, ApJ, 867, 43

Tobin J. J., et al., 2022, ApJ, 925, 39

Toonen S., Nelemans G., Portegies Zwart S., 2012, A&A, 546, A70

Toonen S., Portegies Zwart S., Hamers A. S., Bandopadhyay D., 2020, A&A, 640, A16

Torniamenti S., Ballone A., Mapelli M., Gaspari N., Di Carlo U. N., Rastello S., Giacobbo N., Pasquato M., 2021, MNRAS, 507, 2253

Treviño-Morales S. P., et al., 2019, A&A, 629, A81

VandenBerg D. A., Brogaard K., Leaman R., Casagrande L., 2013, ApJ, 775, 134

Vanzella E., et al., 2022, A&A, 659, A2

Vanzella E., et al., 2023, ApJ, 945, 53

Villaseñor J. I., et al., 2025, A&A, 698, A41

Vincke K., Pfalzner S., 2018, ApJ, 868, 1

Vink J. S., 2022, ARA&A, 60, 203

Vink J. S., Sander A. A. C., 2021, MNRAS, 504, 2051

Vink J. S., de Koter A., Lamers H. J. G. L. M., 2000, A&A, 362, 295

Wagg T., et al., 2025, submitted to ApJ, arXiv:2504.17903

Walch S., Naab T., 2015, MNRAS, 451, 2757

Wall J. E., McMillan S. L. W., Mac Low M.-M., Klessen R. S., Portegies Zwart S., 2019, ApJ, 887, 62

Wall J. E., Mac Low M.-M., McMillan S. L. W., Klessen R. S., Portegies Zwart S., Pellegrino A., 2020, ApJ, 904, 192

Wang L., Nitadori K., Makino J., 2020a, MNRAS, 493, 3398

Wang L., Iwasawa M., Nitadori K., Makino J., 2020b, MNRAS, 497, 536

Weaver R., McCray R., Castor J., Shapiro P., Moore R., 1977, ApJ, 218, 377

Whitmore B. C., et al., 2023, ApJ, 944, L14

Whitmore B. C., et al., 2025, ApJ, 982, 50

Wilhelm M. J. C., Portegies Zwart S., Cournoyer-Cloutier C., Lewis S. C., Polak B., Tran A., Mac Low M.-M., 2023, MNRAS, 520, 5331

Winter A. J., Benisty M., Shuai L., Dûchene G., Cuello N., Anania R., Cadiou C., Joncour I., 2024, A&A, 691, A43

Woosley S. E., 2019, ApJ, 878, 49

Woosley S. E., Weaver T. A., 1995, ApJS, 101, 181

Zapartas E., et al., 2017, A&A, 601, A29

Zapata L. A., Garay G., Palau A., Rodríguez L. F., Fernández-López M., Estalella R., Guzmán A., 2019, ApJ, 872, 176

Zeidler P., et al., 2015, AJ, 150, 78

Zeidler P., Nota A., Grebel E. K., Sabbi E., Pasquali A., Tosi M., Christian C., 2017, AJ, 153, 122

Zeidler P., Sabbi E., Nota A., McLeod A. F., 2021, AJ, 161, 140

CHAPTER 2

EARLY EVOLUTION AND THREE-DIMENSIONAL STRUCTURE OF EMBEDDED STAR CLUSTERS

The content of this chapter is published in the *Monthly Notices of the Royal Astronomical Society* under the following citation:

Cournoyer-Cloutier, C., Sills, A., Harris, W. E., Appel, S. M., Lewis, S. C., Polak, B., Tran, A., Wilhelm, M. J. C., Mac Low, M.-M., McMillan, S. L. W. and Portegies Zwart, S. (2023). Early evolution and three-dimensional structure of embedded star clusters, *MNRAS* **521**(1): 1338–1352.

Abstract

We perform simulations of star cluster formation to investigate the morphological evolution of embedded star clusters in the earliest stages of their evolution. We conduct our simulations with TORCH, which uses the AMUSE framework to couple state-of-the-art stellar dynamics to star formation, radiation, stellar winds, and hydrodynamics in FLASH. We simulate a suite of 10^4 $M_\odot$ clouds at 0.0683 pc resolution for $\sim$2 Myr after the onset of star formation, with virial parameters $\alpha = 0.8, 2.0, 4.0$ and different random samplings of the stellar initial mass function and prescriptions for primordial binaries. Our simulations result in a population of embedded clusters with realistic morphologies (sizes, densities, and ellipticities) that reproduce the known trend of clouds with higher initial α having lower star formation efficiencies. Our key results are as follows: (1) Cluster mass growth is not monotonic, and clusters can lose up to half of their mass while they are embedded. (2) Cluster morphology is not correlated with cluster mass and changes over $\sim$0.01 Myr timescales. (3) The morphology of an embedded cluster is not indicative of its long-term evolution but only of its recent history: radius and ellipticity increase sharply when a cluster accretes stars. (4) The dynamical evolution of very young embedded clusters with masses $\lesssim$ 1000 $M_\odot$ is dominated by the overall gravitational potential of the star-forming region rather than by internal dynamical processes such as two- or few-body relaxation.

Keywords: open clusters and associations: general – galaxies: star clusters: general – galaxies: star formation

2.1 Introduction

Most stars form within embedded clusters (Lada & Lada 2003; Portegies Zwart et al. 2010). They remain shrouded in their natal gas for a few megayears after the onset of star formation (see e.g. Kim et al. 2022, for recent observations), while the cloud is still actively star-forming. Although most stars do not remain in bound star clusters for their whole lives, their formation and early evolution is shaped by the dense stellar environment in which they are born, which is in turn shaped by the interplay between gravity, turbulence, and stellar feedback. On smaller scales, stars also do not form in isolation: most stars form in multiple stellar systems (Offner et al. 2023, and references therein), most often in binaries. Binaries are known to be dynamically important for cluster long-term evolution (Heggie 1975; Hills 1975). Recent simulations by Torniamenti et al. (2021) further suggest that the presence of binaries impacts a cluster's structure over time-scales of a few megayears after it has become free of gas. Despite their ubiquity, binaries in embedded clusters are seldom modelled numerically due the range of physical processes involved and the high numerical cost of modelling concurrently stellar dynamics on the scale of binaries and feedback processes impacting the gas in the embedded cluster.

Simulations of star cluster formation show that star clusters assemble through the merging of smaller embedded clusters over a few megayears (e.g. Fujii et al. 2012; Vázquez-Semadeni et al. 2017; Grudić et al. 2018; Howard et al. 2018; Chen et al. 2021). Karam & Sills (2022) have further shown that those mergers have an important impact on the boundedness of the stars and gas in the resultant cluster: some head-on collisions between clusters do not result in a single bound cluster, while there is mass loss and an increase in radius even in the successful mergers. The simulations conducted by Karam & Sills (2022) however do not account for the formation of new stars during cluster assembly. Recent work by Dobbs et al. (2022), which relies on star particles representing low-mass stellar populations or massive stars to model clusters, also reveals a more complex picture: clusters can not only merge, but also split. They also trace the mass and size of their clusters throughout their simulations and find no clear correlation between mass and size. They however assume a spherical shape when measuring the size of their clusters, which is not the case for observed embedded clusters (e.g. Kuhn et al. 2014). Furthermore, neither of these recent suites of simulations include binaries, which are expected to influence stellar dynamics on the cluster scale, at least once the cluster becomes free of gas.

The virial parameter α of the star-forming cloud of gas, which describes the balance

between the effects of self-gravity and turbulent support of the gas, is also important for cluster formation and evolution. For a spherical cloud, the virial parameter is defined as

$$\alpha = \frac{2T}{|U|} = \frac{5\sigma^2 R}{GM} \tag{2.1}$$

where T is the kinetic energy of the cloud, U is its gravitational potential energy, σ is its velocity dispersion, R is its radius, M is its mass, and G is the gravitational constant (Bertoldi & McKee 1992). Thus clouds with smaller α are more strongly bound, and $\alpha = 1$ corresponds to virial equilibrium. Observed clouds in galaxies cover a large range of virial parameters, from $\alpha \lesssim 0.1$ to $\alpha \gtrsim 100$ (Kauffmann et al. 2013). A cloud's virial parameter systematically affects its star formation efficiency (SFE) and cluster formation efficiency (CFE; Kruijssen 2012; Howard et al. 2016), with regions with higher α generally having lower SFE and CFE.

In this work, we use numerical simulations to investigate the effects of stellar dynamics and cloud-scale hydrodynamics on the structure and evolution of embedded star clusters. To test the relative importance of stellar dynamics, we explore the impact of forming (or not forming) primordial binaries with different underlying populations, as binaries are known to play an important role in setting cluster structure in systems dominated by stellar dynamics (e.g. Heggie 1975; Fujii & Portegies Zwart 2011; Torniamenti et al. 2021). To test the relative importance of cloud-scale hydrodynamics, we vary the cloud's initial virial parameter α, which is known to have a strong effect on the CFE (e.g. Howard et al. 2016). We want to determine (1) whether cloud-scale hydrodynamics or stellar dynamics have the strongest impact on cluster structure (mass, size, and shape) and cluster formation efficiency and (2) how cluster structure evolves during the earliest stages of formation.

In Section 2.2, we describe our numerical framework and our simulations. In Section 2.3, we follow the evolution of the bulk properties of the stars in the simulation domain, we investigate the instantaneous properties of the clusters as a population, and we examine the assembly history of individual clusters; Section 2.3.3 contains the key results of the paper. In Section 2.4, we discuss the broader implications of our findings. We summarize our results in Section 2.5.

2.2 Methods

2.2.1 Numerical Framework

We use Torch (Wall et al. 2019, 2020; Cournoyer-Cloutier et al. 2021), which relies on the Amuse framework (Portegies Zwart et al. 2009; Pelupessy et al. 2013; Portegies Zwart et al. 2013; Portegies Zwart & McMillan 2019) to couple hydrodynamics to stellar dynamics, star and binary formation via sink particles, stellar evolution, and stellar feedback in the form of winds and radiation. Torch is optimized to investigate the effects of stellar and binary dynamics in young, gas-rich clusters, in particular stable multiple systems and dynamical short-range encounters between stars. We model the self-gravitating gas with the adaptive mesh refinement code Flash (Fryxell et al. 2000). We use simultaneously two types of refinement criteria for our adaptive grid. We first require that the Jeans length be resolved by at least four resolution elements in order to avoid numerical fragmentation (Truelove et al. 1997; Federrath et al. 2010). To improve stability, we also refine around sharp changes in pressure, temperature, total energy, and internal energy (i.e. at shocks and contact discontinuities, Lohner 1987; MacNeice et al. 2000). Although Flash can evolve magnetic fields, we do not include them in our simulations due to their high computational cost. We treat gas dynamics with a Harten-Lax-van Leer Riemann solver (Miyoshi & Kusano 2005) and an unsplit (magneto)-hydrodynamics solver (Lee 2013) with third-order piecewise parabolic method reconstruction (Colella & Woodward 1984). We handle the gas self-gravity with a multigrid solver (Ricker 2008) while we handle the gravitational attraction of the gas on the stars and vice-versa with a leapfrog scheme (Wall et al. 2019, based on Fujii et al. 2007).

On the stellar dynamics side, we handle long-range stellar dynamics with the direct N-body code Ph4 (McMillan et al. 2012), which uses a fourth-order Hermite predictor-corrector scheme (Makino & Aarseth 1992). For stable binary (and higher order) systems, resonant encounters and scattering, we use the Amuse module Multiples (Portegies Zwart & McMillan 2019), which itself uses the codes smallN (Hut et al. 1995; McMillan & Hut 1996) and kepler (originally developed as part of Starlab, Portegies Zwart et al. 1999; Hut et al. 2010).

Star formation takes place within sink particles that are treated as star factories. The details of the sink implementation are presented in Wall et al. (2019) for single star formation and Cournoyer-Cloutier et al. (2021) for binary formation. Briefly, a sink particle is formed when the local gas density and convergence criteria outlined in Federrath et al. (2010) are satisfied. Once formed, it samples an initial mass function (Kroupa

2001) between 0.08 $M_\odot$ and 150 $M_\odot$ to generate a list of stars to be formed, using a Poisson sampling method first tested by Sormani et al. (2017) and implemented in TORCH by Wall et al. (2019). Each star in the list is formed when the sink has accreted sufficient mass, in order to ensure quasi-local mass conservation. The sink must also sit in cold ($<$ 100 K) gas to form stars. Stars are formed with a gas-to-star conversion efficiency of 100 per cent. The additive properties of the Poisson distribution ensure that the sampling for the full simulation domain reproduces the IMF, despite possible stochastic variations within individual clusters. The decoupling allows the stars to be handled by the N-body solver PH4, which is fourth-order accurate, instead of the second-order leapfrog scheme used for sink particles. Although the formation of individual stars is unresolved in our simulations, stellar dynamics are followed self-consistently after star formation.

Stars with masses above 7 $M_\odot$ inject radiative and momentum feedback on the grid. The details of the feedback implementation are presented in Wall et al. (2020). The far ultraviolet (between 5.6 eV and 13.6 eV) and ionizing (above 13.6 eV) radiative feedback is implemented within FLASH as a modified version of the adaptive ray-tracing module FERVENT (Baczynski et al. 2015). The total and average photon energy are calculated for each star from the surface temperature and mass obtained from stellar evolution, which is performed with SEBA (Portegies Zwart & Verbunt 1996). All radiative feedback heats the gas. Massive stars further provide feedback in the form of momentum-driven winds with mass loss rates based on Vink et al. (2000). Radiative cooling of the gas from atomic and molecular lines and dust is included (Wall et al. 2019).

2.2.2 Simulations and Star Formation Prescriptions

We conduct a total of 12 simulations, summarized in Table 2.1. All simulations are initialized from a spherical, turbulent cloud of neutral dense gas with a mass of 10^4 $M_\odot$ and a radius of 7 pc in a cubic box of side 17.5 pc, following the model used in Cournoyer-Cloutier et al. (2021). The mean gas surface density is 50 $M_\odot$ pc^{-2}. Those values are consistent with a typical cloud in the Solar neighbourhood (Chen et al. 2020). The cloud follows a Gaussian density profile with a central density 8.75 x 10^{-22} g cm^{-3} and temperature 20.64 K, and sits in a warm neutral medium with density 2.18 x 10^{-24} g cm^{-3} and temperature 6.11 x 10^3 K. These values were chosen to ensure pressure and thermal equilibrium between the cloud and surrounding medium. The free-fall time for the cloud is 1.45 Myr. The gas follows an adiabatic equation of state with $\gamma = 5/3$, although radiative cooling maintains the dense neutral gas almost isothermal. We adopt the same gas spatial resolution of 0.0683 pc at the maximum refinement level and density

Name	α	Primordial binaries	Random seed
B-P0	0.8	Field distribution	Default
B-P1	0.8	10% random pairing	Seed 1
B-P2	0.8	100% random pairing	Seed 2
B-P3	0.8	Field distribution for $M < 0.6 M_{\odot}$ and no close massive binaries	Seed 3
S-R0	0.8	None	Default
S-R1	0.8	None	Seed 4
S-R2	0.8	None	Seed 5
S-R3	0.8	None	Seed 6
B-V2	2.0	Field distribution	Default
S-V2	2.0	None	Default
B-V4	4.0	Field distribution	Default
S-V4	4.0	None	Default

TABLE 2.1: Overview of simulations' initial conditions and star formation prescriptions. $\alpha = 2T/|U|$ denotes the virial parameter; bound clouds have $\alpha < 2$ and unbound clouds have $\alpha > 2$. The prescriptions for primordial binaries are outlined in Appendix 2.A.

threshold for the formation of sink particles of 3.82 x 10^{-21} g cm^{-3} as used in Cournoyer-Cloutier et al. (2021).

We consider four different prescriptions for binaries (described in Appendix 2.A), in addition to models without primordial binaries. Our models with primordial binaries span a range of mass-dependant binary fractions, mass ratios, and orbital periods. We stress that the details of those prescriptions are not the focus of this paper – rather, we test diverse models for primordial binaries to fully explore the impact that a change in stellar dynamics has on embedded cluster structure and evolution. Binaries can also form dynamically, and the properties of primordial and dynamically-formed binaries will be modified by dynamics over the course of our simulations. We refer the interested reader to Cournoyer-Cloutier et al. (2021) for a detailed discussion of the effects of dynamical interactions on the initial population of binaries.

Eight of our 12 simulations (with names starting with B-P and S-R) are initialized with a virial parameter $\alpha = 2T/|U| = 0.8$. The gas is initially gravitationally bound and its collapse is expected to result in abundant star formation. The gas initial conditions, including the random turbulent field, are identical for those 8 simulations. We also perform simulations with larger virial parameters, of $\alpha = 2.0$ and $\alpha = 4.0$. We perform pairs of simulations with our fiducial prescription for binaries and our single-stars only

prescription (both with the default random seed) for both these models, and label them B-V2, S-V2, B-V4 and S-V4. Those initial conditions are set up by scaling up the gas velocities in each cell of the initial conditions for the $\alpha = 0.8$ runs. We therefore increase α but conserve the direction of motion of the gas in each cell.

Beyond the binary prescriptions and virial parameters, we also vary the random seed used to sample the initial mass function and to form binaries, which sets the masses of the stars and the order in which they form. Our simulations labelled with the random seed *default* all use the same random seed; the other simulations all use different random seeds. We use different random seeds to ensure our general conclusions are not affected by the stochastic formation of massive stars. We have shown in Lewis et al. (2023) that early-forming massive stars can promote the formation of smaller, isolated clusters, and prevent the formation of massive clusters. By using different random samplings of the IMF, we can verify that our conclusions are not drawn from a single, extreme case, in which the formation times and masses of the massive stars providing radiative and mechanical feedback would be atypical.

2.2.3 Cluster Identification

Most of our simulations have reached 2 Myr after the onset of star formation, and snapshots are written every 0.01 Myr. We inspect all snapshots in our simulations for clusters, which we identify from a combination of spatial clustering and boundedness. We initially select clusters with DBSCAN (Ester et al. 1996; Pedregosa et al. 2011) based on the positions of the stars. We require each cluster star to have five neighbours (following Sander et al. 1998, for three-dimensional data), which are other stars within a user-determined distance. For our analysis, we fix this distance to the sink accretion radius, 0.17 pc. Following our initial identification of the clusters, we perform a boundedness check on the stars with respect to their associated cluster. For each star, we calculate the gravitational potential energy from the local gas gravitational potential (including the sink particles) and the potential from the cluster's stars. We also calculate the stars' kinetic energy in the cluster's centre of mass frame. We remove stars with positive total energy (i.e. unbound stars) from the cluster. After this boundedness check, clusters that have at least 100 members are saved for subsequent analysis. An example of the clusters satisfying our clustering, boundedness and minimum membership criteria in a given snapshot is shown in the left panel of Fig. 2.1.

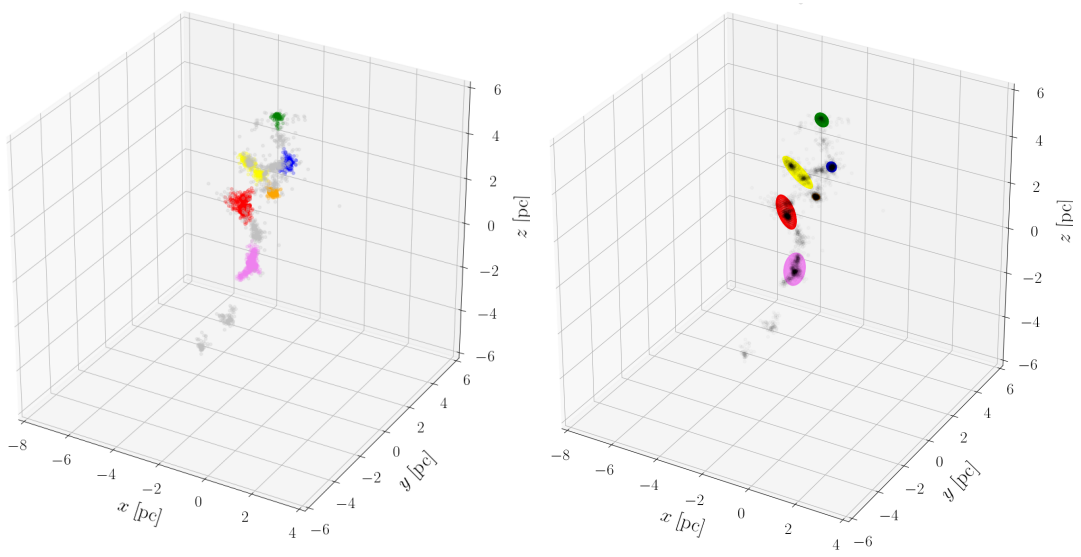

FIGURE 2.1: Left: Example of 3D spatial clustering of the stars in S-R0 at the last snapshot, 2 Myr after the onset of star formation. Member stars for each cluster with at least 100 bound members are shown in a given colour – blue, green, yellow, orange, red, or pink – while unclustered stars are shown in grey. Right: Example of ellipsoids enclosing 90 per cent of the cluster mass for the bound clusters identified in the last snapshot of S-R0, 2 Myr after the onset of star formation. The colours of the ellipsoids match those of the members stars identified on the left.

2.2.4 Cluster Structure

Once clusters are identified, it is useful to describe their size, which in turn requires us to measure their shape. Observational studies have used respectively ellipses (e.g. Kuhn et al. 2014; Zhai et al. 2017) and ellipsoids (e.g. Pang et al. 2021) to describe the 2D and 3D shapes of embedded or open clusters. We similarly use 3D ellipsoids to describe the shape of some inner fraction of the stellar distribution in an individual cluster–here, we use 50 per cent and 90 per cent mass ellipsoids, as proxies for the 50 per cent and 90 per cent Lagrangian radii. We use the fact that any distribution of points can be described by an inertial ellipsoid that shares its rotational properties about its principal axes (see e.g. Goldstein et al. 2001). This technique has been used previously in astrophysics to describe the 3D shape (or projected 2D shape) of dark matter halos in cosmological simulations (see e.g. Velliscig et al. 2015; Thob et al. 2019; Hill et al. 2021; Reina-Campos et al. 2023). We show the 90 per cent mass ellipsoids for the last snapshot of S-R0 (the same example as for the clustering plot) in the right panel of

Fig. 2.1. We present the details of our fitting routine in Appendix 2.B. An example of the 50 per cent and 90 per cent mass ellipsoids for an individual cluster identified in our simulations is also provided in Fig. 2.B1, and the spherical half-mass and 90 per cent Lagragian radii are provided for comparison.

We use our fitted ellipsoids to define a proxy for the radius, to compare our clusters to established mass-radius relations. We do so by taking the geometric mean of the semi-major, intermediate, and semi-minor axes a, b and c to define a characteristic radius

$$\tilde{r} = (abc)^{1/3}, \tag{2.2}$$

which is similar to what is done in observational studies (e.g. Kuhn et al. 2014) to define sizes for elliptical 2D clusters. We can define such a radius for any enclosed mass fraction, and therefore for any Lagrangian radius. To quantify how non-spherical a cluster is, we define an ellipticity (see e.g. Kuhn et al. 2014)

$$\epsilon = \frac{a - c}{a} \tag{2.3}$$

that depends on the ratio between the semi-minor and semi-major axes. A spherical cluster has an ellipticity $\epsilon = 0$ while a very elongated cluster has an ellipticity $\epsilon \to 1$. With equations (2.2) and (2.3), we characterize the size and shape of individual clusters at each snapshot in our simulations.

2.2.5 Cluster History

We follow the evolution of individual clusters throughout the simulations. For each cluster identified in the last snapshot of a simulation, we trace back its main progenitor in earlier snapshots by identifying the cluster sharing the largest fraction of its stellar mass in the previous snapshot. We also look for clusters that are present at earlier times but are no longer present in the last snapshot. We allow for clusters to be missing in some checkpoints (for example, if a cluster with 100 bound members loses one star, then forms one or more later on) but require a cluster to be present over at least 0.1 Myr to trace its history. In practice, this means that a cluster can be used in our analysis of cluster populations (e.g. Sections 2.3.1 and 2.3.2) without being used in our analysis of cluster histories (Section 2.3.3) if it survives for less than 0.1 Myr.

We use our results on cluster histories in three main ways. First, we track the evolution of the mass, size, and shape of individual clusters to investigate the presence of evolutionary trends. Second, we investigate the relative contributions of cluster mergers,

the accretion of unclustered stars, and new star formation to the build-up of our clusters during the first $\sim$ 2 Myr after the onset of star formation. Third, we evaluate what proportion of cluster stellar mass is lost over the same time. Those relative contributions are not final, as the clusters are still growing in mass at the end of the simulations. They however give us a picture of the variations in cluster history during the early stages of embedded cluster evolution.

We rely on the tags given to star particles to follow the assembly of individual clusters. Between two subsequent snapshots in which a cluster is identified, we identify all new star particles and all star particles that left the cluster. For new star particles, we verify whether they were present in the previous snapshot (either in another cluster or as unclustered stars). If they were not present in the previous snapshot, we consider them to be newly-formed stars, and treat them as having formed in the cluster. If they were present, we consider them as accreted stars. Star particles that have left the cluster are recorded as lost stars. For accreted and lost stars, we ensure that there is no double-counting, which could occur for example if a merger is unsuccessful or if a cluster splits. To evaluate cluster assembly, retained stars are therefore treated as formed in the cluster, accreted, or lost, if they respectively fulfill the following criteria:

1. Stars are considered *formed in the cluster* if they were not present (as a clustered or unclustered star) in the snapshot before they are identified as a cluster member, and are present in the cluster in the last snapshot in the simulation. Some of the stars complying with these criteria may have been lost and then re-accreted.

2. Stars are considered *accreted* if they were present in another cluster or as an unclustered star in the snapshot before they are identified as a cluster member, and are present in the cluster in the last snapshot in the simulation. Such stars may also have been lost and then re-accreted.

3. Stars are considered *lost* if they were present in the cluster at any earlier snapshot, and are not present in the cluster in the last snapshot in the simulation. Such stars may also have been lost, re-accreted, and then lost again.

The stars that were cluster members when the cluster was first identified are treated separately to avoid artificially driving up the formed or accreted fractions in low mass clusters. We record the composition of the cluster at the end of our simulations (i.e. the mass in initially-present, formed, and accreted stars), as well as the mass lost throughout the history of the cluster.

2.3 Results

We structure our results in three subsections, corresponding to three different approaches to analysing our simulations. In Section 2.3.1, we summarize the evolution of the full simulation by tracking properties such as the star formation rate (SFR) and the clustered stellar mass. In Section 2.3.2, we track the mass, size, and morphology of the identified clusters as a population, and compare them to observations of Galactic clusters. In Section 2.3.3, we explicitly follow the evolution of the clusters throughout the simulations by tracking how they assemble their mass and how their morphologies change.

2.3.1 Overview: Properties of the Full Simulation Domain

We first look at the global properties of the simulations. The starkest differences are between simulations with different initial virial parameters α. This is already obvious from the plots of the gas column density presented in Fig. 2.2. The three simulations shown in the figure have the same star formation model (single stars only, default random seed) but are initialized with virial parameters of respectively $\alpha = 0.8$, 2.0 and 4.0. Some features in the gas (such as the inverted Y shape made by the densest gas) persist across the three plots, but the gas morphology is nonetheless obviously different in the three simulations. In particular, the gas is less centrally concentrated and closer to the edges of the domain in the simulations with larger virial parameters.

Those morphological differences naturally give rise to differences in the SFR. The SFR and integrated SFE (mass of all formed stars divided by the initial gas mass) for the different simulations are plotted against time since the onset of star formation (SF) in Fig. 2.3. We use a Gaussian filter with a kernel width of 0.1 Myr to smooth both the SFR and the SFE, in order to remove instantaneous peaks in the SFR caused by the formation of individual massive stars. By the time we stop the simulations, the SFR and the SFE are both about half an order of magnitude larger in our simulations with the fiducial $\alpha = 0.8$ than in the simulations with $\alpha = 2.0$, and more than an order of magnitude larger than in the simulations with $\alpha = 4.0$. The different prescriptions for binary formation and the choice of random seed for star formation do not systematically affect the SFR or the SFE. They however cause scatter, which is smaller than the systematic effects associated with variations in α.

Simulations with higher virial parameters begin forming stars earlier than simulations with lower virial parameters. The first stars form respectively at $t_{\rm SF} = 1.12, 1.04, 0.87$

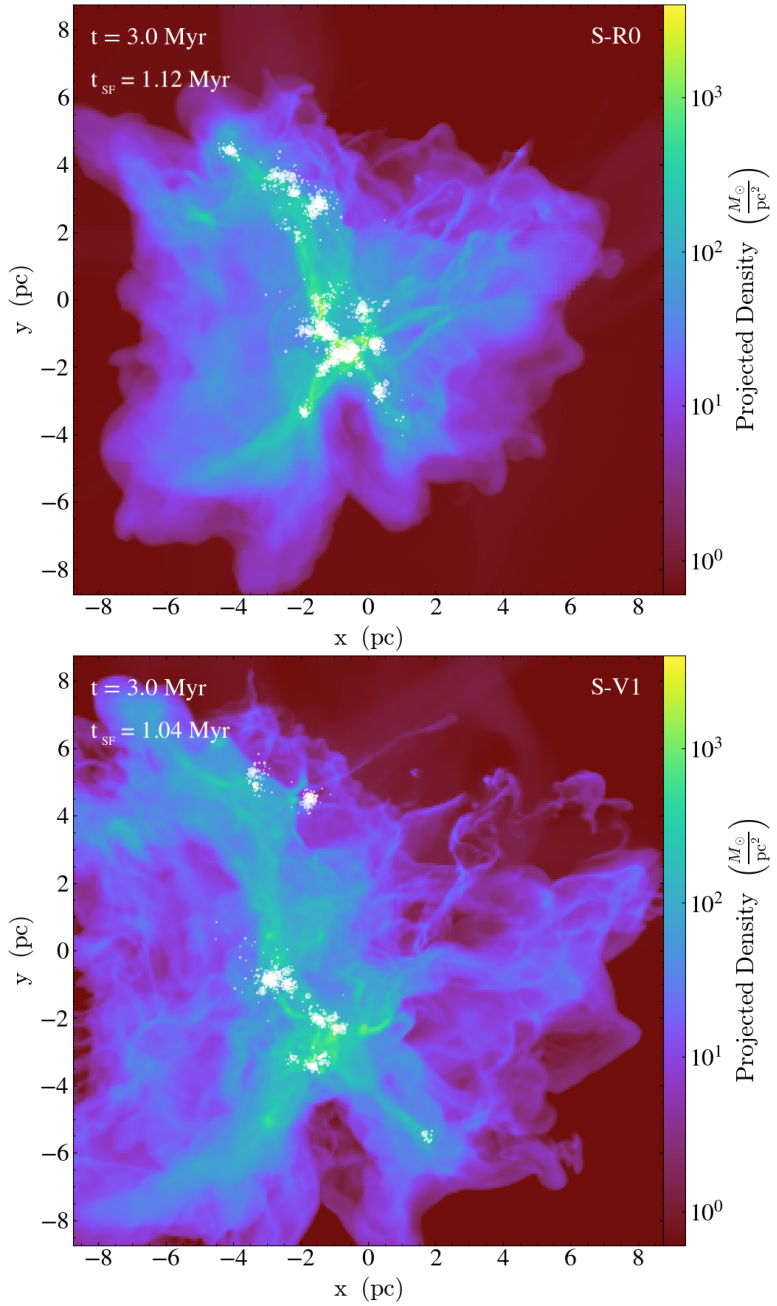

FIGURE 2.2: (1/2) Gas surface density along the z axis for simulations initialized with the different virial parameters α (from top to bottom, $\alpha = 0.8, 2.0, 4.0$), 3.0 Myr after the start of the simulation. Star formation begins at a time $t_{\rm SF}$ (labelled for each frame) after the start of the simulation. All three simulations form single stars only and use the same random seed for star formation. Stars are shown in white, with a marker size proportional to the star's mass.

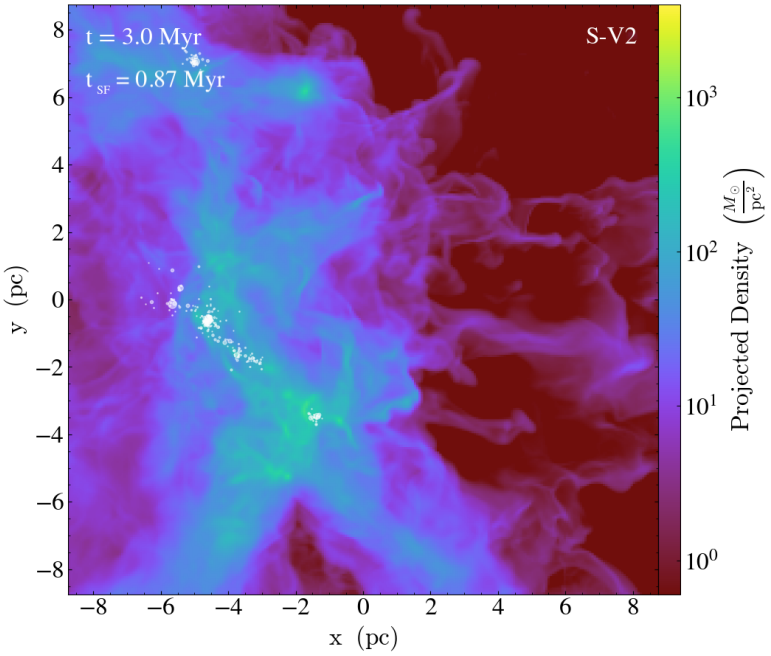

FIGURE 2.2: (2/2) Gas surface density along the z axis for simulations initialized with the different virial parameters α (from top to bottom, $\alpha = 0.8$, 2.0, 4.0), 3.0 Myr after the start of the simulation. Star formation begins at a time $t_{\rm SF}$ (labelled for each frame) after the start of the simulation. All three simulations form single stars only and use the same random seed for star formation. Stars are shown in white, with a marker size proportional to the star's mass.

Myr in simulations with $\alpha = 0.8, 2.0, 4.0$. This is consistent with our expectations: turbulence both promotes star formation–in leading to an earlier onset of SF–and prevents it–in lowering the SFR (Ballesteros-Paredes et al. 2007) but its net effect is to decrease the SFR (Mac Low & Klessen 2004). We also note that the clusters (and the stars) in our simulations with $\alpha = 0.8$ tend to form along a linear chain of width ~ 1 pc (see Fig. 2.1). This is similar to the complexes of embedded clusters in DR 21, NGC 2264, NGC 1893, NGC 6334, and the Carina Nebula observed by Kuhn et al. (2014) in the MYStIX survey.

2.3.2 Average Properties of Individual Clusters

We now turn our attention to the properties of embedded clusters identified in our simulations as a population. For this section, we use all clusters identified at all times in our simulations and measure their masses, sizes, and ellipticities.

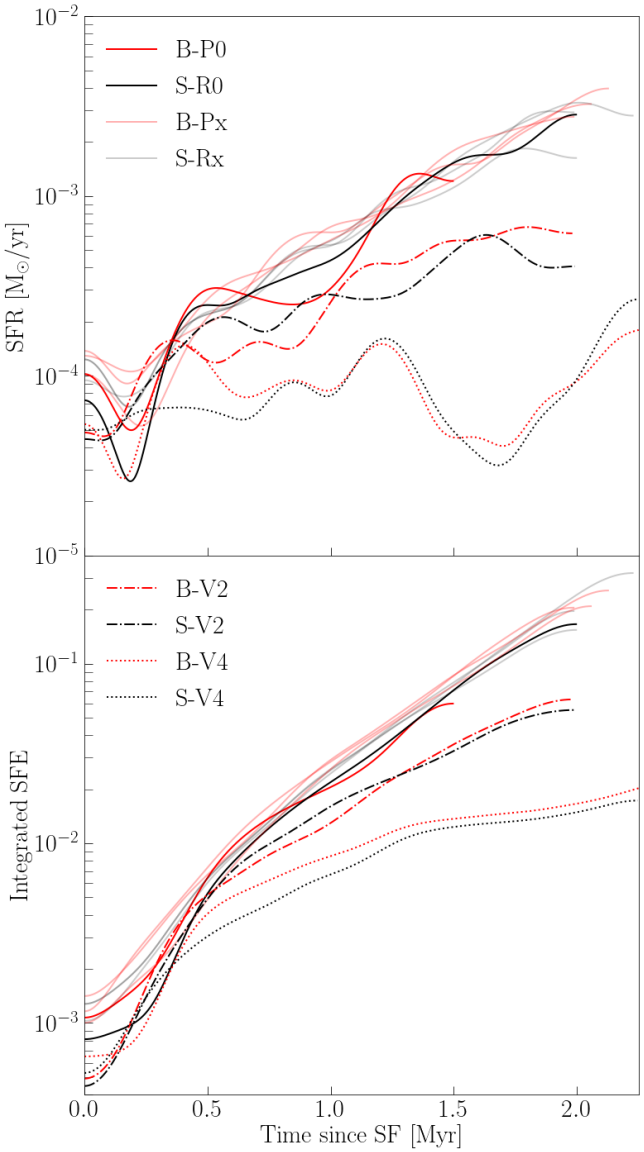

FIGURE 2.3: SFR (top) and integrated SFE (bottom) plotted against the time since the onset of star formation for the different simulations, smoothed over 0.1 Myr using a Gaussian filter. Simulations with primordial binaries are shown in red and simulations with single stars only are shown in black. Transparent red and grey are used for the runs that do not use the default random seed (respectively B-P1, B-P2, and B-P3, and S-R1, S-R2, and S-R3). Solid lines are used for simulations with $\alpha = 0.8$, dashed-dotted lines for simulations with $\alpha = 2.0$, and dotted lines for simulations with $\alpha = 4.0$. Simulations with different α's display different general trends but simulations with the same α and different stellar populations do not.

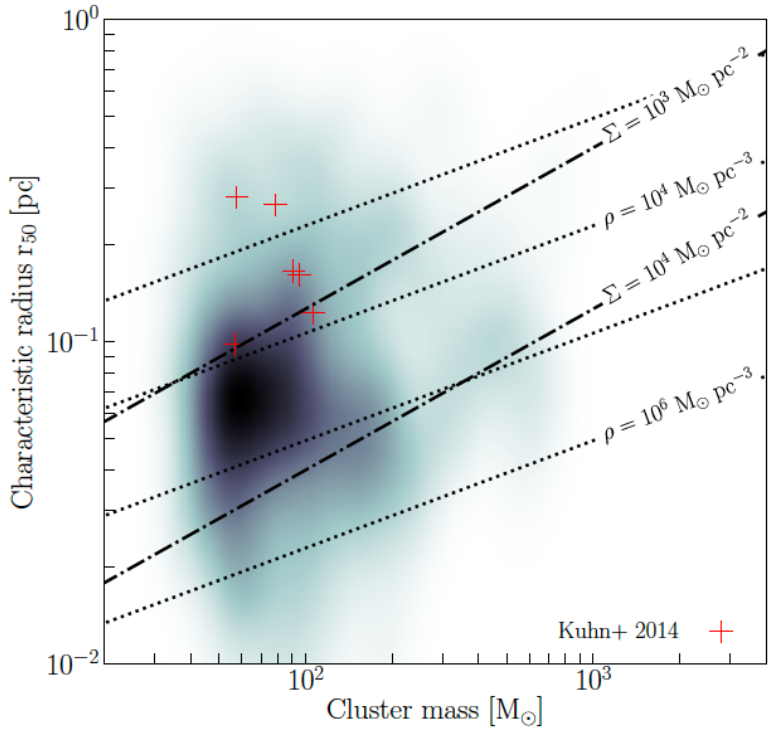

FIGURE 2.4: Distribution of characteristic radius r_{50} against cluster mass, for all clusters identified in each snapshot of our simulations. Brightness decreases linearly with increasing density in parameter space. The dotted lines denote constant densities and the dashed-dotted lines denote constant surface densities. A few high density clusters with masses ∼100 $M_\odot$ and radii <0.01 pc (discussed in-text) lie beyond the limits of the plot. Six deeply embedded clusters with at least 100 members from the MYStIX survey (Kuhn et al. 2014) are shown in red for comparison.

In Fig. 2.4, we present a mass-radius plot for all individual clusters in our simulations, where the characteristic radius r_{50} for the 50 per cent ellipsoid is calculated with equation (2.2) and the cluster mass is obtained from the sum of the masses of all stars identified as cluster members. The diagonal lines denote lines of constant mass density or surface density. We also show in Fig. 2.4 the characteristic radii of six deeply embedded clusters with median X-ray energy in the 0.5-8.0 keV band above 2.0 keV and at least 100 members from the MYStIX survey (Kuhn et al. 2014). Median X-ray energy is a proxy for extinction, and therefore anti-correlated with cluster age; the six selected clusters are expected to be the best match to our simulated cluster population in age

and mass. We calculate the characteristic radii of the observed clusters from

$$\tilde{r} = (ab)^{1/2}, \tag{2.4}$$

where a and b are respectively the semi-major and semi-minor axes of the projected ellipses. We estimate the mass M of the observed clusters from their star counts, using

$$M = 0.485 M_{\odot}\, N, \tag{2.5}$$

where N denotes the star count, and the slope is obtained by fitting the mass against the star count for our simulated clusters. Most identified embedded clusters have masses around 100 $M_{\odot}$, characteristic half-mass radii around 0.05 pc, and therefore densities (calculated within the characteristic half-mass radius) between 10^4 and 10^5 $\mathrm{M_{\odot}\ pc^{-3}}$. The most massive clusters have densities around 10^5 $\mathrm{M_{\odot}\ pc^{-3}}$. This is approximately the same density as the Arches cluster (Serabyn et al. 1998), which has a similar age of $\sim$2 Myr but a mass of a few 10^4 $\mathrm{M_{\odot}}$, about two orders of magnitude larger than our clusters. We therefore conclude that our clusters have densities comparable to the upper limit of observed densities in young Galactic clusters.

Using the two-sample Kolmogorov-Smirnov (KS) test, we find no statistically significant difference in the masses, radii, or densities of the clusters identified in simulations with and without primordial binaries. This supports our earlier conclusion that there are no structural differences in clusters with and without primordial binaries over the timescales spanned by our simulations. Similarly, the clusters formed in simulations with different virial parameters cover similar regions in mass-radius space.

We also find clusters with unphysically high densities (above 10^{10} $\mathrm{M_{\odot}\ pc^{-3}}$) within r_{50}, which is often due to a single star accounting for $\gtrsim$ 30 per cent of the cluster's mass. One star may contribute to up to $\sim$ 50 per cent of the cluster's mass: an extreme example is a $\sim$90 $\mathrm{M_{\odot}}$ star in a $\sim$200 $\mathrm{M_{\odot}}$ cluster, in S-R2. This skews the mass density to much higher than that of observed clusters but the number density remains reasonable. The clusters discussed here are still actively forming, and we expect them to grow via the formation of new stars and mergers with other clusters before star formation halts; the massive star discussed above is therefore expected to become part of a more massive cluster or to be lost as a runaway star.

We plot cluster ellipticity against characteristic radius r_{50} in Fig. 2.5. In the top panel, the ellipticity shown is that of the ellipsoid enclosing 50 per cent of a cluster's mass, calculated with equation (2.3). We compare the radius-ellipticity distribution

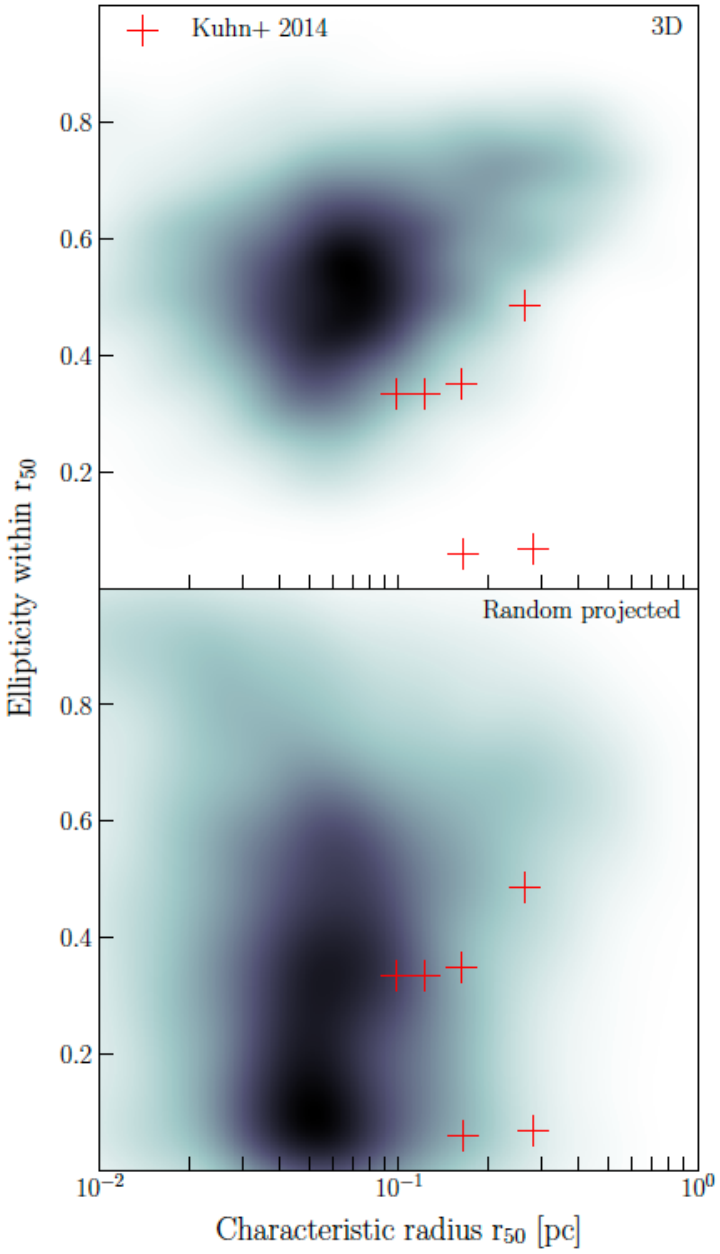

FIGURE 2.5: Ellipticity (top) and ellipticity of the projected ellipses along a random direction (bottom), against effective cluster radius r_{50}. Density in parameter space increases linearly with decreasing brightness. Six deeply embedded clusters with at least 100 members from the MYStIX survey (Kuhn et al. 2014) are shown in red for comparison.

to that of the same six deeply embedded clusters with at least 100 members from the MYStIX survey (Kuhn et al. 2014). For the observed embedded clusters, we calculate the characteristic radius from equation (2.4). Given the apparent mismatch between the simulated and observed clusters, we explore projection effects. To complete this more robust comparison to observations, we calculate the size and ellipticity from 2D projections of the simulated clusters' shapes and present them in the bottom panel. Each 3D ellipsoid is projected along a randomly-selected axis, and the semi-major and semi-minor axes $\tilde{a}$ and $\tilde{b}$ of the projected ellipse are used to calculate the characteristic radius and ellipticity respectively from equations (2.4) and (2.3). When accounting for projection effects, we find that our simulated clusters have ellipticities similar to those of the deeply embedded objects in the MYStIX sample, although our simulated clusters tend to have smaller radii. Kuhn et al. (2014) however find that the sizes of embedded clusters in their sample are positively correlated with cluster age. For their sub-sample of very deeply embedded objects–which are the most comparable in age to our simulated clusters but not limited in star count–they find an average projected radius of 0.04 pc, which is in good agreement with our simulated clusters.

Our simulated embedded clusters have realistic masses, sizes, densities, and ellipticities: conclusions drawn from the study of their evolution can therefore inform our understanding of observed embedded clusters. We further note that there are no systematic differences in the structural properties of our simulated embedded clusters as a population regardless of the presence of primordial binaries or the choice of initial virial parameter for the star-forming cloud.

2.3.3 Time Evolution of Individual Clusters

We now investigate the evolution of individual clusters throughout the simulations. We find no individual cluster satisfying our membership and boundedness criteria that survived more than 0.1 Myr and then merged with another cluster. We however find that some clusters acquire more than ~ 100 $M_\odot$ due to accretion. Two processes contribute to this accretion budget without being registered as mergers. First, clusters satisfying our minimum membership and boundedness criteria may be accreted less than 0.1 Myr after they are first detected, and so before their histories are tracked. Second, groups of stars with fewer than 100 bound members – that are not recorded as clusters – may be accreted. We further find six examples of clusters splitting from an already-formed cluster, four of which survived for more than 0.1 Myr (the other two are identified because they are present in the last snapshot of the simulation).

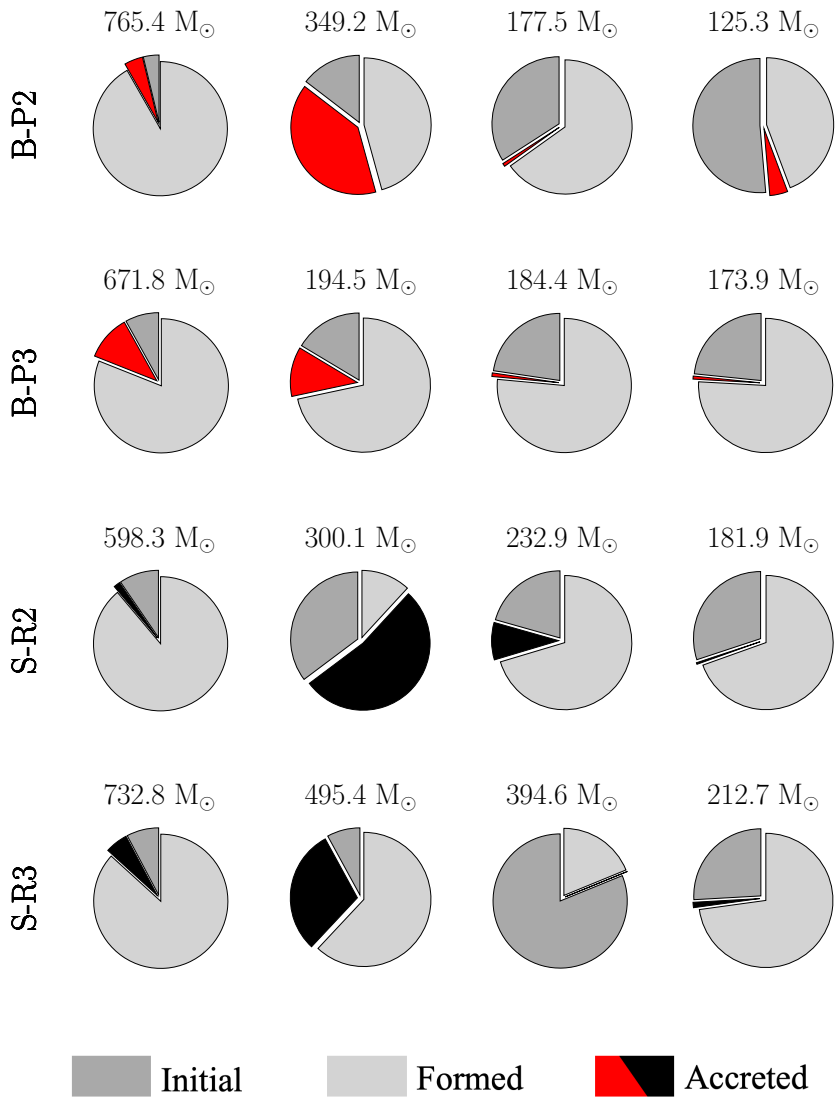

FIGURE 2.6: Contributions of accreted and formed stars to the composition of sixteen example clusters, at the end of our simulations. The examples are the four most massive clusters from the B-P2, B-P3, S-R2 and S-R3 simulations. Dark grey wedges denote the initial (retained) stellar mass and light grey wedges denote the stellar mass formed in the cluster and retained to the last snapshot. Red (in clusters with primordial binaries) and black (in clusters without primordial binaries) wedges denote the accreted stellar mass that is retained to the last snapshot.

In Fig. 2.6, we compare the relative impact of accretion and star formation on the assembly of our simulated embedded clusters. As examples, we show the four most massive clusters from the B-P2, B-P3, S-R2 and S-R3 simulations, which were run respectively to 2.0, 2.1, 2.0, and 2.2 Myr after the onset of star formation. In all cases except the second most massive cluster in S-R2, the formation of new stars within the cluster contributes more mass to the cluster than the accretion of already-formed stars. In that example, accreted mass contributes 53% of the total final mass of the cluster. The most extreme example of splitting is shown in the third most massive cluster in S-R3: the cluster split from the most massive cluster in the simulation 0.1 Myr before the last snapshot, and had a mass of 327 $M_\odot$ just after splitting (see initial mass of the third cluster in the fourth row of Fig. 2.6).

We present in Fig. 2.7 an overview of the relative contributions of mass loss, accretion, and in-cluster star formation to the history of the embedded clusters in our simulations. The lost mass is calculated from the ratio of the mass lost by the cluster to the total mass acquired by the cluster over its history – i.e. the final mass plus the lost mass. The accreted (formed) fraction is calculated as the fraction of the final stellar mass of the cluster that was accreted (formed) after the cluster was first identified. The accreted and formed fractions for a cluster therefore do not add up to 100%, as the stellar mass present in the cluster when it is first identified also contributes. The first violin plot for the lost fractions does not include clusters that split into two clusters surviving for more than 0.1 Myr.

There are no statistically significant differences in the final compositions of clusters with and without primordial binaries, as verified by a series of two-sample KS tests comparing the fractions of the stellar mass lost, accreted, and formed within the cluster for simulations with and without primordial binaries. We also find no statistically significant difference for clusters formed in simulations with $\alpha = 0.8$, $\alpha = 2.0$, and $\alpha = 4.0$. We however find a rich variety of relative contributions from accretion and star formation, at all cluster masses. In other words, we find that there is no single dominant growth mechanism for clusters while they are still deeply embedded and actively star-forming, although generally stars formed *in situ* outnumber accreted stars in a given cluster.

We have shown in Section 2.3.2 that cluster radius and cluster mass are uncorrelated for our full population of simulated embedded clusters. We now investigate how the radii of individual clusters change as they grow in mass. In Fig. 2.8, we present as examples the evolution in radius-mass space of the most massive clusters in the B-P2, B-P3, S-R2 and S-R3 simulations. We find once again no correlation between radius and mass. We

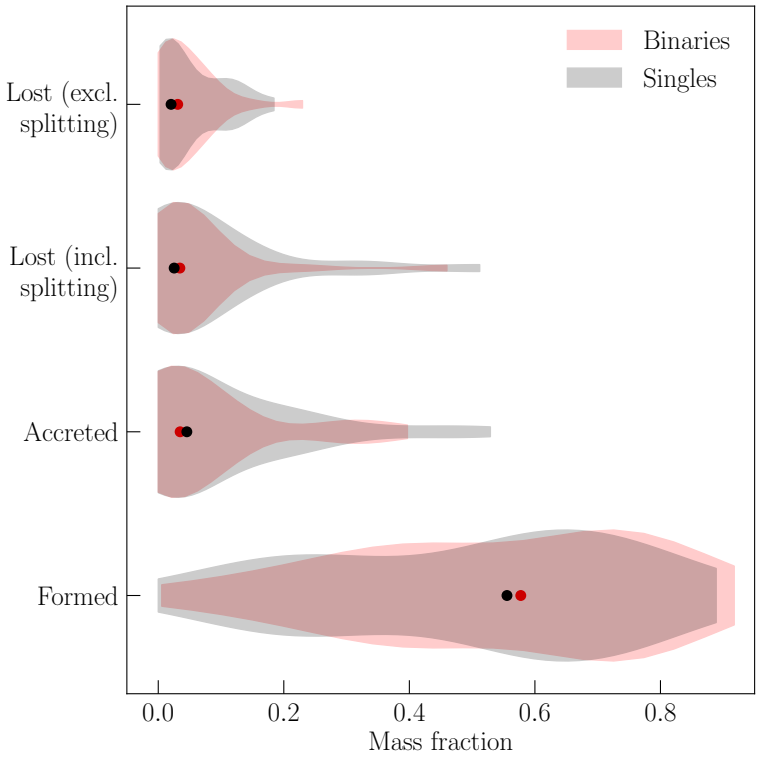

FIGURE 2.7: Distributions of mass fractions of lost, accreted, and formed stars for simulations with primordial binaries (*Binaries*) and without primordial binaries (*Singles*). Medians are shown as solid dots. Note that the accreted and formed fractions do not add up to 100%, as neither includes the stellar mass present in the cluster when it is first identified.

however note that radius can change by up to one order of magnitude without significant changes to the mass (see e.g. S-R3).

We also investigate the evolution of the mass, radius, and ellipticity of individual clusters as a function of the time since they were first identified. In Fig. 2.9, we plot these quantities against the time since cluster formation for all clusters identified in B-P2, B-P3, S-R2, and S-R3. The first important result we glean from this plot is that the mass growth of our simulated clusters is not always monotonic. A clear example is the most massive cluster in S-R3, which loses $\gtrsim 300$ $M_\odot$ within 0.01 Myr as it splits, as discussed above. In most cases, however, the mass of the most massive cluster tends to grow exponentially with time. In all cases except for S-R1, the most massive cluster is also the longest-lived cluster. In most cases, it is however not the one with the highest

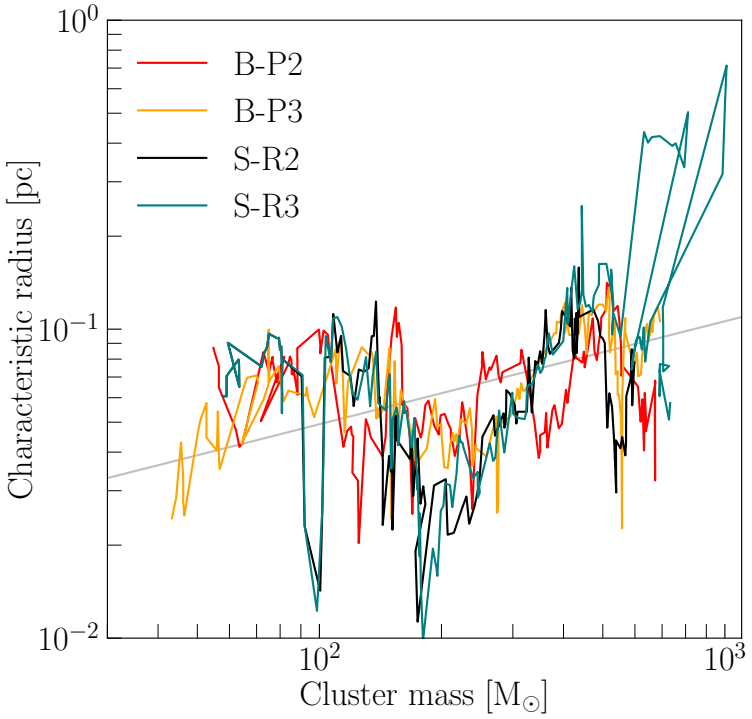

FIGURE 2.8: Characteristic radius r_{50} of the most massive cluster in B-P2, B-P3, S-R2, and S-R3, against its mass. Each line represents the time evolution of a single cluster, with the leftmost end corresponding to the characteristic radius and mass when the cluster is first identified. The grey diagonal line corresponds to a constant density of 10^5 $M_\odot pc^{-3}$.

growth rate, which suggests that another cluster could become more massive at later times. Overall, simulations with and without primordial binaries follow the same general trends.

In Fig. 2.9, we also explore the time evolution of the characteristic radius r_{50} of the clusters in our simulations. We find no correlation between the characteristic radius of a cluster and the time since it was formed. This is an important result as it suggests that the evolution of our embedded simulated clusters is not yet dominated by their internal dynamics, which should cause expansion (see e.g. Torniamenti et al. 2021, for recent simulations). We further highlight that considerable changes in cluster radius, of half an order of magnitude, occur on timescales shorter than 0.01 Myr (i.e. between two consecutive snapshots). We also plot the ellipticity of the distribution of cluster stars enclosed within their characteristic radius r_{50} against time since cluster formation. We once again find no correlation, and find that considerable changes can take place over

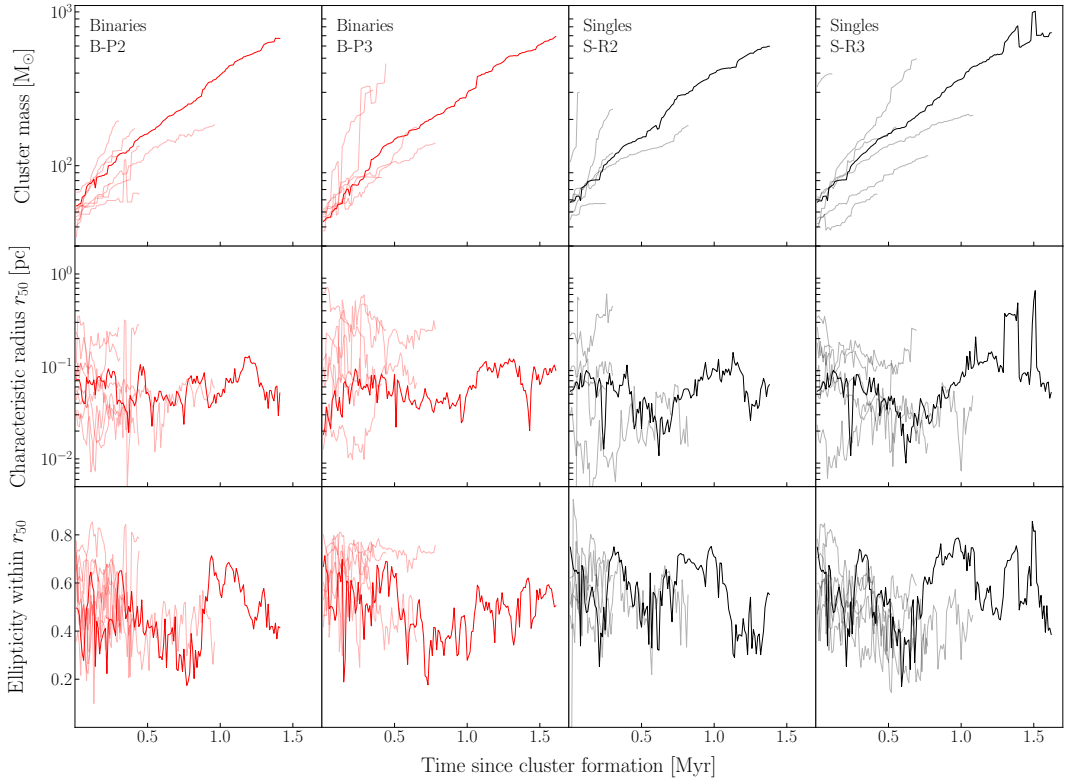

FIGURE 2.9: Mass (top), characteristic radius r_{50} (middle), and ellipticity within the characteristic radius (bottom) of individual clusters in B-P2, B-P3, S-R2, and S-R3 against the time since their formation. The most massive cluster in each simulation is shown in bold; simulations with primordial binaries are shown in red and simulations without primordial binaries are shown in black.

~ 0.01 Myr. Changes in cluster size and shape, while the clusters are actively forming, are therefore driven by physical processes more complex than simply growth in mass or effects from stellar dynamics.

Rapid changes in morphology are driven by accretion and splitting events. We compare the timing of changes in cluster mass, characteristic radius, and ellipticity in Fig. 2.10, and find that they occur at the same times. In particular, we find that the times for the local minima and maxima in characteristic radius and ellipticity match. This is not due to a general correlation between size and shape, as shown in Fig. 2.5: rather, it indicates that clusters grow more elliptical and grow in size at the same time, when they are actively accreting an infalling group of stars. "Failed" accretion events, or

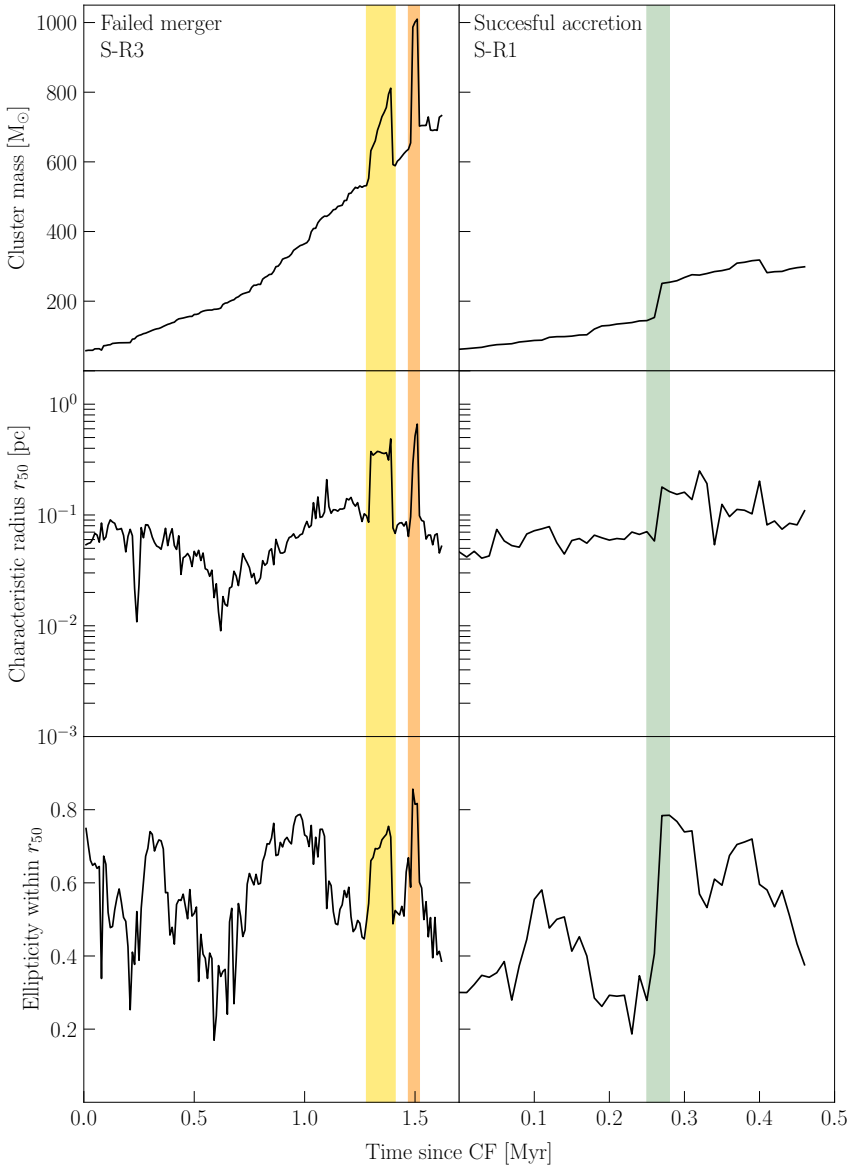

FIGURE 2.10: Morphology histories for the most massive clusters in S-R3 (left) and S-R1 (right). The two regions highlighted in the left panel demonstrate a failed merger. The sudden changes in the stellar mass coincide with very sharp changes in radius and ellipticity. The region highlighted in the right panel denotes a successful accretion event. The growth in mass corresponds to a growth in characteristic radius and in ellipticity. In contrast with the left panel, the radius and ellipticity do not decrease sharply immediately after the event: since the accretion was successful, they decrease more smoothly over the next 0.2 Myr.

events followed by a splitting of the cluster, result in a rapid increase of the radius and ellipticity followed by a rapid decrease of the radius and ellipticity as the cluster returns to its original state (see left panel of Fig. 2.10). When the accretion event is successful, the cluster's radius and ellipticity also grow rapidly but decrease more smoothly after the event (see right panel of Fig. 2.10).

Together, our results indicate that the early structure evolution of embedded clusters is driven by processes arising from the larger cluster-forming region – such as a burst of star formation due to an inflow of gas, or the accretion of a group of stars – rather than by their internal dynamics. In particular, we find that the composition of the clusters is being modified by the formation of new stars or the accretion of already formed stars over timescales much shorter than the clusters' relaxation time. We can obtain back-of-the-envelope estimates of the lower and upper limit on the relaxation times for the clusters in our simulations with

$$t_{\rm relax} \simeq \frac{0.1N}{\ln N} t_{\rm cross} \tag{2.6}$$

where $t_{\rm cross}$ is the crossing time,

$$t_{\rm cross} \simeq \frac{1}{\sqrt{G\rho}} \tag{2.7}$$

and ρ is the average density inside a particle's orbit (Binney & Tremaine 2008). Although both equations are only exact for spherical systems, they nonetheless provide us with a simple estimate of the timescales relevant for our simulated embedded clusters. For the lower limit on the relaxation time, we assume a cluster with 100 members, the minimum possible in our analysis framework, and use a density of 10^4 $\mathrm{M}_\odot$ pc^{-3}, which is towards the low end of our density values but still common. For the upper limit, we assume 1000 members, which is at the high end for our simulated embedded clusters, and use a density of 10^5 $\mathrm{M}_\odot$ pc^{-3}. These give us estimated relaxation times of ~ 0.32 Myr and ~ 0.68 Myr, which are longer than the timescales over which the mass – and therefore the number of stars – of the embedded clusters change. Indeed, sudden accretion events, like the attempted merger shown in the left panel of Fig. 2.10, may change a cluster's characteristic radius r_{50} by up to an order of magnitude, and its mass by a factor of $\sim$ 1.5, over $\sim$ 0.01 Myr. Those timescales are more than 10 times shorter than the estimated relaxation times for the clusters. We conclude that the embedded clusters present in our simulations are not relaxed, despite their small sizes, due to how frequently they form or accrete new stars. Their dynamical evolution is therefore still driven by the overall gravitational potential of the simulation domain, dominated by the gas, rather than by two- or few-body encounters within the cluster.

2.4 Discussion

We now discuss the results presented in Section 2.3. We compare the efficiency of star formation in our simulations to recent observations and simulations of cluster-forming regions. We also discuss the broader implications of our results for observational and computational studies of embedded clusters. We end by outlining areas for future work.

2.4.1 Star Formation Efficiency

We have explored a range of realistic initial virial parameters α, ranging from a low virial parameter typical of more massive clouds in which young massive clusters (YMCs) form to a moderately high virial parameter typical of the 10^4 $M_\odot$ clouds in the solar neighbourhood. The general trend is for our simulations with higher α to have lower SFE and a smaller mass for the most massive cluster, in agreement with observations (e.g. Schruba et al. 2019) and GMC-scale hydrodynamics simulations (e.g. Howard et al. 2016). The physical quantities obtained for the full simulated domain and for individual and average clusters are generally in agreement with observations of Galactic star-forming regions and young clusters. The integrated SFE after one free-fall time is about 1% in our simulations with $\alpha = 4.0$ while it is about 3% in our simulations with $\alpha = 2.0$. Observations suggest a SFE per free-fall time of about 1% on pc-scale clouds, with scatter up to about 3% (Krumholz et al. 2019, and references therein); this is consistent with the results from our simulations.

The integrated SFEs after one free-fall time in our simulations are also consistent with the results from the STARFORGE simulations conducted by Guszejnov et al. (2022) with a cloud mass of 2 x 10^4 $M_\odot$ and virial parameters $\alpha = 1.0, 2.0, 4.0$. Those simulations include models for protostellar outflows, radiation, stellar winds, and supernovae. Our simulations with $\alpha = 0.8$ have SFEs per free-fall time $\lesssim 10\%$, which is similar to what they obtain in their simulations with $\alpha = 1.0$. It is further possible to compare our simulations with $\alpha = 0.8$ to the work conducted by Howard et al. (2016) using FLASH with radiative feedback. The SFR after one free-fall time is $\sim 10^{-3}$ $M_\odot$ yr^{-1} for our 10^4 $M_\odot$ clouds with $\alpha = 0.8$. This is consistent – after scaling for cloud mass – with the SFRs obtained by Howard et al. (2016) for their clouds with $\alpha = 0.5$ and $\alpha = 1.0$, where the SFR after one free-fall time is $\sim 10^{-1}$ $M_\odot$ yr^{-1} for a 10^6 $M_\odot$ cloud.

2.4.2 Implications for Observations

There are two key takeaways from our simulations that can be applied to observed embedded clusters. First, the structure of embedded clusters – such as shape and size – can change considerably over timescales as short as 0.01 Myr, due to new star formation or accretion. Those changes are not monotonic, do not follow a general trend, and are not driven by internal dynamics. This contrasts with studies of the early evolution of gas-free young star clusters. Torniamenti et al. (2021), for example, find that gas-free young clusters expand faster in the presence of primordial binaries. The evolution of the morphology of our embedded clusters, however, is driven primarily by the acquisition of news stars via star formation or accretion. Both processes are themselves driven by gas dynamics: star formation takes place within dense, converging flows of gas, while the accretion of already-formed stars is driven by the gravitational dynamics of the gas, which still accounts for $\gtrsim$ 70% of the mass within the simulation domain at the end of the runs. The simulations presented here focus on the deeply embedded stages of cluster formation. Tentative conclusions about the behaviour of our clusters up to and following gas expulsion can be reached by considering the results from the simulations that we presented in Lewis et al. (2023), albeit with some caveats: the simulations presented in Lewis et al. (2023) have a spatial resolution four times coarser than the present work (0.27 pc versus 0.0683 pc), consider only one virial parameter α selected to promote abundant star formation, and do not include binaries.

We stress therefore that the observed state of Galactic embedded clusters in their first stages of formation is instantaneous. We argue that no conclusions about the future evolution of a very young embedded cluster can be drawn from its current size or ellipticity: the cluster's current state gives no information about whether the radius or ellipticity will increase or decrease in the future. Environment and recent changes in stellar mass play a role at least as important as internal processes such as two- or few-body encounters in setting embedded clusters' dynamical states. We further note that more information about the stellar content and kinematics of very young embedded clusters –including information about binaries – would not allow us to predict their evolution better. We thus also predict that observations of stellar positions and velocities – that could be used to verify boundedness, investigate cluster expansion, and measure cluster shape – cannot be used to infer the presence of a significant number of binaries in embedded clusters.

Second, we find that clusters tend to have large ellipticities and large characteristic radii when they are accreting new stars. Examples are shown in Fig. 2.10. A large

ellipticity for an embedded cluster with a large radius, that persists despite projection effects, could be clear observational evidence that the embedded cluster is currently accreting – or has recently accreted – new stars without requiring any stellar velocity data. Torniamenti et al. (2021), in their simulations of the early evolution of gas-free young clusters, similarly find that clusters in the process of merging appear more elongated. We thus argue that the size and shape of observed embedded clusters can inform our understanding of their recent history but not of their future evolution.

2.4.3 Implications for Larger-Scale Simulations

Simulations of YMC formation with hydrodynamics and stellar feedback require very high gas masses for the initial GMC (three orders of magnitude above what we consider here, around 10^7 $M_\odot$) and thus often model sub-grid clusters with sink particles that can grow in mass by merging with other sinks and accreting gas (e.g. Howard et al. 2016, 2018). Karam & Sills (2022) have highlighted some of the limitations of this model, by showing that collisions between clusters do not always result in a single, merged cluster and that even when they do, the bound mass of the resulting cluster is less than the sum of the bound masses of the progenitors. They also find that cluster radii grow following a merger. We reinforce here those conclusions, and further note that groups of recently formed stars identified as cluster members – that would form within a sub-grid cluster sink – can escape a cluster and can even be identified as a new cluster later in the simulation if they escape together. In particular, clusters can lose up to $\sim 50\%$ of their stellar mass if they split, and up to $\sim 30\%$ without splitting. A significant fraction of the stellar mass formed or accreted by a cluster can be lost on pre-supernova timescales, which is not accounted for in cluster sink models.

Our embedded clusters tend to build up their mass mostly by forming new stars within the cluster, although they can accrete up to $\sim 50\%$ of their mass in already formed stars. Both processes contribute to the clusters' growth in mass on timescales much shorter that the clusters' relaxation times. The dynamical evolution of the clusters remains driven by gravitational processes on the scale of the full simulation domain, such as the collapse of the gas, rather than by internal processes. This is a plausible cause of the diversity of cluster histories within the same simulation, as each individual cluster forms in a different local environment. Howard et al. (2016) found a similar spread for their cluster sinks: for their clusters in the 10^2-10^3 $M_\odot$ mass range, similar to our simulated embedded clusters, they find that between 0% and $\sim 60\%$ of the clusters' stellar mass is accreted.

Approximating embedded clusters as relaxed, spherical collections of gas and stars does not give an accurate representation of the clusters' dynamical state. Furthermore, using spheres as a proxy for the shape of embedded clusters – or as a tool to measure cluster size, e.g. from Lagragian radii – may not be appropriate, as our clusters generally have ellipticities around 0.5, which indicates a factor of 2 difference between the major and minor axes of the stellar distribution.

2.4.4 Directions for Future Work

The simulation time for which we can evolve our models is currently limited by the high computational cost associated with following the dynamics of a large number of close binaries concurrently with radiative transfer and hydrodynamics. Including a self-consistent treatment of binary dynamics in simulations of embedded clusters as they reach gas expulsion is however essential to advancing our understanding of how star clusters form in galaxies. Although our results here indicate that gas dynamics dominate in the deeply embedded phase of cluster formation, the effects of binaries on the dynamics of clusters during gas expulsion remain unknown, and binaries are known to have an important impact on the evolution of gas-free clusters (e.g. Heggie 1975; Hills 1975; Torniamenti et al. 2021). Pursuing similar simulations with a large number of close binaries over timescales sufficient to reach gas expulsion is therefore our next goal. This will require the use of a different N-body and few-body solver, to replace PH4 and MULTIPLES.

Directions for future work also include improvements to the treatment of gas and the stellar feedback in our simulations. Magnetic fields are not used in the current work due to their high computational cost. Future work will include comparisons of simulations with and without magnetic fields, as they are known to participate in the regulation of star formation (Price & Bate 2008). We also note that the amount of mass injected by wind feedback in our simulations is an upper limit, since the Vink et al. (2000) prescription for mass loss rates is likely too high by a factor of $\sim$3 (Smith 2014) and our winds are mass-loaded to avoid extremely short timesteps (Wall et al. 2020). The shock fronts in compact colliding wind binaries are not resolved due to our gas spatial resolution, such that we underestimate the heating from the winds. Any modulation of the feedback coming from interacting binaries is neglected. Including feedback from binaries is non-trivial, but is something we hope to address in future work. Our simulations also currently do not include protostellar jets and outflows. We expect the caveats outlined above to affect the spatial distribution of the feedback in our simulations, but not to significantly under- or overestimate the overall feedback budget.

2.5 Summary

We have conducted a suite of hydrodynamics simulations of star cluster formation with a state-of-the-art treatment of stellar dynamics down to the scale of individual binaries, as well as active star formation via sink particles, and stellar feedback. We have explored a range of realistic initial virial parameters $\alpha = 0.8, 2.0, 4.0$, at a fixed initial cloud mass of 10^4 $M_\odot$, five different models for the formation (or not) of primordial binaries, and seven different random seeds for stochastic star formation. Most of our simulations have progressed to 2.0 Myr after the onset of star formation, which is the same as the timescales we considered in Cournoyer-Cloutier et al. (2021). This allows us to investigate the relative impacts of the cloud-scale gas environment and internal two- or few-body dynamics while gas dynamics are still dominated by the gravitational collapse of the gas and not yet by the effects of stellar feedback. We have used a combination of tools to identify and characterize clusters, and arranged our analysis around three main axes: the properties of the full simulation domain (Section 2.3.1), the properties of the identified clusters as a population (Section 2.3.2), and the time evolution of individual clusters (Section 2.3.3). We have verified that the SFE of our simulation domains, as well as the sizes, densities, and ellipticities of our embedded clusters are consistent with observations.

We explored the relative impact of the cloud's initial virial parameter α and stellar dynamics (using the presence of primordial binaries as a proxy) on cluster structure and evolution. We have found the following:

1. The choice of initial virial parameter α has the largest systematic effect on the global properties of the simulation domain, such as the SFR and SFE.

2. The presence of primordial binaries or individual massive stars causes scatter in the SFR and SFE, but no systematic effect. The scatter is smaller than the systematic effects caused by changes α. Stochastic effects from individual stars are important due to the low cluster masses ($\lesssim 1000$ $M_\odot$) considered in our simulations.

Our simulated embedded clusters are not relaxed, as their mass changes due to accretion or star formation on timescales significantly shorter than their relaxation times. We thus find that their dynamical evolution is driven by the local gravitational potential (from the gas and stars) rather than by two- or few-body encounters (and therefore the presence of binaries). We have also tracked how cluster structure evolves during the earliest stages

of cluster formation. We find considerable variation in cluster histories; examples are shown in Fig. 2.6. We summarize our results on cluster evolution as follows:

3. Cluster mass generally grows through star formation rather than accretion, although some individual clusters acquire up to half of their final mass by accretion.

4. The mass of individual clusters generally grows exponentially, although this growth is not monotonic. Clusters can lose up to half of their mass while they assemble.

5. The size, density, and ellipticity of clusters does not follow any particular trend as the cluster acquires more mass. Changes in size, density, and ellipticity can take place over timescales as short as 0.01 Myr.

6. Recent accretion coincides with simultaneous sharp increases in characteristic radius and ellipticity. We propose that observed embedded clusters with high ellipticities are in the process of accreting stars.

The earliest stages of star cluster formation, when stars are still embedded in their natal gas and stars are still actively forming, are driven by a variety of competing physical processes; the structure of embedded star clusters changes quickly. We caution observers that the state in which an embedded cluster is observed is instantaneous. Over the timescales considered in this work, cluster dynamical evolution is driven by the overall gravitational potential of the star-forming region, as individual clusters acquire new stars on timescales much shorter than their relaxation times.

Acknowledgements

We warmly thank Marta Reina-Campos and James Wadsley for useful discussion. CCC is supported by a Canada Graduate Scholarship – Doctoral from the Natural Sciences and Engineering Research Council of Canada (NSERC). CCC also acknowledges funding from a Queen Elizabeth II Graduate Scholarship in Science and Techonology (QEII-GSST) for the 2021-2022 academic year. AS and WEH are supported by NSERC. SA is grateful for funding from NSF grant AST-2009679. BP is supported through a fellowship from the International Max Planck Research School for Astronomy and Cosmic Physics at the University of Heidelberg (IMPRS-HD). AT was partly supported by NASA FINESST 80NSSC21K1383. AT was also supported through a NASA Cooperative Agreement awarded to the New York Space Grant Consortium. AT, MMML and SLWM were partly supported by NSF grant AST18-15461. SLWM was also supported by NSF grant AST18-14772. MW acknowledges funding from NOVA under project number 10.2.5.12.

The simulations were conducted on the Digital Research Alliance of Canada supercomputer Graham under the resource allocation RRG #4398: *The Formation of Star Clusters in a Galactic Context*, and on the supercomputer Cartesius under the Dutch National Supercomputing Center SURF grant 15520. In addition to the software cited in-text, we have made use of the matplotlib (Hunter 2007), numpy (Harris et al. 2020), scipy (Virtanen et al. 2020) and yt (Turk et al. 2011) Python packages for plotting and analysis.

Data Availability

The data underlying this article will be shared on reasonable request to the corresponding author.

2.A Binary Prescriptions

1. *Field distribution* This is our fiducial distribution, based on statistics for all companions to main sequence stars in the Galactic field. It is presented in detail in Cournoyer-Cloutier et al. (2021) and is based on observations compiled by Moe & Di Stefano (2017) and Winters et al. (2019).

2. *10% random pairing* This prescription is based on that used in Sills & Bailyn (1999); similar prescriptions continue to be used in current state-of-the-art N-body or Monte-Carlo simulations of massive star clusters (see e.g. Kamlah et al. 2022; Wang et al. 2022). It imposes a mass-independent binary fraction of 10%, with a period drawn from a flat distribution in $\log P$ (between 0.5 and 7.5, in days), and an eccentricity drawn from a thermal distribution. This model tends to underproduce binaries compared to the Galactic field, but nonetheless contains low-mass binaries that do not form naturally in models without primordial binaries.

3. *100% random pairing* This prescription is the same as the one described above, with a binary fraction of 100% at all masses.

4. *Field distribution for $M < 0.6 M_\odot$ and no close massive binaries* This prescription is also based on the algorithm presented in Cournoyer-Cloutier et al. (2021), but shifts all the periods to higher values $\tilde{P}$ for stars with masses above 0.6 $M_\odot$ following $\tilde{P} = 10^P$, where P is the period drawn from the algorithm. The specific choice of period shift is motivated by a typo we found in the binary generation algorithm we used in Cournoyer-Cloutier et al. (2021), which caused us to draw

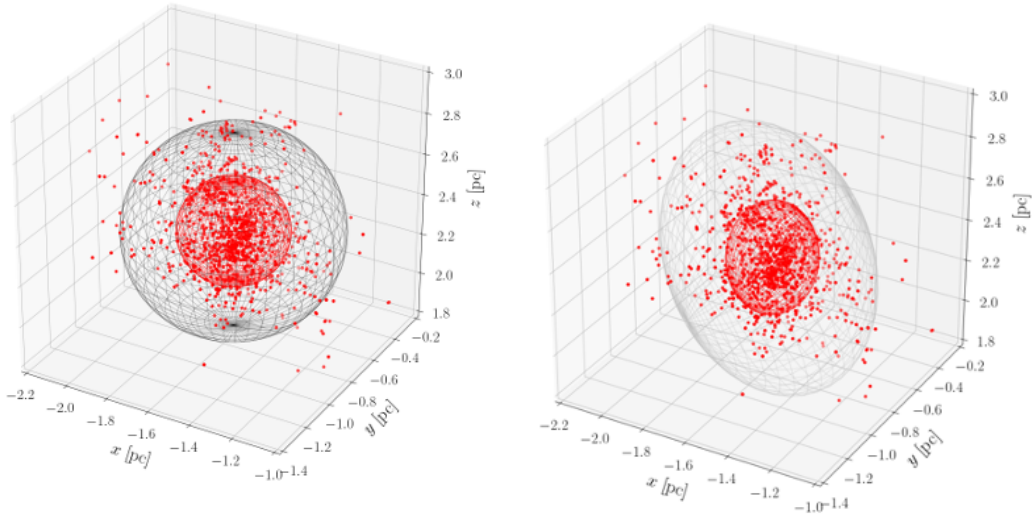

FIGURE 2.B1: 3D spheres (left) and ellipsoids (right) enclosing 50% (red) and 90% (grey) of the stellar mass of the example cluster, taken from S-R3. All individual stars bound to the cluster are shown in red.

$\log P$ instead of P from our observations-based distribution. This typo does not affect the conclusions of the previous paper, as those were drawn from comparisons to the distribution of formed binaries (and not from comparisons to observations).

2.B Ellipsoids from Inertia Tensors

We present in Fig. 2.B1 an example of 3D ellipsoidal surfaces enclosing 50% and 90% of the cluster mass, compared to the 50% and 90% Lagragian radii for the same stellar distribution. We use the reduced inertia tensor (Thob et al. 2019),

$$\mathbf{I} = \begin{pmatrix} \mathrm{I}_{xx} & \mathrm{I}_{xy} & \mathrm{I}_{xz} \\ \mathrm{I}_{xy} & \mathrm{I}_{yy} & \mathrm{I}_{yz} \\ \mathrm{I}_{xz} & \mathrm{I}_{yz} & \mathrm{I}_{zz} \end{pmatrix} \tag{8}$$

where the individual elements I_{ij} are calculated from

$$\mathbf{I}_{ij} = \frac{\sum_a \left(\frac{m_a \left(\mathbb{I} r_a^2 \right)_{ij} - \left(\vec{x}_a \right)_i \left(\vec{x}_a \right)_j}{r_a^2} \right)}{\sum_a \left(\frac{m_a}{r_a^2} \right)} \tag{9}$$

and

$$r_a^2 = \vec{x}_a \cdot \vec{x}_a \tag{10}$$

where $\vec{x}_a$ is the vector distance from star a to the cluster's centre of mass. The reduced inertia tensor minimizes the impact of stars in the outskirts of the cluster on the calculated shape. We obtain the principal axes a, b and c from the eigenvalues λ_i of the reduced inertia tensor, such that

$$\begin{aligned} \lambda_a &\propto b^2 + c^2 \\ \lambda_b &\propto a^2 + c^2 \\ \lambda_c &\propto a^2 + b^2. \end{aligned} \tag{11}$$

Solving this system of equations, we recover initial guesses for the principal axes

$$\begin{aligned} a &\propto \sqrt{-\lambda_a + \lambda_b + \lambda_c} \\ b &\propto \sqrt{\lambda_a - \lambda_b + \lambda_c} \\ c &\propto \sqrt{\lambda_a + \lambda_b - \lambda_c}. \end{aligned} \tag{12}$$

The initial guesses from Equations 11 and 12 are then rescaled iteratively to enclose 50% or 90% of the stellar mass. We adopt the idea of iterative fitting from Thob et al. (2019), and adapt the 2D code from Hill et al. (2021) to handle 3D distributions. The main steps of the fitting algorithm are as follows:

1. Identify the centre of mass of the cluster;
2. Take the stars enclosed within a given Lagrangian radius and get the shape for this distribution from the reduced inertia tensor in Equations 8 and 9;
3. Increase or decrease the size of the ellipsoid until the required (50% or 90%) fraction of the mass is enclosed;
4. Recalculate the shape from the inertia tensor associated with the stars now enclosed in the ellipsoid;
5. Repeat the steps above until the change in shape is less than a given tolerance between two iterations.

The default tolerance is 1% but we raise it to 2% for systems with fewer than 500 (but at least 200) stars and to 5% for systems with fewer than 200 stars. We do not fit an ellipsoid when the most massive star in a cluster accounts for more than 50% of its mass. We encounter this situation for one cluster in a few consecutive snapshots in S-R2.

Bibliography

Baczynski C., Glover S. C. O., Klessen R. S., 2015, MNRAS, 454, 380

Ballesteros-Paredes J., Klessen R. S., Mac Low M. M., Vazquez-Semadeni E., 2007, in Reipurth B., Jewitt D., Keil K., eds, Protostars and Planets V. p. 63 (arXiv:astro-ph/0603357), doi:10.48550/arXiv.astro-ph/0603357

Bertoldi F., McKee C. F., 1992, ApJ, 395, 140

Binney J., Tremaine S., 2008, Galactic Dynamics, 2nd edn. Princeton University Press, Princeton

Chen B. Q., et al., 2020, MNRAS, 493, 351

Chen Y., Li H., Vogelsberger M., 2021, MNRAS, 502, 6157

Colella P., Woodward P. R., 1984, J. Comput. Phys., 54, 174

Cournoyer-Cloutier C., et al., 2021, MNRAS, 501, 4464

Dobbs C. L., Bending T. J. R., Pettitt A. R., Buckner A. S. M., Bate M. R., 2022, MNRAS, 517, 675

Ester M., Kriegel H. P., Sander J., Xiaowei X., 1996, in KDD'96: Proceedings of the Second International Conference on Knowledge Discovery and Data Mining. AAAI Press. https://www.osti.gov/biblio/421283

Federrath C., Banerjee R., Clark P. C., Klessen R. S., 2010, ApJ, 713, 269

Fryxell B., et al., 2000, ApJS, 131, 273

Fujii M. S., Portegies Zwart S., 2011, Science, 334, 1380

Fujii M., Iwasawa M., Funato Y., Makino J., 2007, PASJ, 59, 1095

Fujii M. S., Saitoh T. R., Portegies Zwart S. F., 2012, ApJ, 753, 85

Goldstein H., Poole C. P., Safko J., 2001, Classical Mechanics, 3rd edn. Addison-Wesley, Boston

Grudić M. Y., Guszejnov D., Hopkins P. F., Lamberts A., Boylan-Kolchin M., Murray N., Schmitz D., 2018, MNRAS, 481, 688

Guszejnov D., Grudić M. Y., Offner S. S. R., Faucher-Giguère C.-A., Hopkins P. F., Rosen A. L., 2022, MNRAS, 515, 4929

Harris C. R., et al., 2020, Nature, 585, 357

Heggie D. C., 1975, MNRAS, 173, 729

Hill A. D., Crain R. A., Kwan J., McCarthy I. G., 2021, MNRAS, 505, 65

Hills J. G., 1975, AJ, 80, 809

Howard C. S., Pudritz R. E., Harris W. E., 2016, MNRAS, 461, 2953

Howard C. S., Pudritz R. E., Harris W. E., 2018, Nature Astronomy, 2, 725

Hunter J. D., 2007, Computing in Science & Engineering, 9, 90

Hut P., Makino J., McMillan S., 1995, ApJ, 443, L93

Hut P., McMillan S., Makino J., Portegies Zwart S., 2010, Starlab: A Software Environment for Collisional Stellar Dynamics (ascl:1010.076)

Kamlah A. W. H., et al., 2022, MNRAS, 511, 4060

Karam J., Sills A., 2022, MNRAS, 513, 6095

Kauffmann J., Pillai T., Goldsmith P. F., 2013, ApJ, 779, 185

Kim J., et al., 2022, MNRAS, 516, 3006

Kroupa P., 2001, MNRAS, 322, 231

Kruijssen J. M. D., 2012, MNRAS, 426, 3008

Krumholz M. R., McKee C. F., Bland-Hawthorn J., 2019, ARA&A, 57, 227

Kuhn M. A., et al., 2014, ApJ, 787, 107

Lada C. J., Lada E. A., 2003, ARA&A, 41, 57

Lee D., 2013, J. Comput. Phys., 243, 269

Lewis S. C., et al., 2023, ApJ, 944, 211

Lohner R., 1987, Comput. Methods Appl. Mech. Eng., 61, 323

Mac Low M.-M., Klessen R. S., 2004, Reviews of Modern Physics, 76, 125

MacNeice P., Olson K. M., Mobarry C., de Fainchtein R., Packer C., 2000, Comput. Phys. Commun., 126, 330

Makino J., Aarseth S. J., 1992, PASJ, 44, 141

McMillan S. L. W., Hut P., 1996, ApJ, 467, 348

McMillan S., Portegies Zwart S., van Elteren A., Whitehead A., 2012, in Capuzzo-Dolcetta R., Limongi M., Tornambè A., eds, ASP Conf. Ser. Vol. 453, Advances in Computational Astrophysics: Methods, Tools, and Outcome. San Francisco, p. 129 (`arXiv:1111.3987`)

Miyoshi T., Kusano K., 2005, J. Comput. Phys., 208, 315

Moe M., Di Stefano R., 2017, ApJS, 230, 15

Offner S. S. R., Moe M., Kratter K. M., Sadavoy S. I., Jensen E. L. N., Tobin J. J., 2023, in Inutsuka S., Aikawa Y., Muto T., Tomida K., Tamura M., eds, Astronomical Society of the Pacific Conference Series Vol. 534, Protostars and Planets VII. p. 275 (arXiv:2203.10066), doi:10.48550/arXiv.2203.10066

Pang X., Li Y., Yu Z., Tang S.-Y., Dinnbier F., Kroupa P., Pasquato M., Kouwenhoven M. B. N., 2021, ApJ, 912, 162

Pedregosa F., et al., 2011, Journal of Machine Learning Research, 12, 2825

Pelupessy F. I., van Elteren A., de Vries N., McMillan S. L. W., Drost N., Portegies Zwart S. F., 2013, A&A, 557, A84

Portegies Zwart S., McMillan S. L. W., 2019, Astrophysical Recipes: The Art of Amuse. Institute of Physics Publishing, Bristol

Portegies Zwart S. F., Verbunt F., 1996, A&A, 309, 179

Portegies Zwart S. F., Makino J., McMillan S. L. W., Hut P., 1999, A&A, 348, 117

Portegies Zwart S., et al., 2009, New Astron., 14, 369

Portegies Zwart S. F., McMillan S. L. W., Gieles M., 2010, ARA&A, 48, 431

Portegies Zwart S., McMillan S. L. W., van Elteren E., Pelupessy I., de Vries N., 2013, Computer Physics Communications, 184, 456

Price D. J., Bate M. R., 2008, MNRAS, 385, 1820

Reina-Campos M., Trujillo-Gomez S., Pfeffer J. L., Sills A., Deason A. J., Crain R. A., Kruijssen J. M. D., 2023, MNRAS, 521, 6368

Ricker P. M., 2008, ApJS, 176, 293

Sander J., Ester M., Kriegel H.-P., Xu X., 1998, Data Mining and Knowledge Discovery, 2, 169

Schruba A., Kruijssen J. M. D., Leroy A. K., 2019, ApJ, 883, 2

Serabyn E., Shupe D., Figer D. F., 1998, Nature, 394, 448

Sills A., Bailyn C. D., 1999, ApJ, 513, 428

Smith N., 2014, ARA&A, 52, 487

Sormani M. C., Treß R. G., Klessen R. S., Glover S. C. O., 2017, MNRAS, 466, 407

Thob A. C. R., et al., 2019, MNRAS, 485, 972

Torniamenti S., Ballone A., Mapelli M., Gaspari N., Di Carlo U. N., Rastello S., Giacobbo N., Pasquato M., 2021, MNRAS, 507, 2253

Truelove J. K., Klein R. I., McKee C. F., Holliman John H. I., Howell L. H., Greenough J. A., 1997, ApJ, 489, L179

Turk M. J., Smith B. D., Oishi J. S., Skory S., Skillman S. W., Abel T., Norman M. L., 2011, The Astrophysical Journal Supplement Series, 192, 9

Vázquez-Semadeni E., González-Samaniego A., Colín P., 2017, MNRAS, 467, 1313

Velliscig M., et al., 2015, MNRAS, 453, 721

Vink J. S., de Koter A., Lamers H. J. G. L. M., 2000, A&A, 362, 295

Virtanen P., et al., 2020, Nature Methods, 17, 261

Wall J. E., McMillan S. L. W., Mac Low M.-M., Klessen R. S., Portegies Zwart S., 2019, ApJ, 887, 62

Wall J. E., Mac Low M.-M., McMillan S. L. W., Klessen R. S., Portegies Zwart S., Pellegrino A., 2020, ApJ, 904, 192

Wang L., Tanikawa A., Fujii M. S., 2022, MNRAS, 509, 4713

Winters J. G., et al., 2019, AJ, 157, 216

Zhai M., Abt H., Zhao G., Li C., 2017, AJ, 153, 57

CHAPTER 3

MASSIVE STAR CLUSTER FORMATION WITH BINARIES I. EVOLUTION OF BINARY POPULATIONS

The content of this chapter is published in the *Astrophysical Journal* under the following citation:

Cournoyer-Cloutier, C., Sills, A., Harris, W. E., Polak, B., Rieder, S., Andersson, E. P., Appel, S. M., Mac Low, M.-M., McMillan, S. L. W. and Portegies Zwart, S. (2024). Massive Star Cluster Formation with Binaries. I. Evolution of Binary Populations, *ApJ* **977**:203 (12pp)

Abstract

We study the evolution of populations of binary stars within massive cluster-forming regions. We simulate the formation of young massive star clusters within giant molecular clouds with masses ranging from 2 x 10^4 to 3.2 x 10^5 $M_\odot$. We use Torch, which couples stellar dynamics, magnetohydrodynamics, star and binary formation, stellar evolution, and stellar feedback through the Amuse framework. We find that the binary fraction decreases during cluster formation at all molecular cloud masses. The binaries' orbital properties also change, with stronger and quicker changes in denser, more massive clouds. Most of the changes we see can be attributed to the disruption of binaries wider than 100 au, although the close binary fraction also decreases in the densest cluster-forming region. The binary fraction for O stars remains above 90%, but exchanges and dynamical hardening are ubiquitous, indicating that O stars undergo frequent few-body interactions early during the cluster formation process. Changes to the populations of binaries are a by-product of hierarchical cluster assembly: most changes to the binary population take place when the star formation rate is high, and there are frequent mergers between subclusters in the cluster-forming region. A universal primordial binary distribution based on observed inner companions in the Galactic field is consistent with the binary populations of young clusters with resolved stellar populations, and the scatter between clusters of similar masses could be explained by differences in their formation history.

Unified Astronomy Thesaurus Concepts: Young massive clusters (2049) — Young star clusters (1833) — Star clusters (1567) — Star forming regions (1565) — Star formation (1569) — Binary stars (154)

3.1 Introduction

Young massive clusters (YMCs) are ubiquitous in nearby star-forming galaxies, with populations of massive clusters embedded in their natal gas observed in nearby starbursts (e.g., He et al. 2022; Sun et al. 2024). Observations have also found massive and compact star clusters at high redshift (e.g., $z\sim6$, Vanzella et al. 2023; $z\sim10.2$, Adamo et al. 2024), and globular clusters (GCs) at $z=1.38$ (e.g., Adamo et al. 2023; Claeyssens et al. 2023) and at $z\sim0.3$-0.4 (e.g., Faisst et al. 2022; Lee et al. 2022; Harris & Reina-Campos 2023). These observations serve as growing evidence that GC formation is the extension at high masses of YMC formation in the local Universe. This is also supported by simulations, which have shown that star clusters of masses $\gtrsim 10^6$ $M_\odot$ form naturally within massive giant molecular clouds (GMCs; e.g., Howard et al. 2018; Polak et al. 2024a; Reina-Campos et al. 2025). Detailed analysis of the stellar populations of YMCs and GMCs within which they form are limited to the Milky Way and the LMC/SMC, for which the cluster mass function does not reach the high masses observed in starbursts (Portegies Zwart et al. 2010). This is a challenge for understanding the spatial and kinematic properties of the stars, including the binary fraction, which are largely unknown for the most massive YMCs.

Massive stars, which regulate star formation within their host cluster, have binary fractions approaching unity (Moe & Di Stefano 2017) and two-thirds of all massive stars exchange material with a companion over their lifetimes (Sana et al. 2012). This changes the time distribution of supernovae (Zapartas et al. 2017), increases the amount of ultraviolet radiation (Götberg et al. 2018) and increases the amount of pre-supernova ejecta from a stellar population by a factor of $\sim$6 (Nguyen & Sills 2024). Binaries can produce runaway stars either through the ejection of a newly-unbound companion after a supernova (Blaauw 1961), or through few-body interactions (Poveda et al. 1967). Such runaway stars are known to be ubiquitous around young clusters (e.g., Kalari et al. 2019; Stoop et al. 2023, 2024), and in turn, influence the distribution of feedback within cluster-forming regions, which can affect the long-term evolution of galaxies (Andersson et al. 2020, 2023; Steinwandel et al. 2023).

Clustered environments also influence the binaries found within them: high stellar densities promote few-body interactions that can result in the formation, modification, or disruption of binaries. Observationally, surveys of binaries in clustered environments suggest a dependence of the binary fraction and orbital properties of binaries on cluster density and/or cluster mass. The frequency and orbital properties of close (<10

au) companions to low- and solar-mass stars appears to be set very early in the stars' evolution (e.g., Kounkel et al. 2019) and to persist both in young open clusters (e.g., Deacon & Kraus 2020) and in the field, suggesting that the field properties observed for those systems resemble the primordial ones. On the other hand, the wide binary fraction depends on environment: low-density star forming regions show an excess of wide companions (e.g., Taurus, Kraus et al. 2011; Joncour et al. 2017) while high-density star-forming regions show fewer wide companions (e.g., Orion, Duchêne et al. 2018; Jerabkova et al. 2019). It was suggested that the binary fraction observed in the field arises from a combination of binary fractions inherited from stars formed in embedded clusters of varying densities, which have since dissolved (see Offner et al. 2023, for a discussion). Observations of older clusters do not fully support this picture. For open clusters, surveys have found evidence of binary fraction either increasing (e.g., Niu et al. 2020) or decreasing (Deacon & Kraus 2020) with stellar density, depending on which clusters were observed and what separation range was probed. The older, denser, more massive GCs consistently show low binary fractions, which are anti-correlated with cluster mass but do not, however, show any trends with cluster density (e.g., Milone et al. 2012). Taken together, these results indicate that there is more at play than just the present-day densities for setting the binary fraction and binary properties.

We need to understand how a binary population evolves during the formation of clusters at a range of masses and densities in order to fully understand cluster formation and long-term evolution. Numerical simulations provide us with detailed spatial and kinematic information about each star within a YMC as a function of time. Modeling the stars alongside gas, which is affected by feedback, is crucial: populations of binaries are modified during cluster assembly (Cournoyer-Cloutier et al. 2021), and these changes are driven by subcluster mergers (Cournoyer-Cloutier et al. 2024), which are in turn dependent on the GMC-scale gas environment (Lahén et al. 2020; Guszejnov et al. 2022; Karam & Sills 2024).

We present a suite of simulations with cloud masses ranging from 2 x 10^4 to 3.2 x 10^5 $M_\odot$ to test the dependence of binary properties on environment during star cluster formation. Those simulations include primordial binaries, star formation, and stellar feedback along with collisional stellar dynamics and magnetohydrodynamics (MHD). We describe our simulation methods in Section 3.2 and our suite of simulations in Section 3.3. We present our results in Section 3.4 and discuss their implications for globular cluster formation in Section 4.5. We conclude in Section 5.1.

TABLE 3.1: Parameters for the Simulations

	Definition	Value
$\Delta x_{\rm min}$	Minimum cell size	0.137 pc
$r_{\rm sink}$	Sink particle accretion radius	0.342 pc
$\rho_{\rm sink}$	Gas density for sink formation	93.5 $M_\odot$ pc^{-3}
$M_{\rm sink}$	Minimum sink mass at formation	3.74 $M_\odot$
$T_{\rm wind}$	Wind target temperature	3 x 10^5 K
$r_{\rm out}$	Changeover radius for FDPS	Section 3.2.2
$r_{\rm in}$	Changeover radius for N-body	0.1 $r_{\rm out}$
$r_{\rm bin}$	Changeover radius for SDAR	100 au
$M_{\rm min}$	Minimum stellar mass	0.4 $M_\odot$
$M_{\rm max}$	Maximum stellar mass	150 $M_\odot$
$M_{\rm FB}$	Minimum mass for feedback	13 $M_\odot$
$\mathcal{F}_{\rm bin}$	Binary fraction	Section 3.2.4

Note. $r_{\rm out}$ depends on the simulation time step and is described in Section 3.2.2. $\mathcal{F}_{\rm bin}$ depends on the stellar mass and is described in Section 3.2.4.

3.2 Methods

We perform our simulations with TORCH[1] (Wall et al. 2019, 2020), which couples MHD to star formation, stellar dynamics, stellar evolution, and stellar feedback through the AMUSE framework (Portegies Zwart et al. 2009; Pelupessy et al. 2013; Portegies Zwart et al. 2013; Portegies Zwart & McMillan 2019). The coupling between the different codes is presented in Wall et al. (2019). The physics in our simulations are described in more detail in the following sections. Parameters for star formation, feedback, N-body dynamics and binary formation, which are shared between the simulations, are summarized in Table 3.1.

3.2.1 Magnetohydrodynamics

We use FLASH (Fryxell et al. 2000; Dubey et al. 2014) with a Harten-Lax-van Leer Riemann solver (Miyoshi & Kusano 2005) with third-order piecewise parabolic method reconstruction (Colella & Woodward 1984). We use a multigrid solver (Ricker 2008) for the gas self-gravity. Gravity between the gas and stars is treated with a leapfrog scheme

[1] `https://bitbucket.org/torch-sf/torch/src/binaries-v2.0/`

based on BRIDGE (Fujii et al. 2007). We refine our adaptive grid such that the Jeans length is resolved by at least 12 resolution elements, to ensure that it can be magnetically supported against collapse on scales below the resolution (Heitsch et al. 2001, see also discussion in Federrath et al. 2010). To improve numerical stability in regions with large temperature or pressure gradients, such as HII regions, we also refine where the second derivative of the temperature or pressure is of the order of the sum of its gradients (see Lohner 1987; MacNeice et al. 2000). Sink particles are used to model subgrid star and binary formation. Sinks form in regions of high gas density and converging flows which satisfy the boundedness and gravitational instability criteria outlined in Federrath et al. (2010). The sink accretion radius is set to $2.5\Delta x$ at the highest refinement level, and sinks can only form in regions that are refined to the highest refinement level. We give more details on the formation of stars from sinks in Section 3.2.5.

3.2.2 Stellar dynamics

We handle stellar dynamics, including hard binaries and close encounters, with the N-body code PETAR (Wang et al. 2020b, see Polak et al. 2024a for the implementation in TORCH). PETAR relies on a combination of three different N-body algorithms: long-range interactions are calculated with a Barnes-Hut tree (Barnes & Hut 1986, as implemented in FDPS by Iwasawa et al. 2016), short-range interactions are calculated with a fourth-order Hermite integrator (Makino & Aarseth 1992), and binary systems and few-body encounters are calculated with the slow-down algorithmic regularization (SDAR) method (Wang et al. 2020a).

The changeover radii between these three integration regimes are set by the user. The default values calculated by PETAR are optimized for a spherical stellar system with a fixed number of stars. However, our cluster-forming regions continuously form new stars, and are not well-described by a single spherical cluster at early times. They also span a range of densities. As we are interested in the evolution of binaries within these fast-changing stellar systems, we adopt larger changeover radii than previous work using PETAR: this is less efficient than optimizing PETAR for binaries expected to survive the cluster's long-term evolution, but ensures that we fully capture the complexity of stellar dynamics within the cluster-forming region. Binary systems on scales smaller than $r_{\rm bin}$ are treated by SDAR, ensuring that they do not affect the global time step of the simulation. Forces between stars closer than $r_{\rm in}$ are calculated using the fourth-order Hermite, forces between stars more distant than $r_{\rm out}$ are calculated using the Barnes-Hut tree, and forces between stars with separations between $r_{\rm in}$ and $r_{\rm out}$ are treated using a combination of the Hermite and tree codes.

The changeover radius for SDAR $r_{\rm bin}$ is kept fixed in our simulations. We adopt a value of 100 au as this corresponds to an orbital period of 58 years for a binary with two stars of mass 150 $M_\odot$ (the largest stellar mass in our simulations). As a typical time step for our simulations is between 15.625 years and 62.5 years, this ensures that the orbits of massive binaries (with large orbital velocities) are well-resolved in our simulations. 100 au is also commonly used as the lower semimajor axis limit for wide binaries in observational surveys (see Offner et al. 2023, and references therein).

The changeover radii $r_{\rm in}$ and $r_{\rm out}$ have a strong impact on the performance of the code but must be chosen carefully in conjunction with the simulation time step to ensure that the orbits of binaries wider than 100 au but still strongly bound are well-resolved. TORCH uses a single time step for MHD and stellar dynamics; as we model star-forming regions with shock fronts and high sound speeds, the time step calculated by FLASH decreases drastically after the formation of the first massive star. On the other hand, the PETAR time step must always remain a power of 2 of the initial PETAR time step, which we set to 1000 years. The only allowed time steps for the simulation are therefore

$$\Delta t = \frac{1000}{2^n} \text{ years} \tag{3.1}$$

where n is a positive integer. After the formation of the first star, we set the maximum time step and $r_{\rm out}$ together, such that the orbit of a circular binary with a semimajor axis of $r_{\rm out}$ is resolved by 10 time steps if the two stars have a mass of 10 $M_\odot$. For our simulations, the shortest minimum time step used is 7.8125 years and the longest minimum time step used is 125 years, which correspond respectively to $r_{\rm out} = 0.00112$ pc and $r_{\rm out} = 0.00709$ pc. The inner changeover radius $r_{\rm in}$ is set to 0.1 $r_{\rm out}$ at all times, following the standard approach in PETAR. The computational time is insensitive to our choice of PETAR time step, as the computational time per time step is dominated by FLASH for all time steps used in the paper.

3.2.3 IMF sampling

Star formation takes place via sink particles from which individual stars are spawned. This process is described in details in Wall et al. (2019) and the modifications to this method to allow for primordial binary formation are described in Cournoyer-Cloutier et al. (2021). As each sink is formed, we sample a Kroupa (2002) initial mass function (IMF) and apply a primordial binary prescription, described in Section 3.2.4, to generate a list of stars to be formed. We use a lower limit of 0.4 $M_\odot$ and an upper limit of 150 $M_\odot$ to sample the IMF. The lower limit reduces the number of stars by a factor of 2

TABLE 3.2: Binary Fraction, Close Binary Fraction, Median Semi-major Axis and Median Mass Ratio for Each Mass Range

Mass range	$\mathcal{F}_{\rm bin}$	$\mathcal{F}_{\rm close}$	$a_{\rm median}$	$q_{\rm median}$
0.4-0.8 $M_\odot$	0.30	0.07	44.6 au	0.90
0.8-1.6 $M_\odot$	0.40	0.15	201 au	0.67
1.6-5 $M_\odot$	0.59	0.37	21.6 au	0.41
5-9 $M_\odot$	0.76	0.63	9.92 au	0.34
9-16 $M_\odot$	0.84	0.80	7.08 au	0.35
$\geqslant$ 16 $M_\odot$	0.94	0.94	6.72 au	0.37

Note. Those values are calculated for a fully sampled distribution of binaries.

compared to sampling down to 0.08 $M_\odot$, reducing the load on the N-body integrator while retaining 90% of the stellar mass in stars of the mass predicted by the IMF. Each sampled star corresponds to a star particle to ensure that the shape of the IMF is preserved. Although low-mass binaries are important to the long-term evolution of star clusters once massive stars have evolved, they are not the leading source of binding energy in young cluster-forming regions, which host several massive stars for which the close binary fraction approaches unity. We inject radiative and wind feedback from all stars more massive than 13 $M_\odot$.

3.2.4 Primordial binaries

We use the module for primordial binaries in TORCH that was first presented in Cournoyer-Cloutier et al. (2021), in which we implement an updated sampling binary algorithm. We use a mass-dependent binary fraction based on observations made by Winters et al. (2019) and corrected by Offner et al. (2023) for stars below 0.6 $M_\odot$, and on observations compiled by Moe & Di Stefano (2017) for stars above 0.8 $M_\odot$; the only difference between those fractions and those used in Cournoyer-Cloutier et al. (2021) is the correction by Offner et al. (2023) of the binary fraction for M $\leq$ 0.6 $M_\odot$. The sampling technique for the orbital period, companion mass, and eccentricity also remains the same as in Cournoyer-Cloutier et al. (2021).

The key change in the updated sampling algorithm is in the distribution of orbital periods. The sampling algorithm used in Cournoyer-Cloutier et al. (2021) sampled any companion from a distribution of observed properties, while the new algorithm presented here is designed to sample the inner companion of a hierarchical multiple stellar system.

The triple fraction ranges from 10% for solar-mass stars to 73% for O-type stars (Moe & Di Stefano 2017), which implies that the distribution of *all companions* to O stars is quite different from the distribution of *inner companions* to O stars. The updated algorithm therefore accounts for the dynamical formation of hierarchical triples and higher-order multiples while preserving the observed close binary fraction. For stars with masses above 0.8 $M_\odot$, we impose that a fraction $\mathcal{F}_{\rm close}$ of all stars in each mass range must have a companion with an orbital period shorter than 5000 days. For a binary of total mass 100 $M_\odot$, this corresponds to a semimajor axis of roughly 27 au, while it corresponds to a semimajor axis of about 10 au for a binary with total mass 5 $M_\odot$. For stars with masses below 0.8 $M_\odot$, we use the lognormal distribution of semimajor axes for inner companions from Winters et al. (2019), as reported and corrected in Offner et al. (2023), which corresponds to a mean semimajor axis of 14 au for close binaries. A fraction $\mathcal{F}_{\rm bin} - \mathcal{F}_{\rm close}$ of stars in each mass bin will have a companion with an orbital period longer than 5000 days. The binary fraction, close binary fraction, median semimajor axis, and median mass ratio for each mass bin are reported in Table 3.2.

The sampling algorithm only forms systems that do not fill their Roche lobe while on the zero-age main sequence. This is done using an upper limit on the eccentricity as a function of period based on the semi-analytic formula from Moe & Di Stefano (2017), as described in Cournoyer-Cloutier et al. (2021),

$$e_{\rm max}(P) = \left(\frac{P}{2\,\text{days}}\right)^{-2/3} \tag{3.2}$$

where P is the orbital period in days. Stars are allowed to merge during the simulations, but other binary evolution effects – such as stable or unstable mass transfer – are not taken into account.

3.2.5 Feedback

Radiation from stars more massive than 13 $M_\odot$ is followed using the ray-tracing scheme Fervent (Baczynski et al. 2015), which follows radiation pressure in the far-ultraviolet band (5.6-13.6 eV) and ionizing radiation (above 13.6 eV) from individual massive stars. Momentum-driven winds are also injected into the grid by massive stars. The implementation of both forms of feedback is described in Wall et al. (2020). Torch also includes a scheme for core-collapse supernovae, implemented within Flash; our simulations, however, stop before any supernovae takes place. We mass load our winds by increasing the wind mass loss rate $\dot{M}$ while keeping the wind luminosity L_w fixed, therefore lowering

the wind velocity v_w, following

$$L_w = \frac{1}{2}\dot{M} v_w^2. \tag{3.3}$$

The wind velocity is reduced to reach a target post-shock wind temperature

$$T_w = 1.38 \,\mathrm{x}\, 10^7 \,\mathrm{K} \left(\frac{v_w}{10^3 \,\mathrm{km\,s^{-1}}} \right)^2 \tag{3.4}$$

following Wall et al. (2020). We mass load the winds to a target temperature T_w = 3 x 10^5 K, which was shown to be a reasonable choice in Polak et al. (2024a) and allows for a longer time step. Mass loading makes the wind bubbles momentum-driven rather than energy-driven. Momentum-driven winds are naturally produced by high-resolution hydrodynamics wind simulations (see, e.g., Lancaster et al. 2021): mass loading our winds allows us to reproduce the effects of the winds on cluster-scale at the resolution of our simulations.

3.3 Overview of simulations

3.3.1 Initial conditions

We run a suite of isolated cloud simulations with initial gas masses of 2 x 10^4, 8 x 10^4, and 3.2 x 10^5 $M_\odot$ and an initial cloud radius $R = 7$ pc. Each model is run for at least 2.5 freefall times (calculated for the initial cloud), with the lowest mass model run until gas expulsion. As GMC masses correlate with GMC surface densities but show little to no correlation with GMC radius or virial parameter for extragalactic GMCs (Sun et al. 2022), we vary the initial GMC mass but keep the radius fixed, which changes the surface density and the density between simulations. The surface densities for M1, M2 and M3 are chosen, respectively, to mimic GMC conditions typical of the disk of the Milky Way (e.g., Roman-Duval et al. 2010; Chen et al. 2020), the Central Molecular Zone or centers of barred galaxies (e.g., Sun et al. 2020), and starburst galaxies (e.g., Sun et al. 2018). All simulation domains have a box side of $L = 2.5R = 17.5$ pc. All models are initialized with an initial virial parameter $\alpha = 2T/|U| = 0.5$, a Kolmogorov turbulent velocity spectrum with the same random seed, and a uniform magnetic field $B_z = 3\,\mu G$. The initial GMCs are isolated, and the simulations do not include any external tidal field, which would not affect the clusters' evolution on the short (< 5 Myr) timescales considered (see Miholics et al. 2017). The initial conditions are summarized in Table 3.3. The gas column density overlaid with the stellar distribution is presented in Figure 3.1 for all simulations, shown at the same fractions of their respective initial freefall times.

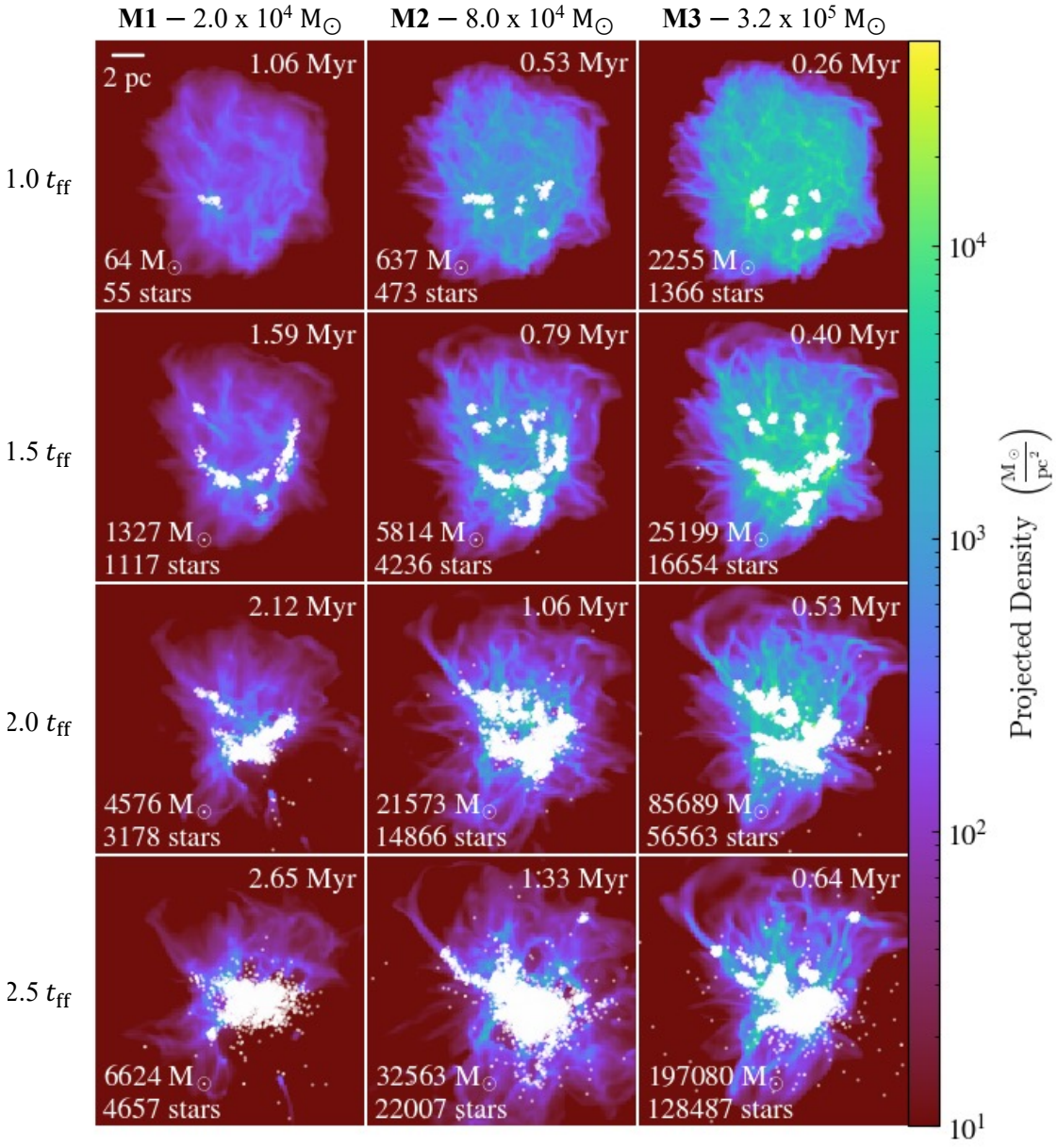

FIGURE 3.1: Gas column density, with stars overplotted as small white circles. The columns correspond to the different simulations while the rows show the distribution of stars and gas at approximately 1.0, 1.5, 2.0 and 2.5 freefall times of the initial GMC.

TABLE 3.3: Initial Conditions and Star Formation Metrics for the Simulations

Cloud	$M_{\rm gas}$ ($M_\odot$)	R (pc)	Σ ($M_\odot$ pc^{-2})	$t_{\rm ff}$ (Myr)	SFE (2.5 $t_{\rm ff}$)	$F_{\rm bound}$ (2.5 $t_{\rm ff}$)	SFE	$M_{\rm formed}$ ($M_\odot$)	$t_{\rm SFR}$
(1)	(2)	(3)	(4)	(5)	(6)	(7)	(8)	(9)	(10)
M1	2 x 10^4	7	130	1.06	0.33	0.98	0.39	7.8 x 10^3	1.56
M2	8 x 10^4	7	520	0.530	0.40	0.99	$\geqslant$ 0.43	3.44 x 10^4	1.64
M3	3.2 x 10^5	7	2080	0.265	0.61	0.99	$\geqslant$ 0.61	1.95 x 10^5	$\gtrsim$ 2.46

Note. Column (1): cloud label. Column (2): initial mass. Column (3): initial radius. Column (4): initial surface density. Column (5): initial freefall time of the gas cloud. Column (6): star formation efficiency after 2.5 $t_{\rm ff}$. Column (7): bound mass fraction after 2.5 $t_{\rm ff}$. Column (8): total star formation efficiency. Column (9): formed stellar mass. Column (10): time at which the star formation rate peaks (in units of freefall times).

3.3.2 Star formation

We summarize the key star formation metrics in Table 3.3, and plot the star formation rate (SFR) as a function of time in Figure 3.2. As expected, the star formation rate increases with initial gas mass, but in excess of the increase in mass – in other words, the increased total gas mass results in more stars formed, but the increased initial surface density also increases both the SFR and the star formation efficiency (SFE). In M1 and M2, the star formation rate peaks after roughly 1.6 $t_{\rm ff}$, and plateaus for the next freefall time. On the other hand, in M3, the SFR continues to increase beyond $\sim$1.5 $t_{\rm ff}$, and is still increasing at $\sim$2.5 $t_{\rm ff}$. The high initial gas mass and surface density ($> 10^3$ $M_\odot$pc^{-2}) prevent the feedback from efficiently stopping star formation (see discussion in Menon et al. 2023; Polak et al. 2024a). We also verify what mass fraction of the stars is bound at 2.5 $t_{\rm ff}$, and find a bound mass fraction above 98% for all three simulations. We note that the differences in SFE lead to super-linear relation between bound stellar mass and initial cloud mass, which allows us to probe a larger range of stellar masses within a cluster-forming region than suggested by the mass range of our initial clouds.

3.3.3 Stellar density

The differences in SFR and SFE have consequences for the density of the subclusters embedded within the GMC. Due to the high degree of substructure and non-sphericity of the systems, rather than calculating a global measure of density, we adopt a local

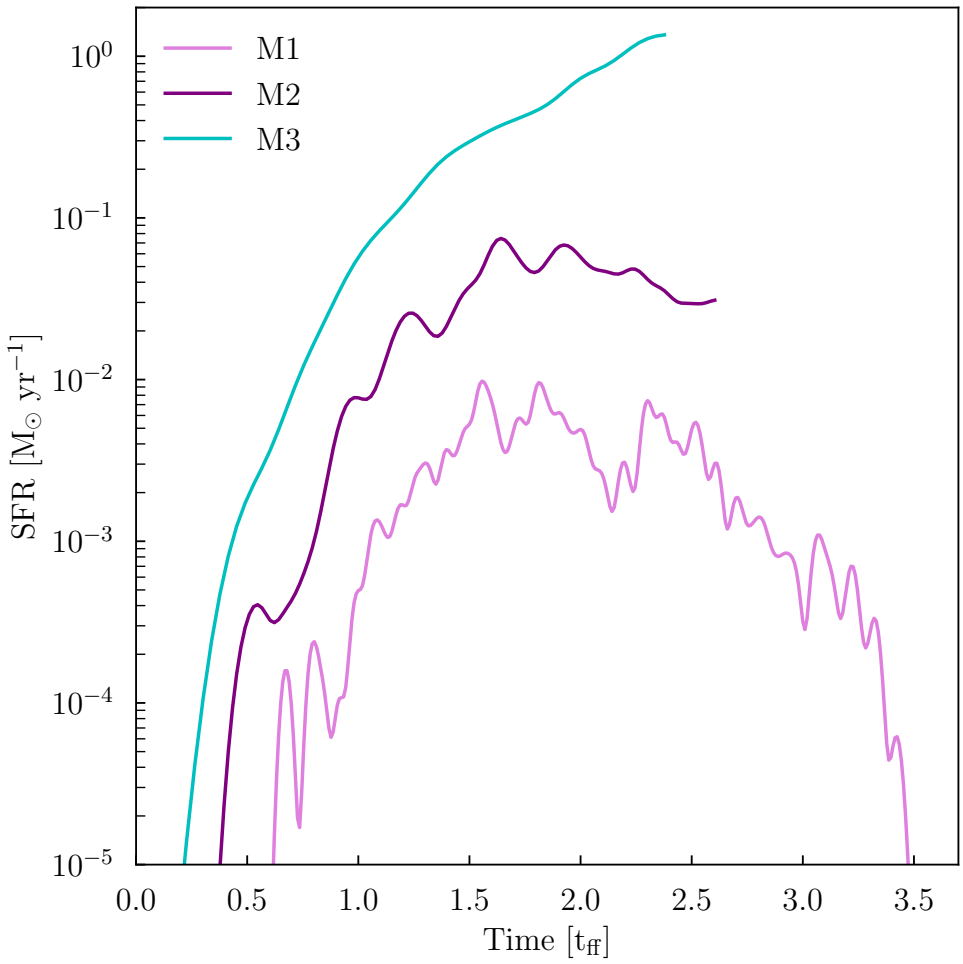

FIGURE 3.2: Star formation rate as a function of time in units of initial GMC freefall time. Note that all lines are slightly truncated at the end due to the Gaussian smoothing.

measure of stellar density. We calculate the local stellar density based on the distance to stars' nearest neighbours and their masses, using

$$\rho = \frac{3}{4\pi r_{10}^3} \sum_{i=1}^{10} m_i \tag{3.5}$$

where m_i is the mass of the i^{th} nearest neighbour and r_{10} is the radial distance to the 10^{th} nearest neighbour, where the star itself is defined as its own closest neighbour. We plot the median and 90^{th} percentile local stellar densities in Figure 3.3.

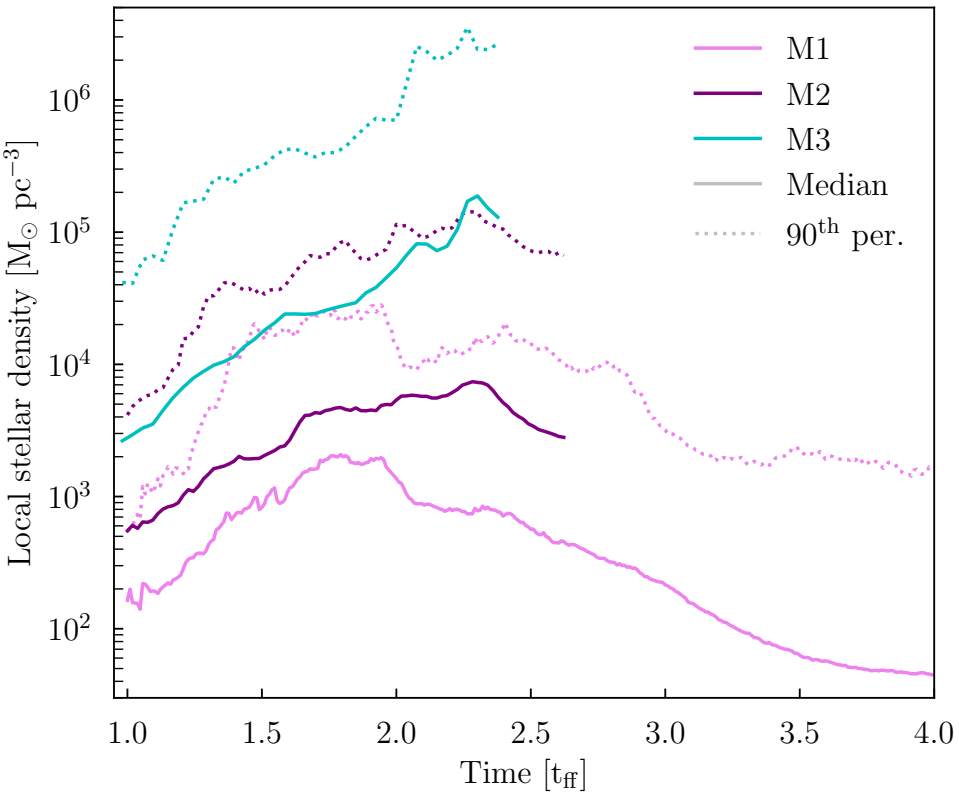

FIGURE 3.3: Median and 90th percentile local stellar density as a function of time in units of initial GMC freefall time.

For M1, the distribution of local densities shifts to higher values while the SFR is increasing and during its plateau. However, once star formation has slowed, the local densities start decreasing, with the median approaching 50 $M_\odot$ pc^{-3} at late times. At all times, the stars in the highest density regions have local densities above 10^4 $M_\odot$ pc^{-3} (with more than 10% of all stars in environments with local density $> 10^4$ $M_\odot$ pc^{-3} between 1.5 and 2 $t_{\rm ff}$), which is a density typical of local YMCs (Portegies Zwart et al. 2010, and references therein). The distribution of local stellar densities even extends to 10^5 $M_\odot$ pc^{-3} at early times. M2 follows similar trends but at higher densities. The decrease in densities also takes place at later times, following the longer plateau in the SFR. M3, on the other hand, exhibits very high densities: at late times, the median local density is above 10^5 $M_\odot$ pc^{-3} and more than 10% of stars have local densities above 10^6 $M_\odot$ pc^{-3}. This environment promotes few-body interactions and is likely to lead to binary disruption, runaway star production, and stellar mergers. The difference in the local density in the different cluster-forming regions demonstrates than we are

probing different regimes for cluster formation with our models at different initial gas mass. Although there is only a factor of 16 difference in the initial gas mass between M1 and M3, the median local stellar density after $\sim 2.5\ t_{\rm ff}$ differs by more than 2 orders of magnitude.

3.4 Evolution of binary populations

Between any two consecutive snapshots, several effects modify the number and properties of the binaries: there is ongoing primordial binary formation (adding new systems sampled from the primordial distribution) combined with dynamical binary formation, disruption, and modification (through exchanges or encounters changing the orbital energy). In this section, we study the relative contributions of those processes to the binary population present in the cluster-forming region as a function of time. In Sections 3.4.1 and 3.4.2, we discuss how the binary fraction and the orbital properties evolve with time. In Section 3.4.3, we discuss how exchanges and dynamical binary formation contribute to observed changes in the distribution, while we discuss the influence of environment in Section 3.4.4.

3.4.1 Time evolution of binary fraction

We plot the binary fraction as a function of time in Figure 3.4. We find that the binary fraction decreases with time in all models. Most of the decrease can be attributed to the loss of binaries wider than 100 au: all three simulations show a clear decrease in their wide binary fraction. The most massive model, M3, is the only cluster-forming region which also shows a decrease in its close binary fraction, most likely due to the very high stellar densities it reaches.

1. For M1, which stops forming stars around $3.5\ t_{\rm ff}$, most of the decrease takes place between ~ 1.5 and $2\ t_{\rm ff}$, while the star formation rate is high and the stellar density increasing. At early times, the number of stars is too small to fully sample the binary population. At late times, once star formation has stopped, the binary fraction shows no significant evolution.

2. In M2, the binary fraction generally decreases, but reaches a small plateau after roughly $1.5\ t_{\rm ff}$ – this corresponds to a peak in the star formation, during which the formation of new primordial binaries balances out the dynamical disruption of wide binaries.

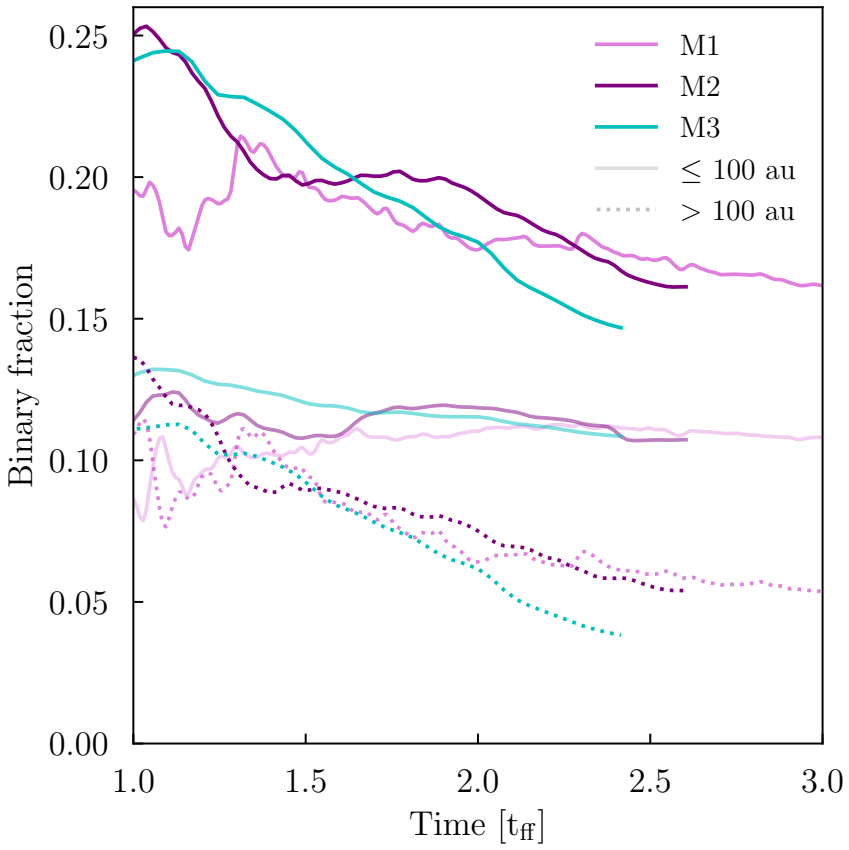

FIGURE 3.4: Binary fraction as a function of time in units of initial GMC freefall time. Binaries with close ($\leqslant$ 100 au) and wide ($>$ 100 au) companions are shown as faint solid and dotted curves. For comparison, a fully sampled binary population with the prescription used in this work has a binary fraction of 21%, with 12% of the stars having a close companion and 9% of the stars having a companion with an orbital separation above 100 au.

3. The decrease in the binary fraction is most obvious, and most rapid, in M3. Both M2 and M3 have binary fractions higher than the primordial binary fraction at early times (before $\sim 1.5\ t_{\rm ff}$), due to the dynamical formation of wide binaries that are disrupted at later times.

3.4.2 Time evolution of orbital properties

In this section, we use M3 as our example for the plots: it contains enough stars to fully sample the IMF and distribution of binary properties, and it exhibits the strongest

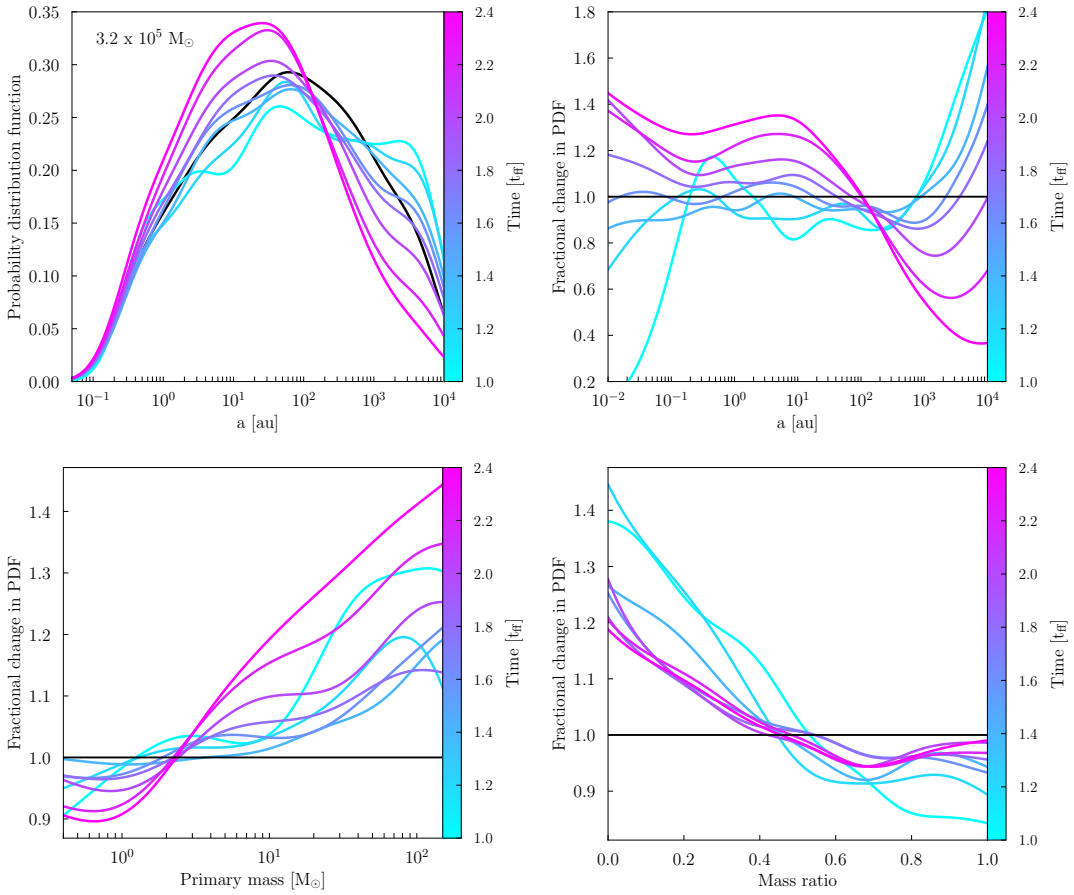

FIGURE 3.5: *Top left:* Probability distribution function of semi-major axes for M3, color-coded as a function of time in units of freefall times of the initial cloud. The black line denotes the primordial distribution. *Top right:* The same, but normalized to the primordial distribution. *Bottom left:* Probability distribution function of primary masses, normalized to the primordial distribution (in black). *Bottom right:* Probability distribution function of mass ratios, normalized to the primordial distribution (in black).

signatures of the evolution of its binary population due to its high density. We do, however, note that all trends discussed below are found in all three cluster-forming regions.

3.4.2.1 Semimajor axis

We plot the probability distribution function (PDF) of semimajor axes for M3 at different times in Figure 3.5 (top left), with the primordial distribution shown in black, accompanied by the distribution normalized to the primordial distribution (top right). The distribution of semimajor axes shifts towards smaller values with time. The largest changes in the distribution are found when the star formation rate is high and the local stellar density is increasing, between 1.5 and 2.5 $t_{\rm ff}$. Before $\sim 1.5\ t_{\rm ff}$, there is a peak at wide separations, associated with dynamically-formed systems. This effect is more obvious before the distribution of primordial binaries is fully sampled ($\sim 1\ t_{\rm ff}$ for M3). Beyond $\sim 1.5\ t_{\rm ff}$, the fraction of binary systems with separations above 100 au tends to decrease. The fraction of binaries with smaller separations increases, with a stronger increase for systems with semimajor axes below 10 au. Taken together with the results presented in Figure 3.4, this indicates that the overall fraction of stars with at least one bound companion decreases, as well as the fraction of stars with a companion within 100 au; among stars with a bound companion, however, the fraction of bound companions within 100 au increases.

3.4.2.2 Primary mass and mass ratio

We plot the probability distribution function of primary masses and mass ratios (normalized to the primordial distribution) as a function of time for M3 in the bottom row of Figure 3.5 (bottom left and bottom right). The primary masses generally shift towards larger values, while the mass ratios shift towards smaller values. The fraction of binaries with OB primaries (above 2 $M_\odot$) increases, with the strongest fractional increase seen for the most massive O-type stars. Lower-mass binaries often have lower binding energies, and are therefore more easily disrupted. On the other hand, massive single stars tend to easily acquire bound companions (as shown in Wall et al. 2019; Cournoyer-Cloutier et al. 2021). Two effects also contribute to the shift in mass ratios. First, dynamically-formed systems, which make up about 5% of all binaries in this simulation, tend to be paired randomly and therefore favour smaller mass ratios, due to the shape of the IMF. Low-mass binaries, which make up most of the disrupted systems (see Section 3.4.4), tend to have mass ratios closer to unity; their disruption therefore shifts the distribution of mass ratios towards smaller values.

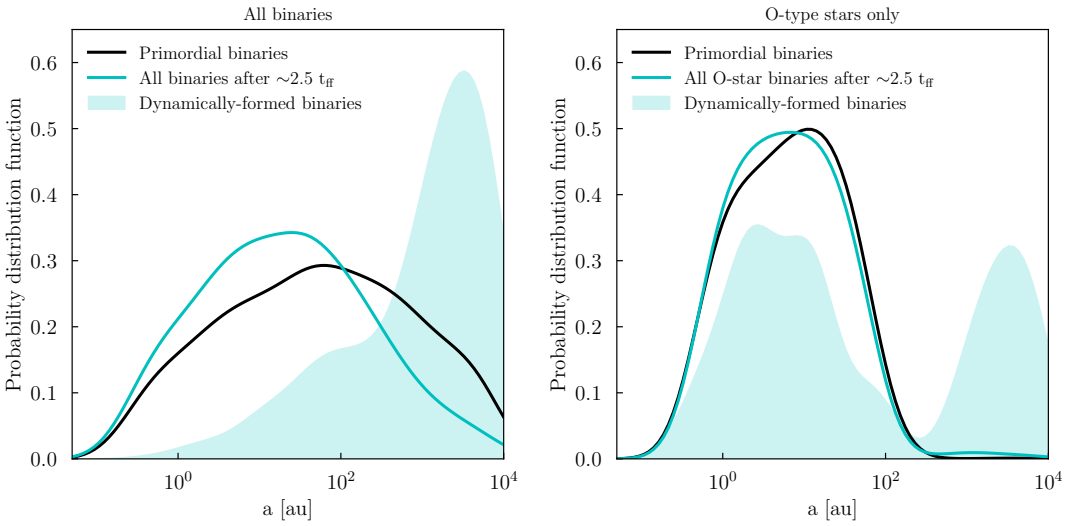

FIGURE 3.6: *Left:* semimajor of primordial binaries, all binaries present in cluster after 2.5 $t_{\rm ff}$, and dynamically formed binaries for M3. *Right:* The same, but for binaries with O-star primaries only.

3.4.3 Dynamical formation & exchanges

We can also turn our attention to the relative contributions of primordial systems – which may be dynamically hardened or softened, or disrupted – and systems formed dynamically, either through exchanges or by capture. In Figure 3.6, we compare the semimajor axis distribution of binaries present in M3 after $\sim 2.5\ t_{\rm ff}$ (which are primordial at $> 95\%$) to those of the subset of dynamically-formed binaries, for all stars and for O-type stars only. For the full distribution, we find that dynamically-formed binaries tend to be much wider than primordial binaries. On the other hand, for the subset of O stars, about half of the dynamically formed binaries ($< 5\%$ of systems) have semimajor axes below 100 au; most of those are formed through exchanges. Despite their high binding energies, several primordial O-star binaries are also disrupted. Dynamical interactions during cluster formation therefore have an impact not only on the population of low-mass binaries, but also on the highest mass systems. Although O stars have a constant binary fraction (see Figure 3.7), several O-star binaries are modified or disrupted.

3.4.4 The influence of environment

We now explicitly compare the evolution of the populations of binaries in the different environments. In Figure 3.7, we plot the binary fraction at $\sim 2.5\ t_{\rm ff}$ as a function of stellar mass for our simulations, compared to the primordial binaries. For M3 and M2,

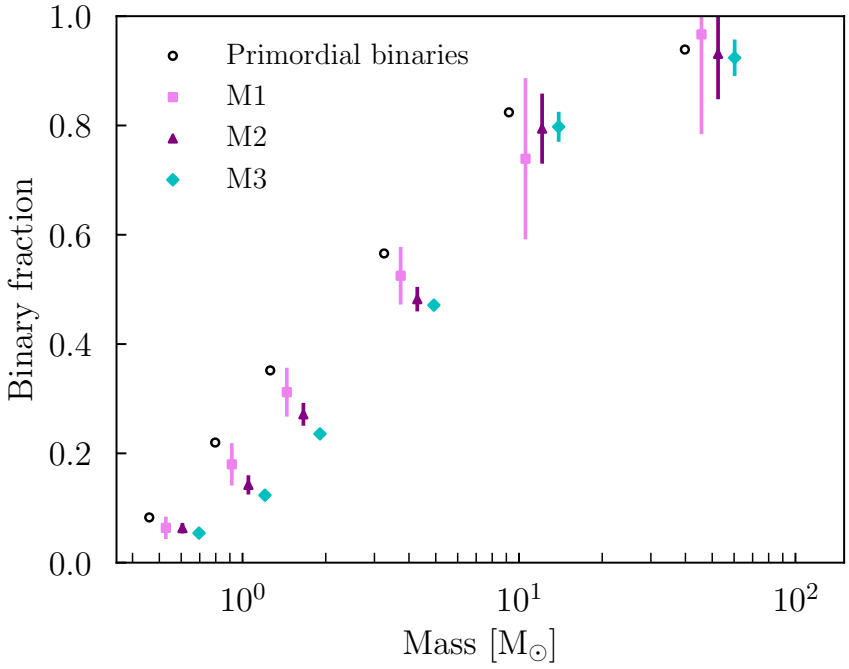

FIGURE 3.7: Binary fraction as a function of stellar mass after 2.5 $t_{\rm ff}$. The vertical lines correspond to the Poisson error, and the different runs are offset along the mass axis for readability. The mass bins used are the same ones as in Table 3.2, with the center of the mass bin at the midpoint between the M1 and M2 data points.

the binary fraction is lower than the primordial binary fraction for stellar masses < 9 $M_\odot$, and is consistent within uncertainties with the primordial binary fraction for stellar masses $\geqslant 9$ $M_\odot$. A similar trend is found for the best estimate of the binary fraction for M1, although the binary fraction is always consistent within uncertainties with the primordial distribution due to the smaller number of stars formed. This indicates clearly that the binary fraction decreases during hierarchical cluster formation for lower-mass stars, while the binary fraction for massive stars is stable.

We also compare the PDF of semimajor axes to one another and to the primordial distribution, at ~ 2.5 $t_{\rm ff}$. We use the distribution of semimajor axes as evidence of the change in the binary population, as it is the metric that shows the clearest signature of change in one direction. For our statistical comparison, we use the two-sample Kolmogorov-Smirnov (KS) test. We are confident at $> 99\%$ that all three distributions have smaller semimajor axes than the primordial distribution, and that M3 has smaller semimajor axes than M2 and M1. This confirms that similar trends in the evolution of

populations of binaries emerge in different cluster-forming environments, and confirms that those trends are stronger in denser, more massive cluster-forming environments. We find that the distributions keep diverging from the primordial distribution of semi-major axes well after the change is reliably detected. This is most obvious for M3, for which the difference keeps increasing throughout the simulation. On the other hand, the distribution of semimajor axes becomes more stable for M1 at late times, following the binary fraction. Taken together with the results from Figures 3.2 and 3.4, this confirms that most of the changes in the binary fraction and binary orbital properties take place during cluster formation, while the star formation rate is high. We present a more detailed discussion of this time evolution in the Appendix 3.A.

3.5 Discussion

3.5.1 Comparison to observations

We have simulated counterparts to cluster-forming regions with physical properties mimicking a large range of observed embedded clusters in the Local Group. Although the cluster-forming regions do not form a single, monolithic cluster within 2.5 $t_{\rm ff}$, we expect they will eventually form bound clusters of mass greater or equal to their current stellar mass.

1. M1, which is evolved until gas expulsion, forms a total stellar mass of 7.8 x 10^3 $M_\odot$, of which 6.9 x 10^3 $M_\odot$ is bound. It can therefore be treated as a simulated counterpart to M16 (8,100 stars), RCW 38 (9,900 stars) or NGC 6357 (12,000 stars) (Kuhn et al. 2015), which are local embedded clusters hosting massive stars.

2. M2, which has formed roughly 3.4 x 10^4 $M_\odot$ of stars (of which $> 99\%$ are bound), is more similar to the Arches cluster, which has a stellar mass between 2 x 10^4 (Espinoza et al. 2009) and $\leqslant$ 7 x 10^4 (Figer et al. 2002), a density above 10^5 $M_\odot$ pc^{-3} in its densest regions (Espinoza et al. 2009), and is known to have a high binary fraction for stars more massive than 50 $M_\odot$ (Clark et al. 2023).

3. M3, with a bound mass approaching 2 x 10^5 $M_\odot$, is more massive than any YMC within the Milky Way (Portegies Zwart et al. 2010, and references therein), and about twice as massive as R136 in the LMC (8.7 x 10^4 M$_\odot$, Cignoni et al. 2015), known to host several stars more massive than 100 $M_\odot$.

Our results confirm that a universal mass-dependent primordial binary fraction and distribution of orbital parameters naturally gives rise to variations in binary population

properties with environment. Most of the changes in the properties of the binary population take place during the cluster assembly process, which is consistent with the decrease in binary fraction and the shift in binary properties being driven by subcluster mergers (as found in Cournoyer-Cloutier et al. 2024). This is important to take into account when comparing to observations. Several clusters for which we have resolved observations show evidence of recent or ongoing mergers between subclusters (e.g., Westerlund 1, Zeidler et al. 2021; R136, Sabbi et al. 2012; Fahrion & De Marchi 2024). However, it is hard to constrain observationally whether a cluster has undergone a recent merger, even with resolved photometry for individual stars: signatures from the shape of the cluster are erased on very short timescales (Cournoyer-Cloutier et al. 2023), and signatures from an anisotropic distribution of runaway stars (Polak et al. 2024b) require high-quality observations away from the cluster center. The recent history of an embedded cluster therefore also likely contributes to setting its wide binary fraction and distribution of orbital properties, in addition to its density, therefore resolving the apparent inconsistency between the excess (Niu et al. 2020) or dearth (Deacon & Kraus 2020) of binaries observed in denser young open star clusters.

Our simulations reproduce the lower number of wide binaries for low- and solar-mass stars that is observed in dense star-forming regions (e.g., Duchêne et al. 2018), as well as the stable close binary fraction for clusters in the mass range of observed clusters in the Milky Way (Deacon & Kraus 2020). For more massive clusters, however, our results suggest that the binary fraction for companions closer than 100 au also decreases during cluster assembly. Clouds with shorter freefall times – and therefore dense, compact clouds – show more rapid changes to their populations of binaries during cluster formation.

3.5.2 Implication for globular cluster formation

Although it is not possible to confirm observationally whether the most massive YMCs in starbursts in the local Universe are forming through sub-cluster mergers – let alone GCs at high redshift – there is strong evidence from simulations that the most massive star clusters assemble from the repeated mergers of smaller subclusters (Howard et al. 2018; Dobbs et al. 2022; Rieder et al. 2022; Reina-Campos et al. 2025). Observations in the local Universe and at high redshift both suggest that the most massive clusters should form from GMCs with high surface densities, and therefore short freefall times: GMCs in local starburst galaxies have surface densities $\geqslant 10^3\ M_\odot\ \mathrm{pc}^{-2}$ (Sun et al. 2018), as do GMCs observed in a strongly-lensed galaxy at $z \sim 1$ (Dessauges-Zavadsky et al. 2023). We therefore expect that clusters forming from those GMCs would exhibit

similar behaviour to that of our M3 model, in which the distribution of binaries is strongly modified at early times in the cluster formation process.

GCs tend to have low binary fractions ($\lesssim 10\%$ assuming a field-like mass ratio distribution, Milone et al. 2012), for stars with masses $\lesssim 0.8\ M_{\odot}$. This corresponds to our lowest mass bin in Figure 3.7, and shows good agreement with our calculated fraction of systems with semimajor axes smaller than 10,000 au. If the primordial binary population is set by the physics of core and disk fragmentation – and therefore the same for cluster-forming environments of the same metallicity – then the hierarchical formation of massive clusters could be sufficient to explain the low binary fraction observed for low-mass stars in old GCs, while allowing for the high binary fraction for massive stars in YMCs.

In a recent paper, Nguyen & Sills (2024) showed that a population of massive binaries between 10 and 40 $M_{\odot}$, following the same distribution of orbital properties as our primordial distribution, loses about 25% of its initial mass as pre-supernova ejecta. This cool ejecta has the right abundances (as originally shown by De Mink et al. 2009) to explain the light abundance variations observed in the vast majority of GCs (known as multiple populations) (see Bastian & Lardo 2018; Gratton et al. 2019; Milone & Marino 2022, for recent reviews). In our simulations, the binary fraction for O-type stars shows very little change during the assembly process, even for the most massive, densest cloud. The semimajor axes however tend to shift to smaller values, and exchanges are ubiquitous, including for originally tight systems. This suggests that Nguyen & Sills (2024) may have underestimated the number of short-period systems present in a massive cluster, and therefore the amount of cool, enriched ejecta. We also suggest that more massive clusters should host even more close binaries than M3, in agreement with the observations that show a stronger signal of enrichment in more massive clusters. As the close binary fraction of massive stars is insensitive to metallicity (Moe et al. 2019), the primordial binary properties for close, massive binaries should be similar for GCs forming at low metallicity and for massive stars observed in the local Universe. Our simulations thus indicate that GCs very likely hosted rich populations of close, massive binaries during their formation, supporting massive interacting binaries as a possible source of enriched material for multiple populations.

3.6 Conclusions

We have conducted simulations of young massive cluster formation within GMCs with masses 2 x 10^4, 8 x 10^4 and 3.2 x 10^5 $M_\odot$, and studied how populations of binary stars evolve during the cluster formation process. We have found that the binary fraction and the distribution of the binaries' orbital properties changes faster and more strongly in more massive and denser clouds. This tendency is exacerbated by the nonlinear relationship between initial gas mass and final stellar density that we find. We summarize the key results below.

1. The binary fraction decreases rapidly in all our simulations while the star formation rate and the local stellar density are increasing. When the star formation rate and the local stellar density decrease, the binary fraction stabilizes.

2. A similar trend is found for the changes in the distributions of orbital properties, due to a combination of binary disruption, exchanges, and dynamical binary formation, along with ongoing star formation. The clearest trends with time are seen for the semimajor axis, which shifts towards smaller values throughout the cluster assembly process.

3. The decrease in the binary fraction is driven by a decrease in the wide (> 100 au) binary fraction, although the most massive, densest cluster-forming region also shows a decrease in its close binary fraction.

4. For the most massive, densest cluster-forming region, the distribution of semimajor axes becomes measurably different from the primordial distribution after about 1.5 $t_{\rm ff}$, despite the ongoing rapid star formation after this point. On the other hand, for lower density environments, the distribution takes a longer time to become measurably different from the primordial distribution, due to the less concentrated star formation.

5. The binary fraction does not change for O-type stars, and the distribution of O stars only shows a small shift towards smaller semimajor axes. Individual systems, including ones with very tight orbits, can however be modified, for example, via exchanges with other systems.

We have found that populations of binaries evolve during clustered star formation within GMCs, and that a universal field-like primordial distribution can naturally explain the observed trends with cluster mass and density for Galactic clusters. Changes are

more rapid and stronger in more massive, denser GMCs, which can naturally explain the differences in binary fractions and binary orbital properties observed in different clustered environments. While the present paper investigates the evolution of the population of binaries during star cluster formation, binaries may also impact their host cluster. In future papers in this series, we will investigate runaway stars and stellar mergers in clusters with realistic populations of binaries, as well as the effects of binary stellar evolution on star formation within cluster-forming regions (Cournoyer-Cloutier et al. 2024, in preparation).

Acknowledgements

C.C.-C. is supported by a Canada Graduate Scholarship – Doctoral (CGS D) from the Natural Sciences and Engineering Research Council of Canada (NSERC). A.S. and W.E.H. are supported by NSERC. This research was enabled in part by support provided by Compute Ontario (`https://www.computeontario.ca/`) and the Digital Research Alliance of Canada (`alliancecan.ca`) via the research allocation FT #2665: The Formation of Star Clusters in a Galactic Context. Some of the code development that facilitated this study was done on Snellius through the Dutch National Supercomputing Center SURF grant 15220. M-M.M.L., B.P., and E.A. were partly supported by NSF grant AST23-07950. E.A. was partly supported by NASA grant 80NSSC24K0935. S.M.A is supported by an NSF Astronomy and Astrophysics Postdoctoral Fellowship, which is supported by the National Science Foundation under award No. AST24-01740; S.M.A. also received support from award No. AST20-09679.

3.A Statistical test of semimajor axis evolution

We compare the distribution of semimajor axes in all of our simulations, at every snapshot, to the primordial distribution. We do so to investigate at what time changes to the population of binaries can be reliably measured in different environments, and whether the population continues to evolve beyond this point. In Figure 3.A1, we plot the probability, as a function of time, that the distribution of semimajor axes has shifted towards smaller values compared to the sampled distribution. The probability is calculated from the KS test, as 1-p. The probability obtained from the KS test, however, only answers the question of whether the semimajor axes are smaller than in the primordial distribution, but does not measure by how much the distributions differ. The KS statistic itself, however, provides a measure of the difference between the two distribution. We also plot it as a function of time in Figure 3.A1. In all cases, we compare the distribution

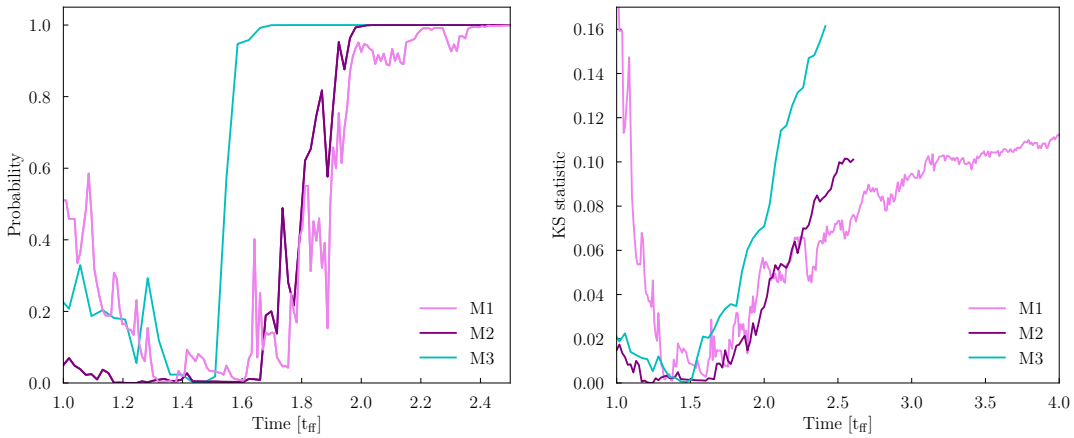

FIGURE 3.A1: *Left:* Probability that the semimajor axes are smaller than in the primordial distribution, as a function of time. M1, M2, and M3 consistently show a difference relative to the primordial distribution after 2.37, 1.98 and 1.66 $t_{\rm ff}$ (2.51, 1.05 and 0.44 Myr). *Right:* KS statistic measuring the amount of change from the primordial distribution, as a function of time.

of binaries present within a cluster-forming region to the primordial distribution. We emphasize that the primordial distribution is not an initial distribution, but rather the distribution for newly-formed binaries; at any given time, the observed binary population arises from the combined contributions of primordial binary formation and the effects of dynamics.

At early times, both the probability and the KS statistic are nonzero in all simulations, due to the small number of stars formed. They approach zero around $\sim 1.5\ t_{\rm ff}$, when the combination of stellar dynamics and new star formation result in a binary population that is very similar to the primordial population. This effect is strongest for M1, which has the fewest stars. At later times, the effects of stellar dynamics start to dominate over the formation of primordial binaries, and changes in the binary population become detectable.

For all three clusters, the probability stabilizes at $> 99\%$. It reaches this value earlier for M3 than for M2, and earlier for M2 than for M1. Changes in massive cluster-forming clouds are stronger, and happen more quickly than in lower-mass clouds. We also note that the lower-mass models, in particular M1, can oscillate strongly between subsequent checkpoints, due to bursts in star formation. The same effect can be seen, albeit more weakly, in M2. M3, on the other hand, goes almost directly to a probability of 100%

and remains there, despite the high star (and therefore primordial binary) formation rate. We can calculate a time τ_c after which the probability is stable at $> 99\%$, i.e., a timescale for a significant change in the binary population, for all simulations. We get values of 2.37, 1.98 and 1.66 t_{ff} (2.51, 1.05 and 0.44 Myr) for M1, M2, and M3. We find that the timescale for change increases with the cloud's initial freefall time. τ_c increases superlinearly with freefall time, like the stellar mass formed in the clouds: more massive, denser clouds undergo more rapid star formation and more rapid changes to their populations of binaries.

Bibliography

Adamo A., Usher C., Pfeffer J., Claeyssens A., 2023, MNRAS, 525, L6

Adamo A., et al., 2024, Nature, 632, 513

Andersson E. P., Agertz O., Renaud F., 2020, MNRAS, 494, 3328

Andersson E. P., Agertz O., Renaud F., Teyssier R., 2023, MNRAS, 521, 2196

Baczynski C., Glover S. C. O., Klessen R. S., 2015, MNRAS, 454, 380

Barnes J., Hut P., 1986, Nature, 324, 446

Bastian N., Lardo C., 2018, ARA&A, 56, 83

Blaauw A., 1961, Bull. Astron. Inst. Netherlands, 15, 265

Chen B. Q., et al., 2020, MNRAS, 493, 351

Cignoni M., et al., 2015, ApJ, 811, 76

Claeyssens A., Adamo A., Richard J., Mahler G., Messa M., Dessauges-Zavadsky M., 2023, MNRAS, 520, 2180

Clark J. S., Lohr M. E., Najarro F., Patrick L. R., Ritchie B. W., 2023, MNRAS, 521, 4473

Colella P., Woodward P. R., 1984, J. Comput. Phys., 54, 174

Cournoyer-Cloutier C., et al., 2021, MNRAS, 501, 4464

Cournoyer-Cloutier C., et al., 2023, MNRAS, 521, 1338

Cournoyer-Cloutier C., Karam J., Sills A., Zwart S. P., Wilhelm M. J. C., 2024, ApJ, 975, 207

Deacon N. R., Kraus A. L., 2020, MNRAS, 496, 5176

Dessauges-Zavadsky M., et al., 2023, MNRAS, 519, 6222

Dobbs C. L., Bending T. J. R., Pettitt A. R., Bate M. R., 2022, MNRAS, 509, 954

Dubey A., et al., 2014, The International Journal of High Performance Computing Applications, 28, 225

Duchêne G., Lacour S., Moraux E., Goodwin S., Bouvier J., 2018, MNRAS, 478, 1825

Espinoza P., Selman F. J., Melnick J., 2009, A&A, 501, 563

Fahrion K., De Marchi G., 2024, A&A, 681, A20

Faisst A. L., Chary R. R., Brammer G., Toft S., 2022, ApJ, 941, L11

Federrath C., Banerjee R., Clark P. C., Klessen R. S., 2010, ApJ, 713, 269

Figer D. F., et al., 2002, ApJ, 581, 258

Fryxell B., et al., 2000, ApJS, 131, 273

Fujii M., Iwasawa M., Funato Y., Makino J., 2007, PASJ, 59, 1095

Götberg Y., de Mink S. E., Groh J. H., Kupfer T., Crowther P. A., Zapartas E., Renzo M., 2018, A&A, 615, A78

Gratton R., Bragaglia A., Carretta E., D'Orazi V., Lucatello S., Sollima A., 2019, A&ARv, 27, 8

Guszejnov D., Markey C., Offner S. S. R., Grudić M. Y., Faucher-Giguère C.-A., Rosen A. L., Hopkins P. F., 2022, MNRAS, 515, 167

Harris W. E., Reina-Campos M., 2023, MNRAS, 526, 2696

He H., Wilson C., Brunetti N., Finn M., Bemis A., Johnson K., 2022, ApJ, 928, 57

Heitsch F., Mac Low M.-M., Klessen R. S., 2001, ApJ, 547, 280

Howard C. S., Pudritz R. E., Harris W. E., 2018, Nature Astronomy, 2, 725

Iwasawa M., Tanikawa A., Hosono N., Nitadori K., Muranushi T., Makino J., 2016, PASJ, 68, 54

Jerabkova T., Beccari G., Boffin H. M. J., Petr-Gotzens M. G., Manara C. F., Prada Moroni P. G., Tognelli E., Degl'Innocenti S., 2019, A&A, 627, A57

Joncour I., Duchêne G., Moraux E., 2017, A&A, 599, A14

Kalari V. M., Vink J. S., de Wit W. J., Bastian N. J., Méndez R. A., 2019, A&A, 625, L2

Karam J., Sills A., 2024, ApJ, 967, 86

Kounkel M., et al., 2019, AJ, 157, 196

Kraus A. L., Ireland M. J., Martinache F., Hillenbrand L. A., 2011, ApJ, 731, 8

Kroupa P., 2002, Science, 295, 82

Kuhn M. A., Getman K. V., Feigelson E. D., 2015, ApJ, 802, 60

Lahén N., Naab T., Johansson P. H., Elmegreen B., Hu C.-Y., Walch S., 2020, ApJ, 904, 71

Lancaster L., Ostriker E. C., Kim J.-G., Kim C.-G., 2021, ApJ, 922, L3

Lee M. G., Bae J. H., Jang I. S., 2022, ApJ, 940, L19

Lohner R., 1987, Comput. Methods Appl. Mech. Eng., 61, 323

MacNeice P., Olson K. M., Mobarry C., de Fainchtein R., Packer C., 2000, Comput. Phys. Commun., 126, 330

Makino J., Aarseth S. J., 1992, PASJ, 44, 141

Menon S. H., Federrath C., Krumholz M. R., 2023, MNRAS, 521, 5160

Miholics M., Kruijssen J. M. D., Sills A., 2017, MNRAS, 470, 1421

Milone A. P., Marino A. F., 2022, Universe, 8, 359

Milone A. P., et al., 2012, A&A, 540, A16

De Mink S. E., Pols O. R., Langer N., Izzard R. G., 2009, A&A, 507, L1

Miyoshi T., Kusano K., 2005, J. Comput. Phys., 208, 315

Moe M., Di Stefano R., 2017, ApJS, 230, 15

Moe M., Kratter K. M., Badenes C., 2019, ApJ, 875, 61

Nguyen M., Sills A., 2024, ApJ, 969, 18

Niu H., Wang J., Fu J., 2020, ApJ, 903, 93

Offner S. S. R., Moe M., Kratter K. M., Sadavoy S. I., Jensen E. L. N., Tobin J. J., 2023, in Inutsuka S., Aikawa Y., Muto T., Tomida K., Tamura M., eds, Astronomical Society of the Pacific Conference Series Vol. 534, Protostars and Planets VII. p. 275 (arXiv:2203.10066), doi:10.48550/arXiv.2203.10066

Pelupessy F. I., van Elteren A., de Vries N., McMillan S. L. W., Drost N., Portegies Zwart S. F., 2013, A&A, 557, A84

Polak B., et al., 2024a, A&A, 690, A94

Polak B., et al., 2024b, A&A, 690, A207

Portegies Zwart S., McMillan S. L. W., 2019, Astrophysical Recipes: The Art of Amuse. Institute of Physics Publishing, Bristol

Portegies Zwart S., et al., 2009, New Astron., 14, 369

Portegies Zwart S. F., McMillan S. L. W., Gieles M., 2010, ARA&A, 48, 431

Portegies Zwart S., McMillan S. L. W., van Elteren E., Pelupessy I., de Vries N., 2013, Computer Physics Communications, 184, 456

Poveda A., Ruiz J., Allen C., 1967, Boletin de los Observatorios Tonantzintla y Tacubaya, 4, 86

Reina-Campos M., Gnedin O. Y., Sills A., Li H., 2025, ApJ, 978, 15

Ricker P. M., 2008, ApJS, 176, 293

Rieder S., Dobbs C., Bending T., Liow K. Y., Wurster J., 2022, MNRAS, 509, 6155

Roman-Duval J., Jackson J. M., Heyer M., Rathborne J., Simon R., 2010, ApJ, 723, 492

Sabbi E., et al., 2012, ApJ, 754, L37

Sana H., et al., 2012, Science, 337, 444

Steinwandel U. P., Bryan G. L., Somerville R. S., Hayward C. C., Burkhart B., 2023, MNRAS, 526, 1408

Stoop M., Kaper L., de Koter A., Guo D., Lamers H. J. G. L. M., Rieder S., 2023, A&A, 670, A108

Stoop M., Derkink A., Kaper L., de Koter A., Rogers C., Ramírez-Tannus M. C., Guo D., Azatyan N., 2024, A&A, 681, A21

Sun J., et al., 2018, ApJ, 860, 172

Sun J., et al., 2020, ApJ, 901, L8

Sun J., et al., 2022, AJ, 164, 43

Sun J., et al., 2024, ApJ, 967, 133

Vanzella E., et al., 2023, ApJ, 945, 53

Wall J. E., McMillan S. L. W., Mac Low M.-M., Klessen R. S., Portegies Zwart S., 2019, ApJ, 887, 62

Wall J. E., Mac Low M.-M., McMillan S. L. W., Klessen R. S., Portegies Zwart S., Pellegrino A., 2020, ApJ, 904, 192

Wang L., Nitadori K., Makino J., 2020a, MNRAS, 493, 3398

Wang L., Iwasawa M., Nitadori K., Makino J., 2020b, MNRAS, 497, 536

Winters J. G., et al., 2019, AJ, 157, 216

Zapartas E., et al., 2017, A&A, 601, A29

Zeidler P., Sabbi E., Nota A., McLeod A. F., 2021, AJ, 161, 140

CHAPTER 4

MASSIVE INTERACTING BINARIES ENHANCE FEEDBACK IN STAR-FORMING REGIONS

The content of this chapter has been accepted for publication in the *Astrophysical Journal* with the following title and author list:

Cournoyer-Cloutier, C., Andersson, E. P., Appel, S. M., Lahén, N., Polak, B., Rantala, A., Toonen, S., Sills, A., Rieder, S., Portegies Zwart, S., Mac Low, M.-M. and Harris, W. E. (2025). Massive Interacting Binaries Enhance Feedback in Star-Forming Regions, accepted for publication in *ApJ*.

Abstract

We present a new framework to incorporate feedback from massive interacting binaries in simulations of star cluster formation. Our new feedback model adds binary stellar evolution to the cluster formation code Torch, and couples it in Amuse to the pre-existing modules for collisional stellar dynamics, magnetohydrodynamics, and mechanical and radiative feedback. Our model accounts for the effects of mass transfer on the stars' mass loss rates, their radiation spectra, and the timing of core-collapse supernovae. It also injects mass lost through non-conservative mass transfer and common envelope ejection into the interstellar medium. We demonstrate the use of our feedback model through simulations of isolated binaries in a gaseous medium, and of embedded clusters of massive binaries. Feedback from interacting binaries efficiently couples with the surrounding interstellar medium. It increases the size of H II regions, increases the kinetic and thermal energy of the gas, and increases the pressure within H II regions compared to models that use single star stellar evolution. Those differences arise from the ionizing radiation, which increases by three orders of magnitude, resulting in H II regions that expand due to thermal pressure rather than radiation pressure. The effects of stellar dynamics and the gravitational potential of the background gas cause the evolution of individual binaries to deviate from the predictions made by secular evolution, impacting the subsequent feedback from the binary. We conclude that massive interacting binaries are an important source of feedback in cluster-forming regions, and must be considered when studying the emerging timescales of young star clusters.

Unified Astronomy Thesaurus Concepts: Binary stars (154) — Massive stars (732) — Interacting binary stars (801) — Stellar dynamics (1596) — Stellar feedback (1602) — Young massive clusters (2049)

4.1 Introduction

Massive stars play an important role in the evolution of star-forming galaxies by injecting energy and momentum into the interstellar medium (ISM) via stellar feedback. O-type stars are the dominant source of feedback in regions forming massive star clusters, rather than protostellar feedback from lower-mass stars (Matzner & Jumper 2015; Plunkett et al. 2015). Different feedback mechanisms dominate at different times: core-collapse supernova (SN) feedback, which injects mass and energy into the ISM after $\gtrsim 3$ Myr, and pre-SN feedback, which acts from the time of star formation. Massive stars regulate star formation by providing mechanical and radiative feedback to the surrounding ISM through stellar winds (Rogers & Pittard 2013; Wareing et al. 2017; Geen et al. 2021; Lancaster et al. 2021b, 2024), radiation (Howard et al. 2017; Barnes et al. 2020; Menon et al. 2023), and core-collapse SNe (Walch & Naab 2015; Körtgen et al. 2016; Lucas et al. 2020). Recent observations of young massive star clusters (YMCs) suggest that pre-SN feedback is sufficient to interrupt star formation and remove the gas from the cluster-forming region (Chevance et al. 2022; Hannon et al. 2022; Deshmukh et al. 2024). However, the masses and radii of YMCs observed in local starburst galaxies (Leroy et al. 2018; He et al. 2022; Levy et al. 2024) and at high z (Vanzella et al. 2023; Adamo et al. 2024) suggest that that they are dense enough to prevent radiative and wind feedback from halting star formation (Krumholz et al. 2019). More work on the effects of pre-SN stellar feedback on the ISM at the scale of individual YMCs is necessary to resolve this tension.

Milky Way O stars have a multiplicity fraction $\gtrsim 95\%$ (Moe & Di Stefano 2017; Offner et al. 2023). Observations reveal high binary fractions for massive stars in local YMCs (Almeida et al. 2017; Ritchie et al. 2022; Clark et al. 2023); those binaries can survive in denser, more massive clusters that mimic those forming in starburst galaxies (Cournoyer-Cloutier et al. 2024b). At least 70% of all O stars have a companion within 10 au; as a consequence, 70% (Sana et al. 2012) to $\gtrsim 90\%$ (Moe & Di Stefano 2017) of O stars undergo a pre-SN mass transfer (MT) episode. This has profound implications for the timing and strength of the feedback injected into the ISM.

Stars in close binaries undergo MT through Roche lobe overflow (RLOF) which is triggered once the radius of a star exceeds its Roche lobe (Paczyński 1971; Eggleton 1983). The donor loses material from its envelope, which is accreted by the companion or lost from the system; those outcomes are respectively known as conservative and non-conservative MT (Soberman et al. 1997). The radii, temperatures, and luminosities of the

stars change due to MT, modifying their radiative and mechanical feedback (Marchant & Bodensteiner 2024, and references therein). MT via RLOF is commonly labeled based on the donor's evolutionary stage: Case A for MT while the donor is on the main sequence (MS), and Cases B and C for to MT on the post-MS before and after the end of core helium burning (Kippenhahn & Weigert 1967; Lauterborn 1970). For massive stars at solar metallicity, Case A and Case B MT can occur for orbital periods of $\lesssim$ 1000 and $\lesssim$ 5000 days (Moe & Di Stefano 2017).

Stars in close binaries may also undergo a common envelope (CE) phase (Paczynski 1976; Ivanova et al. 2013; Röpke & De Marco 2023), during which the donor's envelope engulfs the companion and is subsequently ejected from the system. Both CE ejection and non-conservative MT result in very high instantaneous mass loss rates: CE ejection unbinds the primary's envelope within $\lesssim$1000 years (based on its dynamical timescale, Ivanova et al. 2015) while rapid MT leads to mass loss rates $\lesssim 10^{-2}$ $M_\odot$ yr^{-1} (assuming mass transfer on the thermal timescale, de Mink et al. 2007), both several orders of magnitude larger than wind mass loss rates ($\lesssim 10^{-4}$ $M_\odot$ yr^{-1}, Vink 2022).

Non-conservative MT and CE ejection in massive binaries increase the amount of pre-SN ejecta from a stellar population compared to a population of single stars (e.g. Farmer et al. 2023; Nguyen & Sills 2024). MT also increases the amount of far ultraviolet (FUV, Götberg et al. 2018) and ionizing radiation (Götberg et al. 2020) from massive stars, by rejuvenating accretors and exposing the hot cores of stripped stars. Conservative and non-conservative MT in massive binaries change the timing of core-collapse SNe (Portegies Zwart & Verbunt 1996; Zapartas et al. 2017): they can either hasten or delay SNe in individual systems, change a star's explodability (e.g. Woosley 2019; Antoniadis et al. 2022; Laplace et al. 2025), and change the timing of the first SN in a YMC. Any comprehensive model of stellar feedback should therefore account for the binary evolution of the population of O stars.

YMCs are dynamically rich environments. Few-body interactions may disrupt binaries (Heggie 1975; Hills 1975). Repeated encounters tend to decrease the semimajor axis (Heggie 1975; Hills 1975) and increase the eccentricity (Heggie & Rasio 1996) of a binary, changing the future MT episodes of the system beyond what is predicted by standalone binary stellar evolution. Few-body interactions also result in exchanges (Sigurdsson & Phinney 1993), and massive stars can pair up with a new companion that has already undergone MT. Those interactions are in turn driven by YMC formation: hierarchical cluster assembly leads to bursts of few-body interactions (Fujii et al. 2012;

Rantala et al. 2024) due to violent relaxation (Lynden-Bell 1967), which are strengthened in the presence of primordial binaries and background gas driving the assembly process (Cournoyer-Cloutier et al. 2024a). A comprehensive treatment of feedback from massive binaries must account for stellar dynamics, hydrodynamics, and binary stellar evolution simultaneously.

Previous star-by-star hydrodynamical models of cluster formation have adopted stellar evolution and stellar feedback schemes based on single star models, although some have included dynamical binary formation through collisional stellar dynamics (e.g., Wall et al. 2019; Fujii et al. 2021; Polak et al. 2024b; Lahén et al. 2025) or primordial binaries (Cournoyer-Cloutier et al. 2021, 2023, 2024b). Cluster evolution codes include both primordial binaries and binary stellar evolution, but no hydrodynamics, and therefore no stellar feedback (e.g., Portegies Zwart et al. 1999; Chatterjee et al. 2010; Hypki & Giersz 2013; Wang et al. 2015; Rodriguez et al. 2022; Rantala & Naab 2025). Investigating the effects of coupled binary stellar evolution and dynamics on the feedback budget of YMCs is needed for understanding how stellar feedback halts star formation in massive cluster-forming regions.

In this paper, we present a new framework for feedback from massive interacting binaries in star-forming regions, and demonstrate the importance of feedback from massive interacting binaries on the nearby ISM. The model accounts for the effects of binary evolution on the radiative and mechanical feedback from massive stars, allows for binaries to be modified through the effects of stellar dynamics, and models the binaries alongside the background gas. This framework is implemented within the Torch cluster formation model (Wall et al. 2019), which couples stellar dynamics to star and binary (Cournoyer-Cloutier et al. 2021) formation, and stellar evolution. The coupling of binary evolution to stellar dynamics and hydrodynamics is described in Section 4.2. Section 4.3 gives examples of conservative and non-conservative mass transfer. We discuss a suite of example simulations of compact clusters of massive binaries in Section 4.4, followed by a discussion and summary in Section 4.5.

4.2 Coupling binary evolution with stellar dynamics and hydrodynamics

Binary evolution can change the binary's orbit, trigger mass loss, and change the stars' radiation spectrum due to mass transfer. The effects of gravity from nearby stars and gas can also modify the orbits of the binaries, and in turn influence binary evolution.

It is thus crucial to ensure that the coupling between star and binary evolution, stellar dynamics, stellar feedback, and hydrodynamics allows information to be propagated correctly between the different codes.

4.2.1 Torch

Torch (Wall et al. 2019)[1,2] uses the Amuse framework (Portegies Zwart et al. 2009; Pelupessy et al. 2013; Portegies Zwart et al. 2013; Portegies Zwart & McMillan 2019; Portegies Zwart et al. 2023)[3] to couple radiation magnetohydrodynamics (RMHD) to collisional stellar dynamics and stellar evolution. Torch is designed as a star cluster formation code, and includes star (Wall et al. 2019) and binary (Cournoyer-Cloutier et al. 2021) formation. Stellar evolution is handled by SeBa (Portegies Zwart & Verbunt 1996; Nelemans et al. 2001; Toonen et al. 2012) while mechanical and radiative feedback from massive stars is handled directly in the RMHD code Flash (Fryxell et al. 2000; Dubey et al. 2014). In this paper, we present the implementation of binary stellar evolution and feedback from interacting binary stars in Torch.

The order of operations within one code time step are presented in Figure 4.1. The gravitational interactions between the gas and the stars are handled with a leapfrog scheme based on Bridge (Fujii et al. 2007), which takes a kick-drift-kick approach described in Wall et al. (2019). Each step begins and ends with a *kick* updating the gas velocity from the stars and vice-versa; the corresponding acceleration is calculated with a multi-grid solver (Ricker 2008). Binaries are identified every time step, after the first kick, as described in Section 4.2.4. Once the information about the binaries has been passed to the stellar and binary evolution code, the single stars and the binaries are evolved by a time step Δt. The stellar and binary evolution in SeBa is presented in Section 4.2.5. The output from SeBa is used to update the stars' positions and velocities, and to set the radiative and mechanical feedback properties. We describe in Sections 4.2.6 and 4.2.7 how we adapt the feedback routine to account for binary evolution. After the information from stellar and binary evolution has been passed to the RMHD and stellar dynamics codes, those codes evolve in parallel to complete the *drift* part of the Torch step; the relevant information for the RMHD and stellar dynamics methods is presented in Section 4.2.2 and 4.2.3. The simulation time step Δt is set from the minimum time step of the magnetohydrodynamics (MHD) and stellar

[1] `https://bitbucket.org/torch-sf/torch/commits/tag/interacting-binaries-v1.0`, branch used in this paper

[2] `https://bitbucket.org/torch-sf/torch/commits/tag/torch-v2.0`, current stable version

[3] `https://github.com/amusecode/amuse`, commit `aea5b55`

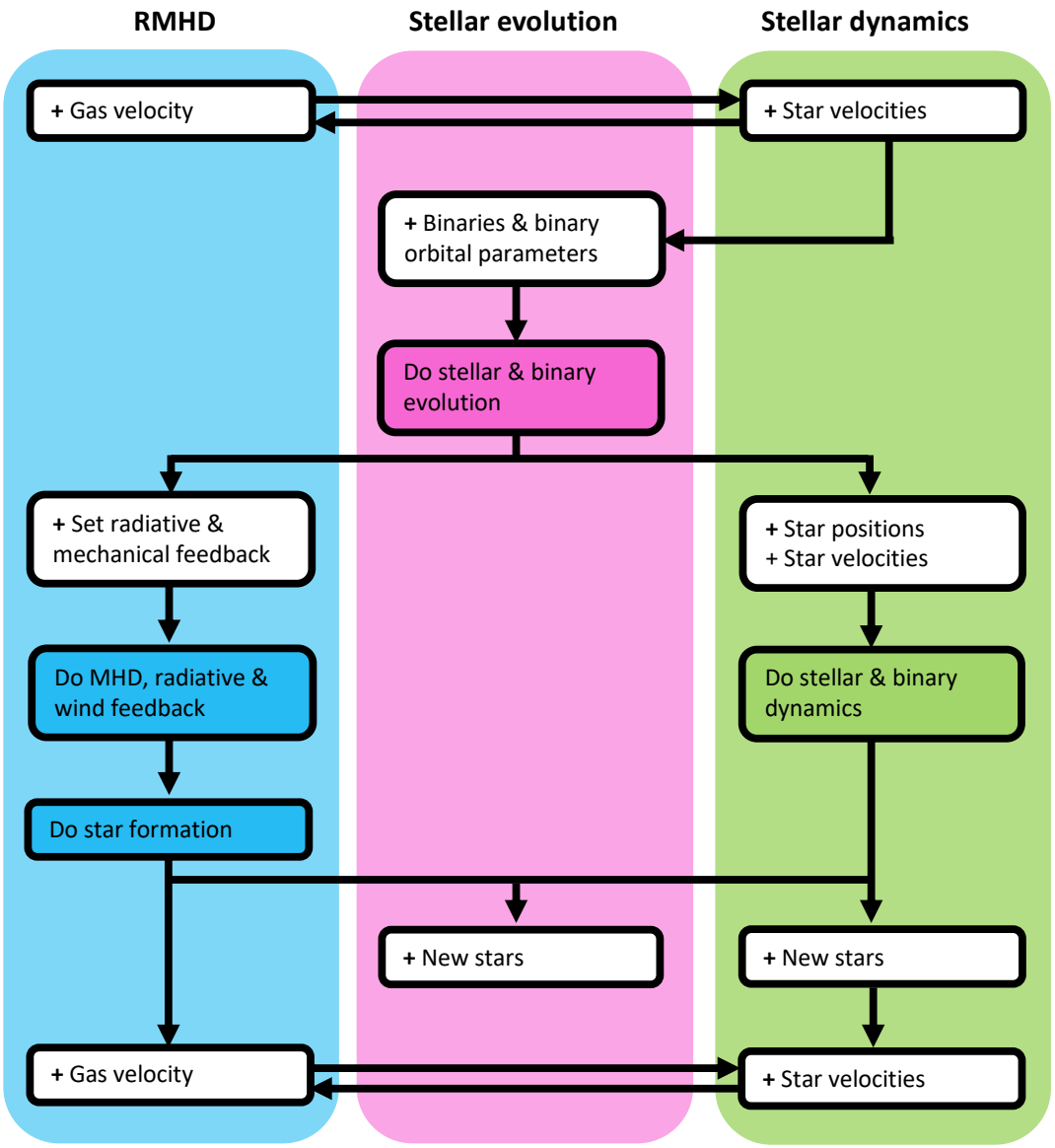

FIGURE 4.1: Flowchart showing the order of operations and information passed between the codes handling RMHD (left, FLASH), stellar and binary evolution (center, SEBA), and stellar dynamics (right, PETAR), for one TORCH time step. The boxes with a white background denote updates from one code to another, while the boxes with a darker background correspond to operations done within one code.

dynamics solvers; the radiation and stellar and binary evolution solvers can adopt shorter time steps and subcycle over Δt as needed.

4.2.2 Radiation magnetohydrodynamics

We use the adaptive mesh refinement code FLASH to evolve MHD and radiation. We use the HLLD Riemann solver (Miyoshi & Kusano 2005) with a multi-grid solver (Ricker 2008) for the gas self-gravity. We refine the grid with the second-derivative criterion (Lohner 1987) for temperature and pressure, and require the Jeans length to be resolved by a minimum of 12 cells (Heitsch et al. 2001; Federrath et al. 2010).

Radiation is handled through the ray-tracing module FERVENT (Baczynski et al. 2015). For numerical stability, we allow the ionization fraction to change by a maximum of 10% per radiation step, and set a minimum ionization fraction of 10^{-8} and a minimum neutral gas fraction of 10^{-4} in each cell. The simulations include heating and ionization from stars, background UV radiation, and background cosmic rays as described in Wall et al. (2020); they also include atomic (Joung & Mac Low 2006), molecular (Neufeld et al. 1995), and dust cooling (Hollenbach & McKee 1989). We assume a dust density of 1% of the gas density when the gas temperature is below $T_{\rm sputter} = 3$ x 10^5 K, and a dust cross-section of 10^{-21} cm^2. The gas is assumed to be at solar metallicity, and we do not follow enrichment from winds or SNe.

4.2.3 Stellar dynamics

We use PETAR (Wang et al. 2020b) to handle collisional stellar dynamics. PETAR combines different approaches to stellar dynamics for different separation regimes. The implementation of PETAR in TORCH is presented in Polak et al. (2024a), with further discussion in Cournoyer-Cloutier et al. (2024b) for the coupling with binaries. We set a global maximum time step for our simulations of $dt_{\rm soft} = 31.25$ yr, set in conjunction with the separations at which each algorithm is used. This allows the simulation time step to vary according to the instantaneous gas conditions while ensuring that the time step remains short enough to resolve the orbits of wide binaries.

For inter-star distances below the regularization radius $r_{\rm bin}$, stars are handled by slow-down algorithmic regularization (Wang et al. 2020a). For inter-star distances between $r_{\rm bin}$ and $r_{\rm in}$, a direct N-body approach is adopted, with a fourth-order Hermite integrator (Makino & Aarseth 1992). At separations greater than $r_{\rm out} = 10\, r_{\rm in}$, gravity between the stars is calculated with a tree code (Barnes & Hut 1986, as implemented by Iwasawa et al. 2016). Between those last two regimes, a weighted average of the

direct N-body and tree approaches is adopted (with weight depending on the distance, see Wang et al. 2020b, for the changeover function). Individual stars can have larger $r_{\rm in}$ and $r_{\rm out}$ if they are more massive than the average stellar mass in the simulation; their changeover radii are then increased by a factor of $(m_i/\langle m \rangle)^{1/3}$. We adopt $r_{\rm bin} = 50$ au and $r_{\rm out} = 625$ au (which corresponds to $r_{\rm out} = 12.5\, r_{bin}$, following the default PeTar ratio).

4.2.4 Binary identification

We identify binaries before every stellar evolution step. We build a tree of neighbors from the three-dimensional positions of the stars, and use it to calculate the pairwise binding energy for each star and its 10 nearest neighbors. The most bound companion, for each star, is saved if its binding energy is positive and the semimajor axis of the corresponding binary is smaller than 10,000 au. Stars are allowed to change companions throughout the simulation, and updating the binary pairs every time step allows us to account for modifications to the orbits and exchanges due to few-body encounters.

4.2.5 Stellar and binary evolution

Our model for binary feedback is designed to be used alongside stellar dynamics, which may modify the binaries' orbits beyond what is expected from the evolution of the system in isolation, or result in exchange interactions involving post-mass transfer systems. Being able to restart from previously evolved stars is therefore a necessary feature. We use the stellar and binary evolution code SeBa (Portegies Zwart & Verbunt 1996; Nelemans et al. 2001; Toonen et al. 2012)[4] to obtain all stellar properties throughout our simulations. SeBa is a rapid stellar evolution code that uses the analytical fits of Hurley et al. (2000) to model the stellar evolution of the stars. In contrast with other rapid stellar and binary evolution codes, SeBa uses the instantaneous properties of a star – such as its mass, core mass, and age – in addition to its zero-age main sequence (ZAMS) properties to calculate its subsequent evolution. SeBa includes prescriptions for wind mass loss from MS and evolved stars, SN mass loss, SN kicks, binary mass transfer, and binary orbital evolution.

4.2.5.1 Wind mass loss rate

A star's mass loss rate depends on its current mass, luminosity, metallicity, and surface gravity. We use the default SeBa wind mass loss rates for solar metallicity ($Z_\odot = 0.02$),

[4] `https://github.com/amusecode/SeBa`, commit `a6f4b64`

which are described in detail in Toonen et al. (2012, their appendix A.1). The wind mass loss rates for OB MS stars are based on the rates from Vink et al. (2000, 2001) and from Nieuwenhuijzen & de Jager (1990), with a correction factor of 1/3 to account for wind-clumping effects (Björklund et al. 2021). The mass loss rates for the Hertzsprung gap (HG) stars are identical to the ones for OB MS stars, except in the luminous blue variable (LBV) regime, where a mass loss rate of 1.5 x 10^{-4} $M_{\odot}$ yr^{-1} is used (Belczynski et al. 2010). For helium stars, the mass loss rates are the maximum of rates from Reimers (1975) and Hurley et al. (2000). For giants with a hydrogen envelope, the adopted mass loss rates are the maximum of the (corrected) Nieuwenhuijzen & de Jager (1990) rates and of the Reimers (1975) rates, with the same LBV correction as the HG stars.

4.2.5.2 Luminosities

For each star, we calculate the luminosity in the FUV (5.6–13.6 eV) and ionizing (> 13.6 eV) bands from the stellar radii and surface temperatures calculated in SeBa. We calculate the luminosity assuming blackbody emission for the FUV band. For the ionizing band, we use the atmospheric model of Lanz & Hubeny (2003) for stars with surface temperatures between 27,500 and 55,000 K, and assume blackbody emission beyond those temperatures.

4.2.5.3 Supernovae

We use the default SeBa prescription for core-collapse SNe, which is itself based on the prescription by Fryer et al. (2012). This prescription provides us with the remnant mass and ejecta mass; we describe in Section 4.2.7.1 the injection of the ejecta in the simulation. For SNe in binaries, we update the velocity of both the star and the remnant self-consistently from the instantaneous change in primary mass, with an additional contribution from the SN's natal kick. As the stellar evolution code has no information about the exact positions of the stars, only their orbital parameters, the resultant kick is calculated for a random time in the binary's orbit.

4.2.5.4 Mass transfer & common envelope

The masses and radii of both stars are evolved concurrently in SeBa. SeBa detects MT due to RLOF and the ejection of a common envelope if they occur. The exact criteria to identify those phases of binary evolution are presented in detail in Toonen et al. (2012, their appendices A.2 and A.3). The two key quantities that we use are the total amount of mass lost by the system during the interaction and the change in semimajor axis due

to the interaction. For the binary evolution calculations, we use the default SeBa values for α and λ, which describe the efficiency of the envelope's unbinding from CE evolution, and β, which describes the MT efficiency.

4.2.5.5 Orbital evolution

Wind mass loss, conservative and non-conservative MT, CE evolution, and tidal circularization all result in changes to the orbital parameters of a binary. For detached binaries (i.e., binaries in which neither star fills its Roche lobe), mass loss results in the binary becoming less bound, and can even result in the disruption of the binary in the case of rapid mass loss from SNe. The fractional increase in semimajor axis due to the mass loss will be approximately equal to the fractional decrease in the binary's total mass (see Toonen et al. 2012). Conservative MT results in a decrease in the semimajor axis while $M_1 > M_2$. For non-conservative MT, the semimajor axis may either decrease or increase depending on the mass ratio M_2/M_1, the angular momentum imparted to the ejected material, and the MT efficiency (see Nuijten & Nelemans 2025; Rodríguez-Segovia et al. 2025, for recent observations and simulations). The semimajor axis decreases in the case of a CE phase or under the effects of tidal circularization.

4.2.6 Interaction detection

We consider a binary to be interacting, for a given time step, if it meets any of the following criteria:

1. It is identified by SeBa as a semi-detached or contact binary, or as undergoing CE evolution;
2. Its binding energy has increased over the stellar evolution step;
3. Its semimajor axis has decreased over the stellar evolution step;
4. One of the stars in the binary has accreted mass.

Interactions may be missed by using only criterion (1), as the timescales for MT and CE evolution are much shorter than the time step dictated by cloud-scale hydrodynamics. We calculate the change in binding energy from

$$\Delta E_{\rm orbit} = \frac{G}{2}\left(\frac{M_{1,\rm f}M_{2,\rm f}}{a_{\rm f}} - \frac{M_{1,0}M_{2,0}}{a_0}\right) \tag{4.1}$$

where M_1 and M_2 denote the primary and companion mass, and a denotes the semimajor axis. The subscript 0 corresponds to the values before applying stellar and binary evolution, while the subscript f corresponds to the values after stellar and binary evolution. If the stars do not interact, a normal binary evolution step results in wind mass loss from both stars and an increase in semimajor axis, leading to $\Delta E_{\rm orbit} < 0$. If the stars interact, the binary may become more bound, leading to $\Delta E_{\rm orbit} > 0$. This is always the case for CE ejection; we therefore use the CE ejection scheme (Section 4.2.7.3) if the binary's binding energy has increased. If the binary's binding energy has decreased despite an interaction being detected – for example in the case of MT resulting in an increase in semimajor axis – we inject the mass lost from the system as a wind from the star that has lost the most mass (Section 4.2.7.2).

4.2.7 Injecting mass loss on the grid

Core-collapse SNe, stellar winds, CE ejection, and non-conservative MT all increase the amount of gas, handled with different injection schemes in the code.

4.2.7.1 Core-collapse supernovae

The SN prescription corresponds to the default TORCH prescription, presented in Wall et al. (2020). For each SN, a mixture of kinetic and thermal energy is injected on the grid over the 27 cells closest to the SN, with the fraction of kinetic energy proportional to the background density over the surface area of the nearby cells, following Simpson et al. (2015). The SN energy is fixed at 10^{51} ergs, and the amount of mass injected by each SN is calculated from the difference between the stellar mass before the supernova, and the remnant mass.

4.2.7.2 Stellar winds

We use the wind injection routine described in Wall et al. (2020). The wind is injected over a spherical region of radius $3.5\sqrt{3}\Delta x$, where Δx is the cell size at the highest refinement level; all cells over which wind is injected must be at the highest refinement level. The wind material is injected into the ISM with a velocity based on terminal wind velocities derived from observations. We conserve momentum when injecting wind material within the simulation domain. The final gas velocity within a cell in the injection region is

$$v = \frac{\rho_{\rm w} v_{\rm w} + \rho_0 v_0}{\rho_{\rm w} + \rho_0} \tag{4.2}$$

where $\rho_{\rm w}$ is the wind density (calculated from the mass loss rate and volume of the injection region), $v_{\rm w}$ is the wind terminal velocity, and ρ_0 and v_0 are respectively the background gas density and velocity.

The wind terminal velocities are calculated based on the prescription by Kudritzki & Puls (2000) and Vink et al. (2000). The velocity $v_{\rm w}$ of the injected material depends on the surface temperature T and the effective escape velocity $v_{\rm esc}$ as

$$v_{\rm w} = \begin{cases} v_{\rm esc} & T < 10^4 \text{ K} \\ 1.4\, v_{\rm esc} & 10^4 \text{ K} < T < 2.1 \text{ x } 10^4 \text{ K} \\ 2.65\, v_{\rm esc} & T \geq 2.1 \text{ x } 10^4 \text{ K}. \end{cases} \tag{4.3}$$

The effective escape velocity is calculated from

$$v_{\rm esc} = \sqrt{\frac{2GM(1-\Gamma_{\rm e})}{R}} \tag{4.4}$$

where M and R are the star's current mass and radius. The Eddington ratio $\Gamma_{\rm e}$ depends on the ratio of radiation pressure to gravity, as

$$\Gamma_{\rm e} = \frac{L\sigma_{\rm e}}{4\pi cGM} \tag{4.5}$$

where L and M are the star's current luminosity and mass, and $\sigma_{\rm e}$ is the electron scattering cross-section. We cap $\Gamma_{\rm e}$ at 0.8. Recent samples of non-interacting O stars (Bestenlehner et al. 2014; Bestenlehner 2020; Brands et al. 2022) find values of $\Gamma_{\rm e} \lesssim 0.8$ for MS and Wolf-Rayet stars, and this value is sufficiently high to capture the transition into the optically-thick wind regime (Vink 2022, and references therein). We implement this limit to ensure that stars out of thermodynamical equilibrium due to binary interactions do not get assigned unphysically low wind velocities.

4.2.7.3 Common envelope ejection and non-conservative mass transfer

As discussed in Section 4.2.6, the simulation time step may frequently be longer than the evolutionary timescales for MT and CE, which prevents us from clearly distinguishing those cases at runtime. We therefore adopt an approach which separates the interacting systems into those for which the binding energy of the binary has decreased over the time step, and those for which the binding energy of the binary has increased. The first

group will be composed only of systems having undergone MT from RLOF, while the second may contain both systems that have undergone RLOF or CE ejection.

Massive binaries are more likely to undergo non-conservative MT than a CE phase (see, e.g., Pavlovskii et al. 2017); for those undergoing MT via RLOF, an increase in orbital period is common (e.g. Lechien et al. 2025; Nuijten & Nelemans 2025). Most massive interacting binaries in our simulations therefore show a decrease in orbital energy over their mass transfer phase. We treat mass loss from such systems as a wind from the donor star, and inject it with a velocity calculated with Equation 4.3.

A smaller fraction of systems show an increase in orbital energy. For those systems, we adopt an approach based on the energy formalism (van den Heuvel 1976; Webbink 1984) for CE ejection, which is often used to describe the efficiency of the envelope's ejection. Under the energy formalism, binary evolution codes calculate the change in orbital energy $\Delta E_{\rm orbit}$ following CE ejection from

$$E_{\rm bind} = \alpha \Delta E_{\rm orbit}, \tag{4.6}$$

where $E_{\rm bind}$ is the envelope's binding energy and α an efficiency parameter. This approach assumes that the energy supplied to unbind material from the star is related to the orbital energy lost by the binary by an efficiency α. The presence of other energy sources beyond the gravitational potential energy (such as H recombination energy, see e.g. Ivanova 2018) may result in $\alpha > 1$. The exact value of α is highly uncertain, and may vary as a function of stellar mass. Compilations of observations and simulations (Iaconi & De Marco 2019; Röpke & De Marco 2023) yield values from $\lesssim 0.1$ to $\gtrsim 1$ for low to intermediate masses. For massive stars, accounting for convection (Wilson & Nordhaus 2022) and radiation pressure support in the envelope (Lau et al. 2022) however yields $\alpha \approx 1$.

Population synthesis studies adopt a fixed value of α, with a common choice being $\alpha = 1$ (e.g. Hurley et al. 2002; Fragos et al. 2023), and use this value in Equation 4.6 to calculate the change in orbital separation following CE ejection. We invert this approach to calculate the ejecta velocity by using the change in orbital separation to calculate the energy imparted to the ejecta. The compiled value of the binary evolution parameters within SeBa remain set to their default values and we assume that the energy supplied

to the ejecta is supplied as kinetic energy. We set the ejecta velocity to

$$v = \left(\frac{2 v_{\rm CE} \Delta E_{\rm orbit}}{M_{\rm lost}} \right)^{1/2} \tag{4.7}$$

where $M_{\rm lost}$ is the binaries' mass loss over the time step and $v_{\rm CE}$ is treated as a velocity scaling for the ejecta. We adopt a value of $v_{\rm CE} = 1$ (i.e. all the energy supplied to unbind the envelope is injected as kinetic energy for $\alpha = 1$), which yields ejecta velocity on the order of the stars' wind velocity. The material is injected over a spherical region of radius $3.5\sqrt{3}\Delta x$, following the wind injection routine.

4.3 Isolated binaries

Here, we present simulations of feedback from interacting binaries, which we compare to simulations in which the same two massive stars are evolved using a single star stellar evolution scheme. For those comparisons, the same initial binary properties – i.e., the masses of both stars, the semimajor axis, and the eccentricity – are used. The TORCH simulations are initialized just before the onset of MT, which then changes the properties of both stars and, subsequently, of the nearby ISM. We outline the initial conditions for the gas background medium, then describe the impact of conservative and non-conservative MT and CE ejection on the nearby gas for our tests problems.

4.3.1 Gas initial conditions

The isolated binary simulations are conducted in a box of size $L = 4$ pc. We use a uniform background density without turbulence and an initial temperature of 100 K. There is no initial magnetic field. We refine up to a refinement level of 4, which corresponds to a resolution of 3.125 x 10^{-2} pc. We use two different background densities to mimic different star-forming environments. We use surface densities of 10^2 and 10^3 $M_\odot$ pc^{-2}, similar to surface densities typical of giant molecular clouds in the disks of star-forming spiral galaxies and in starburst galaxies (see, e.g. Sun et al. 2018). We present an overview of the test simulations in Table 4.1. The run names starting with MT correspond to conservative MT simulations, those starting with nMT correspond to non-conservative MT simulations, and those starting with CE correspond to CE ejection simulations. LD and HD respectively denote the low and high density background medium. The final letter in the run label corresponds to the stellar evolution scheme used: B denotes binary stellar evolution and S denotes single star stellar evolution.

TABLE 4.1: Overview of the isolated binaries' simulations.

Name	BE	$v_{\rm CE}$	Σ	$M_{1,0}$	$M_{2,0}$	a_0	e_0	$M_{1,\rm f}$	$M_{2,\rm f}$	$a_{\rm f}$	$e_{\rm f}$	$L_{\rm FUV}$	$L_{\rm ion}$	$r_{\rm ion}$
			($M_\odot$ pc^{-2})	($M_\odot$)	($M_\odot$)	(au)		($M_\odot$)	($M_\odot$)	(au)		($L_\odot$)	($L_\odot$)	(pc)
(1)	(2)	(3)	(4)	(5)	(6)	(7)	(8)	(9)	(10)	(11)	(12)	(13)	(14)	(15)
MT-LD-B	✓	1	10^2	148	128	2.87	0.37	30.3	108	10.5	0	3.89E5	9.56E5	0.98
MT-LD-S		-	10^2	148	128	2.87	0.37	69.4	69.0	5.75	0.37	3.12E5	2.16E3	0.29
MT-HD-B	✓	1	10^3	148	128	2.87	0.37	30.2	108	10.6	0	4.01E5	9.54E5	0.23
MT-HD-S		-	10^3	148	128	2.87	0.37	69.4	69.0	5.75	0.37	3.11E5	2.16E3	0.16
nMT-LD-B	✓	1	10^2	148	96	18.7	0.64	30.2	71.9	14.6	0	3.97E5	8.95E5	0.22
nMT-LD-S		-	10^2	148	96	18.7	0.64	68.8	71.6	32.7	0.65	3.12E5	3.93E3	0.38
nMT-HD-B	✓	1	10^3	148	96	18.7	0.64	30.2	71.9	14.4	0	6.10E5	9.27E3	0.05
nMT-HD-S		-	10^3	148	96	18.7	0.64	68.8	71.6	32.8	0.65	3.13E5	3.93E3	0.21
CE-LD-B	✓	1	10^2	148	10	5.00	0.40	29.7	10.0	0.22	0	9.64E3	4.66E5	0.21

Note. All simulations are conducted in a uniform cubic box with side $L = 4$ pc, with an initial temperature of 100 K and no initial turbulence. Columns (5) to (8) correspond to the ZAMS values while columns (9) to (15) correspond to values 1 kyr after the mass transfer event. Columns: (1) simulation label, (2) use of binary stellar evolution, (3) velocity parameter for common envelope ejection, (4) initial gas surface density of the background medium, (5) ZAMS primary mass, (6) ZAMS companion mass, (7) initial semimajor axis, (8) initial eccentricity, (9) final primary mass, (10) final companion mass, (11) final semimajor axis, (12) final eccentricity, (13) final FUV luminosity, (14) final ionizing luminosity, (15) final size of the H II region.

4.3.2 Conservative mass transfer

The first test is a case of conservative MT. This changes the temperature, luminosity, and mass loss rates of both stars, but does not result in the injection of additional material into the ISM from the mass transfer event. The properties of the binary and the gas 1 kyr after the mass transfer event are presented in Table 4.1, along with the ZAMS properties of the binary. We evolve the system in SeBa for 3.285 Myr (i.e. just before the primary moves off the MS) before placing the stars within the simulation box. The evolved stars have masses $M_1 = 69.42$ M$_\odot$ and $M_2 = 69.46$ M$_\odot$, and the semimajor axis has increased to 5.72 au due to the wind mass loss. For convenience, we will continue to refer to the initially most massive star – i.e. the donor star – as the primary, despite the other star being more massive at late times.

4.3.2.1 Stellar and binary evolution

Between the start of the simulation and the onset of mass transfer, the primary evolves into a HG star, and its radius increases rapidly. In the simulations with binary stellar evolution, this increase in radius leads to RLOF: material is stripped from the primary and accreted by the companion. During the MT event, which lasts $\lesssim 100$ yr, approximately 39 M$_\odot$ of material is removed from the primary and accreted by the companion. The orbit circularizes and the semi-major axis increases to 10.5 au. The primary becomes a stripped star, exposing its helium core, while the companion is rejuvenated by the accretion of the primary's envelope. This has an important impact on the FUV (5.6 – 13.6 eV) and ionizing ($\geq$ 13.6 eV) luminosity of the stars. We report those values in Table 4.1 for the stars 1 kyr after the MT event. Accounting for binary evolution increases both the FUV luminosity and the ionizing luminosity, but has the largest effect on the ionizing luminosity, which increases by almost three orders of magnitude for this system. The total system mass is not directly affected by the mass transfer event, as the MT is conservative; the $\sim$0.2 M$_\odot$ difference in the final total masses is due to the differences in the wind mass loss rates of the post-MT stars compared to the stars evolved with single star stellar evolution.

4.3.2.2 Gas properties

We present in Figure 4.2 the density, temperature, and ionization fraction in the midplane, 1 kyr after the mass transfer event, for all four MT simulations. Including the effects of MT results in a larger bubble with a hotter wind, and a larger H II region. The differences are more subtle in the higher density medium, but the H II region is larger

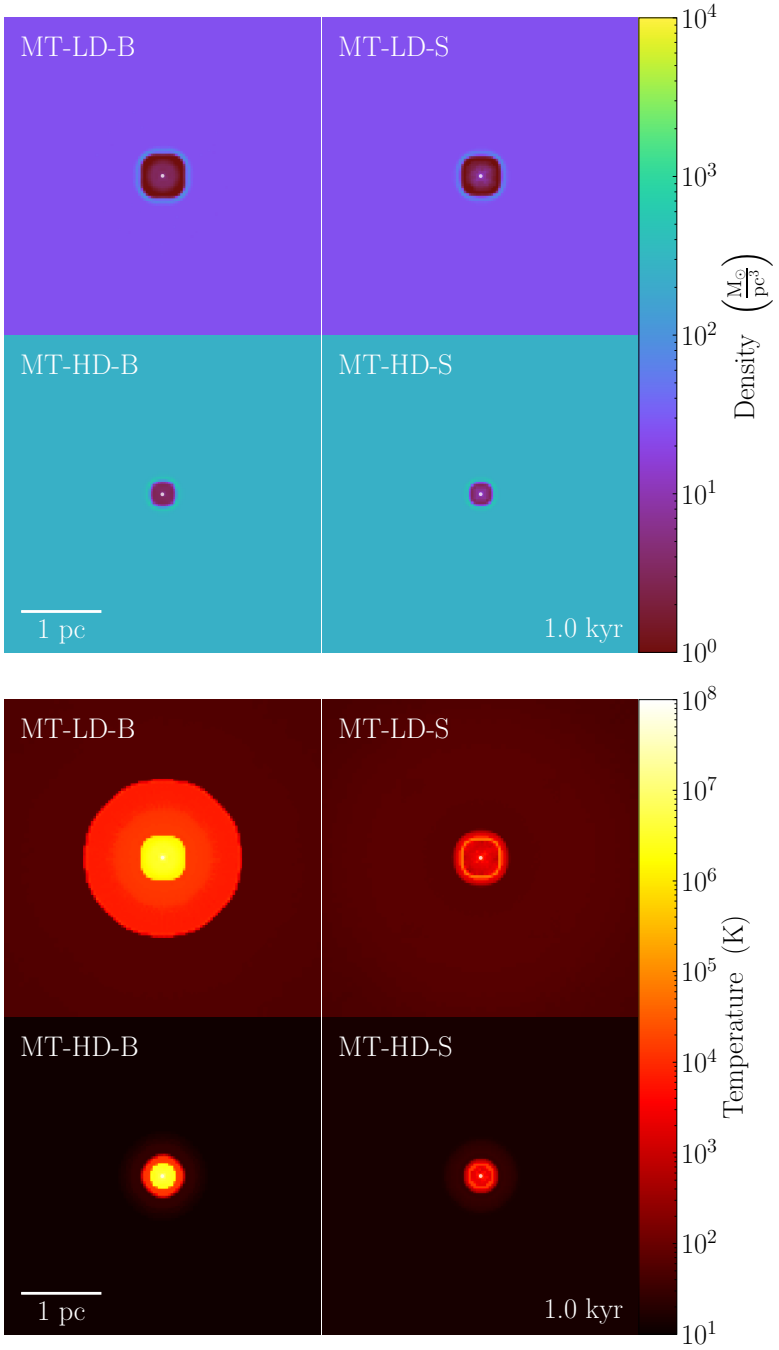

FIGURE 4.2: (1/2) Density (top), temperature (middle) and ionization fraction (bottom) in the midplane for the conservative MT simulations, 1 kyr after the mass transfer event. For each panel, the simulations on the left correspond to runs with binary stellar evolution, and those on the right to runs with single star stellar evolution.

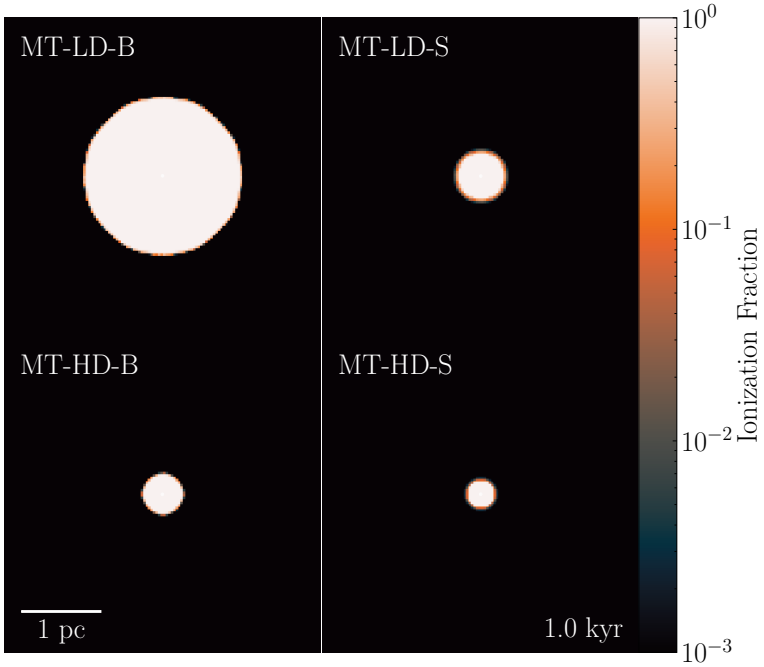

FIGURE 4.2: (2/2) Density (top), temperature (middle) and ionization fraction (bottom) in the midplane for the conservative MT simulations, 1 kyr after the mass transfer event. For each panel, the simulations on the left correspond to runs with binary stellar evolution, and those on the right to runs with single star stellar evolution.

in the simulation with binary evolution, and the temperature within the H II region is higher. Those changes are driven by the change in surface temperature of the stars due to the primary's RLOF.

In Figure 4.3, we plot the ionization fraction and the density as a function of distance to the system's center of mass, for the simulations with the lower gas surface density, MT-LD-B and MT-LD-S. Both simulations show an H II region around the binary and develop wind bubbles with a shock front; the wind bubble is also larger in the simulation with binary evolution, although the difference is more subtle. We obtain the H II region radius from the volume of gas with an ionization fraction above 99%; we then assume that the H II region is spherical and calculate the equivalent radius as

$$r_{\rm ion} = \left(\frac{3V_{\rm ion}}{4\pi} \right)^{1/3} \tag{4.8}$$

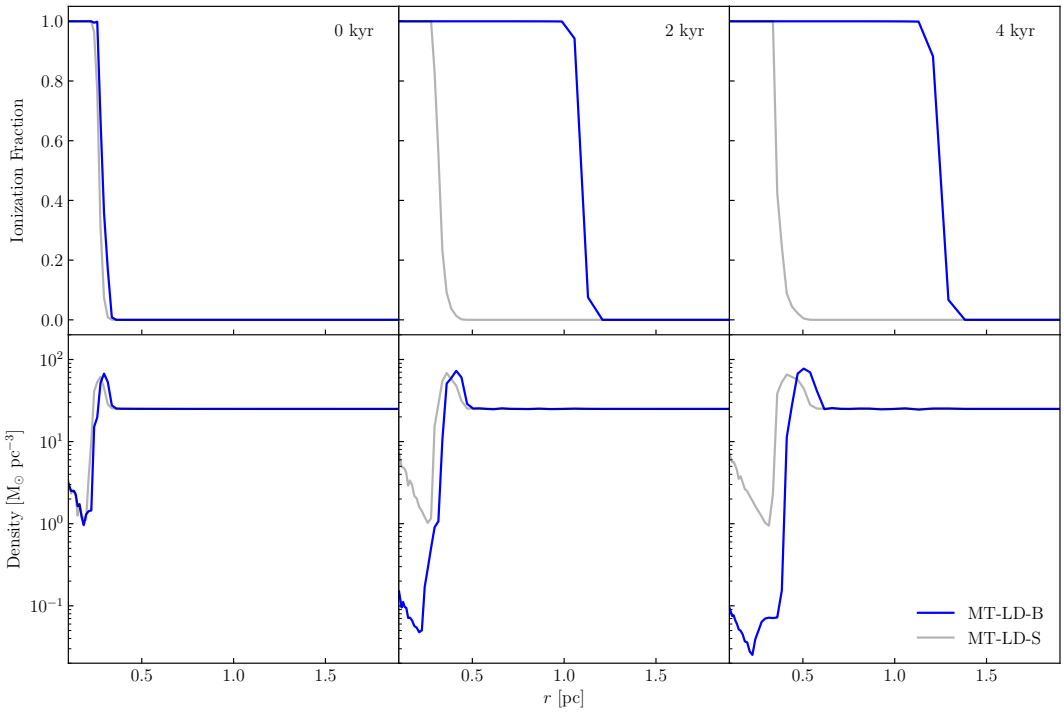

FIGURE 4.3: Ionization fraction (top) and density (bottom) as a function of radial distance to the binary's center of mass, for the conservative MT simulations in the lower density medium, 0 kyr, 2kyr and 4 kyr after the mass transfer event. Each radial bin is the mass-weighted average of the gas properties at this radial distance from the binary's center of mass. The blue line corresponds to the simulation with binary stellar evolution and the grey line to the simulation with single star stellar evolution.

where $V_{\rm ion}$ is the volume of ionized gas and $r_{\rm ion}$ the calculated equivalent radius. We report it in Table 4.1.

4.3.3 Non-conservative mass transfer

The second test case we simulate is non-conservative MT: the primary fills its Roche lobe and starts transferring mass onto its companion, but the mass cannot be fully accreted and some is ejected from the system. This changes the temperature, luminosity, and mass loss rates of both stars, and results in a very high mass loss rate during the MT event. We evolve the binary with SEBA for 3.285 Myr before placing it in the simulation; the stars have masses $M_1 = 69.41$ M$_\odot$ and $M_2 = 71.73$ M$_\odot$, and are still on the MS when we start the simulation, while the semimajor axis has increased to 32.3 au due to

wind mass loss. The properties of the binary and the gas 1 kyr after the MT event are also presented in Table 4.1, along with the binary's ZAMS properties.

4.3.3.1 Stellar and binary evolution

The primary evolves into a HG star just before the onset of mass transfer. During the MT event, which lasts $\sim$ 200 yr, $\sim$ 38 $M_\odot$ of material is removed from the primary. The companion however only successfully accretes $\sim$0.3 $M_\odot$, resulting in an instantaneous mass loss rate of $\sim$ 0.2 $M_\odot$ yr^{-1} for the MT event. This is about three orders of magnitude higher than the mass loss rates of the evolved stars in the single star stellar evolution scheme.The helium core of the primary is also exposed, which results in an increase of the binary's ionizing luminosity by up to two and a half orders of magnitude and a more modest increase in the binary's FUV luminosity. The semimajor axis decreases to $\sim$ 14.5 au following the MT event, while the orbit becomes more circular. In contrast with the conservative MT runs, where the evolution of the binary itself was almost identical in the low and high density background media, the non-conservative mass transfer runs show variations in the final semimajor axis a_f and eccentricity e_f between the runs. Those differences arise from the gravitational attraction of the ejecta on the stars and – by affecting the orbital evolution of the binary and therefore the MT event – lead to differences in the post-MT radii and temperatures of the stars, and therefore in the final FUV and ionizing luminosities of the binary.

4.3.3.2 Gas properties

We present in the left panel of Figure 4.4 the density in the midplane immediately after, 2 kyr, and 4 kyr after the non-conservative MT event, for the lower gas background density. We plot the radial ionization fraction and density profiles in Figure 4.5. During the early stages of MT, the binary becomes more bound, and the ejecta are injected with a velocity calculated from the change in energy. Most of the mass is injected using the wind routine, however, because despite the orbit shrinking due to mass transfer, the increase in binding energy from the change in semimajor axis is not sufficient to offset the decrease in binding energy from the mass loss, resulting in $\Delta E_\mathrm{orbit} < 0$ (Equation 4.1). The inner, thicker shell – which contains most of the ejecta – however moves faster than the outer shell and eventually sweeps it up. Although the ejecta from non-conservative mass transfer is injected using the wind velocity, and therefore the same velocity as the outer shell, the gas velocity in each cell is calculated from momentum conservation. Larger ejecta masses therefore result in larger changes to the gas velocity around the stars. The loss of stellar material from the non-conservative MT event results in a smaller

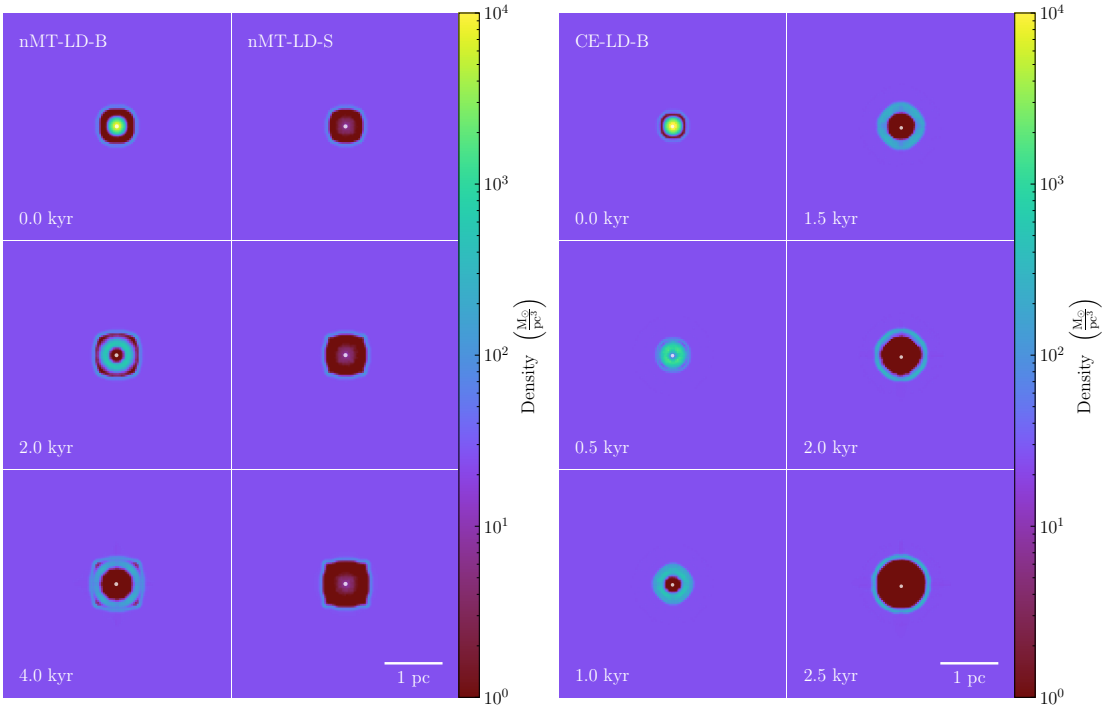

FIGURE 4.4: The left panel shows density slices in the midplane for the non-conservative MT simulations immediately, 2 kyr, and 4 kyr after the mass transfer event. The right panel shows density slices in the midplane for the CE ejection simulation immediately after the envelope is ejected, then in 0.5 kyr increments until 2.5 kyr. All simulations shown are conducted in the lower density medium.

ionization region right after the MT event. As the ejecta are heated and moves away from the star, the ionization region grows again, reaching a size similar to that of the single star stellar evolution case within 4 kyr.

The case of non-conservative MT involves not only changes to the stars themselves but also changes to their environment. This is illustrated by the gas density profiles in the top panel of Figure 4.5, where developing a clear shock front is not instantaneous. In this case as well, the behavior of the binaries in the gas background differs from what is predicted by standalone SEBA binary evolution simulations. As mass transfer takes place over several time steps, the behavior of the binary after the onset of MT is influenced by the presence of the ejecta and its effects on the local gravitational potential. The region closest to the binary is dominated by the ejecta rather than the background medium; in this case, $\sim$38 $M_\odot$ of stellar material is injected within a radius $r \lesssim 0.2$ pc. This results

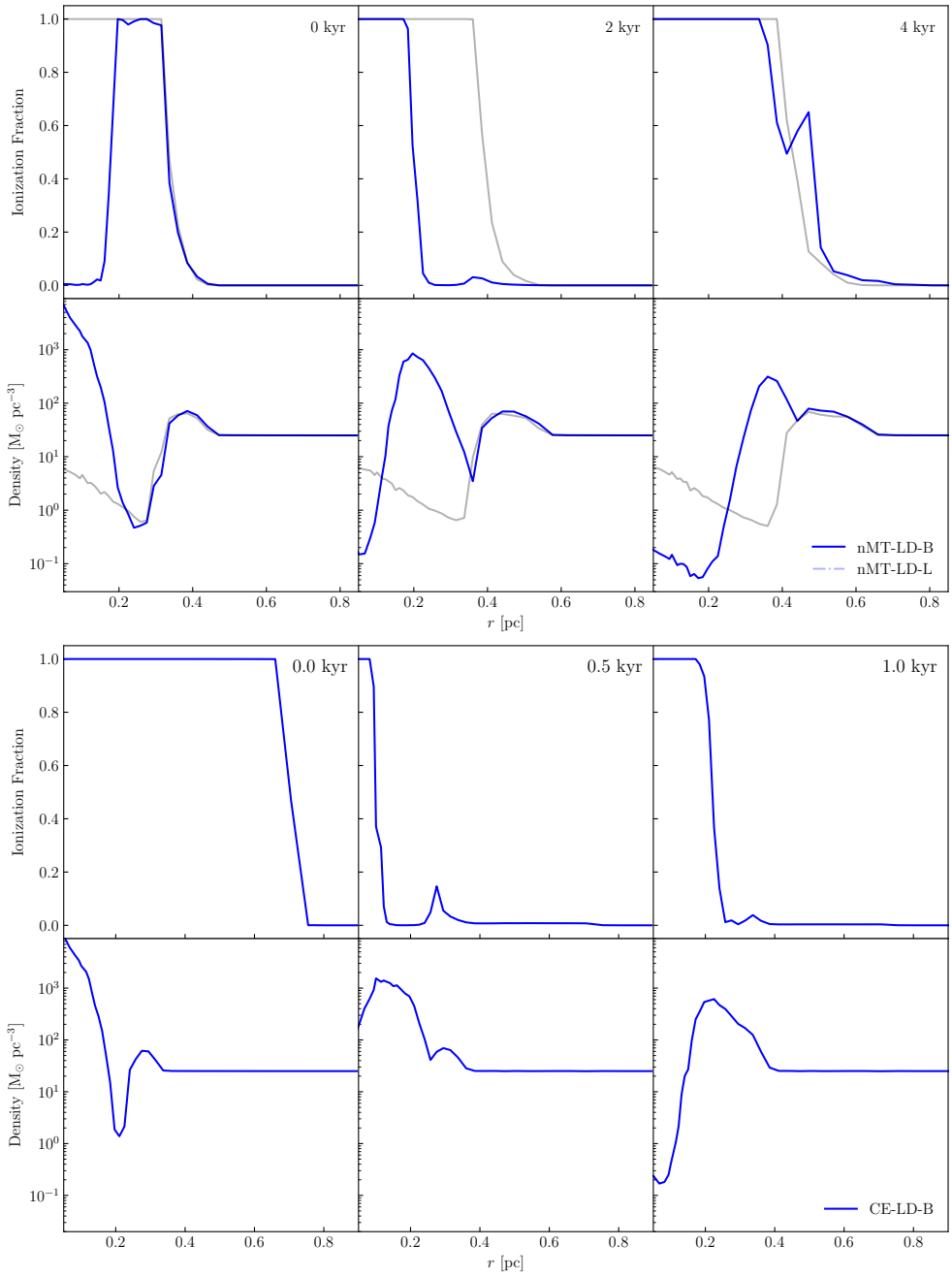

FIGURE 4.5: Ionization fraction (top row) and density (bottom row) as a function of radius for the non-conservative MT (top panel) and CE (bottom panel) simulations, at the same times as in Figure 4.4. Each radial bin is the mass-weighted average of the gas properties at this radial distance from the binary's center of mass. The solid blue line corresponds to the simulation with binary stellar evolution and the grey line (in the top panel) to the simulation with single star stellar evolution.

in differences in the semimajor axes and luminosities for the simulations with different background gas densities, as reported in Table 4.1. Those differences are however much smaller than the differences between the runs with binary stellar evolution and without binary stellar evolution.

4.3.4 Common envelope ejection

We also present test simulations of CE ejection. The binary consists of a 10 $M_\odot$ black hole orbiting a star of initially 148 $M_\odot$, with a semimajor axis of 5 au and an eccentricity of 0.4. The system has a small mass ratio M_2/M_1 at the time of RLOF, leading to CE ejection (Pavlovskii et al. 2017). We use $v_{\rm CE} = 1$ to calculate the ejecta velocity with Equation 4.7. Due to the instantaneous nature of CE ejection in our simulations, the background density does not influence the evolution of the system; we therefore only present one background density. The properties of the binary and the gas 1 kyr after the mass transfer event are also reported in Table 4.1.

4.3.4.1 Stellar and binary evolution

We evolve the primary for 3.285 Myr before placing it in the simulation. At the start of the simulation, the primary has a mass $M_1 = 69.41$ $M_\odot$ and is still on the MS. It evolves into a HG star just before the CE phase. The CE ejection removes almost 40 $M_\odot$ of material from the primary, circularizes the orbit, and decreases the semimajor axis to 0.22 au.

4.3.4.2 Gas properties

We present the density in the midplane immediately after the envelope is ejected, then in 0.5 kyr increments until 2.5 kyr in the right panel of Figure 4.4. The ejecta forms a thick shell around the star. The velocity of the ejecta is sufficient to clear out an ionized, low-density bubble around the star within 1 kyr. We plot the radial ionization fraction and density profiles in the bottom panel of Figure 4.5. Although the gas near the star is ionized at the time of CE ejection, the dense ejecta cool quickly, so that the gas close to the star is not fully ionized at early times. CE ejection also increases the gas density close to the star. The CE simulation nonetheless forms an H II region within 1 kyr. The calculated ejecta velocities for $v_{\rm CE} = 1$ are at most a few hundreds of km s^{-1}, which results in slower ejecta than fast O-star winds with feedback bubbles that retain the overall behavior of a normal H II region.

TABLE 4.2: Overview of the cluster simulations.

Name	BE	Stars	Σ ($M_\odot$ pc^{-2})	ΔM ($M_\odot$)	$L_{\rm FUV}$ ($L_\odot$)	$L_{\rm ion}$ ($L_\odot$)	$N_{\rm str}$	$N_{\rm acc}$	$N_{\rm a\downarrow}$	$N_{\rm a\uparrow}$	$r_{\rm ion}$ (pc)
(1)	(2)	(3)	(4)	(5)	(6)	(7)	(8)	(9)	(10)	(11)	(12)
C1-LD-B	✓	Set 1	10^2	297	1.19E6	2.88E6	7	0	6	2	9.69
C1-LD-S		Set 1	10^2	16.4	2.49E6	1.23E6	-	-	-	-	2.93
C1-HD-B	✓	Set 1	10^3	89.5	2.67E6	2.12E6	2	0	2	0	1.67
C1-HD-S		Set 1	10^3	16.4	2.49E6	1.23E6	-	-	-	-	1.42
C2-LD-B	✓	Set 2	10^2	172	2.71E6	1.01E7	12	8	1	9	6.40
C2-LD-S		Set 2	10^2	93.4	1.04E6	7.25E3	-	-	-	-	1.32
C2-HD-B	✓	Set 2	10^3	137	2.71E6	1.04E7	13	7	1	9	2.90
C2-HD-S		Set 2	10^3	93.4	1.04E6	7.25E3	-	-	-	-	0.76
C3-LD-B	✓	Set 3	10^2	149	3.45E6	1.19E7	10	10	1	9	9.23
C3-LD-S		Set 3	10^2	76.4	1.72E6	1.31E4	-	-	-	-	1.94
C3-HD-B	✓	Set 3	10^3	56.4	3.63E6	1.23E7	9	9	0	8	2.42
C3-HD-S		Set 3	10^3	76.4	1.73E6	1.31E4	-	-	-	-	1.13

Note. The quantities for columns (5) to (12) are calculated at the end of the simulation, after 50 kyr. Columns: (1) simulation name, (2) use of binary stellar evolution, (3) set of evolved stars, (4) initial gas surface density, (5) mass loss during the simulation, (6) cluster FUV luminosity, (7) cluster ionizing luminosity, (8) number of stripped stars, (9) number of stars rejuvenated by accretion, (10) number of binaries with semimajor axes decreased by mass transfer, (11) number of binaries with semimajor axes increased by mass transfer, (12) equivalent radius of the ionized region. All the stars are still in binaries at the end of the runs, in their original pairings.

4.4 Demonstration problem: Cluster of massive binaries

We present a suite of simulations of small groups of massive binaries, to showcase the simultaneous handling of stellar dynamics and stellar evolution. Each simulation contains 10 massive binaries (20 massive stars) and is run for 50 kyr. We present the initial conditions for the gas background medium and the stars (Section 4.4.1), the selection of the binaries (Section 4.4.2), and the evolution of the stars and binaries during the simulations (Section 4.4.3). The results from the cluster simulations are presented then discussed in Sections 4.4.4, 4.4.5 and 4.4.6.

4.4.1 Initial conditions

We select the positions and velocities of the binary centers of mass from the positions of the most massive stars in a recent cluster formation simulations (Cournoyer-Cloutier et al. 2024b). This cluster has a stellar mass of 2 x 10^5 $M_\odot$ and a binary fraction $> 90\%$ for massive stars. We use the center of mass information for ten massive systems clustered together near the cluster center. The masses of both stars in each binary are selected following the procedure outlined in Section 4.2.3. No other stars beyond those ten binaries are included in the simulations presented in this section. This results in a compact ($\lesssim$ 1 pc) configuration of 10 massive binaries. The high binding energies of the binaries ($> 10^{47}$ erg) and their initial slightly infalling velocities ensure that the group of binaries remains bound. Comparable or higher concentrations of massive binaries are observed in the Arches (Clark et al. 2023) and R136 (Sana et al. 2013) YMCs.

The binaries are placed in a uniform medium, within a box of size $L = 16$ pc. The background is turbulent, with an initial velocity dispersion of 5 km s^{-1}. The initial temperature is 100 K and there is no initial magnetic field. We use a refinement level of 4, which corresponds to a finest resolution of 0.125 pc. We use the same initial background gas surface densities of 10^2 and 10^3 $M_\odot$ pc^{-2} as for the isolated binaries.

4.4.2 Binary sampling

Fully sampling a population of binaries requires a stellar mass much higher than a population of single stars because the companion mass, semimajor axis, and eccentricity of a binary influence its evolution in addition to the primary mass. When accounting for the effects of mass transfer on a stellar population's radiation spectrum, stellar populations with masses up to $\sim 10^6$ $M_\odot$ are expected to exhibit significant sample-to-sample variations (Stanway & Eldridge 2023). Such stellar masses may only be achieved by the most massive YMCs in starburst galaxies (He et al. 2022; Levy et al. 2024), while YMCs in the Local Group have lower masses (see Portegies Zwart et al. 2010). To estimate the importance of feedback from massive binaries on local YMC formation, it is then crucial to include test cases that do not fully sample the parameter space of close massive binaries.

We run Torch simulations for three different stellar samplings, with two different background gas densities, with and without binary stellar evolution. We select the clusters for our simulation from the following procedure:

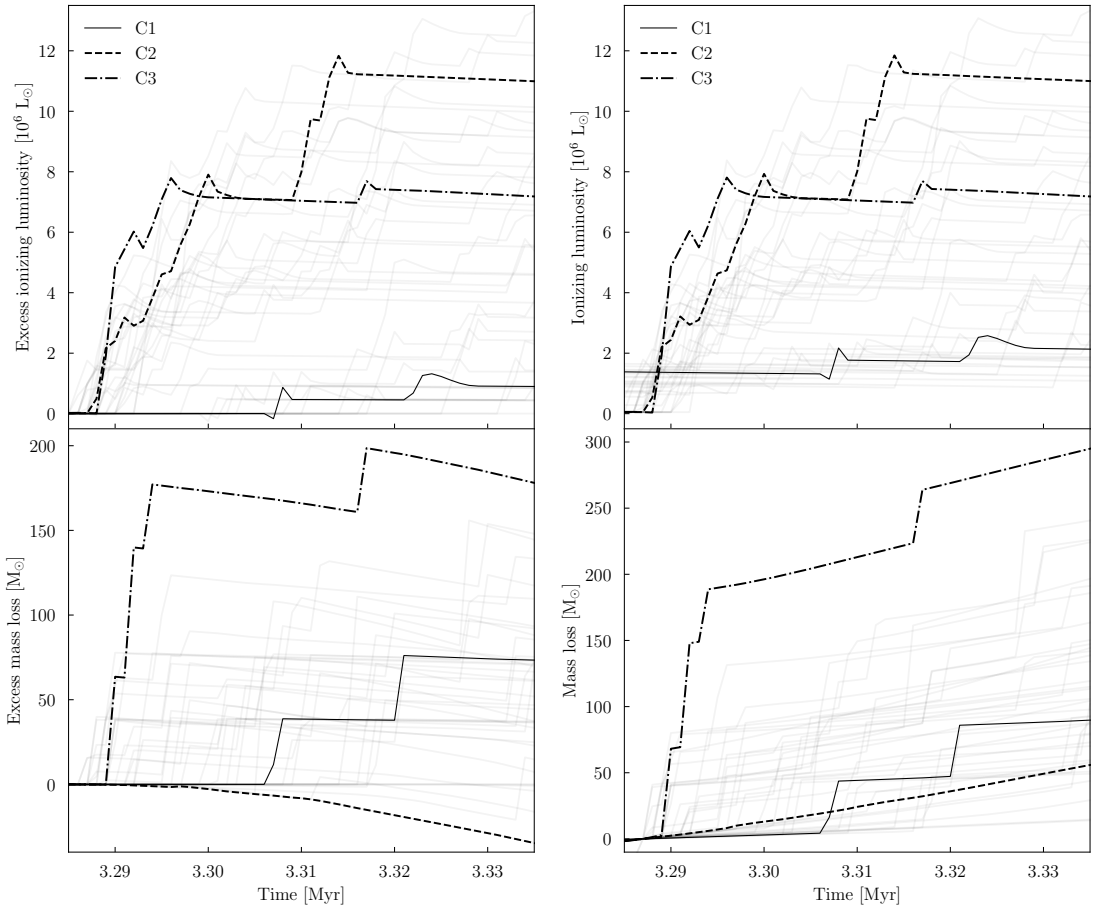

FIGURE 4.6: Excess (left) and true (right) ionizing luminosity (top) and cumulative mass loss (bottom) from the 40 sampled clusters run with SEBA's binary stellar evolution scheme. The excess is calculated compared to the same stars evolved with a single star stellar evolution scheme. The black solid, dashed, and dashed-dotted lines (labeled C1, C2, and C3) represent the three clusters we use for the full TORCH runs. They are chosen to span the range of ionizing luminosities and mass loss. The fainter lines represent the 37 other clusters for which we only run stellar evolution simulations.

1. We sample a Kroupa (2001) initial mass function (between 0.08 $M_\odot$ and 150 $M_\odot$) and the binary generation algorithm from Cournoyer-Cloutier et al. (2024b, based on observations compiled by Moe & Di Stefano 2017) a total of 40 times (ten times each for clusters of total stellar mass 4 x 10^4, 2 x 10^5, 1 x 10^6, and 5 x 10^6 $M_\odot$). The inclinations, eccentric anomalies, longitudes of the ascending node, and arguments of periapsis are sampled from uniform distributions.

2. For each sampled cluster, we keep the 10 most massive binaries, which dominate the pre-SN feedback budget and provide most of the total radiative feedback due to their very large ionizing luminosities (Eldridge & Stanway 2022). We use this set of 10 binaries to represent the clusters' main feedback sources. In the text below, *cluster* refers to this subset of simulated massive stars.

3. We simulate the 40 clusters in SeBa, with a single star stellar evolution scheme and a binary stellar evolution scheme.

4. For each cluster, we compare the mass loss (as a proxy for the strength of the wind feedback) and ionizing luminosity (for radiative feedback) in the SeBa runs with the two different stellar evolution schemes. We present the absolute values of the mass loss and the ionizing luminosity, and the difference in those values between the SeBa runs, in Figure 4.6.

5. We use this comparison to choose three clusters for our full Torch simulations. They are chosen to represent cases with large, medium, and small differences between the single stars and binaries models; the chosen clusters are shown as darker lines in Figure 4.6.

The simulated clusters are labelled C1, C2, and C3. Each cluster is simulated for the two gas background densities, and the two stellar evolution schemes. C1 is made up of the 10 most massive binaries from a 4 x 10^4 $M_\odot$ cluster. The binaries cover a fairly large of primary masses (59 – 138 $M_\odot$), semimajor axes (0.95 – 99 au), mass ratios (0.12 – 0.67) and eccentricities (0 – 0.84). C2 and C3 come from 5 x 10^6 $M_\odot$ clusters, which fully sample the distribution of binary parameters. They have primary masses $\gtrsim$ 120 $M_\odot$ and mass ratios close to unity, with semimajor axes $\lesssim$ 50 au for C2 and $\lesssim$ 15 au for C3. The clusters simulated with Torch are selected to encapsulate the full range of excess ionizing luminosity and excess mass loss. From the SeBa simulations, C2 shows the largest difference in the ionizing luminosity compared to single star stellar evolution, and C3 shows the largest difference in the mass loss.

4.4.3 Stellar and binary evolution

We evolve the binaries for 3.285 Myr in SeBa before starting the Torch simulations. All stars are on the MS at that time. We initialize all simulations with the same stellar positions and velocities. The binary center of mass positions and velocities are taken from cluster formation simulations, while the primary and companion relative positions and velocities are taken from the SeBa runs with binary evolution. We adopt $v_{\rm CE} = 1$ for

all our cluster runs. We report in Table 4.2 initial and final properties of the simulations. The simulation names use the LD/HD labels for low and high density background, and the B/S labels for binary stellar evolution and single star stellar evolution from the previous section. The first part of the label corresponds to the cluster sampling (C1, C2, or C3). In the following section, we will use the B, S, C1, C2, C3, LD and HD to refer to sets of runs with a shared property.

We report ΔM, the amount of mass lost by the stars during each simulation. For each set of runs, ΔM is different in the low and high density media for the B runs. ΔM also differs from the prediction from the SeBa run. This is due to the effects of gravitational dynamics from nearby stars and the background gas. In all the B runs except C3-HD-B, ΔM is larger than in the corresponding S run. This is in contrast with the prediction from pure stellar evolution, in which ΔM is predicted to be with smaller with binary stellar evolution for the C2 runs. This mass loss influences the FUV and ionizing luminosities of the clusters. For all clusters, accounting for binary stellar evolution strongly increases the ionizing luminosity: it does so by approximately three orders of magnitude for the C2 and C3 runs, and by a factor of $\sim$2 for the C1 runs. It also increases the FUV luminosity by a factor of ~ 2 for the C2 and C3 runs, increases it very slightly for C1-HD-B, and decreases it by a factor of ~ 2 for C1-LD-B.

We report in Table 4.2 the number of stars stripped (partly or fully) of their envelope via MT or wind self-stripping (following an earlier MT episode), and the number of stars that accreted material via conservative MT. We calculate those values by comparing the masses of each star in the B and S runs. All B simulations show large numbers of stars stripped of their envelopes, with on average almost half of all stars in the simulation losing their envelope. The number of stars that successfully accrete material varies more, ranging from 0 in C1-LD-B and C1-HD-B, to 10 in C3-HD-B. For the clusters that fully sample the distribution of binary orbital parameters (and that we can therefore treat as the proxies for the most massive YMCs), C2 and C3, almost every star has been affected by binary evolution. The orbits of the binaries are also affected by the MT process; for C2 and C3, most of the MT events are conservative, which results in a widening of the orbits once the donor becomes less massive than the accretor. This is not the case for C1 (in particular C1-LD-B), where the MT events are not conservative, and generally lead to a decrease in orbital separation.

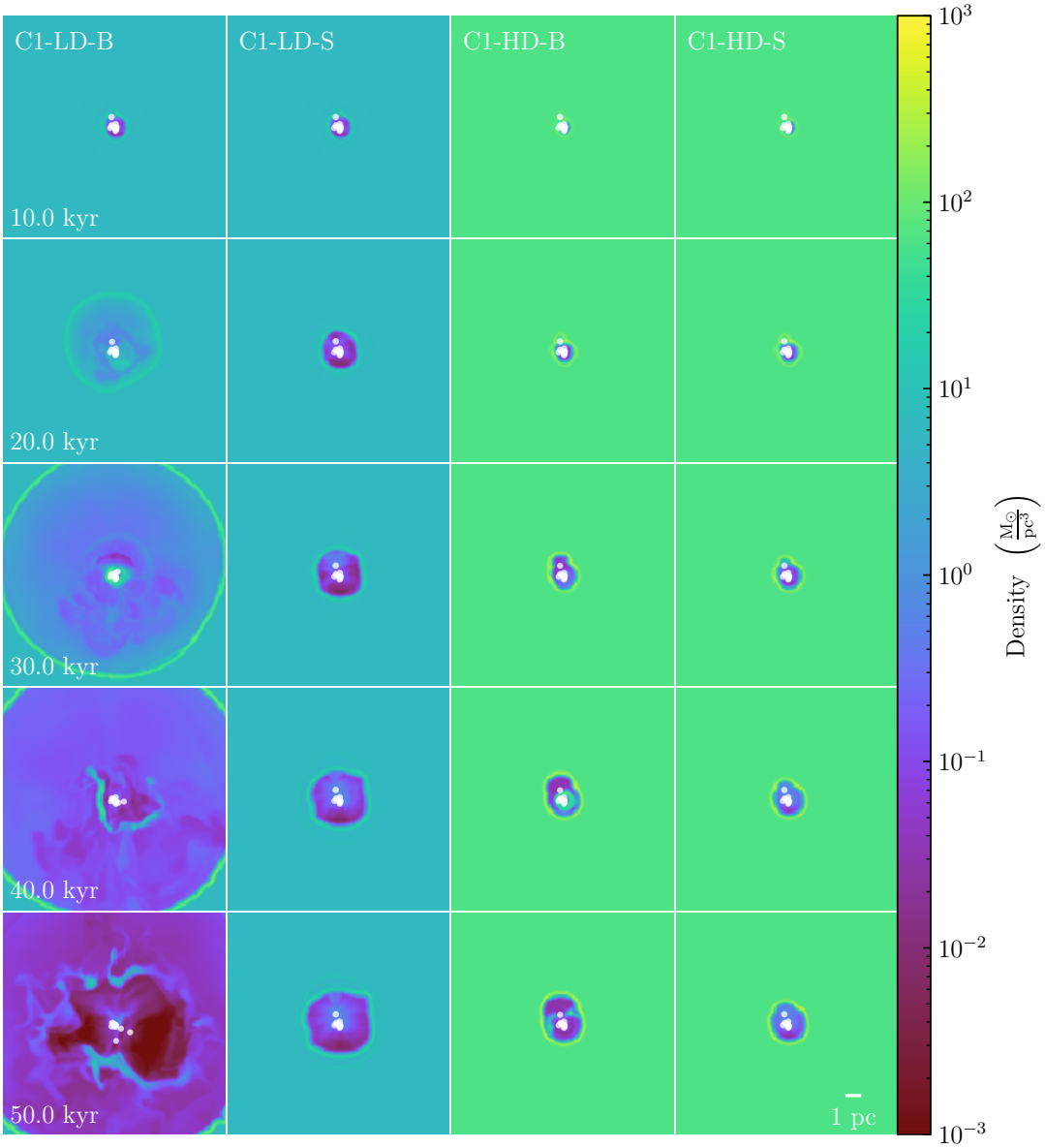

FIGURE 4.7: Time evolution of the density in the midplane for the C1 simulations, as a function of time. The B simulations shown in the first and third columns use binary stellar evolution while the S simulations shown in the second and fourth column use single star stellar evolution.

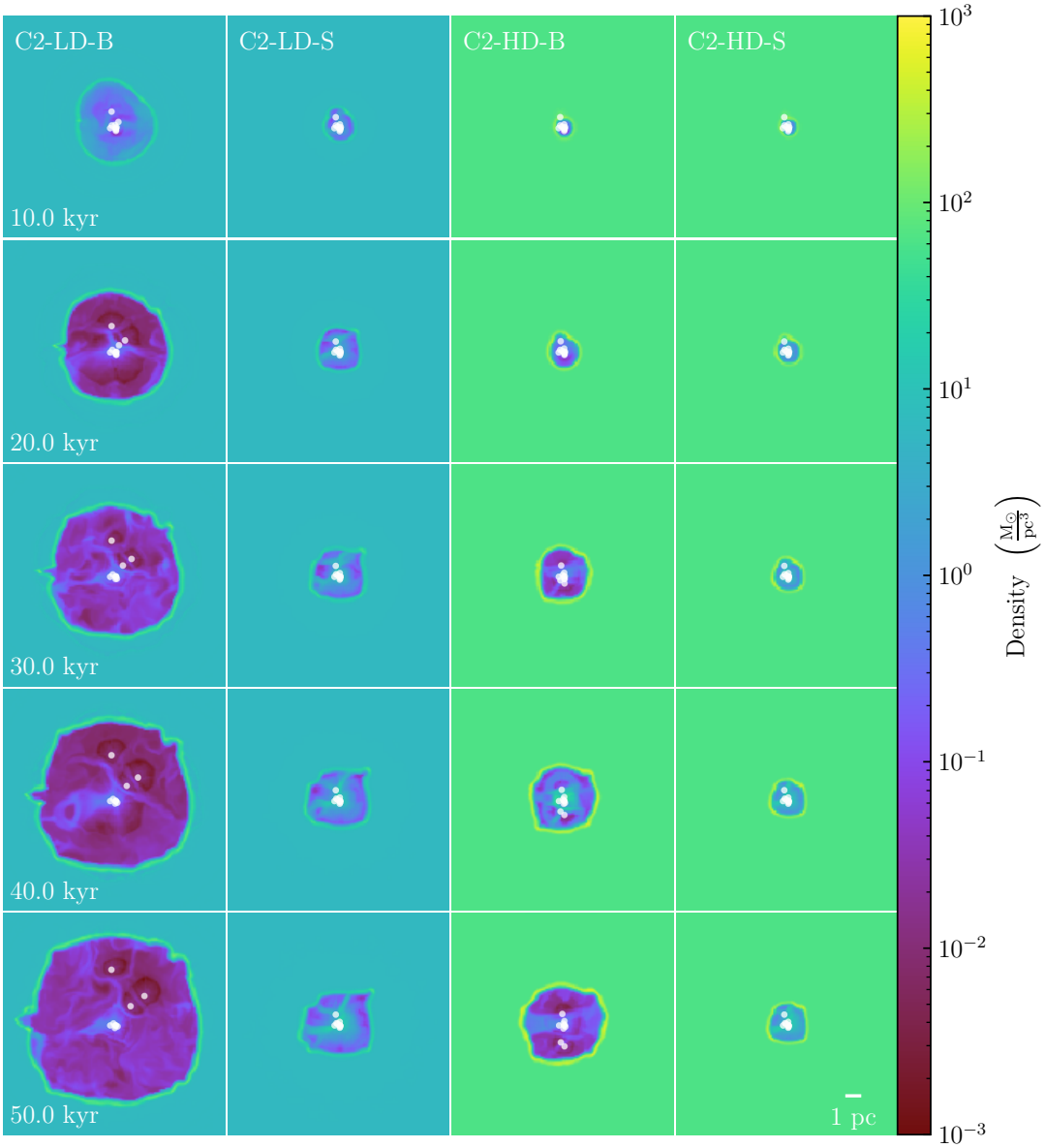

FIGURE 4.8: Same as Figure 4.7 for the C2 simulations.

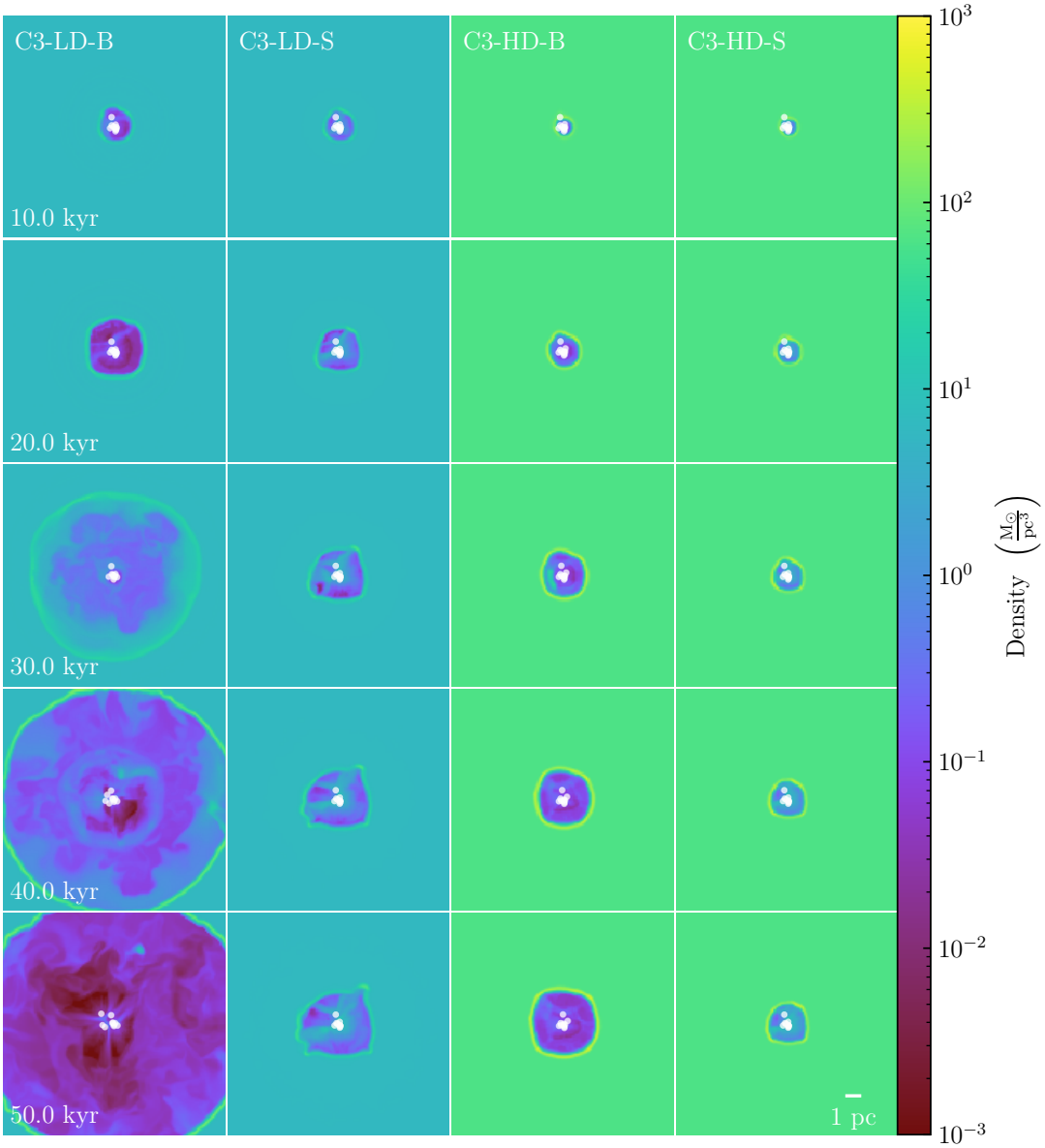

FIGURE 4.9: Same as Figure 4.7 for the C3 simulations.

4.4.4 Overview of Torch simulations

We present the density in the midplane every 10 kyr, for the C1, and C2, and C3 runs, in Figures 4.7, 4.8, and 4.9. Each row shows the four simulations initialized with the same stars, with the two background densities and the two different stellar feedback models. For each pair of simulations with the same stars and the same background gas density, the B simulation forms a larger feedback bubble than the corresponding S simulation. The density structure inside the feedback bubbles exhibits a high degree of asymmetry, due to the three-dimensional distribution of the stars. The density substructures in the feedback region are apparent in all runs.

In the C1 simulations, the differences between the B and S runs are obvious in the four later plots for the LD runs, and the three later plots for the HD runs. The feedback bubble in C1-LD-B is larger than in C1-LD-S, and exhibits more substructured dense gas from the binaries' episodic mass loss. The positions of the stars are also different which highlights the fact that the different stellar evolution schemes impact the stellar dynamics; we explore this in more detail in Section 4.4.5. The difference between the sizes of the feedback bubbles is greater in the lower density background medium, with the largest bubble forming in C1-LD-B. The difference in the H II region sizes is more modest for C1-HD-B and C1-HD-S, due to the low number of stars stripped of their envelope by interactions (see Table 4.2). The three-dimensional configuration of the stars contributes to shaping this feedback bubble. The massive binary above the cluster clears out its surroundings more quickly when binary stellar evolution is used, as illustrated by the 30 kyr snapshot for C1-HD-B and C1-HD-S. This is followed by significant mass loss from the stars below, resulting in the higher gas density around the clustered stars in the 40 kyr snapshot.

In the C2 simulations, the differences between the B and S simulations are already apparent in the first snapshot shown, after 10 kyr. The main cause of those differences is the rapid start of conservative MT, increasing the ionizing luminosity of the cluster and decreasing the gas density near the stars. In later snapshots, density substructures arise from the different modes of radiative and mechanical feedback coming from individual stars. The stars' positions and velocities differ between C2-LD-B and C2-HD-B, with three fast-moving binaries above the cluster in C2-LD-B and a pair of fast moving binaries in the bottom right quadrant in C2-HD-B. Mass transfer lowers the masses not just of the donor stars, but also of some accretors, post-MT. This results in 12/20 stars having lower masses (by $\gtrsim 20\%$) in C2-LD-B than in C2-LD-S, and 13/20 having lower masses in C2-HD-B than C2-HD-S.

In the C3 simulations, the size of the feedback bubble also increases with the use of binary stellar evolution, and decreases with increasing background gas density. In C3-LD-B, all ten primaries successfully transfer mass to their companions, increasing both the FUV and ionizing luminosity. C3-LD-B has lost approximately 75 $M_\odot$ in excess of C3-LD-S, in agreement with the prediction from the SeBa simulation without stellar dynamics. C3-HD-B and C3-HD-S are the only pair of simulations in which accounting for binary interactions results in a larger stellar mass by the end of the simulation, in contrast with the expectation from the SeBa simulation, which illustrates clearly that the presence of a background gravitational potential – from the gas and other stars – may change the outcome predicted by population synthesis studies.

A visual inspection of the gas density, temperature, ionization fraction and pressure in the simulations confirms the large impact of binary stellar evolution on the feedback from star clusters, as predicted by population synthesis studies. The stellar positions and velocities confirm that accounting for binary stellar evolution impacts the dynamics of massive binaries in clustered environments; binary evolution effects should be accounted for when studying the production of massive runaway stars. The gravity from the background gas also affects stellar dynamics, and therefore impacts individual binaries and their subsequent evolution.

4.4.5 Effects of stellar dynamics

The C1-LD-S and C1-HD-S runs develop small ($\lesssim 1\%$) differences in their semimajor axes, which arise from differences in the gas potential due to the different initial gas background densities and subsequent different effects of feedback on that gas. The similar differences in C1-LD-B and C1-HD-B are sufficient to affect the exact timing and stability of mass transfer: the first binary to undergo non-conservative MT does so almost 3 kyr earlier in C1-LD-B than C1-HD-B. Those runs diverge from this point on, leading to the smaller number of stripped stars in C1-HD-B and therefore the more modest increase in feedback bubble size compared to C1-HD-S. All stars are still in binaries after 50 kyr in all C1 runs, but the properties of those binaries have been affected by mass transfer. In C1-LD-B, six systems have shown significant decrease in the semimajor axis following MT, while two systems have seen their semimajor axes increase. In C1-HD-B, only two binaries see their semimajor axes decrease.

Mass transfer starts at the same time in C2-LD-B and C2-HD-B, and two systems undergo MT within 3 kyr in each simulation. Subsequent MT occurs in C2-LD-B before

C2-HD-B, however. In both simulations, mass transfer widens the orbit of the binary in nine cases out of ten.

In C3-LD-B and C3-HD-B, MT begins within 2 kyr for the two most massive systems. The first difference between C3-LD-B and C3-HD-B arises following a mass transfer episode $\sim$ 25 kyr after the start of the simulation, when MT widens the orbit in C3-HD-B but tightens it in C3-LD-B. The two runs diverge beyond that point. The post-MT stellar masses are systematically higher in C3-HD-B than C3-LD-B and most of the semimajor axes (8/9 for mass transfer) are smaller in C3-HD-B than C3-LD-B.

The cluster simulations all display behavior that diverges from the expectation for population synthesis studies due to the effects of the nearby gas and stars. This can be seen by comparing the ΔM and luminosity values reported in Table 4.2 to the values from standalone stellar evolution presented in Figure 4.6, and by comparing the ΔM and luminosity values for the pairs of LD and HD runs. Although the binaries remain bound and remain in their original pairings in all simulations, the contributions of other stars and the background gas to the gravitational potential cause the LD and HD runs to diverge not only in their gas properties – as expected from the different background densities – but also in their stellar properties. This is most striking for C1, where the ΔM is larger by a factor of $\sim$ 3.3, the ionizing luminosity is larger by a factor of $\sim$ 1.4, and the FUV luminosity is smaller by a factor of $\sim$ 2.2 in C1-LD-B compared to C1-HD-B. This is caused by the different number of stripped stars and accretors, which is in turn driven by differences in the semimajor axes of the widest binaries in the simulations. The differences in luminosities are smaller but still present for C2 and C3, which show important differences in ΔM. This illustrates the need to model stellar dynamics, hydrodynamics, stellar evolution and stellar feedback in concert.

Another interesting feature is the presence of fast-moving binaries in C1-LD-B (just below and to the right of the cluster), C2-HD-B (below the cluster) and most obviously in C2-LD-B (above the cluster). None of the S runs show this behavior, and runs with the same initial stars but different background densities do not result in the same (or similar) stellar positions and velocities. Although it is not possible to fully disentangle the effects of the background gas from the effects of stellar dynamics (since the first MT event results immediately in changes to both the orbital properties and the properties of the nearby gas), this behavior illustrates clearly that the gravitational potential in which the binaries reside – shaped by both nearby stars and the background gas – affects the binaries' evolution.

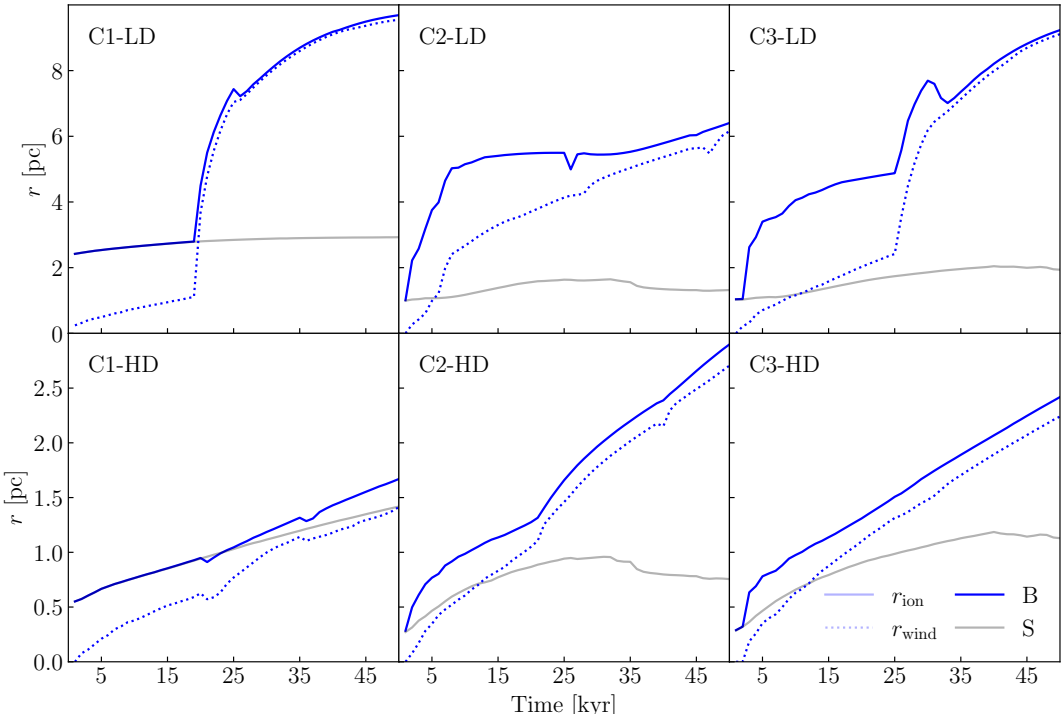

FIGURE 4.10: Equivalent radius of the ionized region and shocked wind region (for the B runs) as a function of time, for the cluster runs in the lower (top) and higher (bottom) density medium. The runs with binary stellar evolution are plotted in blue while the runs with single star stellar evolution are shown in grey; the solid lines denote the ionized region and the dotted lines denote the shocked wind region. Dense ejecta from non-conservative mass transfer episodes cause the non-monotonic behavior.

4.4.6 Expansion of H II regions

In addition to the qualitative description of the gas behavior presented in Section 4.4.4, we investigate the physical properties of the gas and use them to probe the physical mechanisms driving the expansion of the feedback bubbles in the simulations.

4.4.6.1 Size of H II regions

We calculate the equivalent radius of the H II region from Equation 4.8. For the wind bubble, we follow a similar procedure with the volume of gas with temperature above 10^6 K, which corresponds to the shocked wind (Lancaster et al. 2021a). This temperature cut also traces well the gas with velocity above 200 km s^{-1}, separating the ejecta from the

background medium. We only calculate the wind radius bubble for the simulations with binary stellar evolution, as the simulations with single star stellar evolution do not form a clear wind bubble with shocked wind, due to the low velocities of the bloated evolved stars' winds. The sizes of the H II regions after 50 kyr are summarized in Table 4.2, and plotted as a function of time in Figure 4.10 (along with the sizes of the wind bubbles for the B runs). The radii for C1-LD-B and C3-LD-B, in which the low-density feedback bubbles reach the edges of the simulation domain, are lower limits.

All simulations show very clear differences between the B and S runs, with larger H II regions in the B runs. The smallest difference is for C1-HD-B, in which only two systems undergo mass transfer. For C1, the H II region radii are equal for the pairs of B and S runs until the onset of non-conservative MT in the first system, after approximately 20 kyr. The radius of the H II region then increases smoothly due to the increased ionizing radiation from the stripped primary. The non-monotonic behavior of the H II region and wind radius for C1-HD-B, and of the H II region for C1-LD-B, are caused by the presence of ejecta from non-conservative MT, which are colder than the bubble interior and therefore decrease the volume of hot ionized gas.

The C2 runs diverge very quickly, following the first MT episode. In the high density medium, C2-HD-B exhibits the largest difference with the single star stellar evolution model, in which the gas successfully recombines as the stars cool and move off the MS, leading to a decrease in the ionized volume at late times. Two episodes of non-conservative MT (around 20 and 40 kyr) lead to the two small bumps in the radii for C1-HD-B.

C3-HD-B follows the smoothest evolution: after the initial MT episode, very early in the simulation, both measures of the size of the feedback bubble keep increasing, reaching values about twice that of the H II region radius for C3-HD-S after 50 kyr. C3-LD-B shows the most obvious non-monotonic behavior in the expansion of its H II region. Non-conservative MT just before 30 kyr results in an increase in the gas density near the stars which is apparent from the 2nd and 3rd rows of Figure 4.9.

4.4.6.2 Energetics of H II regions

We investigate the energetics of the gas in the simulations, by comparing the kinetic, thermal and gravitational potential of the gas. We calculate the total kinetic energy K of the gas as

$$K = \frac{1}{2} \sum_i m_i |v_i|^2 \tag{4.9}$$

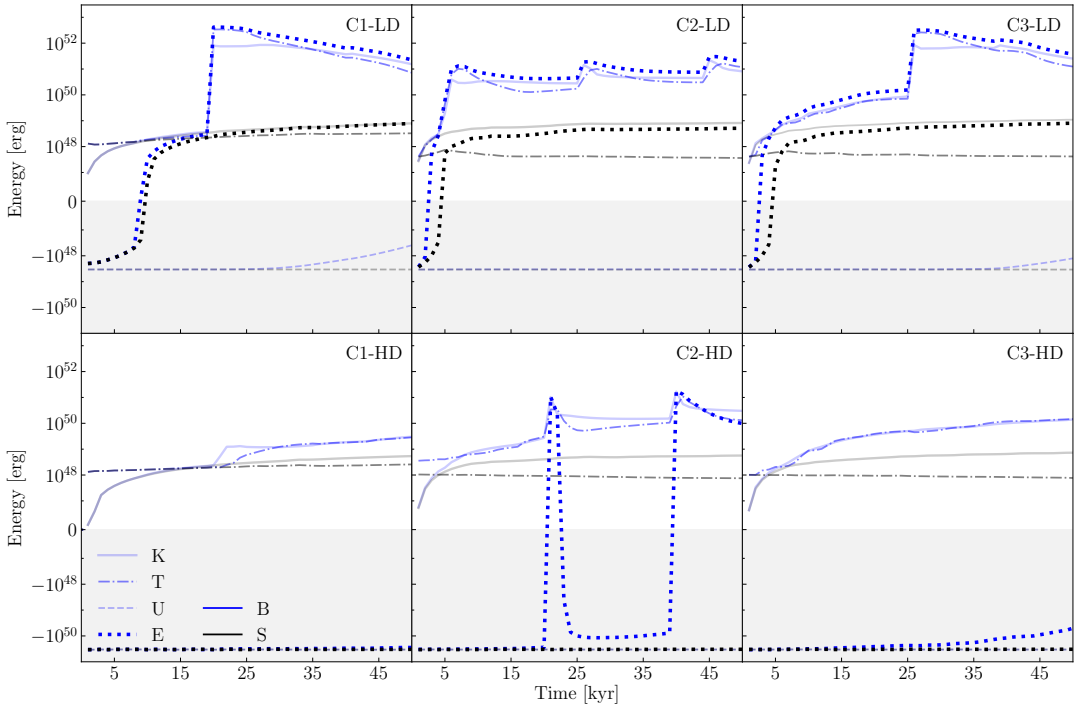

FIGURE 4.11: Energetics of the gas in the cluster simulations, as a function of time. Each sub-plot corresponds to a pair of simulations with the same stars and background density (labeled in the top right), with the blue lines corresponding to the runs with binary stellar evolution and the black lines corresponding to the runs with single star stellar evolution. The solid line represents the kinetic energy, the dashed-dotted line represents the thermal energy, the dashed line represents the potential energy and the dotted line represents the total energy. The symlog scale is linear between -10^{47} and 10^{47} ergs. The grey shaded region highlights where the energy is < 0 ergs, i.e. where the gas is globally bound. In all pairs of simulations, the energy is larger with binary stellar evolution.

where m_i and v_i are the gas mass and velocity in each FLASH cell. We calculate the total thermal energy T as

$$T = \sum_i \frac{k_{\rm B} m_i T_i}{\mu_i m_{\rm H} (\gamma - 1)} = \frac{3 k_{\rm B}}{2 m_{\rm H}} \sum_i \frac{m_i T_i}{\mu_i} \tag{4.10}$$

where $k_{\rm B}$ is the Boltzmann constant, $m_{\rm H}$ is the mass of an hydrogen atom. We use an adiabatic index $\gamma = 5/3$ and calculate the mean molecular weight μ_i for each cell from the ionization fraction. We use $\mu = 0.6$ for fully ionized gas and $\mu = 1.3$ for neutral gas,

corresponding to gas with solar metallicity. T_i and m_i are the temperature and gas mass in each cell. We calculate the gravitational potential energy of the gas U from

$$U = \frac{1}{2} \sum_i \Phi_i m_i \tag{4.11}$$

where Φ_i and m_i are the gravitational potential and gas mass in each cell. We also calculate the total energy

$$E = K + T - U \tag{4.12}$$

and each component of the energy as a function of time, and plot them in Figure 4.11. In all pairs of simulations, the total energy of the gas is higher when accounting for the effects of binary evolution; the smallest difference is found between C1-HD-B and C1-HD-S, where the kinetic and thermal energies are about one order of magnitude larger in C1-LD-B than in C1-LD-S, but the total energy remains dominated by the potential energy. The evolution of C3-HD-B and C3-HD-S is similar: by the end of the simulation, the total energy is about one order of magnitude less negative in C3-HD-B than C3-HD-S. The largest difference for the HD runs is for C2: accounting for binary stellar evolution successfully unbinds the gas in C2-HD-B while it remains bound in C2-HD-S. The differences in total energy are large ($\gtrsim$ 2 orders of magnitude) in all the LD runs.

4.4.6.3 Sources of pressure in H II regions

We investigate the time evolution of the pressure within the H II region surrounding the cluster, to understand what feedback mechanism dominates the evolution of the H II region. We evaluate different components of the pressure, following the approach taken in observations of H II regions (e.g. Lopez et al. 2014; Barnes et al. 2020, 2021). We obtain the thermal pressure $P_{\rm therm}$ from

$$P_{\rm therm} = \frac{2\rho T}{\mu m_{\rm H}} \tag{4.13}$$

where ρ is the gas density, T the gas temperature, and μ the mean molecular weight. We take the volume average for the ionized gas volume identified in Section 4.4.6.1; as the gas is fully ionized, we adopt $\mu = 0.6$. We also calculate the volume-averaged radiation pressure $P_{\rm rad}$ from

$$P_{\rm rad} = \frac{3L}{4\pi r_{\rm ion}^2 c k_{\rm B}} \tag{4.14}$$

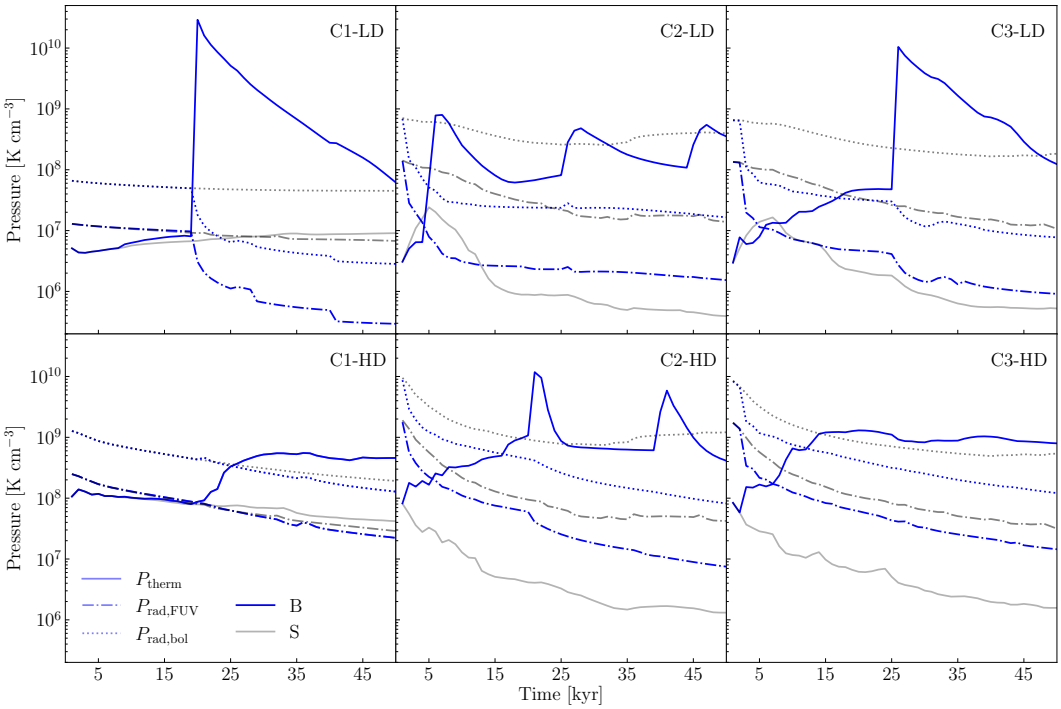

FIGURE 4.12: Pressure from radiative feedback as a function of time for the cluster runs. Each column corresponds to a set of stars and each row to a background density. The solid lines denote the thermal pressure from ionized gas (from Equation 4.13), the dashed-dotted lines denote the direct radiation pressure from FUV radiation (from Equation 4.14), and the dotted lines denote the direct radiation pressure calculated from the bolometric luminosity. The very rapid increases in thermal pressure match the timing of mass transfer events, which change the ionizing radiation budget of the cluster on short timescales.

where L is the luminosity of the stars. We calculate the radiation pressure both using the bolometric luminosity (as done in observations) and using only the FUV band (5.6-13.6 eV), as the gas in our simulations is only affected by FUV radiation pressure. We plot those three measures of the pressure in Figure 4.12.

For each pair of simulations, the pressure is higher in the simulation with binary stellar evolution due to the enhanced thermal pressure. This is well in line with the energy analysis presented above, with large increases in gas thermal and kinetic energy due to binary evolution, and significant increases in the volume of hot ionized gas. A

striking example is C1-LD-B, in which the thermal pressure reaches a value almost four orders of magnitude higher than that in C1-LD-S following the onset of mass transfer. Another key difference between the B and S simulations is the presence of several spikes in the time-evolution plot of the thermal pressure. Those maxima are associated with the very high instantaneous mass loss rate from mass transfer events. The first such peak in C1-LD-B and C3-LD-B, after $\sim$ 20 kyr, matches the rapid increase in H II region radius (Figure 4.10) and in kinetic and thermal energy (Figure 4.11).

Radiation pressure (evaluated from the FUV or bolometric luminosity) is lower in the B runs than the S runs: although the amount of FUV radiation is higher in the B runs than the corresponding S runs (except C1-LD), the inverse square dependence on the radius of the H II region (which increases due to the increased thermal pressure) dominates, resulting in a decrease in the pressure. In contrast with the B runs, the expansion of the H II regions in the S runs is driven by radiation pressure rather than thermal pressure. The only potential exception is C1-HD-S, in which the FUV radiation pressure is slightly lower than the thermal pressure (but the bolometric radiation pressure is about one order of magnitude higher).

4.5 Summary & Discussion

In this paper, we have presented the first implementation of mechanical and radiative feedback from massive interacting binaries for star formation simulations. We have implemented this new feedback module in the cluster formation code Torch, which includes a treatment of magnetohydrodynamics, collisional stellar dynamics, star and binary formation, and stellar feedback. Our new feedback model accounts for the effects of conservative and non-conservative mass transfer (including common envelope ejection) on the mass loss rates, FUV luminosity, and ionizing luminosity of binary interaction products; those changes self-consistently result in changes to the timing of core-collapse SNe. Our feedback module injects the mass lost via non-conservative mass transfer and common envelope ejection in the simulation as a source of mechanical feedback. Our new model also accounts for the gravitational effects of other stars and gas on the binaries, allowing their orbits to be modified both by binary stellar evolution and gravitational dynamics.

We have tested our new feedback implementation on isolated binaries undergoing conservative and non-conservative mass transfer, as well as common envelope ejection, in Section 4.3. We have futher presented a suite of simulations of clusters of massive

binaries in a turbulent medium, allowing us to demonstrate the effects of the coupling between stellar dynamics and binary stellar evolution. Our key results are as follows:

1. As predicted by isolated binary stellar evolution models, accounting for mass transfer increases the ionizing luminosity and the mass loss rate of populations of massive binaries.

2. Feedback from interacting binaries efficiently couples with the surrounding gas and strongly impacts the nearby ISM.

3. Accounting for the effects of binary stellar evolution on stellar feedback increases the size of the H II regions, increases the kinetic and thermal energy of the surrounding gas, and increases the pressure within the H II regions.

4. The expansion of the H II regions is driven by thermal pressure (rather than radiation pressure) in the presence of interacting binaries.

5. Stellar dynamics and the gravitational potential of the background gas affect binary stellar evolution by causing changes to the orbits of the binaries. Those changes can affect the timing and efficiency of mass transfer, and therefore the cluster's feedback budget and the evolution of its associated H II region.

6. Binary stellar evolution also affects stellar dynamics: accounting for the effects of binary stellar evolution may promote few-body interactions and the ejection of massive stars from their birth environments.

A consistent result across our different simulations – regardless of the background gas density and the initial stellar sampling – is that accounting for binary stellar evolution increases the strength of the radiative and mechanical feedback. We conclude that feedback from massive interacting binaries is important to the feedback budget of YMCs of all masses, from the $\gtrsim 10^4$ $M_\odot$ YMCs observed in the Milky Way (Portegies Zwart et al. 2010) to the $\gtrsim 10^6$ $M_\odot$ YMCs observed in starburst galaxies (e.g. He et al. 2022; Levy et al. 2024). This additional source of pre-SN feedback may prove crucial in understanding the timescales over which YMCs emerge from their birth environment and stop forming stars. Although the simulations presented here are a demonstration that feedback from massive interacting binaries has a strong impact on the ISM, they represent an idealized situation. The effects from more realistic cluster environments may further enhance the impact of feedback from massive interacting binaries.

The simulations were set up to allow Case B MT. MS O-star binaries with orbital periods $\lesssim$ 1000 days (which represent $\sim$50% of O stars, Moe & Di Stefano 2017) can undergo Case A MT if their orbit is sufficiently eccentric. As repeated few-body encounters tend to increase eccentricity (Heggie & Rasio 1996), many O stars will undergo Case A MT in dense cluster environments. Using a combination of observations and simulations, Schneider et al. (2014) predict that the first mass transfer event should take place within $\sim$ 2.5 Myr for 10^4 $M_\odot$ YMCs, and within $\sim$ 1 Myr for 10^5 $M_\odot$ YMCs. The efficiency of feedback from massive interacting binaries in disrupting the gas may also be enhanced by the previous effects of feedback from non-interacting O stars during the earliest stages of cluster formation, which lowers the gas density in the central regions.

Another potentially important contribution of massive interacting binaries to the feedback budget of galaxies is through the enhanced production of runaway stars. The increased cross-section of the post-interaction systems increase the likelihood that they would undergo few-body interactions ejecting them from the cluster, as has been the case for the fast-moving ($>$ 30 km s^{-1}) binaries in C1-LD-B, C2-LD-B, and C2-HD-B. We expect such ejected binaries to be ubiquitous in massive, dense clusters, in which few-body encounters are frequent. Observations of the rotational velocities of runaway stars around R136 (Sana et al. 2022) suggest that a significant fraction of runaways around YMCs are binary interaction products. It is crucial to study concurrently runaway star production and binary interactions in cluster formation models.

Using the new framework presented in this paper in full simulations of star cluster formation is the next logical step. In the meantime, however, simulations that cannot directly include those effects – due to a lack of (primordial) close binaries or to a stellar evolution scheme that does not include binary evolution – should still account for the increased feedback budget due to massive interacting binaries. As the expansion of the H II regions in the runs with binary stellar evolution is driven by the thermal pressure arising from the enhanced ionizing radiation, a simple approach is to mimic the effects of non-conservative mass transfer by instantaneously injecting the mass associated with post-MS mass loss as soon as a star leaves the MS, for half of the O stars. Those stripped stars can be evolved as hot Wolf-Rayet stars for the duration of their post-MS lifetimes, increasing the amount of ionizing radiation emitted by the stellar population.

This first study of massive interacting binaries as a source of radiative and mechanical feedback in cluster-forming regions shows that stellar dynamics, hydrodynamics, and stellar evolution are inter-connected. Our results clearly demonstrate that binary stellar evolution has a strong effect on a cluster's feedback budget and may play an important

role in setting the timescale for gas removal in cluster-forming regions. In future studies of star cluster formation, feedback from massive interacting binaries should be considered along with feedback from single stars, hydrodynamics, and collisional stellar dynamics.

Acknowledgements

C.C.-C. is grateful for the hospitality of the Max Planck Institute for Astrophysics, where this work was started during an extended visit in 2023. C.C.-C. warmly thanks Thorsten Naab for his hospitality during this visit and numerous discussions about stellar feedback and numerical methods. C.C-C. is also grateful to Stephen Justham for several discussions about binary stellar evolution.

C.C.-C. is supported by a Canada Graduate Scholarship (CGS) – Doctoral from Natural Science and Engineering Research Council of Canada (NSERC). C.C.-C. also acknowledges funding from a CGS – Michael Smith Foreign Studies Supplement from NSERC which supported the visit to MPA. A.S. and W.E.H. are supported by NSERC. E.A. acknowledges support from the NASA Astrophysics Theory Program grant 80NSSC-24K0935. S.M.A. is supported by a National Science Foundation Astronomy & Astrophysics Postdoctoral Fellowship under Award No. 2401740. M.-M.M.L. and B.P. acknowledge funding from NSF grant AST23-07950. S.T. acknowledges support from the Netherlands Research Council NWO (VIDI 203.061 grant).

The code development for this project was done in part on the HPC system Freya at the Max Planck Computing and Data Facility. This research was enabled in part by support provided by Scinet (`https://scinethpc.ca/`), Compute Ontario (`https://www.computeontario.ca/`) and the Digital Research Alliance of Canada (`alliancecan.ca`) via the research allocation FT #2665: The Formation of Star Clusters in a Galactic Context. This work used Stampede3 at TACC through allocation PHY240335 from the Advanced Cyberinfrastructure Coordination Ecosystem: Services & Support (ACCESS) program, which is supported by U.S. National Science Foundation grants #2138259, #2138286, #2138307, #2137603, and #2138296.

Software: AMUSE (Portegies Zwart et al. 2009; Pelupessy et al. 2013; Portegies Zwart et al. 2013; Portegies Zwart & McMillan 2019; Portegies Zwart et al. 2023), FLASH (Fryxell et al. 2000; Dubey et al. 2014), `matplotlib` (Hunter 2007), `numpy` (Harris et al. 2020), `scikit-learn` (Pedregosa et al. 2011), TORCH (Wall et al. 2019, 2020), and `yt` (Turk et al. 2011).

Bibliography

Adamo A., et al., 2024, Nature, 632, 513

Almeida L. A., et al., 2017, A&A, 598, A84

Antoniadis J., et al., 2022, A&A, 657, L6

Baczynski C., Glover S. C. O., Klessen R. S., 2015, MNRAS, 454, 380

Barnes J., Hut P., 1986, Nature, 324, 446

Barnes A. T., Longmore S. N., Dale J. E., Krumholz M. R., Kruijssen J. M. D., Bigiel F., 2020, MNRAS, 498, 4906

Barnes A. T., et al., 2021, MNRAS, 508, 5362

Belczynski K., Bulik T., Fryer C. L., Ruiter A., Valsecchi F., Vink J. S., Hurley J. R., 2010, ApJ, 714, 1217

Bestenlehner J. M., 2020, MNRAS, 493, 3938

Bestenlehner J. M., et al., 2014, A&A, 570, A38

Björklund R., Sundqvist J. O., Puls J., Najarro F., 2021, A&A, 648, A36

Brands S. A., et al., 2022, A&A, 663, A36

Chatterjee S., Fregeau J. M., Umbreit S., Rasio F. A., 2010, ApJ, 719, 915

Chevance M., et al., 2022, MNRAS, 509, 272

Clark J. S., Lohr M. E., Najarro F., Patrick L. R., Ritchie B. W., 2023, MNRAS, 521, 4473

Cournoyer-Cloutier C., et al., 2021, MNRAS, 501, 4464

Cournoyer-Cloutier C., et al., 2023, MNRAS, 521, 1338

Cournoyer-Cloutier C., Karam J., Sills A., Zwart S. P., Wilhelm M. J. C., 2024a, ApJ, 975, 207

Cournoyer-Cloutier C., et al., 2024b, ApJ, 977, 203

Deshmukh S., et al., 2024, ApJ, 974, L24

Dubey A., et al., 2014, The International Journal of High Performance Computing Applications, 28, 225

Eggleton P. P., 1983, ApJ, 268, 368

Eldridge J. J., Stanway E. R., 2022, ARA&A, 60, 455

Farmer R., Laplace E., Ma J.-z., de Mink S. E., Justham S., 2023, ApJ, 948, 111

Federrath C., Banerjee R., Clark P. C., Klessen R. S., 2010, ApJ, 713, 269

Fragos T., et al., 2023, ApJS, 264, 45

Fryer C. L., Belczynski K., Wiktorowicz G., Dominik M., Kalogera V., Holz D. E., 2012, ApJ, 749, 91

Fryxell B., et al., 2000, ApJS, 131, 273

Fujii M., Iwasawa M., Funato Y., Makino J., 2007, PASJ, 59, 1095

Fujii M. S., Saitoh T. R., Portegies Zwart S. F., 2012, ApJ, 753, 85

Fujii M. S., Saitoh T. R., Hirai Y., Wang L., 2021, PASJ, 73, 1074

Geen S., Bieri R., Rosdahl J., de Koter A., 2021, MNRAS, 501, 1352

Götberg Y., de Mink S. E., Groh J. H., Kupfer T., Crowther P. A., Zapartas E., Renzo M., 2018, A&A, 615, A78

Götberg Y., de Mink S. E., McQuinn M., Zapartas E., Groh J. H., Norman C., 2020, A&A, 634, A134

Hannon S., et al., 2022, MNRAS, 512, 1294

Harris C. R., et al., 2020, Nature, 585, 357

He H., Wilson C., Brunetti N., Finn M., Bemis A., Johnson K., 2022, ApJ, 928, 57

Heggie D. C., 1975, MNRAS, 173, 729

Heggie D. C., Rasio F. A., 1996, MNRAS, 282, 1064

Heitsch F., Mac Low M.-M., Klessen R. S., 2001, ApJ, 547, 280

Hills J. G., 1975, AJ, 80, 809

Hollenbach D., McKee C. F., 1989, ApJ, 342, 306

Howard C. S., Pudritz R. E., Harris W. E., 2017, MNRAS, 470, 3346

Hunter J. D., 2007, Computing in Science & Engineering, 9, 90

Hurley J. R., Pols O. R., Tout C. A., 2000, MNRAS, 315, 543

Hurley J. R., Tout C. A., Pols O. R., 2002, MNRAS, 329, 897

Hypki A., Giersz M., 2013, MNRAS, 429, 1221

Iaconi R., De Marco O., 2019, MNRAS, 490, 2550

Ivanova N., 2018, ApJ, 858, L24

Ivanova N., Justham S., Avendano Nandez J. L., Lombardi J. C., 2013, Science, 339, 433

Ivanova N., Justham S., Podsiadlowski P., 2015, MNRAS, 447, 2181

Iwasawa M., Tanikawa A., Hosono N., Nitadori K., Muranushi T., Makino J., 2016, PASJ, 68, 54

Joung M. K. R., Mac Low M.-M., 2006, ApJ, 653, 1266

Kippenhahn R., Weigert A., 1967, Z. Astrophys., 65, 251

Körtgen B., Seifried D., Banerjee R., Vázquez-Semadeni E., Zamora-Avilés M., 2016, MNRAS, 459, 3460

Kroupa P., 2001, MNRAS, 322, 231

Krumholz M. R., McKee C. F., Bland-Hawthorn J., 2019, ARA&A, 57, 227

Kudritzki R.-P., Puls J., 2000, ARA&A, 38, 613

Lahén N., Rantala A., Naab T., Partmann C., Johansson P. H., Hislop J. M., 2025, MNRAS, 538, 2129

Lancaster L., Ostriker E. C., Kim J.-G., Kim C.-G., 2021a, ApJ, 914, 90

Lancaster L., Ostriker E. C., Kim J.-G., Kim C.-G., 2021b, ApJ, 922, L3

Lancaster L., Ostriker E. C., Kim C.-G., Kim J.-G., Bryan G. L., 2024, ApJ, 970, 18

Lanz T., Hubeny I., 2003, ApJS, 146, 417

Laplace E., Schneider F. R. N., Podsiadlowski P., 2025, A&A, 695, A71

Lau M. Y. M., Hirai R., González-Bolívar M., Price D. J., De Marco O., Mandel I., 2022, MNRAS, 512, 5462

Lauterborn D., 1970, A&A, 7, 150

Lechien T., de Mink S. E., Valli R., Rubio A. C., van Son L. A. C., Klement R., Jin H., Pols O., 2025, arXiv:2505.14780

Leroy A. K., et al., 2018, ApJ, 869, 126

Levy R. C., et al., 2024, ApJ, 973, L55

Lohner R., 1987, Comput. Methods Appl. Mech. Eng., 61, 323

Lopez L. A., Krumholz M. R., Bolatto A. D., Prochaska J. X., Ramirez-Ruiz E., Castro D., 2014, ApJ, 795, 121

Lucas W. E., Bonnell I. A., Dale J. E., 2020, MNRAS, 493, 4700

Lynden-Bell D., 1967, MNRAS, 136, 101

Makino J., Aarseth S. J., 1992, PASJ, 44, 141

Marchant P., Bodensteiner J., 2024, ARA&A, 62, 21

Matzner C. D., Jumper P. H., 2015, ApJ, 815, 68

Menon S. H., Federrath C., Krumholz M. R., 2023, MNRAS, 521, 5160

Miyoshi T., Kusano K., 2005, J. Comput. Phys., 208, 315

Moe M., Di Stefano R., 2017, ApJS, 230, 15

Nelemans G., Yungelson L. R., Portegies Zwart S. F., Verbunt F., 2001, A&A, 365, 491

Neufeld D. A., Lepp S., Melnick G. J., 1995, ApJS, 100, 132

Nguyen M., Sills A., 2024, ApJ, 969, 18

Nieuwenhuijzen H., de Jager C., 1990, A&A, 231, 134

Nuijten M., Nelemans G., 2025, A&A, 695, A117

Offner S. S. R., Moe M., Kratter K. M., Sadavoy S. I., Jensen E. L. N., Tobin J. J., 2023, in Inutsuka S., Aikawa Y., Muto T., Tomida K., Tamura M., eds, Astronomical Society of the Pacific Conference Series Vol. 534, Protostars and Planets VII. p. 275 (arXiv:2203.10066), doi:10.48550/arXiv.2203.10066

Paczyński B., 1971, ARA&A, 9, 183

Paczynski B., 1976, in Eggleton P., Mitton S., Whelan J., eds, IAU Symposium Vol. 73, Structure and Evolution of Close Binary Systems. p. 75

Pavlovskii K., Ivanova N., Belczynski K., Van K. X., 2017, MNRAS, 465, 2092

Pedregosa F., et al., 2011, Journal of Machine Learning Research, 12, 2825

Pelupessy F. I., van Elteren A., de Vries N., McMillan S. L. W., Drost N., Portegies Zwart S. F., 2013, A&A, 557, A84

Plunkett A. L., Arce H. G., Corder S. A., Dunham M. M., Garay G., Mardones D., 2015, ApJ, 803, 22

Polak B., et al., 2024a, A&A, 690, A94

Polak B., et al., 2024b, A&A, 690, A207

Portegies Zwart S., McMillan S. L. W., 2019, Astrophysical Recipes: The Art of Amuse. Institute of Physics Publishing, Bristol

Portegies Zwart S. F., Verbunt F., 1996, A&A, 309, 179

Portegies Zwart S. F., Makino J., McMillan S. L. W., Hut P., 1999, A&A, 348, 117

Portegies Zwart S., et al., 2009, New Astron., 14, 369

Portegies Zwart S. F., McMillan S. L. W., Gieles M., 2010, ARA&A, 48, 431

Portegies Zwart S., McMillan S. L. W., van Elteren E., Pelupessy I., de Vries N., 2013, Computer Physics Communications, 184, 456

Portegies Zwart S., et al., 2023, AMUSE: the Astrophysical Multipurpose Software Environment, doi:10.5281/zenodo.8409512, `https://doi.org/10.5281/zenodo.8409512`

Rantala A., Naab T., 2025, MNRAS,

Rantala A., Naab T., Lahén N., 2024, MNRAS, 531, 3770

Reimers D., 1975, Memoires of the Societe Royale des Sciences de Liege, 8, 369

Ricker P. M., 2008, ApJS, 176, 293

Ritchie B. W., Clark J. S., Negueruela I., Najarro F., 2022, A&A, 660, A89

Rodríguez-Segovia N., Ruiter A. J., Seitenzahl I. R., 2025, Publ. Astron. Soc. Australia, 42, e012

Rodriguez C. L., et al., 2022, ApJS, 258, 22

Rogers H., Pittard J. M., 2013, MNRAS, 431, 1337

Röpke F. K., De Marco O., 2023, Living Reviews in Computational Astrophysics, 9, 2

Sana H., et al., 2012, Science, 337, 444

Sana H., et al., 2013, A&A, 550, A107

Sana H., et al., 2022, A&A, 668, L5

Schneider F. R. N., et al., 2014, ApJ, 780, 117

Sigurdsson S., Phinney E. S., 1993, ApJ, 415, 631

Simpson C. M., Bryan G. L., Hummels C., Ostriker J. P., 2015, ApJ, 809, 69

Soberman G. E., Phinney E. S., van den Heuvel E. P. J., 1997, A&A, 327, 620

Stanway E. R., Eldridge J. J., 2023, MNRAS, 522, 4430

Sun J., et al., 2018, ApJ, 860, 172

Toonen S., Nelemans G., Portegies Zwart S., 2012, A&A, 546, A70

Turk M. J., Smith B. D., Oishi J. S., Skory S., Skillman S. W., Abel T., Norman M. L., 2011, The Astrophysical Journal Supplement Series, 192, 9

Vanzella E., et al., 2023, ApJ, 945, 53

Vink J. S., 2022, ARA&A, 60, 203

Vink J. S., de Koter A., Lamers H. J. G. L. M., 2000, A&A, 362, 295

Vink J. S., de Koter A., Lamers H. J. G. L. M., 2001, A&A, 369, 574

Walch S., Naab T., 2015, MNRAS, 451, 2757

Wall J. E., McMillan S. L. W., Mac Low M.-M., Klessen R. S., Portegies Zwart S., 2019, ApJ, 887, 62

Wall J. E., Mac Low M.-M., McMillan S. L. W., Klessen R. S., Portegies Zwart S., Pellegrino A., 2020, ApJ, 904, 192

Wang L., Spurzem R., Aarseth S., Nitadori K., Berczik P., Kouwenhoven M. B. N., Naab T., 2015, MNRAS, 450, 4070

Wang L., Nitadori K., Makino J., 2020a, MNRAS, 493, 3398

Wang L., Iwasawa M., Nitadori K., Makino J., 2020b, MNRAS, 497, 536

Wareing C. J., Pittard J. M., Falle S. A. E. G., 2017, MNRAS, 470, 2283

Webbink R. F., 1984, ApJ, 277, 355

Wilson E. C., Nordhaus J., 2022, MNRAS, 516, 2189

Woosley S. E., 2019, ApJ, 878, 49

Zapartas E., et al., 2017, A&A, 601, A29

de Mink S. E., Pols O. R., Hilditch R. W., 2007, A&A, 467, 1181

van den Heuvel E. P. J., 1976, in Eggleton P., Mitton S., Whelan J., eds, IAU Symposium Vol. 73, Structure and Evolution of Close Binary Systems. p. 35

CHAPTER 5

CONCLUSIONS & FUTURE DIRECTIONS

The formation of binary systems within embedded clusters is a natural outcome of the star formation process. It is by far the most common outcome for massive O-type stars, which are formed in clusters, with at least one close companion. The interplay between binary stars and star cluster formation was explored under different angles in this thesis. We presented three separate studies investigating the effects of binary stars and their host clusters on one another during the cluster formation process. Those studies all used numerical simulations, but leveraged new analysis techniques and newly-developed code to tackle different questions. In Chapter 2, we used simulations of cluster formation within GMCs of masses typical of the Milky Way disk to investigate *how the morphology of embedded clusters evolves during star cluster assembly.* In Chapter 3, we used an improved treatment of stellar dynamics to examine *how populations of binaries evolve during the assembly of clusters of different masses.* In Chapter 4, we developed a new framework to incorporate feedback from massive interacting binaries in simulations, to determine *what role feedback from massive interacting binaries plays in halting star formation in massive cluster-forming regions.* We summarize the main results and their implications for massive star cluster formation in Section 5.1, and discuss avenues for future investigation in Section 5.2, before presenting our concluding remarks in Section 5.3.

5.1 Key results and their implications

The concurrent formation of binaries and their host clusters is driven by the competition between gravity, which promotes star formation and drives stellar dynamics, and stellar evolution, which results in mechanical and radiative feedback driving turbulence into the ISM and ejecting gas from star-forming regions. One of the most challenging aspects of this problem, however, is that neither binary evolution nor cluster formation is independent of the other: the cluster formation process modifies the binaries formed within the cluster, while the binaries also affect the evolution of their host cluster via their effects on stellar dynamics and stellar feedback. In Section 5.1.1, we present an overview of the simulations conducted in each chapter, and their key results. We then tie together those results and discuss their broader implications for the formation of massive star clusters by organizing our results into the effects of cluster assembly on populations of binaries (Section 5.1.2) and the effects of binaries on cluster formation (Section 5.1.3).

5.1.1 Overview

In Chapter 2, we studied the assembly process of embedded clusters similar to the ones forming in the Solar neighbourhood. All of our simulations were initialized from spherical GMCs of mass of 10^4 $M_\odot$ and surface density of 50 $M_\odot$ pc^{-2}. We varied the initial virial parameter from $\alpha_{vir} = 0.8$ to $\alpha_{vir} = 4$, and explored different prescriptions for binaries, including simulations with no primordial binaries. We studied the formation history of embedded clusters by characterizing the relative contributions of in-situ star formation, the accretion of stars along filaments, and mergers between subclusters to the clusters' stellar mass, and followed morphological changes associated with these mechanisms. Our simulated clusters have sizes and ellipticities consistent with observed nearby embedded clusters (e.g. Kuhn et al. 2014). We however found that those morphology metrics change on very short timescales ($\lesssim 0.01$ Myr), and provides information about recent or ongoing subcluster mergers and accretion events. We further found that embedded clusters can lose up to half their mass during their assembly. This mass loss is a consequence of the assembly process driven by the large-scale gas structures, which dominate the gravitational potential in low-mass cluster-forming regions. Despite the presence of binaries and the short dynamical timescales of the clusters, internal dynamics do not dominate their evolution, as the timescales for star formation and the accretion of already-formed stars are shorter still than the clusters' crossing times.

An important motivation for the work presented in this thesis was our previous finding that the distributions of binary orbital properties – the primary masses, semi-major

axes, mass ratios, and eccentricities – are modified in the earliest stages of star cluster formation (Cournoyer-Cloutier et al. 2021). This study was however limited to cluster masses of $\lesssim 2 \times 10^3$ $M_\odot$, due to the limitations of our collisional dynamics code, discussed in Section 1.3.2. In Chapter 3, we used an updated treatment of stellar dynamics to study the evolution of binary populations during the formation of clusters of mass $\sim 7.8 \times 10^3$, $\sim 3.4 \times 10^4$, and $\sim 2.0 \times 10^5$ $M_\odot$. Those simulations were initialized from spherical GMCs with masses of 2×10^4, 8×10^4, and 3.2×10^5 $M_\odot$, and surface densities of 130, 520, and 2080 $M_\odot$ pc^{-2}. We used a fixed virial parameter $\alpha_{\rm vir} = 0.5$ and a fixed prescription for primordial binaries, based on observations of binaries and the inner companion in higher-order systems compiled by Moe & Di Stefano (2017). In this chapter, we studied the time evolution of the binary fraction and the distributions of orbital properties in those different environments. At all cluster masses, the binary fraction decreases during cluster formation. The decrease is more pronounced for more massive clusters, and for lower-mass stars within the cluster. It is primarily driven by the disruption of wide ($a > 100$ au) binaries, which proceeds at a higher rate than the formation of wide binaries. The disruption happens in the early stages of cluster formation, when there is a high star formation rate and frequent mergers between subclusters.

In Chapter 4, we presented the first study of massive interacting binaries as a source of feedback in star formation simulations. This required the implementation of a new coupling between stellar dynamics and binary and stellar evolution in Torch, as well as extensive modifications to our feedback and stellar evolution routines. Due to the novelty of both the underlying science question and the numerical techniques used to address it, the simulations presented in Chapter 4 use a more idealized setup than the ones presented in Chapters 2 and 3. For all simulations presented in this study, we compared two background gas surface densities – 10^2 and 10^3 $M_\odot$ – and two treatments of feedback based on single star stellar evolution and binary stellar evolution. The first suite of simulations demonstrates the effects of conservative mass transfer, non-conservative mass transfer, and common envelope ejection for isolated massive binaries in a gaseous medium. The second suite of simulations explores feedback from clusters of massive binaries, in which the combined effects of binary stellar evolution, stellar dynamics, and the gravitational potential of the background gas influence the feedback budget of the cluster. We found that accounting for binary stellar evolution increases the size of H II regions due to the increased thermal pressure compared to the same stars evolved with a single star stellar evolution scheme. We also found that the effects of the gravitational potential from the background gas and nearby stars affect the orbits of the binaries in such a way that their subsequent evolution – and therefore subsequent

feedback – differs from predictions made by standalone binary stellar evolution codes.

5.1.2 The impact of cluster formation on binaries

One of the most important results from this thesis is the fact that *the cluster formation process dictates the properties of a cluster's binary population.* The idea that the cluster formation process itself is responsible for the disruption of binaries beyond the expectation from N-body simulations is further supported by our findings in Cournoyer-Cloutier et al. (2024), which demonstrate that there are bursts of binary disruption associated with subcluster mergers, and that binaries with higher binding energies may be disrupted during those bursts. In our ~ 2 x 10^5 $M_\odot$ cluster, the total binary fraction and the binary fraction for stars with masses below 0.8 $M_\odot$ reach respectively $\sim 15\%$ and $\sim 5\%$ by the end of the simulation, which is consistent with the binary fraction observed in GCs (Milone et al. 2012, 2016). This paints a picture in which the binary fraction of massive star clusters is dictated by their assembly process rather than their evolution as gas-free, spherical systems; this is consistent with the large spread in binary fractions observed for open clusters (Niu et al. 2020; Cordoni et al. 2023; Donada et al. 2023). It may be further connected with the difference in binary fractions observed between enriched and non-enriched stars in GCs (Lucatello et al. 2015; Kamann et al. 2020; Milone et al. 2025): stars with different abundances must be formed either in different locations or at different times, and would therefore experience a different assembly history. Our result stresses the importance of using simulations of cluster formation to inform the initial conditions for N-body simulations of long-term GC evolution.

The cluster formation process is very efficient at disrupting more loosely bound binaries, including fairly close binaries for low-mass stars. Close massive binaries ($a \lesssim$ 100 au) however survive as a population, even if individual system can be disrupted or modified. Another central result of this thesis is thus the fact that although the global binary fraction varies with cluster environment, the fraction of close massive binaries is fairly insensitive to environment, and *massive binaries retain close binary fraction approaching unity in dense YMCs.* This has very important implications for massive cluster formation across cosmic times, as it confirms that feedback (Chapter 4) and enrichment (De Mink et al. 2009; Nguyen & Sills 2024) from massive interacting binaries must be considered when studying GC formation. The populations of close massive binaries in massive star clusters are likely to be even more important at high redshift. Although almost all O stars have a close companion at solar metallicity, this is not the case for B stars, which have close binary fractions $\lesssim 80\%$ (Moe & Di Stefano 2017)

with larger orbital separations than O-star binaries (Offner et al. 2023). Recent observations (Villaseñor et al. 2025) however indicate that the close binary fraction of B-type stars may be larger at lower metallicity, and therefore suggest that close B-type and O-type binaries were ubiquitous in GCs when they formed.

5.1.3 The impact of binaries on cluster formation

Another central result from this thesis is the fact *mass transfer in binaries enhances feedback in cluster-forming regions* by increasing the ionizing luminosity and, to a lesser extent, the FUV luminosity and wind mechanical luminosity compared to models based on single star stellar evolution. The effects of feedback from massive interacting binaries on the ISM are important, as it increases the size of H II regions due to their enhanced thermal pressure, and kinetic and thermal energy. This additional source of feedback may have important consequences for the clearing timescales of YMCs, as binary interaction products can provide significant amounts of feedback prior to the first SN. Although the study presented in Chapter 4 investigated the effects of mass transfer on the post-MS, binary interaction products are expected to be ubiquitous in massive clusters even while massive O-stars are on the MS. Schneider et al. (2014) predict that binary interaction products are expected within the first Myr of the cluster's evolution for YMCs more massive than 10^5 $M_\odot$. The actual timescale may be even shorter, as Schneider et al. (2014) assumed circular orbits for all binaries, and including the effects of high eccentricities increases the fraction of systems that are predicted to interact (Moe & Di Stefano 2017). Dynamical interactions in YMCs are expected to further decrease the semi-major axes (e.g. Heggie 1975; Hills 1975) and increase the eccentricity (Heggie & Rasio 1996; Ivanova et al. 2006) of surviving systems, both of which should lower the timescale for interaction compared to population synthesis studies.

This leads to another important result from this thesis: *the outcome of binary evolution in YMCs is different from that predicted by standalone stellar evolution codes, due to the effects of the gravitational potential from gas and nearby stars on the binaries' orbits.* All the clusters of massive binaries we simulated in Chapter 4 resulted in different timing and stability of mass transfer compared to predictions from standalone binary evolution, and therefore in different mass loss histories and radiation spectra. The differences noted in Chapter 4 are likely a lower limit on the differences expected once we follow the full cluster formation process with interacting binaries. First, the presence of very large numbers of lower-mass stars and binaries will increase the frequency of few-body interactions, and therefore boost the changes to the massive binaries' orbits. Second, the longer evolutionary timescales for the full cluster formation process will also

increase the number of few-body interactions – and therefore increase the amount of changes to the orbits – prior to the onset of mass transfer. Third, the cluster assembly process itself promotes bursts of few-body interactions (e.g. Cournoyer-Cloutier et al. 2024), which may lead to enhanced orbital changes or exchanges. It is therefore expected that the outcome of binary evolution for massive binaries in a cluster will be very different from that predicted by population synthesis studies, or even by studies of binary evolution in gas-free, spherical clusters.

The work presented in Chapter 2 also suggests that *the size and shape of embedded clusters is dictated by ongoing star formation, subcluster mergers, and the accretion of already-formed stars*, and therefore is insensitive to the presence of binaries. The cluster assembly process therefore appears to be responsible for several of the observable properties of embedded clusters. It does not follow, however, that the presence of binaries does not affect stellar dynamics in those clusters. Binaries act as an energy sink during subcluster mergers (Cournoyer-Cloutier et al. 2024), leading to their disruption but preventing the production of unbound stars from the merger process. Using the simulations presented in Chapter 3, Laverde-Villareal et al. (2025) further showed that the presence of binaries speeds up mass segregation in young clusters.

5.2 Looking ahead: the next steps for simulations

The code development and science questions tackled in this thesis open the door for future investigations of the effects of massive binaries on the formation of massive star clusters. In particular, the ability to model feedback from massive binaries that are affected by their environment enables future studies tackling several outstanding questions regarding the formation of massive star clusters in the local Universe and at high redshift. In this section, we outline timely avenues for future investigation as well as possible directions for future code development.

5.2.1 Runaway stars around young massive clusters

Massive stars can be ejected from their birth clusters with high velocities; such massive runaways are observed around the Galactic YMCs M16 (Stoop et al. 2023), NGC 3603 (Drew et al. 2019), and Wd 2 (Drew et al. 2018; Zeidler et al. 2021), as well as around R136 in the LMC (Lennon et al. 2018; Sana et al. 2022; Stoop et al. 2024). The high stellar densities and high multiplicity fraction of massive stars both contribute to the production of runaway stars due to few-body interactions (Poveda et al. 1967), kicks from SNe in binaries (Blaauw 1961), and mergers between subclusters (Stoop et al. 2024;

Polak et al. 2024; Cournoyer-Cloutier et al. 2024). Such massive runaway stars are important for the long-term evolution of galaxies (Kim & Ostriker 2017; Andersson et al. 2020, 2023; Steinwandel et al. 2023); understanding the distribution of ejection times and velocities would therefore lead to an improved understanding of the mechanisms driving galaxy evolution. Wagg et al., (Wagg et al.) have recently provided fits for the distance from their birth cluster at which massive stars undergo SN, based on isolated binary evolution models. Those have however not included the effects of stellar dynamics on the timing and velocity distribution of runaway stars, as their model does not include stellar dynamics, and further assumes that all stars within a cluster are formed simultaneously.

The simulation tools developed in this thesis provide us with all the necessary machinery to make significant progress on this question, as we can now simulate simultaneously hierarchical cluster assembly, collisional stellar dynamics with primordial binaries, and binary stellar evolution. This enables us to self-consistently model all the mechanisms that are currently known to produce runaway stars. Simulations of cluster formation making use of all the code development summarized in this thesis would make it possible to derive fits for SN distance, as done by Wagg et al., (Wagg et al.), that could then be used in galaxy simulations. Such simulations could also be used to investigate the relative contributions of few-body interactions, cluster assembly, and binary evolution to the runaway stars produced by cluster of different masses.

5.2.2 Stellar mergers and the formation of very massive stars

Another natural extension of the work presented in this thesis is the investigation of the formation of very massive stars (VMS, > 100 $M_\odot$) from stellar collisions and binary mergers in YMCs. There is increasing indirect observational evidence for the presence of VMS in high redshift compact star clusters (from signatures of nitrogen enrichment, Smith et al. 2023; Vink 2023). The presence of VMS is expected to impact the subsequent evolution of the clusters, as collision products have different evolutionary timescales and radiation spectra from the pre-merger stars. VMS have high mass loss rates and can make significant contributions to the enrichment of the star-forming gas, with enrichment patterns consistent with the observed enriched population in GCs (Gieles et al. 2018). VMS formation from repeated mergers during hierarchical YMC formation is predicted by simulations that include either primordial binaries (e.g. Rantala & Naab 2025) or star formation and hydrodynamics (e.g. Lahén et al. 2025), but has not yet been investigated in simulations that include both concurrently.

Investigating VMS formation in YMCs in simulations of cluster formation with binary evolution therefore appears as an obvious next step, since hierarchical cluster assembly (Rantala et al. 2024; Lahén et al. 2025), the presence of primordial binaries (Rantala & Naab 2025), and mass transfer (Marchant & Bodensteiner 2024, and references therein) all promote stellar mergers. The simulation framework developed in this thesis allows us to investigate the occurrence rate of stellar mergers in YMCs and whether those mergers are sufficient to form VMS. Accounting for stellar mergers will further change the feedback budget of YMCs, and would thus be a natural extension of our study of feedback from other binary interaction products. Studying concurrently interacting binaries and VMS formation in YMCs would also provide insights on the enrichment sources of the observed light element abundance variations in GCs (Bastian & Lardo 2018).

5.2.3 Self-consistent initial conditions from galaxy simulations

To understand the physical processes driving YMC formation, we need to self-consistently model cluster formation from the scale of massive GMCs ($\gtrsim$ 100 pc) shaped by their host galaxy down to the orbits of individual massive binaries ($\lesssim$ 0.1 au), with an accurate treatment of MHD, star formation, collisional stellar dynamics, and feedback from massive stars and binaries. It is not currently possible to model high-precision stellar dynamics and stellar feedback from individual stars on the scale of entire galaxies. Recent efforts have made it possible to model individual stars in star-forming dwarf galaxies (e.g. Andersson et al. 2023; Lahén et al. 2023; Deng et al. 2024) with collisional stellar dynamics around massive stars (Lahén et al. 2025). Such methods however cannot model individual stars for starbursting spiral galaxies or galaxy mergers – which host the most massive YMCs observed in the local Universe – and have not been attempted with primordial binaries, which increase the computational cost of the stellar dynamics.

An alternative approach is to inherit initial conditions from galaxy simulations. In Lewis et al. (2025), we developed a technique to extract initial conditions from galaxy simulations conducted with an Arepo (Springel 2010; Weinberger et al. 2020) Voronoi mesh and map the gas distribution to an adaptive mesh, as shown in Figure 5.1. Such simulations can be conducted with the collisional stellar dynamics and feedback physics – including feedback from massive interacting binaries – designed for GMC-scale simulations, while providing a more realistic large-scale gas structure. They will allow us to better constrain the formation timescales of YMCs and to calculate age spreads for stars in massive clusters. As the cluster formation process affects both the production of runaway stars (Polak et al. 2024) and binary disruption (Cournoyer-Cloutier et al.

2024), the improved realism of the initial conditions will also improve our treatment of the effects of stellar dynamics on cluster evolution, and allow us to revisit the questions outlined above. The increased ionizing radiation from stripped stars may also affect gas at larger spatial scales, on the order of the size of GMC complexes drawn from galaxy simulations. An outstanding question is whether this enhanced feedback can halt star formation elsewhere in the cluster-forming complex. The effects of binary interaction products ejected from a YMC as runaway stars, for example, can only be investigated with such simulations. Combining initial conditions from galaxy simulations to feedback from massive interacting binaries will therefore be a major step forward.

5.2.4 The role of metallicity and indirect radiation pressure

One important limitation of our cluster formation models is that they are currently restricted to solar metallicity. GCs however most often have sub-solar metallicities (e.g., Carretta et al. 2009; Caldwell et al. 2011; Villaume et al. 2019; Fahrion et al. 2020) while YMCs forming in the local Universe can have solar or slightly super-solar metallicities (e.g., Lardo et al. 2015; Hernandez et al. 2019; Gunawardhana et al. 2020). Metallicity affects gas cooling and therefore star formation (Klessen & Glover 2016), as well as stellar and binary evolution (Shenar et al. 2020) and stellar feedback through wind mass loss rates and velocities (Vink 2022). As metallicity also affects the dust-to-gas ratio (Klessen & Glover 2016), it affects the efficiency of radiation pressure. This leads into another possible limitation of the feedback model currently implemented in Torch, which does not include indirect radiation pressure from reprocessed IR radiation. Such radiation pressure is expected to be important for the most compact star clusters (Krumholz et al. 2019, and references therein).

To compare more directly the formation of massive star clusters in the local Universe to the formation of GC progenitors in metal-poor galaxies at high redshift, updating both the treatment of metallicity and radiation pressure would be necessary. The initial gas-phase metallicity should be allowed to vary, and this metallicity should propagate to the stellar and binary evolution codes. The more challenging update would be to the gas-phase metallicity, which would require an updated treatment of cooling, heating, and radiation pressure. The second part may be more straightforward, as SeBa can be used at different metallicities. Being able to compare the formation of low-metallicity and solar-metallicity clusters with stellar dynamics and feedback from massive interacting binaries would provide us with the most direct comparison between YMC formation in the local Universe and GC formation at high redshift.

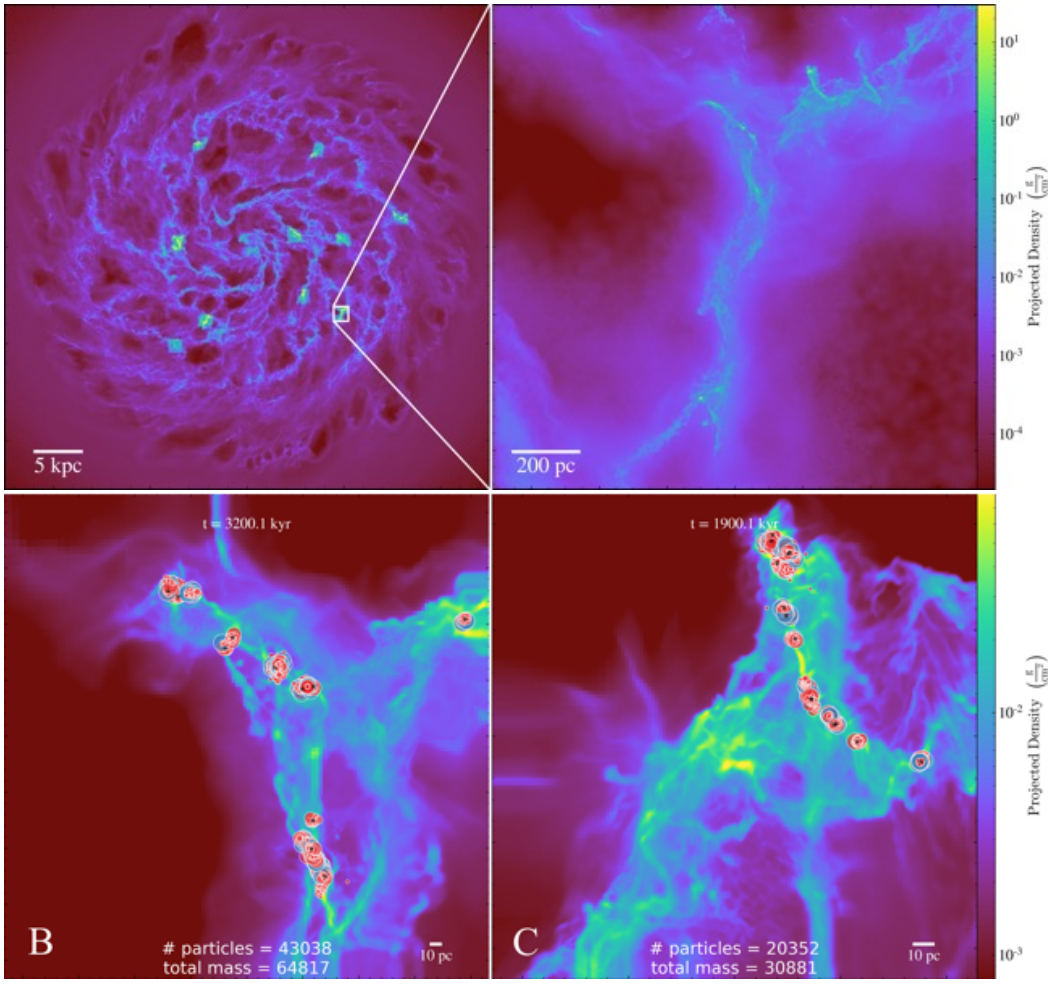

FIGURE 5.1: Extraction of initial conditions from a galaxy simulation (top left), selection of cluster-forming regions of interest (top right), and proof-of-concept simulations of the early stages of YMC formation in the regions of interest (bottom). Adapted from Lewis et al. (2025).

5.3 Concluding remarks

The most common outcome of massive star formation is the formation of a close binary within a star cluster. Previous studies of cluster formation, while acknowledging that massive clusters host rich populations of massive stars – which return large amounts of energy and momentum to their host galaxies and therefore drive their evolution – have however glossed over the fact that almost all of those massive stars are in close

binaries. In this thesis, we have investigated the effects of close binaries on the dynamics and feedback of massive stars, along with the effects of the cluster environment on the binaries it hosts. The numerical methods developed as part of this thesis will also enable us to tackle several questions pertaining to the formation of massive star clusters in the future.

We have demonstrated that the cluster formation process is efficient at disrupting low-mass binaries while allowing massive stars to retain binary fractions approaching unity. This high binary fraction in turn influences cluster formation by enhancing the feedback from the massive stars due to the effects of mass transfer in close binaries. Those results highlight that stellar dynamics, star formation, and stellar feedback are fundamentally interconnected, and that studying one without the others overlooks important physical processes that act over similar timescales during the star formation process.

Bibliography

Andersson E. P., Agertz O., Renaud F., 2020, MNRAS, 494, 3328

Andersson E. P., Agertz O., Renaud F., Teyssier R., 2023, MNRAS, 521, 2196

Bastian N., Lardo C., 2018, ARA&A, 56, 83

Blaauw A., 1961, Bull. Astron. Inst. Netherlands, 15, 265

Caldwell N., Schiavon R., Morrison H., Rose J. A., Harding P., 2011, AJ, 141, 61

Carretta E., Bragaglia A., Gratton R., D'Orazi V., Lucatello S., 2009, A&A, 508, 695

Cordoni G., et al., 2023, A&A, 672, A29

Cournoyer-Cloutier C., et al., 2021, MNRAS, 501, 4464

Cournoyer-Cloutier C., Karam J., Sills A., Zwart S. P., Wilhelm M. J. C., 2024, ApJ, 975, 207

De Mink S. E., Pols O. R., Langer N., Izzard R. G., 2009, A&A, 507, L1

Deng Y., Li H., Liu B., Kannan R., Smith A., Bryan G. L., 2024, A&A, 691, A231

Donada J., et al., 2023, A&A, 675, A89

Drew J. E., Herrero A., Mohr-Smith M., Monguió M., Wright N. J., Kupfer T., Napiwotzki R., 2018, MNRAS, 480, 2109

Drew J. E., Monguió M., Wright N. J., 2019, MNRAS, 486, 1034

Fahrion K., et al., 2020, A&A, 637, A27

Gieles M., et al., 2018, MNRAS, 478, 2461

Gunawardhana M. L. P., et al., 2020, MNRAS, 497, 3860

Heggie D. C., 1975, MNRAS, 173, 729

Heggie D. C., Rasio F. A., 1996, MNRAS, 282, 1064

Hernandez S., et al., 2019, ApJ, 872, 116

Hills J. G., 1975, AJ, 80, 809

Ivanova N., Heinke C. O., Rasio F. A., Taam R. E., Belczynski K., Fregeau J., 2006, MNRAS, 372, 1043

Kamann S., et al., 2020, A&A, 635, A65

Kim C.-G., Ostriker E. C., 2017, ApJ, 846, 133

Klessen R. S., Glover S. C. O., 2016, Saas-Fee Advanced Course, 43, 85

Krumholz M. R., McKee C. F., Bland-Hawthorn J., 2019, ARA&A, 57, 227

Kuhn M. A., et al., 2014, ApJ, 787, 107

Lahén N., et al., 2023, MNRAS, 522, 3092

Lahén N., Naab T., Rantala A., Partmann C., 2025, submitted to MNRAS, arXiv:2504.18620

Lardo C., Davies B., Kudritzki R. P., Gazak J. Z., Evans C. J., Patrick L. R., Bergemann M., Plez B., 2015, ApJ, 812, 160

Laverde-Villareal E., Sills A., Cournoyer-Cloutier C., Arias Callejas V., 2025, ApJ, 989, 22

Lennon D. J., et al., 2018, A&A, 619, A78

Lewis S. C., Polak B., Mac-Low M.-M., McMillan S. L. W., Cournoyer-Cloutier C., Li H., Wilhelm M., Simon P., 2025, submitted to ApJ

Lucatello S., Sollima A., Gratton R., Vesperini E., D'Orazi V., Carretta E., Bragaglia A., 2015, A&A, 584, A52

Marchant P., Bodensteiner J., 2024, ARA&A, 62, 21

Milone A. P., et al., 2012, A&A, 540, A16

Milone A. P., et al., 2016, MNRAS, 455, 3009

Milone A. P., et al., 2025, A&A, 698, A247

Moe M., Di Stefano R., 2017, ApJS, 230, 15

Nguyen M., Sills A., 2024, ApJ, 969, 18

Niu H., Wang J., Fu J., 2020, ApJ, 903, 93

Offner S. S. R., Moe M., Kratter K. M., Sadavoy S. I., Jensen E. L. N., Tobin J. J., 2023, in Inutsuka S., Aikawa Y., Muto T., Tomida K., Tamura M., eds, Astronomical Society of the Pacific Conference Series Vol. 534, Protostars and Planets VII. p. 275 (arXiv:2203.10066), doi:10.48550/arXiv.2203.10066

Polak B., et al., 2024, A&A, 690, A207

Poveda A., Ruiz J., Allen C., 1967, Boletin de los Observatorios Tonantzintla y Tacubaya, 4, 86

Rantala A., Naab T., 2025, MNRAS, 542, L78

Rantala A., Naab T., Lahén N., 2024, MNRAS, 531, 3770

Sana H., et al., 2022, A&A, 668, L5

Schneider F. R. N., et al., 2014, ApJ, 780, 117

Shenar T., Gilkis A., Vink J. S., Sana H., Sander A. A. C., 2020, A&A, 634, A79

Smith L. J., et al., 2023, ApJ, 958, 194

Springel V., 2010, MNRAS, 401, 791

Steinwandel U. P., Bryan G. L., Somerville R. S., Hayward C. C., Burkhart B., 2023, MNRAS, 526, 1408

Stoop M., Kaper L., de Koter A., Guo D., Lamers H. J. G. L. M., Rieder S., 2023, A&A, 670, A108

Stoop M., et al., 2024, Nature, 634, 809

Villaseñor J. I., et al., 2025, A&A, 698, A41

Villaume A., Romanowsky A. J., Brodie J., Strader J., 2019, ApJ, 879, 45

Vink J. S., 2022, ARA&A, 60, 203

Vink J. S., 2023, A&A, 679, L9

Wagg T., et al.„ submitted to ApJ, arXiv:2504.17903

Weinberger R., Springel V., Pakmor R., 2020, ApJS, 248, 32

Zeidler P., Sabbi E., Nota A., McLeod A. F., 2021, AJ, 161, 140